

MECHANISTIC STUDIES OF WATER OXIDATION AND CARBON DIOXIDE  
REDUCTION USING TRANSITION METAL CATALYSTS  
WITH PROTIC LIGANDS

by

DALTON BODINE BURKS

ELIZABETH T. PAPISH, COMMITTEE CHAIR  
DAVID A. DIXON  
PAUL A. RUPAR  
KEVIN H. SHAUGHNESSY  
JASON E. BARA

A DISSERTATION

Submitted in partial fulfillment of the requirements  
for the degree of Doctor of Philosophy in the  
Department of Chemistry and Biochemistry  
in the Graduate School of  
The University of Alabama

TUSCALOOSA, ALABAMA

2019

Copyright Dalton Bodine Burks 2019  
ALL RIGHTS RESERVED

## ABSTRACT

The majority of energy produced in the world is derived from fossil fuels which are finite and have deleterious environmental effects. For a sustainable and environmentally-friendly energy future, alternative, renewable energy sources are desired. Two reactions that could have applications towards developing renewable energy sources are water oxidation to produce hydrogen and carbon dioxide reduction to form various products (e.g. formic acid or carbon monoxide); however, these reactions require catalysts to efficiently produce the desired products. Efforts to synthesize, characterize, and study catalysts for these reactions are discussed in this dissertation.

The first chapter serves as an introduction to energy-related catalytic reactions. In Chapter 2, 6,6'-dihydroxybipyridine (6,6'-dhbp)—a protic ligand used with several metals to produce catalysts for energy-related reactions—is studied to determine its thermodynamic acidity. In the following chapter, 6,6'-dhbp is used as a ligand with copper to form complexes that are water oxidation catalysts.

Chapters 4 and 5 focus on iridium and ruthenium complexes containing new bidentate ligands composed of pyridinol and N-heterocyclic carbenes (NHCs). These complexes, along with an iridium complex of 6,6'-dhbp, were used as catalysts for the hydrogenation of carbon dioxide to formate and the reverse dehydrogenation of formic acid to carbon dioxide and hydrogen. However, the complexes containing the new

bidentate pyridinol-NHC ligands were found to be precatalysts as they undergo transformations and decomposition during the course of the reaction.

A nickel-pincer complex with a protic CNC-pincer derived of pyridinol and NHCs was used as a photocatalyst for carbon dioxide reduction in Chapter 6. The protic state of the hydroxy group in the 4-position of the pyridine ring was determined to be important for catalysis, as the deprotonated hydroxy group results in 10 times the catalytic ability as the protonated form.

In the penultimate chapter, ruthenium-pincer complexes that are active carbon dioxide photoreduction catalysts are studied mechanistically by UV/vis and IR spectroscopies. The most active catalyst was studied in greater detail with real-time IR spectroscopy to help elucidate potential reaction pathways. The final chapter serves as a conclusion to summarize the results discussed in the dissertation.

## LIST OF ABBREVIATIONS AND SYMBOLS

aq	Aqueous
Å	Angstrom
ATR-IR	Attenuated Total Reflectance Infrared Spectroscopy
BIH	1,3-dimethyl-2-phenyl-2,3-dihydro-1H- benzo[d]-imidazole
bipy	2,2'-bipyridine
CNC	Pincer complex with C, N, and C binding to metal center
Cp*	Pentamethylcyclopentadienyl anion
CV	Cyclic Voltammetry
deHY	Dehydrogenation
DFT	Density Functional Theory
DLG	Deidra L. Gerlach
DMF	Dimethylformamide
DMSO	Dimethylsulfoxide
dhbp	Dihydroxybipyridine
6,6'-dhbp	6,6'-dihydroxy-2,2'-bipyridine
dmbp	Dimethoxybipyridine
6,6'-dmbp	6,6'-dimethoxy-2,2'-bipyridine
EA	Elemental Analysis
Eq.	Equivalent

EPR	Electron Paramagnetic Resonance Spectroscopy
ESI-MS	Electrospray Ionization Mass Spectrometry
FA	Formic Acid
Fc	Ferrocene
h	Hour
HCO <sub>2</sub> H	Formic Acid
<sup>1</sup> H-NMR	Proton Nuclear Magnetic Resonance
HY	Hydrogenation
Hz	Hertz
Im	Imidazole
IR	Infrared Spectroscopy
J	Joule
KC <sub>8</sub>	Potassium-Intercalated Graphite
L	Ligand
M	Metal
MeCN	Acetonitrile
Me	Methyl
MLCT	Metal-to-Ligand Charge Transfer
MS	Mass Spectrometry
NaHCO <sub>3</sub>	Sodium Bicarbonate
NHC	N-Heterocyclic Carbene
NHC-py <sup>OR</sup>	Bidentate ligand composed of NHC and pyridinol
NHE	Normal Hydrogen Electrode
OEC	Oxygen Evolving Complex

OH	Hydroxy
OMe	Methoxy
O <sup>t</sup> Bu	tert-Butoxy
OTf	Trifluoromethanesulfonate (or triflate)
PCET	Proton-Coupled Electron Transfer
PF <sub>6</sub>	Hexafluorophosphate
Ph	Phenyl
PS	Photosensitizer
PSII	Photosystem II
psig	Pounds Per Square Inch Gauge
Py	Pyridine
QToF	Quadrupole Time of Flight
SB	Salome Bhagan
SD	Sacrificial Donor
SHE	Standard Hydrogen Electrode
SI	Supporting Information
SS	Sophie Siek
TEA	Triethylamine
TfOH	Triflic Acid
THF	Tetrahydrofuran
TON	Turnover Number
TOF	Turnover Frequency
XRD	X-ray Diffraction

## ACKNOWLEDGEMENTS

I am happy to be able to thank everyone who helped shape my research projects and shape myself into the scientist I am today. First and foremost, I would like to thank my advisor, Dr. Elizabeth Papish, for always mentoring and supporting me throughout my time in graduate school. I would also like to thank the remainder of my committee—Dr. David Dixon, Dr. Paul Rugar, Dr. Kevin Shaughnessy, and Dr. Jason Bara—for taking the time to give insightful input and encouragement on my research throughout my time in graduate school.

I was fortunate to work with other members of the Papish group—graduate students, undergraduates, and postdocs, both past and present—who were willing to provide suggestions and tips for my research. I especially thank Dr. Deidra Gerlach for mentoring me in the lab early in my graduate school career. I would also like to thank the rest of the lab: Dr. Fengrui Qu, Dr. Sophie Siek, Jessica Gray, Sanjit Das, Chance Boudreaux, Wenzhi Yao, Courtney Thompson, Jamie Tesh, Jack Fitzgerald, Alexa DeRegnaucourt, Stefan Knorr, and Daniel Hayes.

I would like to express appreciation to the chemistry departmental staff for helping and advising on experiments, including Dr. Ken Belmore for help with NMR and Dr. Qiaoli Liang for help with MS. I would also like to thank all of the collaborators I've had the pleasure to work with in the course of my research, including Dr. Jared Delcamp and group (The University of Mississippi), Dr. Edwin Webster and Robert

Lamb (Mississippi State University), and Dr. Doug Grotjahn and group (San Diego State University).

While in graduate school, I was lucky to receive several fellowships, so I would like to acknowledge the Graduate Council Fellowship, the GAANN fellowship program, and the National Alumni Association Graduate Fellowship. I would also like to acknowledge The University of Alabama, the Department of Chemistry and Biochemistry, and the National Science Foundation for further financial support.

Finally, I would also like to thank all of my family and friends, especially my parents, for their endless support and encouragement.

## CONTENTS

ABSTRACT .....	ii
LIST OF ABBREVIATIONS AND SYMBOLS.....	iv
ACKNOWLEDGEMENTS .....	vii
LIST OF TABLES .....	xii
LIST OF FIGURES.....	xv
CHAPTER 1: INTRODUCTION.....	1
CHAPTER 2: THERMODYNAMIC ACIDITY STUDIES OF 6,6'-DIHYDROXY-2,2'- BIPYRIDINE: A COMBINED EXPERIMENTAL AND COMPUTATIONAL APPROACH.....	9
2.1 Introduction .....	9
2.2 Results and Discussion .....	12
2.3 Conclusion .....	34
2.4 Experimental .....	35
2.5 Author Contribution .....	36
2.6 References.....	36
2.7 Supporting Information.....	39
CHAPTER 3: STUDIES OF THE PATHWAYS OPEN TO COPPER WATER OXIDATION CATALYSTS CONTAINING PROXIMAL HYDROXY GROUPS DURING BASIC ELECTROLYSIS.....	44
3.1 Introduction .....	44
3.2 Results and Discussion .....	46
3.3 Conclusion .....	66

3.4 Experimental .....	67
3.5 Author Contribution .....	67
3.6 References.....	67
3.7 Supporting Information.....	70
<b>CHAPTER 4: IRIDIUM AND RUTHENIUM COMPLEXES OF N-HETEROCYCLIC CARBENE- AND PYRIDINOL-DERIVED CHELATES AS CATALYSTS FOR AQUEOUS CARBON DIOXIDE HYDROGENATION AND FORMIC ACID DEHYDROGENATION: THE ROLE OF THE ALKALI METAL.....</b>	
4.1 Introduction .....	75
4.2 Results and Discussion.....	77
4.3 Conclusion .....	97
4.4 Experimental .....	98
4.5 Author Contribution .....	102
4.6 References.....	102
4.7 Supporting Information.....	108
<b>CHAPTER 5: RUTHENIUM(II) AND IRIDIUM(III) COMPLEXES OF N-HETEROCYCLIC CARBENE AND PYRIDINOL DERIVED BIDENTATE CHELATES: SYNTHESIS, CHARACTERIZATION, AND REACTIVITY.....</b>	
5.1 Introduction .....	145
5.2 Results and Discussion .....	148
5.3 Conclusion.....	156
5.4 Experimental.....	156
5.5 Author Contribution .....	158
5.6 References.....	158
5.7 Supporting Information.....	165

CHAPTER 6: NICKEL(II) PINCER COMPLEXES DEMONSTRATE THAT THE REMOTE SUBSTITUENT CONTROLS CATALYTIC CARBON DIOXIDE REDUCTION .....	171
6.1 Introduction .....	171
6.2 Results and Discussion .....	173
6.3 Conclusion .....	180
6.4 Experimental .....	181
6.5 Author Contribution .....	182
6.6 References.....	182
6.7 Supporting Information.....	186
CHAPTER 7: SPECTROSCOPIC AND MECHANISTIC STUDIES OF RUTHENIUM-CNC PINCER COMPLEXES FOR CARBON DIOXIDE REDUCTION CATALYSIS.....	218
7.1 Introduction.....	218
7.2 Results and Discussion .....	223
7.3 Conclusion.....	235
7.4 Experimental.....	236
7.5 Author Contribution .....	238
7.6 References.....	238
7.7 Supporting Information.....	242
CHAPTER 8: CONCLUSION AND FUTURE WORK.....	260
REFERENCES .....	264

## LIST OF TABLES

1.1 The reactions of water oxidation, hydrogen evolution reaction, and overall water splitting. Standard potentials are in aqueous solution at pH 0.....	3
1.2 Selected aqueous CO <sub>2</sub> reduction processes and standard reduction potentials. <sup>a</sup> Reduction potential of CO <sub>2</sub> to CO in acetonitrile.....	4
2.1 Relative energies (kcal/mol).....	21
2.2 UV-Vis transitions and intensities as predicted by TD-DFT at the B <sub>3</sub> LYP/DZVP2 level.....	27
2.3 Calculated and Experimental <sup>1</sup> H-NMR chemical shifts in ppm. ....	30
2.4 Calculated and Experimental <sup>13</sup> C-NMR chemical shifts in ppm.....	30
2.5 G3(MP2) gas phase acidities (kcal/mol) and pK <sub>a</sub> values.....	33
4.1 Thermodynamic acidity (pK <sub>a</sub> ) values for the protic metal complexes ( <b>2</b> , <b>4Ru</b> , <b>4Ir</b> ) studied herein and the free ligand, 6,6'-dhbp.....	80
4.2 Catalytic hydrogenation of CO <sub>2</sub> with <b>1-5</b> .....	83
4.3 Effect of the Lewis acid on CO <sub>2</sub> hydrogenation with <b>4Ir</b> .....	85
4.4 Dehydrogenation of formic acid by catalysts <b>1-5</b> .....	88
4.S1 Quantitative poisoning of <b>3</b> during CO <sub>2</sub> hydrogenation.....	111
4.S2 Quantitative poisoning attempts during CO <sub>2</sub> hydrogenation.....	112
4.S3 Table of the calculation of k <sub>obs</sub> for <b>1</b> during CO <sub>2</sub> hydrogenation from the pressure vs time data.....	114
4.S4 Table of the calculation of k <sub>obs</sub> for <b>2</b> during CO <sub>2</sub> hydrogenation from the pressure vs time data.....	116
4.S5 Table of the calculation of k <sub>obs</sub> for <b>3</b> during CO <sub>2</sub> hydrogenation from the pressure vs time data.....	118

4.S6 Table of the calculation of $k_{\text{obs}}$ for <b>4Ir</b> during CO <sub>2</sub> hydrogenation from the pressure vs time data .....	120
4.S7 Table of the calculation of $k_{\text{obs}}$ for <b>5Ir</b> during CO <sub>2</sub> hydrogenation from the pressure vs time data .....	122
4.S8 Table of the calculation of $k_{\text{obs}}$ for <b>4Ru</b> during CO <sub>2</sub> hydrogenation from the pressure vs time data .....	124
4.S9 Table of the calculation of $k_{\text{obs}}$ for <b>5Ru</b> during CO <sub>2</sub> hydrogenation from the pressure vs time data .....	126
4.S10 The $k_{\text{obs}}$ , calculated as the slope a linear fit of pressure vs time for hours 2-18, for all 7 catalysts .....	126
4.S11 TON of <b>1</b> calculated from the pressure data collected during a standard hydrogenation reaction.....	127
4.S12 TON of <b>2</b> calculated from the pressure data collected during a standard hydrogenation reaction.....	129
4.S13 TON of <b>3</b> calculated from the pressure data collected during a standard hydrogenation reaction.....	131
4.S14 TON of <b>4Ir</b> calculated from the pressure data collected during a standard hydrogenation reaction.....	133
4.S15 TON of <b>5Ir</b> calculated from the pressure data collected during a standard hydrogenation reaction.....	135
4.S16 TON of <b>4Ru</b> calculated from the pressure data collected during a standard hydrogenation reaction.....	137
4.S17 TON of <b>5Ru</b> calculated from the pressure data collected during a standard hydrogenation reaction.....	139
4.S18 The experimental TON and pressure-estimated TON at 18 h for <b>1-5</b> .....	142
5.1 Numbering scheme for the compounds studied here .....	149
5.2 Selected bond lengths and angles of the complexes <b>8-15</b> .....	154
5.3 Catalytic CO <sub>2</sub> hydrogenation and FA dehydrogenation of complex <b>8</b> and <b>9</b> .....	156
5.S1 Single Crystal X-Ray Structure Determination Parameters .....	168
6.1 Photocatalytic CO <sub>2</sub> reduction under varied conditions.....	179

6.S1 $\omega_{\text{CO}}$ and $\nu_{\text{CO}}$ of <b>3</b> , <b>3A</b> , and select carbonyl containing compounds (in $\text{cm}^{-1}$ ) .....	213
6.S10 Photocatalysis in the absence and presence of Hg over time .....	217
7.1 Catalyst performance of complexes <b>1-5</b> for carbon dioxide reduction to carbon monoxide without a photosensitizer .....	219
7.2 Observed frequencies from the IR spectra of reduced <b>5</b> after 20 minutes of exposure to $\text{CO}_2$ or $^{13}\text{CO}_2$ .....	228

## LIST OF FIGURES

1.1 The structure of the protic ligand 6,6'-dihydroxybipyridine in the protonated and deprotonated form, along with the resonance forms of the deprotonated form .....	2
2.1 UV-vis spectra of an aqueous solution of 6,6'-dhbp at varying pH from 2 to 14.....	13
2.2 (Top) UV-vis spectra of an aqueous solution of dhbp at varying pH from 8.5 to 14. (Bottom) Shows the presence of minor peaks around 500 nm at pH 10-11.....	14
2.3 (Top) <sup>1</sup> H-NMR spectra as a function of pH. (Bottom) Assignments of peaks in the <sup>1</sup> H-NMR spectra.....	16
2.4 <sup>13</sup> C NMR spectra at pH 11.29 and 12.12.....	17
2.5 Optimized structures for isomers and protonation states (-2 to +2) for 6,6'-dhbp. Bond lengths (G3(MP2) level in Å) reported for the lowest energy isomers in gas phase and solution .....	21
2.6 Optimized structures for the cis isomer of 6,6'-dhbp lactam and 6,6'-dhbp lactam <sup>-1</sup> with (a) three water molecules for the neutral lactam, (b) two water molecules for the anion, and (c) three water molecules for the anion .....	28
2.7 Overlay of experimental UV-vis spectra at 3 different pHs with TD-DFT spectra of the proposed dhbp species at each pH (represented by columns) .....	29
2.8 Optimized structures for isomers and protonation states (-1 to +1) for pyridin-2-ol .....	32
2.S1 ATR-FTIR spectrum of 6,6'-dhbp in the solid state.....	39
2.S2 ATR-FTIR spectrum of 6,6'-dhbp in DMSO .....	40
2.S3 IR spectrum of 6,6'-dhbp in anhydrous DMSO .....	40
2.S4 UV-vis spectra of an aqueous solution of 6,6'-dhbp from 200-500 nm and pH of ~2 to ~13.5 .....	41
2.S5 UV-vis spectra of an aqueous solution of 6,6'-dhbp from 200-600 nm and pH of ~8.5 to ~14 .....	41
2.S6 UV-vis absorbance values of 6,6'-dhbp at 340 nm (black squares) and 354 nm (red circles) with the pH changing from 2 to 14 .....	42

2.S7 Linear fits of the linear region of Figure 2.S6, approximately pH 7 to 10, for both the absorbance values at 340 nm (black) and 354 nm (red) .....	42
2.S8 The UV-vis absorbance values of 6,6'-dhbp at 332 nm (black squares) and 354 nm (red circles) with the pH changing from 8.5 to 14 .....	43
2.S9 Linear fits of the linear region of Figure S8, approximately pH 11 to 13.5, for both the absorbance values at 332 nm (black) and 354 nm (red) .....	43
3.1 Structural diversity of complexes (1 – 5) prepared for this study .....	46
3.2 Structural diagram of the fully protonated complex, [(6,6'-dhbp) <sub>2</sub> Cu(CH <sub>3</sub> OH)]SO <sub>4</sub> ( <b>1a</b> ) .....	49
3.3 Structural diagram of the doubly deprotonated complex, [(6-OH-6'-O-bpy) <sub>2</sub> Cu]•(CH <sub>3</sub> OH) <sub>2</sub> ( <b>1c</b> ) .....	49
3.4 Copper (II) complex of 6,6'-dimethoxybipyridine ( <b>3</b> ) with the formula unit [(6,6'-dmbp) <sub>2</sub> Cu(NO <sub>3</sub> ) <sub>2</sub> ][Cu(NO <sub>3</sub> ) <sub>4</sub> ]. Ellipsoids are shown at 30% probability .....	51
3.5 Structural diagram of [(6,6'-dmbp)Cu(SO <sub>4</sub> )(CH <sub>3</sub> OH)] ( <b>4</b> ) .....	51
3.6 Structural diagram of [(6,6'-dhbp) <sub>2</sub> Zn](ClO <sub>4</sub> ) <sub>2</sub> •3CH <sub>3</sub> CN ( <b>5</b> ) .....	52
3.7 Left: UV-Vis absorption spectra of aqueous solutions of [(6,6'-dhbp) <sub>2</sub> Cu]SO <sub>4</sub> ( <b>1</b> ) as a function of pH from pH = 2.5-11 at 25 °C. Middle: Same as left but from pH = 4.5 – 6.5 in 0.1 pH increments, and the inset shows the full peak shape. Right: Plot of absorbance (at λ = 369 nm) vs. pH at 25°C, and the inset shows the same plot from pH 5.0 to 6.5.....	54
3.8 UV-Vis absorption spectra of aqueous solutions of [(6,6'-dhbp) <sub>2</sub> Cu]SO <sub>4</sub> ( <b>1</b> ) as a function of pH from pH = 9.3-13.4 at 25 °C.....	54
3.9 Calculated speciation diagram from pH 2.5 to 10 based upon the pK <sub>a</sub> values for [Cu(6,6'-dhbp) <sub>2</sub> ] <sup>2+</sup> ( <b>1a</b> ) and the EPR experiments .....	56
3.10 HYSCORE spectrum at pH 11 of Left) complex <b>1</b> and Right) CuSO <sub>4</sub> in 10% glycol. ....	59
3.11 Cyclic voltammogram (CV) plots (non-background corrected) of 1.0 mM [(6,6'-dhbp) <sub>2</sub> Cu]SO <sub>4</sub> ( <b>1a</b> ) as a function of pH on glassy carbon, scan rate = 100 mV/s in water with 0.1 M NaOAc/NaOH.....	61
3.12 CV plots as a function of scan rate of for a 1.0 mM pH 12.6 solution of complex <b>1</b> on glassy carbon in water with 0.1 M NaOAc/NaOH, corrected for background .....	62

3.13 Simulated CVs of aqueous complex <b>1</b> at varied scan rate compared to experimental (Figure 3.11) for the mechanistic fitting of the data .....	62
3.14 Comparison of 1 mM solution of complexes <b>1</b> , <b>4</b> , and <b>5</b> at pH 12.6 in 0.1M NaOAc at glassy carbon electrode at 100 mV/s scan rate .....	64
3.S1 Titration of complex <b>1</b> using UV/vis from pH 2.5 to 10.9 .....	71
3.S2 Titration of complex <b>1</b> using UV/vis from pH 9.3 to 13.4.....	71
3.S3 (Left) Plot of absorbance at 357 and 331 nm vs pH from above titration experiment (Figure S2). (Right) Expanded view of absorbance vs pH plot for determining the pH at which 50 % of complex <b>1</b> has lost the 6,6'-dhhbp ligand.....	72
3.S4 Titration of complex <b>2</b> using UV/vis from pH 3.5 to 11.5.....	72
3.S5 Plot of absorbance vs pH for complex <b>2</b> from above titration.....	73
3.S6 Speciation diagram showing the relative amount of Species A-D via CW simulations of complex <b>1</b> ranging from pH 10 to 13.3 .....	73
3.S7 Cyclic voltammogram of the scan rate dependence of blank electrolyte NaOAc .....	74
4.1 The aqueous UV/visible absorption spectra of the yellow complexes <b>1</b> , <b>2</b> , <b>3</b> , <b>4<sub>Ir</sub></b> and <b>5<sub>Ir</sub></b> show absorptions primarily in the UV region .....	81
4.2 Diagram of minima with relative energies (solvent corrected energies in kcal/mol) of CO <sub>2</sub> hydrogenation catalyzed by <b>4<sub>Ir</sub></b> and <b>5<sub>Ir</sub></b> with the assistance of Na <sup>+</sup> ion .....	90
4.3 The free energy diagram (solvent corrected energies in kcal/mol) of CO <sub>2</sub> insertion into the iridium hydride of <b>4<sub>Ir</sub></b> and <b>5<sub>Ir</sub></b> with and without the assistance of a Na <sup>+</sup> ion .....	93
4.4 Diagram of minima with relative energies (solvent corrected energies in kcal/mol) of intramolecular proton transfer involved formic acid dehydrogenation catalyzed by <b>4<sub>Ir</sub></b> and <b>5<sub>Ir</sub></b> .....	95
4.5 Diagram of minima with relative energies (solvent corrected energies in kcal/mol) of intermolecular proton transfer involved formic acid dehydrogenation catalyzed by <b>4<sub>Ir</sub></b> and <b>5<sub>Ir</sub></b> .....	95
4.S1 Potentiometric titration curve for the pK <sub>a</sub> determination of complex <b>2</b> .....	108
4.S2 Comparison of aqueous UV/vis absorption spectra of complexes <b>1-3</b> to the in situ generation of the aqua bound complexes <b>1'-3'</b> with AgOTf shows only minor changes in the absorption spectra with halide removal .....	109

4.S3 UV/vis absorption spectra of aqueous [Cp*IrCl(NHC <sup>Me</sup> -py <sup>OR</sup> )]OTf complexes before and after hydrogenation. ....	109
4.S4 UV/vis absorption spectra of aqueous [Cp*IrCl(dxbp)]OTf complexes before and after hydrogenation. ....	110
4.S5 Plots of pressure vs time (grey) and temperature vs time (crimson) for <b>1</b> over the 18 h reaction period of CO <sub>2</sub> hydrogenation, under the standard reaction conditions as listed in the experimental section of the manuscript .....	113
4.S6 Plot of pressure vs time for <b>1</b> from 1-18 h with a linear fit of the curve .....	113
4.S7 Plots of pressure vs time (grey) and temperature vs time (crimson) for <b>2</b> over the 18 h reaction period of CO <sub>2</sub> hydrogenation, under the standard reaction conditions as listed in the experimental section of the manuscript .....	115
4.S8 Plot of pressure vs time for <b>2</b> from 1-18 h with a linear fit of the curve.....	115
4.S9 Plots of pressure vs time (grey) and temperature vs time (crimson) for <b>3</b> over the 18 h reaction period of CO <sub>2</sub> hydrogenation, under the standard reaction conditions as listed in the experimental section of the manuscript .....	117
4.S10 Plot of pressure vs time for <b>3</b> from 1-18 h with a linear fit of the curve .....	117
4.S11 Plots of pressure vs time (grey) and temperature vs time (crimson) for <b>4<sub>Ir</sub></b> over the 18 h reaction period of CO <sub>2</sub> hydrogenation, under the standard reaction conditions as listed in the experimental section of the manuscript .....	119
4.S12 Plot of pressure vs time for <b>4<sub>Ir</sub></b> from 1-18 h with a linear fit of the curve.....	119
4.S13 Plots of pressure vs time (grey) and temperature vs time (crimson) for <b>5<sub>Ir</sub></b> over the 18 h reaction period of CO <sub>2</sub> hydrogenation, under the standard reaction conditions as listed in the experimental section of the manuscript .....	121
4.S14 Plot of pressure vs time for <b>5<sub>Ir</sub></b> from 1-18 h with a linear fit of the curve .....	121
4.S15 Plots of pressure vs time (grey) and temperature vs time (crimson) for <b>4<sub>Ru</sub></b> over the 18 h reaction period of CO <sub>2</sub> hydrogenation, under the standard reaction conditions as listed in the experimental section of the manuscript .....	123
4.S16 Plot of pressure vs time for <b>4<sub>Ru</sub></b> from 1-18 h with a linear fit of the curve.....	123
4.S17 Plots of pressure vs time (grey) and temperature vs time (crimson) for <b>5<sub>Ru</sub></b> over the 18 h reaction period of CO <sub>2</sub> hydrogenation, under the standard reaction conditions as listed in the experimental section of the manuscript .....	125
4.S18 Plot of pressure vs time for <b>5<sub>Ru</sub></b> from 1-18 h with a linear fit of the curve.....	125

4.S19 Plot of the pressure-estimated TON vs time for <b>1</b> .....	130
4.S20 Plot of the pressure-estimated TON vs time for <b>2</b> .....	130
4.S21 Plot of the pressure-estimated TON vs time for <b>3</b> .....	132
4.S22 Plot of the pressure-estimated TON vs time for <b>4<sub>Ir</sub></b> .....	134
4.S23 Plot of the pressure-estimated TON vs time for <b>5<sub>Ir</sub></b> .....	136
4.S24 Plot of the pressure-estimated TON vs time for <b>4<sub>Ru</sub></b> .....	138
4.S25 Plot of the pressure-estimated TON vs time for <b>5<sub>Ru</sub></b> .....	140
4.S26 Overlaid plots of the pressure-estimated TON vs time for <b>1-5</b> .....	141
4.S27 Plot of pressure (crimson) and temperature (grey) vs reaction time for CO <sub>2</sub> hydrogenation reaction with <b>4<sub>Ir</sub></b> in 0.5 M NaHCO <sub>3</sub> .....	143
4.S28 Plot of pressure (crimson) and temperature (grey) vs reaction time for CO <sub>2</sub> hydrogenation reaction with <b>4<sub>Ir</sub></b> in 0.5 M KHCO <sub>3</sub> .....	143
4.S29 Plot of pressure (crimson) and temperature (grey) vs reaction time for CO <sub>2</sub> hydrogenation reaction with <b>4<sub>Ir</sub></b> in 0.5 M CsHCO <sub>3</sub> .....	144
4.S30 Plot of pressure (crimson) and temperature (grey) vs reaction time for CO <sub>2</sub> hydrogenation reaction with <b>4<sub>Ir</sub></b> in 0.5 M NH <sub>4</sub> HCO <sub>3</sub> .....	144
5.1 The ORTEP diagrams with 50% probability ellipsoids of [( <i>p</i> -cym)Ru(NHC <sup>Me</sup> - py <sup>OMe</sup> )Cl]OTf <b>8</b> (top left), [( <i>p</i> -cym)Ru(NHC <sup>Me</sup> -py <sup>OTBu</sup> )Cl]OTf <b>9</b> (top right), and [( <i>p</i> -cym)Ru(NHC <sup>Me</sup> -py <sup>OH</sup> )Cl]OTf <b>10</b> (bottom).....	152
5.2 The ORTEP diagrams with 50% probability ellipsoids of [( <i>p</i> -cym)Ru(NHC <sup>Me</sup> - py <sup>OTBu</sup> )Cl]PF <sub>6</sub> <b>11</b> (left) and [( <i>p</i> -cym)Ru(NHC <sup>Et</sup> -py <sup>OMe</sup> )Cl]PF <sub>6</sub> <b>12</b> (right) .....	153
5.3 The ORTEP diagrams with 50% probability ellipsoid of [Cp*Ir(NHC <sup>Me</sup> -py <sup>OTBu</sup> )Cl]PF <sub>6</sub> <b>14</b> (top) and [Cp*Ir(NHC <sup>Me</sup> -py <sup>OH</sup> )Cl]PO <sub>2</sub> F <sub>2</sub> <b>15</b> (bottom). .....	153
6.1 (a) Ru(II) photocatalysts ( <b>1</b> : TON =250, <b>2</b> : TON = 3) for CO <sub>2</sub> reduction and (b) Ni(II) complexes <b>3</b> and <b>4</b> .....	173
6.2 CVs of <b>3</b> under argon, CO <sub>2</sub> , and CO <sub>2</sub> with added water .....	175
6.3 An energy level diagram with each catalyst, an estimated reduction potential range for CO <sub>2</sub> , the PS, and each SD .....	176
6.4 Turnover number versus time plot for photocatalytic reactions with complexes <b>3</b> and <b>4</b> .....	178

6.5 Computational study of CO <sub>2</sub> reduction from two different protonation states. Relative energies are in blue.....	180
6.S1 NMR formate calibration curve in d <sub>3</sub> -MeCN with ferrocene as an internal standard with Verkade's base .....	188
6.S2 Example GC-trace for photocatalytic reaction with <b>Catalyst 3</b> after 5hrs .....	188
6.S3 Example GC-trace for photocatalytic reaction with <b>Catalyst 4</b> after 5hrs .....	189
6.S4 Cyclic voltammograms of complex <b>3</b> initially under argon (black), after being exposed to ambient light at room temperature for an hour under argon (blue) and under CO <sub>2</sub> (red) .....	190
6.S5 Cyclic voltammograms of complex <b>3</b> under argon (black), after being exposed to ambient light at room temperature for various times under argon. ....	191
6.S6 A generic photocatalytic cycle for the reductive disproportionation of CO <sub>2</sub> to CO and CO <sub>3</sub> <sup>2-</sup> .....	191
6.S7 CV of proton sponge in MeCN under Ar atmosphere. 0.1 M Bu <sub>4</sub> NPF <sub>6</sub> used as the supporting electrolyte and glassy carbon as the working electrode, and Pt is the counter and pseudo reference electrodes.....	192
6.S8 CVs of <b>3</b> under argon, CO <sub>2</sub> and with TfOH present under argon.....	192
6.S9 <sup>1</sup> H-NMR (360 MHz) spectrum of complex <b>3</b> in d <sub>6</sub> -DMSO.....	193
6.S10 ESI(+)-MS of complex <b>3</b> where M is NiON <sub>5</sub> C <sub>13</sub> H <sub>12</sub> and HCOOH is formic acid from the MS solvent.....	194
6.S11 FT-IR (ATR) of complex <b>3</b> in the solid state.....	194
6.S12 <sup>1</sup> H-NMR (360 MHz) spectra of complex <b>3</b> in d <sub>6</sub> -DMSO (blue spectrum) with the addition of 0.5 equivalents of AgOTf (green spectrum), 1.0 equivalents of AgOTf (red spectrum), and 10 equivalents of AgOTf (purple spectrum) .....	196
6.S13 <sup>1</sup> H-NMR (360 MHz) spectra of complex <b>3</b> in d <sub>6</sub> -DMSO (red spectrum) with the addition of 10 equivalents of acetonitrile (grey spectrum). ....	196
6.S14 UV-vis spectra of complex <b>3</b> (0.26 mM) in DMSO with the addition of a 0.08 M triflic acid solution in DMSO.....	197
6.S15 UV-vis spectra of complex <b>3</b> (0.26 mM) in DMSO with the addition of a 0.08 M sulfamic acid solution in DMSO.....	197

6.S16 UV-vis spectra of complex <b>3</b> (0.28 mM) in DMSO with the alternating addition of triflic acid (1 eq., red spectra) and proton sponge (1 eq., blue spectra), showing the reversibility of the protonation and deprotonation. ....	198
6.S17 FT-IR spectra of complex <b>3</b> (8.3 mM) in DMSO (black spectra) with the addition of 1 equivalent of triflic acid (red spectra). ....	198
6.S18 (Left) FT-IR spectrum of DMSO after a background of DMSO was taken. (Right) FT-IR spectrum of triflic acid in DMSO .....	199
6.S19 FT-IR spectra of complex <b>3</b> (5.5 mM) in DMSO (black spectra) with the addition of 1 equivalent of deuterated-triflic acid (red spectra). ....	199
6.S20 FT-IR spectrum of d-triflic acid in DMSO .....	200
6.S21 FT-IR spectra of complex <b>3</b> (6.5 mM) in DMSO (black spectra) with the addition of multiple equivalents of sulfamic acid. ....	200
6.S22 FT-IR spectrum of sulfamic acid in DMSO .....	201
6.S23a <sup>1</sup> H-NMR spectra of a solution of complex <b>3</b> in d <sub>6</sub> -DMSO (blue spectrum) with the addition of 1 equivalent of triflic acid (red spectrum), followed by the addition of 1 equivalent of proton sponge (violet spectrum). ....	201
6.S23b The aromatic region of the <sup>1</sup> H-NMR spectra shown in Figure S21a .....	202
6.S24 <sup>1</sup> H-NMR (360 MHz) spectrum of complex <b>3A</b> in d <sub>6</sub> -DMSO .....	203
6.S25 Overlaid <sup>1</sup> H-NMR spectra of complexes <b>3</b> (crimson spectrum) and <b>3A</b> (grey spectrum) in d <sub>6</sub> -DMSO. ....	204
6.S26 <sup>19</sup> F-NMR (338.8 MHz) spectrum of complex <b>3A</b> in d <sub>6</sub> -DMSO .....	205
6.S27 FT-IR (ATR) spectrum of complex <b>3A</b> in the solid state .....	205
6.S28 FT-IR (ATR) spectra of complexes <b>3</b> (black spectrum) and <b>3A</b> (red spectrum) in the solid state. ....	206
6.S29a MALDI-MS spectrum of complex <b>3A</b> .....	206
6.S29b MALDI-MS spectrum of complex <b>3A</b> . ....	207
6.S30 Changes in select bond lengths (Å), ω <sub>CO</sub> (cm <sup>-1</sup> ), and percent change in negative charge, % (as measured by change in NAO charges for protonation, reduction, or chloride dissociation events) with PCM-B3LYP/BS1 .....	210

6.S31 Changes in select bond lengths ( $\text{\AA}$ ), $\omega_{\text{CO}}$ ( $\text{cm}^{-1}$ ), and percent change in negative charge, % (as measured by change in NAO charges for protonation, reduction, or chloride dissociation events) with PCM-PBEPBE-auto/BS1.....	211
6.S32 Computed $\omega_{\text{CO}}$ vs experimental $\nu_{\text{CO}}$ for neutral carbonyl containing compounds.....	214
6.S33 Possible electrochemical events with <b>3</b> for generation of species responsible for catalysis in acetonitrile (PCM-B3LYP/BS1). .....	215
6.S34 Possible reactions of <b>3</b> and <b>5</b> with triflate in DMSO (PCM-B3LYP/BS1).....	216
6.S35 Relative energy ( $\text{kcal mol}^{-1}$ ) of binding of $\text{CO}_2$ to the neutral vs. protonated proposed catalyst (PCM-B3LYP/BS1).....	217
7.1 Structures of $\text{CO}_2$ reduction catalysts studied by the Papish group. <b>1–5</b> are studied in this chapter .....	220
7.2 Pathways for $\text{CO}_2$ reduction by a metal-centered catalyst.....	221
7.3 Coordination modes of $\text{CO}_2$ .....	222
7.4 UV/vis spectra of a 0.15 mM solution of <b>5</b> in acetonitrile: unreduced (black), reduced with 2 equivalents of $\text{KC}_8$ (crimson), and reduced with 2 equivalents of $\text{KC}_8$ followed by exposure to $\text{CO}_2$ (grey) .....	223
7.5 ATR-IR spectra in the solid state of unreduced <b>5</b> (black), reduced <b>5</b> ( <b>5<sub>red</sub></b> , reduced with 2 equivalents $\text{KC}_8$ , crimson), and reduced <b>5</b> with $\text{CO}_2$ ( <b>5<sub>red</sub>+CO<sub>2</sub></b> , grey). .....	225
7.6 (Left) ReactIR spectra of <b>5</b> (reduced with 2 eq. $\text{KC}_8$ ) and $\text{CO}_2$ monitored over a 20 minute period. (Right) Overlaid IR spectra obtained from the ReactIR after 0 minutes (black), 5 minutes (red), 10 minutes (blue), and 20 minutes (green) exposure to $\text{CO}_2$ .....	226
7.7 (Left) ReactIR spectra of <b>5</b> (reduced with 2 eq. $\text{KC}_8$ ) and $^{13}\text{CO}_2$ monitored over a 90 minute period. (Right) Overlaid IR spectra obtained from the ReactIR after 0 minutes (black), 10 minutes (red), 20 minutes (blue), 60 minutes (green), and 90 minutes (purple) exposure to $^{13}\text{CO}_2$ .....	227
7.8 Overlaid IR spectra of <b>5</b> (reduced with 2 eq. $\text{KC}_8$ ) after 20 minutes of exposure to $\text{CO}_2$ (blue) or $^{13}\text{CO}_2$ (red) .....	228
7.9 Possible binding pathways of $\text{CO}_2$ to <b>5</b> .....	229
7.10 ReactIR spectra of unreduced <b>5</b> and $\text{CO}_2$ over a 90 minute period.....	229
7.11 ReactIR spectra of unreduced <b>5</b> and $^{13}\text{CO}_2$ over a 90 minute period.....	229

7.12 (Left) Full IR spectrum of reduced <b>5</b> in acetonitrile after stirring under 240 psig of CO(g) for 24 h. (Right) Area of interest of the IR spectrum of reduced <b>5</b> with CO. Peaks of interest are labeled in wavenumbers (cm <sup>-1</sup> ) .....	231
7.13 Proposed catalytic cycle for carbon dioxide reduction to carbon monoxide with a proton source present .....	234
7.S1 UV/vis spectra of a 0.15 mM solution of <b>1</b> in acetonitrile .....	242
7.S2 UV/vis spectra of a 0.15 mM solution of <b>2</b> in acetonitrile .....	242
7.S3 UV/vis spectra of a 0.15 mM solution of <b>3</b> in acetonitrile .....	243
7.S4 UV/vis spectra of a 0.15 mM solution of <b>4</b> in acetonitrile .....	243
7.S5 ATR-IR spectra in the solid state of unreduced <b>1</b> (black), reduced <b>1</b> ( <b>1<sub>red</sub></b> , reduced with 4 equivalents KC <sub>8</sub> , crimson), and reduced <b>1</b> with CO <sub>2</sub> ( <b>1<sub>red</sub>+CO<sub>2</sub></b> , grey) .....	244
7.S6 ATR-IR spectra in the solid state of unreduced <b>2</b> (black), reduced <b>2</b> ( <b>2<sub>red</sub></b> , reduced with 3 equivalents KC <sub>8</sub> , crimson), and reduced <b>2</b> with CO <sub>2</sub> ( <b>2<sub>red</sub>+CO<sub>2</sub></b> , grey).....	244
7.S7 ATR-IR spectra in the solid state of unreduced <b>3</b> (black), reduced <b>3</b> ( <b>3<sub>red</sub></b> , reduced with 3 equivalents KC <sub>8</sub> , crimson), and reduced <b>3</b> with CO <sub>2</sub> ( <b>3<sub>red</sub>+CO<sub>2</sub></b> , grey).....	244
7.S8 ATR-IR spectra in the solid state of unreduced <b>4</b> (black), reduced <b>4</b> ( <b>4<sub>red</sub></b> , reduced with 2 equivalents KC <sub>8</sub> , crimson), and reduced <b>4</b> with CO <sub>2</sub> ( <b>4<sub>red</sub>+CO<sub>2</sub></b> , grey) .....	245
7.S9 QToF-ESI-MS of <b>1<sub>red</sub>+CO<sub>2</sub></b> .....	246
7.S10 QToF-ESI-MS of <b>2<sub>red</sub>+CO<sub>2</sub></b> .....	247
7.S11 QToF-ESI-MS of <b>3<sub>red</sub>+CO<sub>2</sub></b> .....	248
7.S12 QToF-ESI-MS of <b>4<sub>red</sub>+CO<sub>2</sub></b> .....	249
7.S13 QToF-ESI-MS of <b>5<sub>red</sub>+CO<sub>2</sub></b> .....	250
7.S14 QToF-ESI-MS of reduced <b>5</b> after stirring for 24 h under 240 psig of CO(g). .....	251
7.S15 (Left) ReactIR spectra of <b>5</b> (reduced with 2 eq. KC <sub>8</sub> ) and CO monitored over a 90 minute period. (Right) Overlaid IR spectra obtained from the ReactIR after 0 minutes (black), 10 minutes (red), 20 minutes (blue), 60 minutes (green), and 90 minutes (purple) exposure to CO .....	252

7.S16 (Left) ReactIR spectra of unreduced <b>5</b> with CO over a 90 minute period. (Right) Overlaid IR spectra obtained from the ReactIR after 0 minutes (black), 10 minutes (red), 20 minutes (blue), 60 minutes (green), and 90 minutes (purple) exposure to CO.....	252
7.S17 (Left) ReactIR spectra of <b>5</b> (reduced with 2 eq. KC <sub>8</sub> ) and <sup>13</sup> CO monitored over a 90 minute period. (Right) Overlaid IR spectra obtained from the ReactIR after 0 minutes (black), 10 minutes (red), 20 minutes (blue), 60 minutes (green), and 90 minutes (purple) exposure to <sup>13</sup> CO.....	253
7.S18 (Left) IR spectrum of acetonitrile purged with CO(g) for 30 minutes, measured with the ReactIR instrument. The doublet of peaks at 1995 and 2024 cm <sup>-1</sup> are assigned to CO. (Right) IR spectrum of acetonitrile purged with CO <sub>2</sub> (g) for 5 minutes, measured with the ReactIR instrument.....	253
7.S19 (Left) ReactIR spectra of <b>5</b> (reduced with 2 eq. KC <sub>8</sub> ) and formic acid (FA) monitored over a 90 minute period. (Right) Overlaid IR spectra obtained from the ReactIR after 0 minutes (black), 10 minutes (red), 20 minutes (blue), 60 minutes (green), and 90 minutes (purple) exposure to FA. ....	254
7.S20 (Left) ReactIR spectra of unreduced <b>5</b> and formic acid (FA) monitored over a 90 minute period. (Right) Overlaid IR spectra obtained from the ReactIR after 0 minutes (black), 10 minutes (red), 20 minutes (blue), 60 minutes (green), and 90 minutes (purple) exposure to FA.....	254
7.S21 IR spectrum of formic acid in acetonitrile.....	255
7.S22 Possible reaction pathways with computed energies.....	257

## CHAPTER 1: INTRODUCTION

Global energy consumption in 2018 grew to  $6 \times 10^{20}$  J, and fossil fuels accounted for 80 percent of the total energy sources.<sup>1</sup> Consequently, energy-related CO<sub>2</sub> emissions hit a record high in 2018.<sup>1</sup> Because of the large CO<sub>2</sub> emissions, the use of non-renewable fossil fuels results in several negative impacts, including climate change, health issues, and economic losses, among other problematic issues.<sup>2-3</sup> With a growing population and growing energy demand in developing countries, global energy consumption is expected to increase. Due to the inevitable depletion of fossil fuels and the negative impacts, alternative sources of energy production are desired.

There are several potential reactions that could have applications toward developing sustainable, renewable sources of energy production. Some of these reactions are water oxidation,<sup>4</sup> CO<sub>2</sub> reduction,<sup>5</sup> and biomass conversion to fuels.<sup>6-8</sup> However, there is a need for catalysts to effectively and efficiently drive these reactions, and the development of catalysts for these reactions is a large area of research. In addition, the development of catalysts containing first-row transition metals, which are cheaper and more abundant than precious metals, is desired if a catalyst is going to be used on an industrial scale. Catalysts containing precious metals are generally more active than analogous catalysts containing first-row transition metals; however, the use

of an appropriate ligand system can influence the catalytic ability, giving a first-row transition metal-containing catalyst high catalytic activity.

Protic ligands have been used in the literature as catalysts for several types of reactions, including hydrogenation/dehydrogenation<sup>9-13</sup> and water oxidation.<sup>14-15</sup> Protic ligands offer several advantageous benefits. Deprotonation of a hydroxy group results in a strong electron-donating oxyanion, which can enhance catalytic activity.<sup>14</sup> Oxyanion groups can also act as pendant bases to help hold a proton near the metal-center, where catalysis occurs, which can help facilitate catalysis involving proton transfer events.<sup>10, 13</sup>

One example of a protic ligand is 6,6'-dihydroxybipyridine (6,6'-dhbp, Figure 1.1). 6,6'-dhbp has been used as a ligand with several metals to create catalysts for multiple types of reactions.<sup>13-14</sup> When deprotonated, the oxyanion donates more electron density toward the metal center which can enhance the catalytic ability of the catalyst.<sup>14</sup>

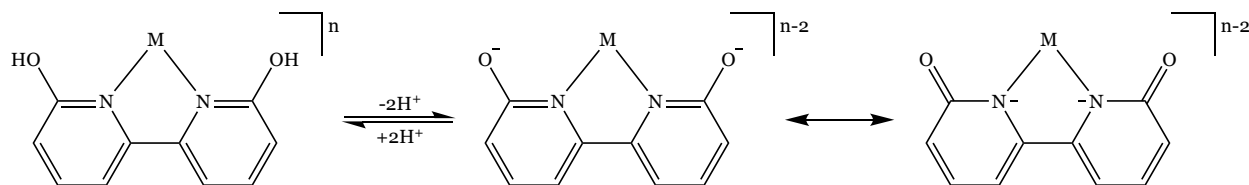


*Figure 1.1.* The structure of the protic ligand 6,6'-dihydroxybipyridine in the protonated and deprotonated form, along with the resonance forms of the deprotonated form.

The splitting of water—formally water oxidation and proton reduction, Table 1.1—is a method to produce hydrogen gas, which could be used as a fuel source, for example in hydrogen fuel cells, or as a source of hydrogen gas for chemical synthesis (e.g. hydrogenations). In nature, photosynthesis converts water to protons, electrons, and dioxygen in the oxygen-evolving complex (OEC) of Photosystem II (PSII).<sup>16</sup> The OEC is composed of a cluster of four manganese atoms and a calcium atom, and the structure of the OEC is conserved in all photosynthetic plants.<sup>17</sup>

Due to the efficiency and ubiquity of the OEC in nature, many catalysts have been designed to try to replicate the efficiency of the OEC. The first homogeneous water oxidation catalyst published in the literature was Meyer’s blue dimer, published in 1982, which is a ruthenium-containing complex.<sup>18</sup> Since then, many complexes have been synthesized as catalysts for water oxidation; these catalyst have used several metal centers, both precious metals and first-row transition metals, including ruthenium,<sup>19</sup> iridium,<sup>20-22</sup> manganese,<sup>23-24</sup> iron,<sup>25-26</sup> cobalt,<sup>27-28</sup> copper,<sup>29-30</sup> and nickel.<sup>31-32</sup>

The standard potential for converting water to dioxygen, 4 protons, and 4 electrons is 1.23 V vs NHE in aqueous solution at pH 0 (Table 1.1). However, due to the high kinetic barrier of oxygen production, an overpotential—the voltage applied in excess of the standard potential—is usually necessary to drive the reaction to an appreciable amount.<sup>4</sup> A low overpotential is desired for a practical water oxidation catalyst, and efforts to produce catalysts with low overpotentials are ongoing in the literature. One potential method to achieve a lower overpotential is to use catalysts that can promote proton-coupled electron transfer (PCET). In PCET, the electron and proton are transferred concertedly in one-step which can result in lower potentials by resulting in more stable intermediates.<sup>19, 33</sup>

Water Oxidation	$2\text{H}_2\text{O} \rightarrow \text{O}_2 + 4\text{H}^+ + 4\text{e}^-$	$E^\circ = 1.23\text{ V vs NHE}$
Hydrogen Evolution Reaction	$2\text{H}^+ + 2\text{e}^- \rightarrow \text{H}_2$	$E^\circ = 0.00\text{ V vs NHE}$
Overall Water Splitting	$2\text{H}_2\text{O} \rightarrow \text{O}_2 + 2\text{H}_2$	$\Delta G^\circ = 113.5\text{ kcal/mol}$

*Table 1.1.* The reactions of water oxidation, hydrogen evolution reaction, and overall water splitting. Standard potentials are in aqueous solution at pH 0.<sup>5</sup>

Carbon dioxide reduction is another potential method to produce possible alternative fuels (e.g. methanol), traditional carbonaceous fuels (e.g. reduction to CO

followed by Fischer-Tropsch chemistry), or C1 feedstock chemicals.<sup>34-36</sup> Carbon dioxide reduction can be performed either thermochemically, electrochemically, or photochemically. The direct reduction of CO<sub>2</sub> to CO<sub>2</sub><sup>-</sup> has a fairly large negative potential; however, the involvement of protons and multiple electrons can reduce the energy required for CO<sub>2</sub> reduction (Table 1.2). PCET can also decrease the energy required for CO<sub>2</sub> reduction by lowering the activation barrier relative to electron transfer followed by protonation due to the formation of more thermodynamically stable products.<sup>37</sup> The reduction potentials of CO<sub>2</sub> reductions shift slightly when performed in nonaqueous solution; for example, the potential of the reduction of CO<sub>2</sub> to CO shifts from -0.53 V vs NHE in aqueous solution to -0.75 V vs NHE in acetonitrile, a common solvent for CO<sub>2</sub> reduction reactions (Entry 7 in Table 1.2).<sup>38</sup> Catalysts are required to efficiently reduce CO<sub>2</sub> to the desired product—the catalyst, therefore, must be selective for the desired product (e.g. CO or CH<sub>3</sub>OH) and must be selective for CO<sub>2</sub> reduction over proton reduction.

Entry	Reduction Process	E <sup>0</sup> (V vs NHE)
1	CO <sub>2</sub> + e <sup>-</sup> → CO <sub>2</sub> <sup>-</sup>	-1.9
2	CO <sub>2</sub> + 2H <sup>+</sup> + 2e <sup>-</sup> → CO + H <sub>2</sub> O	-0.53
3	CO <sub>2</sub> + 2H <sup>+</sup> + 2e <sup>-</sup> → HCO <sub>2</sub> H	-0.61
4	CO <sub>2</sub> + 4H <sup>+</sup> + 4e <sup>-</sup> → HCHO + H <sub>2</sub> O	-0.48
5	CO <sub>2</sub> + 6H <sup>+</sup> + 6e <sup>-</sup> → CH <sub>3</sub> OH + H <sub>2</sub> O	-0.38
6	CO <sub>2</sub> + 8H <sup>+</sup> + 8e <sup>-</sup> → CH <sub>4</sub> + 2H <sub>2</sub> O	-0.24
7 <sup>a</sup>	CO <sub>2</sub> + 2H <sup>+</sup> (solv) + 2e <sup>-</sup> → CO + H <sub>2</sub> O(solv)	-0.75 <sup>a</sup>

*Table 1.2.* Selected aqueous CO<sub>2</sub> reduction processes and standard reduction potentials.<sup>5</sup>  
<sup>a</sup>Reduction potential of CO<sub>2</sub> to CO in acetonitrile.<sup>38</sup>

Thermochemical reduction of CO<sub>2</sub> typically involves a hydrogenation reaction, commonly to formic acid or methanol (the thermal equivalents of Entry 3 and 5, respectively, in Table 1.2).<sup>39-41</sup> Due to problems with storing and transporting gaseous hydrogen and the low volumetric energy density of hydrogen gas, hydrogenated products of carbon dioxide could serve as hydrogen storage media if the products can be dehydrogenated to release hydrogen at the point of use.<sup>42</sup> Conveniently, some catalysts that promote hydrogenation of carbon dioxide also promote the reverse dehydrogenation reaction of formic acid.<sup>43-46</sup>

The first homogeneous catalyst for CO<sub>2</sub> hydrogenation was reported by Inoue et al. in 1976.<sup>47</sup> Since then, many homogeneous catalysts have been reported for CO<sub>2</sub> hydrogenation that include precious metals, such as iridium,<sup>10-11, 48-50</sup> and ruthenium.<sup>51</sup> Catalysts containing first-row transition metals, such as Fe<sup>52-54</sup> and Co,<sup>12, 55-57</sup> have also been studied. CO<sub>2</sub> hydrogenation reactions typically involve high temperatures, high pressures of CO<sub>2</sub>(g) and H<sub>2</sub>(g), and/or strong base.

Aqueous reactions are desired due to the use of water as a green solvent; however, CO<sub>2</sub> hydrogenation in aqueous solution is complicated by the acid-base equilibria of CO<sub>2</sub> in water. When dissolved in water, CO<sub>2</sub> partially forms bicarbonate (HCO<sub>3</sub><sup>-</sup>) and carbonate (CO<sub>3</sub><sup>2-</sup>); the amounts of each are dependent upon several variables, including pH of the solution, pressure of CO<sub>2</sub>, and temperature.<sup>58-59</sup> However, in the literature, “hydrogenation of CO<sub>2</sub>” is commonly used to cover the hydrogenation of CO<sub>2</sub> and potentially its dissolved products, CO<sub>3</sub><sup>2-</sup> and HCO<sub>3</sub><sup>-</sup>.

Photochemical and electrochemical reduction of CO<sub>2</sub> avoid the high temperatures and pressures required for hydrogenations. Electrochemical reduction of CO<sub>2</sub> on an industrial scale would be enormously energy intensive; however, photochemical

reduction has the benefit of using solar energy to power the reduction.<sup>34</sup> Photochemical reduction to carbon monoxide (Entry 2, Table 2) is of interest due to the ability to convert carbon monoxide into traditional carbonaceous fuels (e.g. gasoline) through the Fischer-Tropsch process<sup>60</sup> or to be used as a C1 building block in chemical synthesis (e.g. carbonylation reactions).<sup>61-63</sup>

Typical photocatalytic CO<sub>2</sub> reduction systems involve a catalyst, sacrificial electron and proton donors, and a photosensitizer. In a typical photocatalytic cycle, the photosensitizer is photoexcited and then accepts an electron from the sacrificial electron donor. The reduced photosensitizer then transfers an electron to the catalyst, resulting in a reduced catalyst. This process of light absorption by the photosensitizer and subsequent reduction of the catalyst can be repeated to produce the necessary electrons for the reduction of CO<sub>2</sub>.<sup>64</sup> While the use of a photosensitizer is most common, some catalysts in the literature are also able to act as photosensitizers themselves.<sup>65-66</sup>

Ultimately, an ideal system for generating alternative fuels would couple a reductive step with an oxidative step and be powered by abundant sunlight in a form of artificial photosynthesis. Artificial photosynthesis is a means to store solar energy directly in chemical bonds using solar energy as the driving force for the reaction. In artificial photosynthesis, the oxidation step (e.g. water oxidation) mimics Photosystem II (PSII), and the reductive step (e.g. CO<sub>2</sub> reduction) takes the place of Photosystem I (PSI).<sup>67</sup> For example, carbon dioxide reduction could be coupled with water oxidation to mimic photosynthesis—the oxidation of water results in protons and electrons that can be used for the reduction of CO<sub>2</sub>.<sup>68</sup>

The work described herein will include results from synthesis, characterization, catalytic studies, and mechanistic studies of catalysts used for energy-related catalytic

reactions. In chapter 2, a protic ligand, 6,6'-dihydroxybipyridine (6,6'-dhbp), is studied by UV/vis, IR, and NMR spectroscopies to determine the  $pK_a$  values and tautomeric states of the free ligand, which has applications for synthesizing catalysts containing 6,6'-dhbp. The following chapter focuses on copper complexes containing 6,6'-dhbp as catalysts for water oxidation. The  $[Cu(6,6'\text{-dhbp})_2]^{2+}$  complex was studied by UV/vis to determine the  $pK_a$  of the complex and to determine the pH at which demetallation occurs.

The next two chapters focus on ruthenium and iridium complexes of bidentate ligands containing a N-heterocyclic carbene (NHC) and/or pyridinol; these complexes were tested as catalysts for aqueous carbon dioxide hydrogenation to formate and the reverse dehydrogenation of formic acid to  $CO_2$ . In Chapter 4, the iridium complex containing a protic bidentate ligand was studied to determine the acidity of the hydroxyl group, and the iridium complexes were tested as catalysts to determine their efficacy as catalysts and to determine the effect that the alkali metal has on catalysis. In Chapter 5, the crystal structures of the ruthenium bidentate ligand complexes were reported, as well as the results of catalytic testing.

Chapter 6 includes the synthesis and characterization of a nickel complex containing a protic CNC-pincer ligand composed of pyridinol and NHCs which was used as a catalyst for photochemical  $CO_2$  reduction. The Ni-pincer complex was characterized by NMR, UV/vis, IR, and MS spectroscopies, and the  $pK_a$  of the complex was studied in DMSO. In the penultimate chapter, ruthenium complexes of CNC-pincer ligands that are  $CO_2$  reduction photocatalysts were studied mechanistically by several spectroscopic techniques, including UV/vis, MS, IR, and real-time IR spectroscopies, to help elucidate

potential catalytic pathways of CO<sub>2</sub> reduction to CO. The final chapter serves as a conclusion to summarize the results presented herein.

CHAPTER 2:  
THERMODYNAMIC ACIDITY STUDIES OF 6,6'-DIHYDROXY-2,2'-BIPYRIDINE:  
A COMBINED EXPERIMENTAL AND COMPUTATIONAL APPROACH

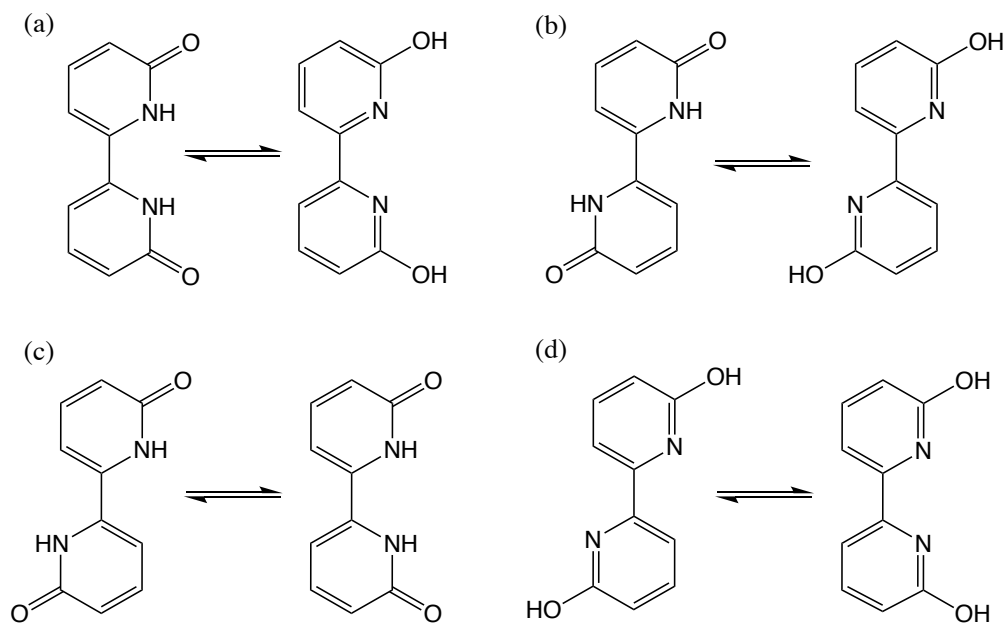
Adapted from Burks, D. B.; Vasiliu, M.; Dixon, D. A.; Papish, E. T. *J. Phys. Chem. A*, 2018, 122, 2221-2231.

## 2.1 Introduction

Our group and others have performed extensive work on metal complexes of 6,6'-dihydroxy-2,2'-bipyridine (6,6'-dhbp, Scheme 1) which serve as catalysts for many organic and inorganic transformations.<sup>1-3</sup> The organic molecule, 6,6'-dhbp, was known prior to our studies,<sup>4-5</sup> but its low solubility in several solvents hindered its initial use in the synthesis of metal complexes and other applications. When 6,6'-dhbp is bound to a late transition metal, the chelation through two nitrogen donor atoms means that OH groups (or O<sup>-</sup> groups when deprotonated) are near the metal center but cannot readily bind to that metal. This means that the OH/O<sup>-</sup> groups in pyridinol based ligands can serve to facilitate proton transfer steps in catalysis in a biomimetic fashion.<sup>6-9</sup> Metal complexes of 6,6'-dhbp are catalysts or pre-catalysts in many reactions including the hydrogenation of carbon dioxide,<sup>10-14</sup> dehydrogenation of formic acid<sup>11-12, 15</sup> and alcohols,<sup>16</sup> and water oxidation.<sup>17-19</sup> Most significantly, this ligand allows for the catalytic

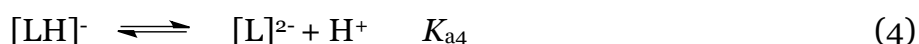
ability and other properties to be tuned by changes in pH, as the deprotonated ligand pushes more electron density towards the metal center.<sup>17-18, 20-21</sup>

The neutral free ligand 6,6'-dhbp can exist in two tautomeric forms, the pyridinol tautomer and the amide (lactam) tautomer (Scheme 1). The free ligand actually exists as the amide tautomer as identified by IR spectroscopy, but the pyridinol tautomer has the proper configuration to bind transition metals.<sup>1, 22-24</sup> The free ligand has two rotational conformers: cis or trans (Scheme 1c and 1d). As shown in Scheme 1, there are various ligand interconversion processes that can occur involving both tautomerization and sigma bond rotation. Only the cis-pyridinol tautomer is configured properly to bind transition metals, but experimental and computational work (*vide infra*) shows the trans-lactam isomer is the ground state. A critical goal of this study was to determine the lowest energy conformation for each protonation state.

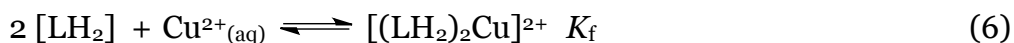
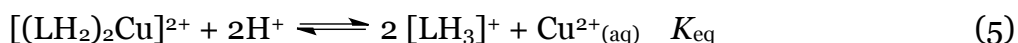


**Scheme 2.1.** Interconversion of structures of 6,6'-dhbp involving the (a) amide or lactam (left) and the pyridinol (right) cis tautomers, (b) lactam (left) and pyridinol (right) trans tautomers, (c) trans- (left) and cis- (right) lactam rotational conformers, and (d) trans- (left) and cis- (right) pyridinol rotational conformers.

Knowledge of the thermodynamic acidity for the 6,6'-dhbp ligand ( $\text{LH}_2$ ) in terms of both protonation ( $+\text{H}^+$ ,  $+2\text{H}^+$ ) and deprotonation ( $-\text{H}^+$ ,  $-2\text{H}^+$ ) is necessary for understanding how the formation constants ( $K_f$ ) for the metal complexes change as a function of pH. We can define four  $K_a$  values according to equations 1-4.



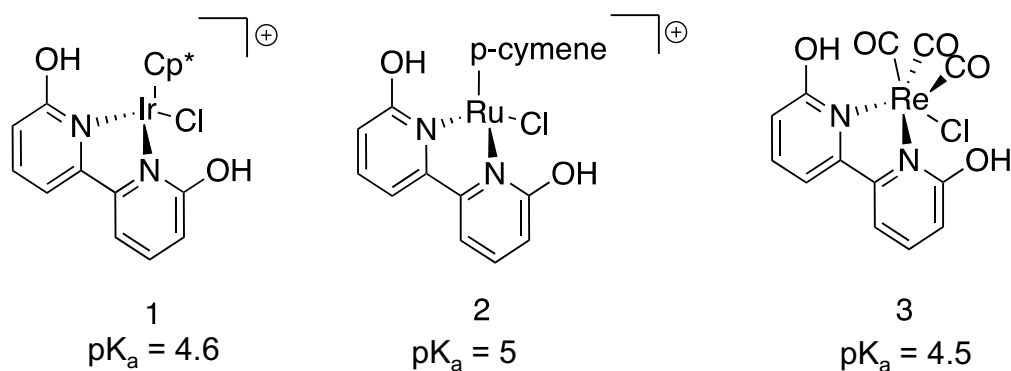
Since the anionic forms of 6,6'-dhbp, namely  $[\text{LH}]^-$  and  $[\text{L}]^{2-}$ , are stronger ligands than the neutral form, it would be helpful to know the pH at which these anionic forms predominate to better control synthetic procedures. Furthermore, the equilibrium between a metal complex of 6,6'-dhbp and the products that result upon addition of acid (e.g. eq. 5<sup>25</sup> which involves  $[\text{Cu}(\text{6,6}'\text{-dhbp})_2]^{2+}$ )<sup>18</sup> can only be well understood if all the  $\text{p}K_a$  values are known. The thermodynamic acidity values then allow us to derive formation constants (eq. 6) from pH dependent equilibrium constants (like those in eq. 5).



However, the free ligand 6,6'-dhbp (and also 4,4'-dhbp) have solubility properties that render quantitative measures of acidity difficult. As neutral molecules, these compounds are insoluble in water, alcohols (except trifluoroethanol), and most organic solvents at room temperature. This insolubility stems from very strong hydrogen bonds between molecules in the dilactam form; strong hydrogen bonds are well-precedented for related molecules such as 4-hydroxyterpyridine.<sup>23</sup> Not surprisingly, deprotonation or

protonation of 4,4'-dhbp or 6,6'-dhbp results in better solubility in water and acetonitrile, due to formation of charged moieties, but still solubility in the neutral state is needed to measure the  $pK_a$  accurately. Lin and co-workers were able to estimate  $pK_{a3}$  at 8.5 (eq. 3)<sup>22</sup> but thus far the remaining  $pK_a$  values have not been determined. In this work, we have taken a combined computational and spectroscopic approach to determine these  $pK_a$  values despite solubility limitations.

Notably, the solubility of metal complexes of 6,6'-dhbp is much improved relative to the free ligand. For example, metal complexes **1**, **2**, and **3** have  $pK_a$  values of 4.6,<sup>17</sup> 5,<sup>1</sup> and 4.5,<sup>24</sup> respectively (Scheme 2). These  $pK_a$  values represent the simultaneous removal of two protons from the coordinated 6,6'-dhbp ligand. Of course, ligand complexation to a cationic metal should result in lower  $pK_a$  values than that of the free ligand,<sup>26-27</sup> as here the  $pK_a$  values of **1-3** are 3 to 4 orders of magnitude lower than that of the free ligand.



*Scheme 2.2.* Examples of metal complexes of 6,6'-dhbp in the literature.

## 2.2 Results and Discussion

### 2.2.1 UV-vis Spectroscopy

A UV-vis titration was performed of 6,6'-dhbp in aqueous solution (Figure 2.1). At low pH, the absorption maximum is at 340 nm but red shifts upon an increase in pH to a maximum absorption at 354 nm. Then, the absorption maximum undergoes a blue shift to 343 nm above pH = 10.5. From this data, there are clearly two equivalence points. The first equivalence point is assigned to  $pK_{a3}$  and was determined to be 8.5 (Figures 2.S6-2.S7). This is consistent with the reported value of approximately 8.5 for the deprotonation of 6,6'-dhbp.<sup>22</sup> To better interpret the second equivalence point, a second UV-vis titration was performed in smaller pH increments (Figure 2.2). From this titration, the  $pK_{a4}$  was determined to be 11.7 (Figures 2.S8-2.S9). As discussed below, comparison of these spectra to our computations shows that  $pK_{a4}$  corresponds to formation of the dianion by double deprotonation of 6,6'-dhbp.

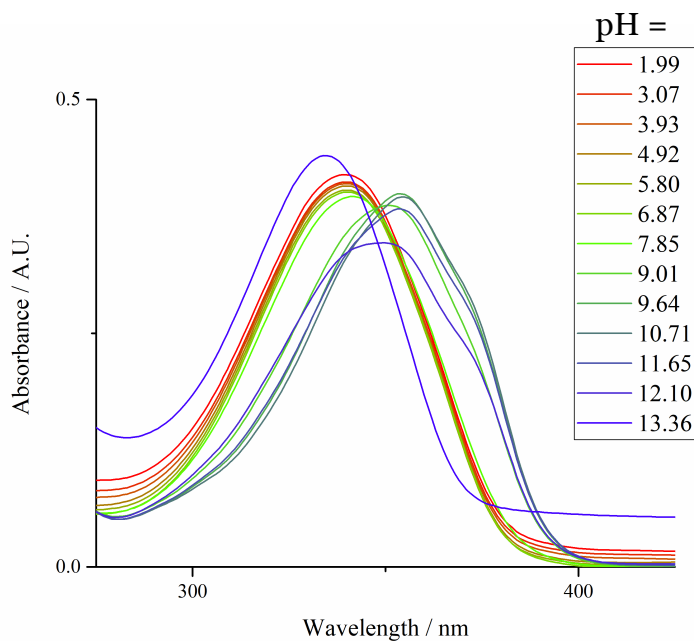


*Figure 2.1.* UV-vis spectra of an aqueous solution of 6,6'-dhbp at varying pH from 2 to 14. The pH was adjusted with aqueous solutions of NaOH or H<sub>2</sub>SO<sub>4</sub>.

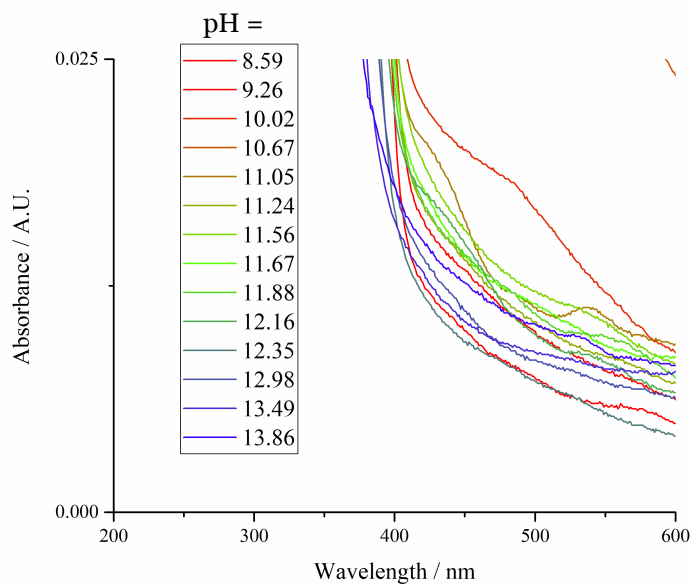
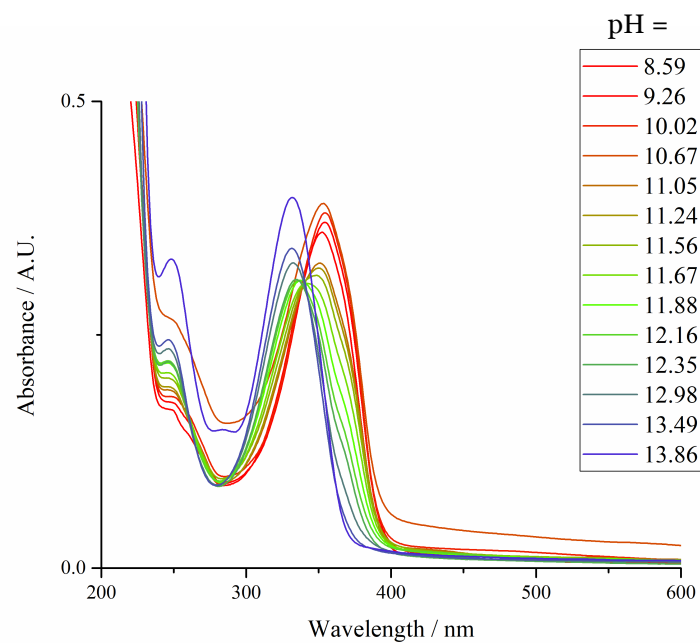


*Figure 2.2.* (Top) UV-vis spectra of an aqueous solution of dhbp at varying pH from 8.5 to 14. The pH was adjusted with aqueous solutions of NaOH or H<sub>2</sub>SO<sub>4</sub>. (Bottom) Shows the presence of minor peaks around 500 nm at pH 10-11.

### *2.2.2 Experimental NMR Spectroscopy*

To provide additional insight into the determination of the second equivalence point, we performed NMR experiments as a function of pH. The results are shown in Figure 2.3 for the proton chemical shifts. The  $^1\text{H}$  NMR shows a distinct change between pH 11.29 and 12.12 with all three resonances shifting upfield with increased pH. These changes are consistent with  $\text{p}K_{\text{a}4}$  occurring in this pH range as deprotonation would result in the protons becoming more shielded due to increased electron density on the lactam rings. Figure 2.4 shows the  $^{13}\text{C}$  NMR spectra at pH 11.29 and 12.12, and similar upfield shifts upon deprotonation are observed. The NMR results are consistent with the  $\text{p}K_{\text{a}4}$  value of 11.7 from UV-Vis spectroscopy (above). Unfortunately, 6,6'-dhbp is too insoluble in  $\text{D}_2\text{O}$  at low pH to permit observation of  $\text{p}K_{\text{a}3}$  by NMR methods.

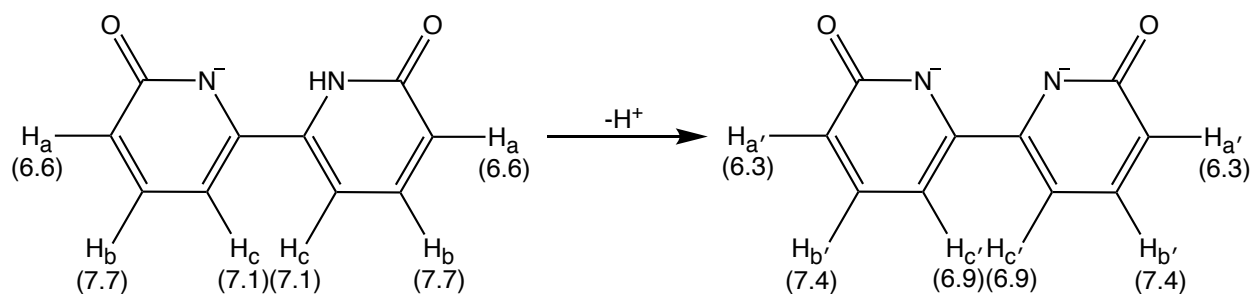
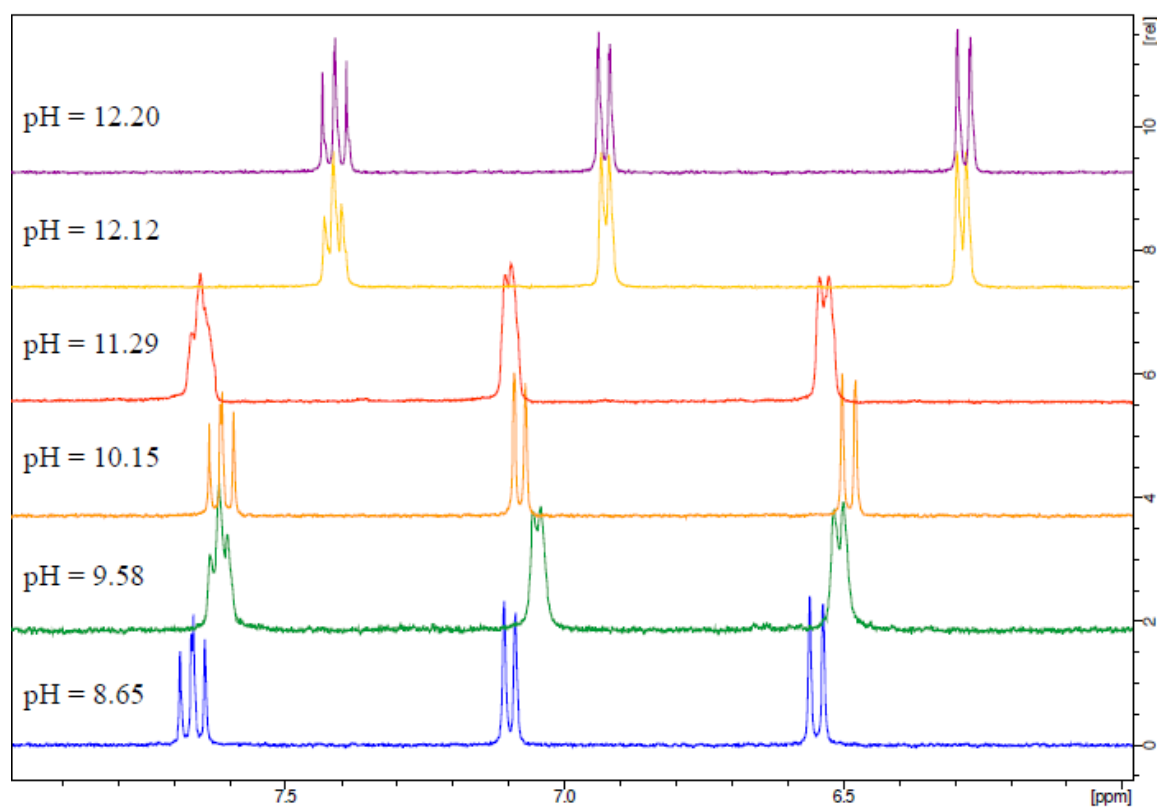


Figure 2.3. (Top)  $^1\text{H}$ -NMR spectra as a function of pH. (Bottom) Assignments of peaks in the  $^1\text{H}$ -NMR spectra. Chemical shifts (in ppm) are shown in parentheses below the corresponding proton.

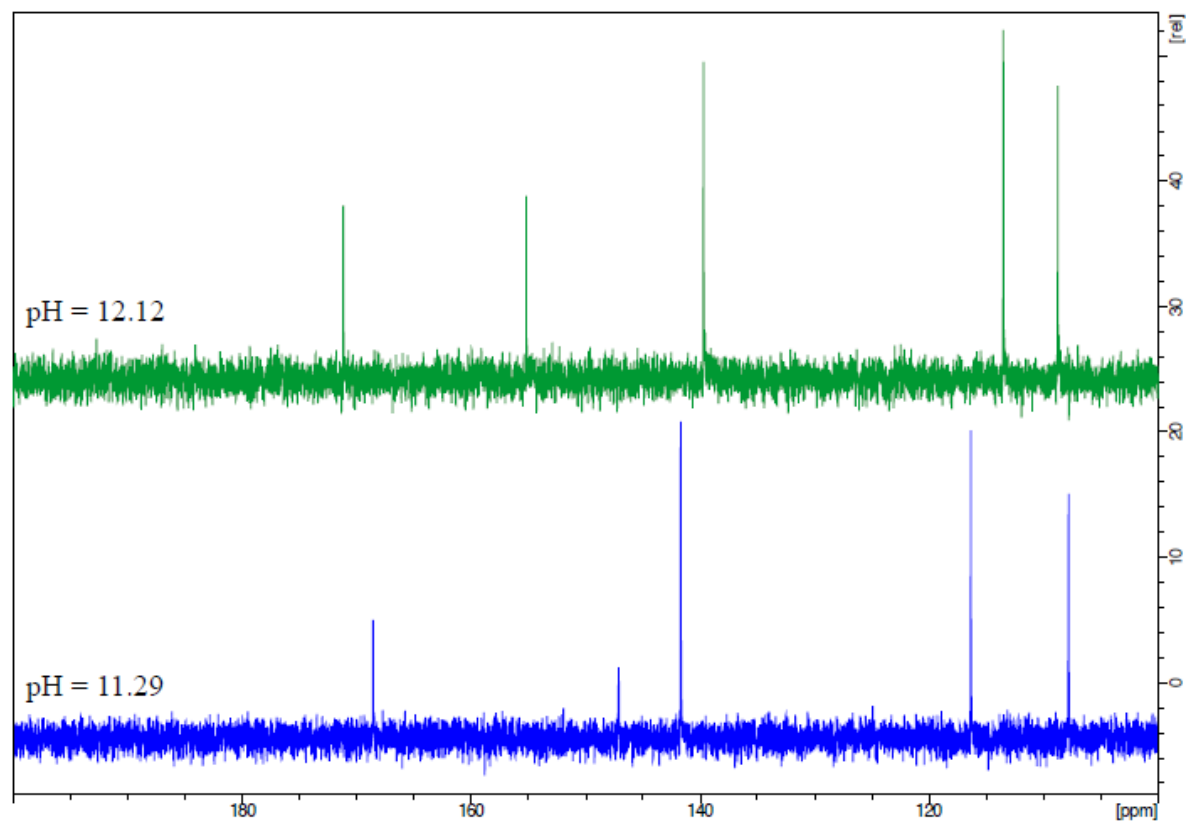


Figure 2.4.  $^{13}\text{C}$  NMR spectra at pH 11.29 and 12.12

### 2.2.3 Computational results: Gas phase structures and relative energetics

Computational studies were performed by Monica Vasiliu of the Dixon group. The structures of all possible gas phase isomers and conformers and protonation states (-2 to +2) were optimized and the results are shown in Figure 2.5(a) to 2.5(d). The relative energies are given in Table 2.1. The ground state of gas phase 6,6'-dhbp is predicted to be trans-6,6'-dhbp in the pyridinol form which is planar with  $C_{2h}$  symmetry. The cis conformer is 3.9 kcal/mol higher in energy and the trans-6,6'-dhbp lactam tautomer is 6.5 kcal/mol higher in energy. The trans-cis energy difference is  $\sim 1$  kcal/mol for the 6,6'-dhbp lactam tautomers.

The lowest energy isomer/conformer in the gas phase is planar and the three remaining isomers and tautomers for the gas phase neutral species are twisted about the central C-C bond giving structures with  $C_2$  symmetry and torsion angles between  $24^\circ$  and  $37^\circ$ . The C-C bond distances in the 6-member ring are similar to those in benzene and the C-C bond connecting the rings is typical of that for an  $sp^2$ - $sp^2$  single bond. The C-N bond distances are consistent with those of an aromatic ring. The lactam exhibits geometry changes due to the presence of the C=O group which lengthens the C-N bond distances as well as some C-C bond distances. The C-C single bond connecting the rings does not change much.

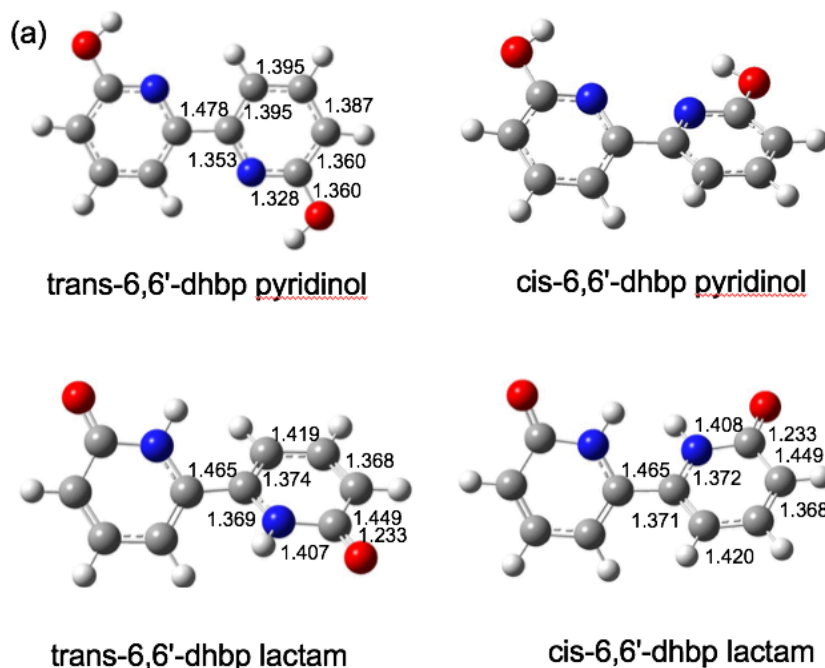
The lowest energy gas phase structure after removal of a proton is cis-6,6'-dhbp lactam<sup>-1</sup> which is planar with  $C_s$  symmetry. The trans isomer is 4.5 kcal/mol higher in energy and the trans-6,6'-dhbp pyridinol<sup>-1</sup> tautomer is 9.1 kcal/mol higher in energy. The trans-cis energy difference is 5.7 kcal/mol for the pyridinol<sup>-1</sup> tautomer. Both cis-trans energy differences are larger in the anion than in the neutral. Note that cis-6,6'-dhbp lactam<sup>-1</sup> is more stable than the trans isomer in contrast to what was found for the neutral species. The geometry of the rings does not change much from that of the neutral lactam and the C-C single bond connecting the rings lengthens slightly.

Addition of a proton to 6,6'-dhbp leads to the same ordering of the gas phase structures for the protonated +1 structures as for the neutral structures. The pyridinols are more stable than the lactams with larger energy differences except for the protonated cis-pyridinol which is more stable than the trans-pyridinol. The conformational energy change from trans-6,6'-dhbp pyridinol<sup>+1</sup> to the cis conformer is 5.7 kcal/mol and the cis-6,6'-dhbp lactam<sup>+1</sup> is 17.5 kcal/mol higher in energy. The cis-trans energy difference for the lactam<sup>+1</sup> conformer is 3.4 kcal/mol and again the cis

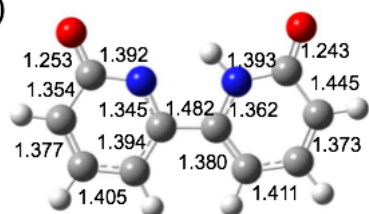
conformer is more stable than the trans. Again, there are only modest changes in the bond distances on protonation of the N in the pyridinol.

We note that the gas phase dianion generated by removing two protons is planar with  $C_{2h}$  symmetry and a trans structure. The planar cis structure optimizes to a transition state with a single imaginary frequency and is 6.3 kcal/mol higher in energy in the gas phase. The C-C bond between the two rings lengthens, and the C=O bond distances lengthen as well as compared to the neutral. Some of the other C-C bonds in the ring also elongate slightly.

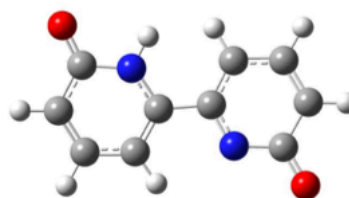
For the dication generated by adding two protons, the trans conformer with  $C_2$  symmetry is 1.8 kcal/mol more stable than the cis in the gas phase. The geometry does not change much in terms of the bond distances and the C-C single bond connecting the two rings changes by  $< 0.01 \text{ \AA}$ .



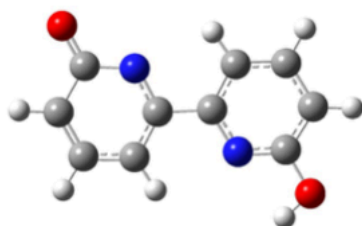
(b)



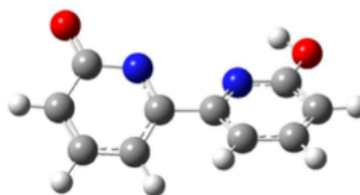
cis-6,6'-dhbp lactam<sup>-1</sup>



trans-6,6'-dhbp lactam<sup>-1</sup>

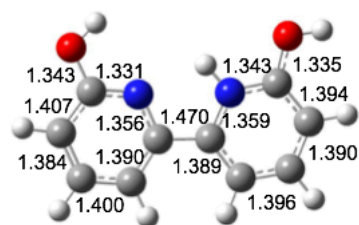


trans-6,6'-dhbp pyridinol<sup>-1</sup>

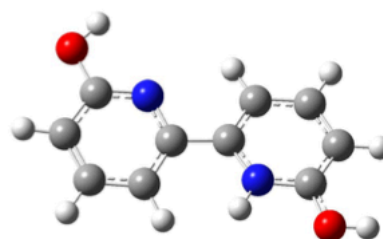


cis-6,6'-dhbp pyridinol<sup>-1</sup>

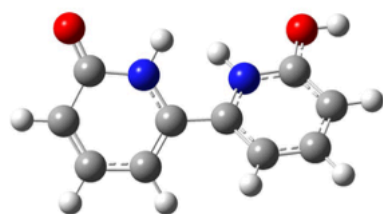
(c)



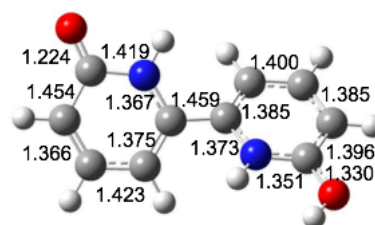
cis-6,6'-dhbp pyridinol<sup>+1</sup>



trans-6,6'-dhbp pyridinol<sup>+1</sup>



cis-6,6'-dhbp lactam<sup>+1</sup>



trans-6,6'-dhbp lactam<sup>+1</sup>

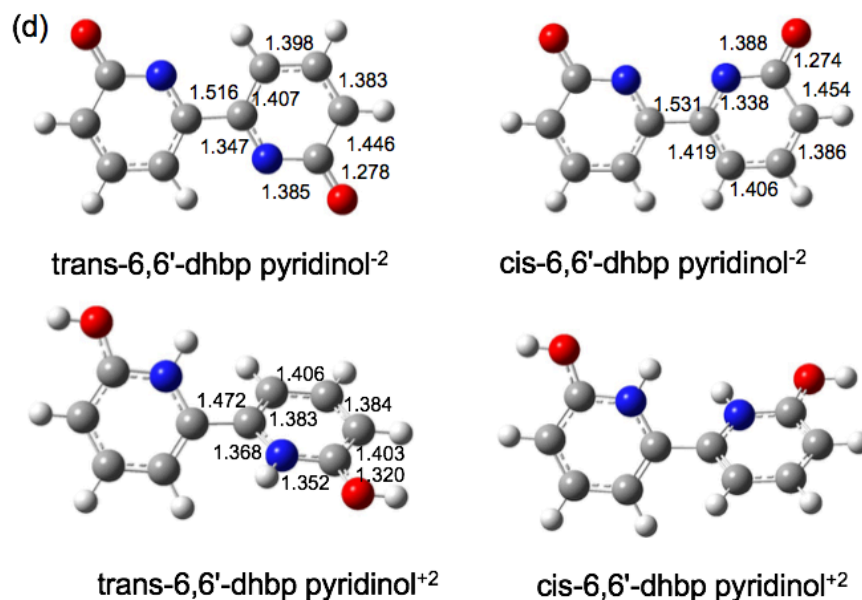


Figure 2.5. Optimized structures for isomers and protonation states (-2 to +2) for 6,6'-dhbp. Bond lengths (G3(MP2) level in Å) reported for the lowest energy isomers in gas phase and solution. The Cartesian x,y,z coordinates for all structures are given in the Supporting Information.

Table 2.1. Relative energies (kcal/mol)<sup>a</sup>

Molecule	sym	$\Delta H(g,298)^b$	$\Delta G(g,298)^b$	$\Delta G(aq,298)^c$
[trans-6,6'-dhbp pyridinol] <sup>-2</sup>	C <sub>2h</sub>	0.0	0.0	9.5
[cis-6,6'-dhbp pyridinol] <sup>-2</sup>	C <sub>2</sub>	6.3	7.8	0.0
[cis-6,6'-dhbp lactam] <sup>-1</sup>	C <sub>s</sub>	0.0	0.0	0.0
[trans-6,6'-dhbp lactam] <sup>-1</sup>	C <sub>1</sub>	4.5	4.9	4.5
[trans-6,6'-dhbp pyridinol] <sup>-1</sup>	C <sub>s</sub>	9.1	9.5	8.2
[cis-6,6'-dhbp pyridinol] <sup>-1</sup>	C <sub>1</sub>	14.8	15.1	6.3
trans-6,6'-dhbp pyridinol	C <sub>2h</sub>	0.0	0.0	7.4
cis-6,6'-dhbp pyridinol	C <sub>2</sub>	3.9	3.9	7.9
trans-6,6'-dhbp lactam	C <sub>2</sub>	6.5	6.4	0.0
cis-6,6'-dhbp lactam	C <sub>2</sub>	7.6	7.5	0.7
[cis-6,6'-dhbp pyridinol] <sup>+1</sup>	C <sub>s</sub>	0.0	0.0	1.1
[trans-6,6'-dhbp pyridinol] <sup>+1</sup>	C <sub>1</sub>	5.7	5.7	3.5
[cis-6,6'-dhbp lactam] <sup>+1</sup>	C <sub>1</sub>	17.5	17.6	1.5
[trans-6,6'-dhbp lactam] <sup>+1</sup>	C <sub>1</sub>	20.9	20.6	0.0
[trans-6,6'-dhbp pyridinol] <sup>+2</sup>	C <sub>2</sub>	0.0	0.0	0.0
[cis-6,6'-dhbp pyridinol] <sup>+2</sup>	C <sub>1</sub>	1.8	1.0	0.2

<sup>a</sup> The most stable isomer for each charge state is set at 0.0 kcal/mol for both the gas phase (g) and aqueous solution (aq). <sup>b</sup> Gas phase (g). <sup>c</sup> Aqueous solution (aq).

#### 2.2.4 Computational results: Aqueous phase relative energetics

Using the gas phase geometries, the solvation free energies in water at 298 K were calculated using the self-consistent reaction field (SCRF) approach<sup>28</sup> with the COSMO parameters<sup>29-30</sup> as implemented in Gaussian 03<sup>31</sup> at the same B3LYP/DZVP2 level of theory using the radii developed by Klamt and co-workers to define the cavity.<sup>29-30</sup> The aqueous Gibbs free energy (free energy in aqueous solution),  $\Delta G_{\text{aq}}$ , was calculated from Eq. 7

$$\Delta G_{\text{aq}} = \Delta G_{\text{gas}} + \Delta\Delta G_{\text{solv}} \quad (7)$$

where  $\Delta G_{\text{gas}}$  is the gas phase free energy and  $\Delta\Delta G_{\text{solv}}$  is the aqueous solvation free energy calculated as differences between the conjugate base and the acid ( $\text{HA} \rightarrow \text{H}^+ + \text{A}^-$ ). A dielectric constant of 78.39 corresponding to that of bulk water was used in the COSMO calculations. The solvation energy is reported as the electrostatic energy (polarized solute – solvent).

The presence of the intrinsic solvation reaction field stabilized the lactam over the pyridinol for the neutral species so that the trans conformer of the lactam is the most stable followed by the cis-lactam < 1 kcal/mol higher in energy. The trans-pyridinol is now about 7 kcal/mol higher in energy. We would thus expect to find about 30% of the cis-lactam isomer in solution with respect to the trans-lactam and no pyridinol.

The change in stabilization of the lactam relative to the pyridinol is due to the differences in solvation energy. The trans-pyridinol does not have a dipole moment due to symmetry, whereas the trans (1.82 D) and cis (6.49 D) lactam do and hence the lactam conformers are stabilized in solution. The cis-pyridinol also has a dipole moment (2.52 D) and this reduces the energy difference between the cis- and trans-pyridinol in

solution from that in the gas phase. The presence of a dipole moment is not the entire reason for the change in solvation energies as the trans-lactam is still more stable than the cis-lactam in solution even though the cis has the larger dipole moment. (Dipole moments for the ions are not reported as they are origin dependent due to the presence of the charge.) 6,6'-dhbp is in the lactam form in the solid state<sup>1, 4</sup> and in DMSO consistent with our predictions. The cis-trans energy difference for both the lactam and the pyridinol are both reduced in solution as compared to the gas phase.

For the monoanion in solution, the energy ordering of the isomers does not change except that the cis-pyridinol anion is now more stable than the trans-pyridinol anion and the energy difference between the cis-lactam anion and the cis-pyridinol anion is significantly reduced from the gas phase difference. For the dianion in aqueous solution, the energy ordering reverses as the cis dianion is more stable than the trans by 9.5 kcal/mol. We would not expect to observe any other isomer than the cis for the mono- and dianions in solution with only  $5 \times 10^{-4}$  of the trans monoanion present with respect to the cis monoanion and much less for the trans dianion with respect to the cis dianion.

Addition of a proton to the neutral species has a dramatic effect on the relative energies of the isomers and conformers. The energies of the four cation structures are now < 4 kcal/mol apart rather than up to 21 kcal/mol apart. The trans-lactam cation is now the minimum followed by the cis-pyridinol cation about 1 kcal/mol higher in energy. The trans form of the dication is the most stable one in the gas phase and in aqueous solution. These changes in the structural stability in solution impact the basicity and acidity values discussed below.

### 2.2.5 Computational results: UV-vis spectra

The UV-vis spectra of all possible isomers and conformers and protonation states (-2 to +2) were calculated by using time dependent-density functional theory (TD-DFT) calculations<sup>32-33</sup> at the B3LYP/DZVP2 level at the same level optimizations. The first large transition in all cases is a HOMO  $\rightarrow$  LUMO transition and the values are given in Table 2.2 as well. The HOMO and LUMO orbitals for the molecules in bold, the ones which are of interest, from Table 2.2 are shown in the Supporting Information. The HOMO for cis-6,6'-dhbp lactam has two C-C  $\pi$  bonds adjacent to the C-C single bond with some component of a  $\pi$  bond on the C=O. The LUMO is a  $\pi^*$  combination on both rings with a contribution from the two C atoms involved in the C-C single bond so that the  $\pi \rightarrow \pi^*$  is somewhat localized. The presence of three H<sub>2</sub>O molecules near the C=O groups does not change the nature of the orbitals.

For the cis-6,6'-dhbp lactam monoanion and the corresponding compounds solvated by two and three H<sub>2</sub>O molecules, the HOMO is localized on the deprotonated ring and the LUMO is localized on the other ring. Although the transition is a  $\pi \rightarrow \pi^*$ , it has a charge-transfer component as well. The HOMO  $\rightarrow$  LUMO transition for the dianion is very similar to that for the neutral lactam.

The HOMO on the cis-pyridinol protonated cation, which is the most stable cation in the gas phase, is localized on the ring that is not protonated and the LUMO is localized on the protonated ring. Thus, this resembles the  $\pi \rightarrow \pi^*$  transition with a charge-transfer component predicted for the anion. Although the protons are in different positions for the protonated trans-lactam, which is more stable in aqueous solution, the same type of  $\pi \rightarrow \pi^*$  transition is predicted with the HOMO on the protonated ring and the LUMO on the neutral ring. When the asymmetry between the

rings is removed by the addition of a second proton, the charge transfer component is no longer present and the HOMO  $\rightarrow$  LUMO transition looks like that in the neutral molecule.

The neutral pyridinol is predicted to have transitions near 300 nm and the tautomer is predicted to have transitions near 360 nm. The cis-6,6'-dhbp lactam monoanion is predicted to have a peak near 475 nm and the remaining three conformers and tautomers are predicted to have the transition at  $520 \pm 6$  nm with 2 to 3 fold lower intensity. Figure 2.2b shows some weak absorption bands (broad peaks at  $\sim 450$ - $550$  nm) present at pH = 10-12 that can be assigned to the trans- and cis-6,6'-dhbp lactam monoanions. The pyridinol monocation is predicted to have a transition at  $\sim 360$  nm and its conformer is predicted to have a transition at 380 nm. The cis and trans-lactam monocations are predicted to have peaks at 470 and 495 nm, respectively. The dianion is predicted to have a peak near 365 nm and the two dication conformers are predicted to have peaks between 300 and 310 nm.

Clearly, the gas phase spectra for the monoanion do not match the experimental data as well as the results for the neutral molecule and dianion. In order to provide a better model for the spectral predictions, we performed additional TD-DFT calculations in the presence of a self-consistent reaction field (SCRF) for cis-6,6'-dhbp lactam, cis-6,6'-dhbp lactam<sup>-1</sup>, and the cis- and trans-6,6'-dhbp pyridinol<sup>-2</sup>. These SCRF results (Table 2.2) showed a small blue shift for the neutral molecule and for the dianion and a much larger red shift for the monoanion. The large blue shift for the monoanion now places the computational results in better agreement with experiment. We also included explicit solvent molecules for cis-6,6'-dhbp lactam and cis-6,6'-dhbp lactam<sup>-1</sup> (Figure 2.6 and Table 2.2) and predicted a slight red shift for the neutral molecule and a significant

blue shift for the monoanion. Inclusion of the SCRF led to a larger blue shift for the monoanion and a smaller blue shift for the neutral molecule in the presence of explicit water molecules. The intensities of the absorptions are also predicted to increase in the presence of aqueous solvent.

The TD-DFT/SCRF spectra for the proposed structures in the  $pK_{a3}$  and  $pK_{a4}$  scheme are shown in Figure 2.7, together with the experimentally observed spectra at three different pH values. *Without explicit water molecules present*, deprotonation of the neutral cis-lactam to form the cis-lactam monoanion is predicted to cause a red shift of the transition (Table 2.2) from 356 nm to 400 nm (0.38 eV). *When three waters of solvation are present*, the analogous predicted red shift upon neutral lactam deprotonation is from 371 nm to 386 nm (0.13 eV). The corresponding experimental shift is from 341 nm to 353 nm (0.12 eV). Upon further increasing the pH, there is a blue shift in the experimental spectrum from 353 nm to 335 nm (0.19 eV). The blue shift for the monoanion to the dianion from 400 nm to 370 nm (0.25 eV) is not as large as the experimental shift. However, the correct trend for a red shift from the neutral to the monoanion and a blue shift from the monoanion to the dianion are reproduced computationally providing us with confidence in our assignment of the solution structures. From these comparisons, the proposed scheme for two subsequent deprotonation events is shown in Scheme 3.

Table 2.2. UV-Vis transitions and intensities as predicted by TD-DFT at the B3LYP/DZVP2 level.<sup>a</sup>

Molecule	sym	transition	nm	eV	f	nm	eV	f
			gas			H <sub>2</sub> O		
[trans-6,6'-dhbp pyridinol] <sup>-2</sup>	C <sub>2h</sub>	<sup>1</sup> B <sub>u</sub>	363.7	3.41	0.187	353.1	3.51	0.335
[cis-6,6'-dhbp pyridinol] <sup>-2</sup>	C <sub>2v</sub>	<sup>1</sup> B <sub>2</sub>	380.2	3.26	0.162	370.0	3.35	0.328
[cis-6,6'-dhbp lactam] <sup>-1</sup>	C <sub>s</sub>	<sup>1</sup> A'	475.2	2.61	0.123	396.8	3.12	0.309
[cis-6,6'-dhbp lactam(H <sub>2</sub> O) <sub>2</sub> ] <sup>-1</sup>	C <sub>1</sub>	<sup>1</sup> A	411.5	3.01	0.175	384.5	3.22	0.348
[cis-6,6'-dhbp lactam(H <sub>2</sub> O) <sub>3</sub> ] <sup>-1</sup>	C <sub>1</sub>	<sup>1</sup> A	434.4	2.85	0.151	386.0	3.21	0.329
[trans-6,6'-dhbp lactam] <sub>1</sub> <sup>-</sup>	C <sub>1</sub>	<sup>1</sup> A	514.4	2.41	0.040	399.4	3.10	0.175
[trans-6,6'-dhbp pyridinol] <sub>1</sub> <sup>-</sup>	C <sub>s</sub>	<sup>1</sup> A'	523.5	2.37	0.040	382.5	3.24	0.177
[cis-6,6'-dhbp pyridinol] <sub>1</sub> <sup>-</sup>	C <sub>1</sub>	<sup>1</sup> A	518.7	2.39	0.062	374.0	3.31	0.201
trans-6,6'-dhbp pyridinol	C <sub>2h</sub>	<sup>1</sup> B <sub>u</sub>	302.2	4.10	0.399	308.8	4.02	0.512
cis-6,6'-dhbp pyridinol	C <sub>2</sub>	<sup>1</sup> A	296.9	4.18	0.360	304.3	4.08	0.483
trans-6,6'-dhbp lactam	C <sub>2</sub>	<sup>1</sup> B	361.6	3.43	0.338	355.8	3.48	0.466
<b>cis-6,6'-dhbp lactam</b>	C <sub>2</sub>	<sup>1</sup> B	362.3	4.42	0.344	355.5	3.49	0.466
<b>cis-6,6'-dhbp lactam (H<sub>2</sub>O)<sub>3</sub></b>	C <sub>1</sub>	<sup>1</sup> A	372.3	3.33	0.365	370.6	3.35	0.496
[cis-6,6'-dhbp pyridinol] <sup>+1</sup>	C <sub>s</sub>	<sup>1</sup> A'	358.7	3.46	0.307	339.0	3.66	0.485
[trans-6,6'-dhbp pyridinol] <sup>+1</sup>	C <sub>1</sub>	<sup>1</sup> A	380.5	3.26	0.175	341.6	3.63	0.391
[cis-6,6'-dhbp lactam] <sup>+1</sup>	C <sub>1</sub>	<sup>1</sup> A	469.1	2.64	0.217	387.1	3.20	0.380
[trans-6,6'-dhbp lactam] <sup>+1</sup>	C <sub>1</sub>	<sup>1</sup> A	495.2	2.50	0.130	384.7	3.22	0.292
[trans-6,6'-dhbp pyridinol] <sup>+2</sup>	C <sub>2</sub>	<sup>1</sup> B	309.1	4.01	0.440	315.3	3.93	0.529
[cis-6,6'-dhbp pyridinol] <sup>+2</sup>	C <sub>1</sub>	<sup>1</sup> A	301.8	4.11	0.384	305.7	4.06	0.464

<sup>a</sup> All are HOMO → LUMO transitions, π → π\*.

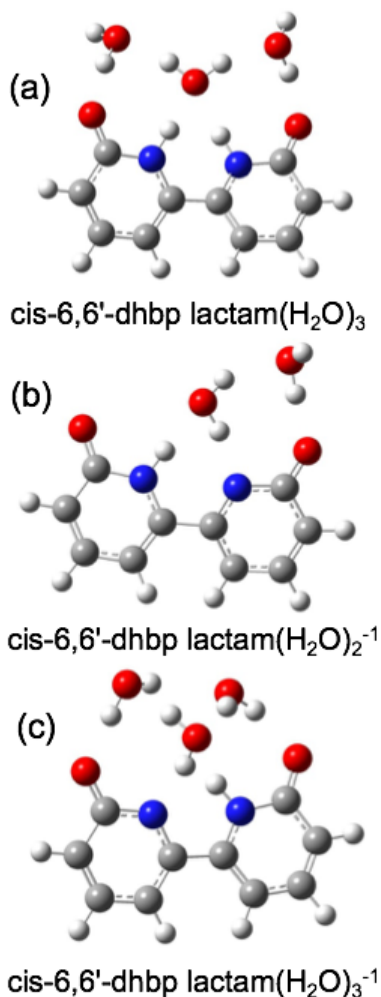


*Figure 2.6.* Optimized structures for the cis isomer of 6,6'-dhbp lactam and 6,6'-dhbp lactam<sup>-1</sup> with (a) three water molecules for the neutral lactam, (b) two water molecules for the anion, and (c) three water molecules for the anion.

### 2.2.6 Computational results: NMR spectra

Further support for the assigned structures comes from a comparison of the calculated (in aqueous solution) and experimental chemical shifts as shown in Table 2.3 for the <sup>1</sup>H-NMR and in Table 2.4 for the <sup>13</sup>C-NMR. The optimized B3LYP/DZVP2 geometries were used to predict the <sup>1</sup>H-NMR and <sup>13</sup>C-NMR chemical shifts at the B3LYP level with a valence triple- $\zeta$  basis set with polarization functions (VTZP) from Ahlrichs and coworkers.<sup>34</sup> The nuclear magnetic shielding tensors were calculated using the gauge-

independent atomic orbital (GIAO) approach.<sup>35</sup> The NMR chemical shifts were calculated in H<sub>2</sub>O using the COSMO self-consistent reaction field approach. The <sup>1</sup>H and <sup>13</sup>C chemical shifts are calculated relative to TMS in H<sub>2</sub>O. The <sup>1</sup>H-NMR for the two lowest energy isomers for the monoanion and dianion in aqueous solution are within 0.2 ppm of the observed values and essentially show the same trends, further confirming our assignments of the structure of the anion and dianion. The calculated <sup>13</sup>C-NMR chemical shifts are also consistent with the experimental values with most of the predicted shifts within 10 ppm and only two chemical shifts in the dianion that differ by 13 and 14 ppm. The trends in the experimental <sup>13</sup>C-NMR chemical shifts are also reproduced by the computations.

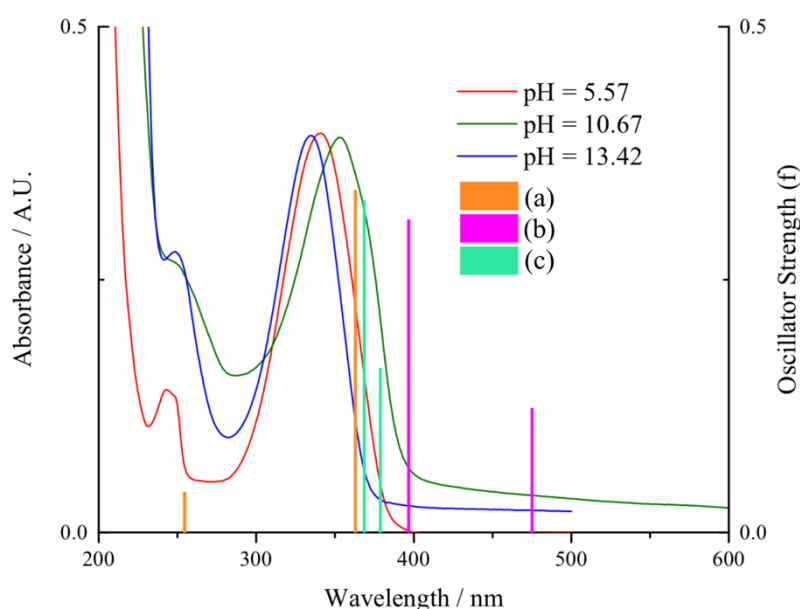
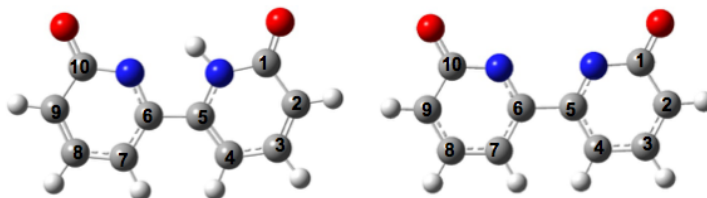


*Figure 2.7.* Overlay of experimental UV-vis spectra at 3 different pHs with TD-DFT spectra of the proposed dhp species at each pH (represented by columns). The labeling for the computational results (a), (b), and (c) are given in Scheme 3.

Table 2.3. Calculated and Experimental  $^1\text{H}$ -NMR chemical shifts in ppm. The major species present at pH 8.65-11.29 is the cis-6,6'-dhbp lactam $^{-1}$  and at pH 12.12-12.20 is the cis-6,6'-dhbp pyridinol $^{-2}$ ; these are labeled in the headings below.

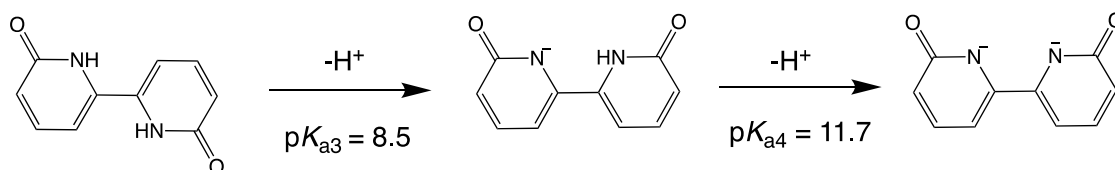
Molecule	triplet	doublet	doublet
<i>Expt NMR. Major species in solution: [cis-6,6'-dhbp lactam]<math>^{-1}</math></i>			
pH = 8.65	7.70	7.13	6.58
pH = 9.58	7.71	7.14	6.60
pH = 10.15	7.65	7.12	6.52
pH = 11.29	7.74	7.19	6.62
<i>Expt NMR. Major species in solution: [cis-6,6'-dhbp pyridinol]<math>^{-2}</math></i>			
pH = 12.12	7.47	6.98	6.34
pH = 12.20	7.42	6.94	6.29
<i>Calc NMR of different species</i>			
[cis-6,6'-dhbp lactam] $^{-1}$	7.7	7.0	6.4
[cis-6,6'-dhbp pyridinol] $^{-2}$	7.5	7.1	6.2
trans-6,6'-dhbp lactam	7.9	6.8	6.7
cis-6,6'-dhbp lactam	7.9	6.8	6.7

Table 2.4. Calculated and Experimental  $^{13}\text{C}$ -NMR chemical shifts in ppm.



Molecule	type	$^{13}\text{C}$ -NMR chemical shifts (ppm)				
		C1,C10	C5,C6	C3,C8	C2,C9	C4,C7
pH = 11.29	Expt	169	147	141	117	108
pH = 12.12	Expt	172	155	140	113	109
[cis-6,6'-dhbp lactam] $^{-1}$	Calc(Ave)	177 <sup>a</sup>	155 <sup>b</sup>	149 <sup>c</sup>	125 <sup>d</sup>	108 <sup>e</sup>
[cis-6,6'-dhbp pyridinol] $^{-2}$	Calc	186	168	146	119	109

<sup>a</sup> C1 = 172 ppm, C10 = 182 ppm; <sup>b</sup> C5 = 156 ppm, C6 = 154 ppm; <sup>c</sup> C3 = 151 ppm, C4 = 147 ppm; <sup>d</sup> C2 = 126 ppm, C9 = 125 ppm; <sup>e</sup> C4 = 108 ppm, C7 = 108 ppm;



(a) trans-6,6'-dhbp lactam

(b) cis-6,6'-dhbp lactam $^{-1}$

(c) cis-6,6'-dhbp pyridinol $^{-2}$

Scheme 3. Proposed scheme for  $pK_{a3}$  and  $pK_{a4}$ .

### 2.2.7 Computational results: $pK_a$ values

Theoretical  $pK_a$  values in aqueous solution were calculated from Eq. 8 where  $R$  is the gas constant and  $T = 298$  K is the temperature.

$$pK_a = \Delta G_{aq}/(2.303RT) \quad (8)$$

For benchmark purposes, we studied the single ring 2-pyridone and the corresponding alcohol tautomer (Figure 2.8). The alcohol tautomer is lower in energy than the pyridone by 1.4 kcal/mol at 298 K in the gas phase but the 2-pyridone tautomer becomes more stable by 6.6 kcal/mol in aqueous solution. The gas phase acidity of 2-pyridone is 340.0 kcal/mol (Table 2.5) corresponding to a calculated  $pK_a$  of 14.5; the corresponding experimental value is 11.62. The gas phase acidity of the alcohol tautomer is 341.3 kcal/mol leading to an aqueous solution  $pK_a$  of 9.7. The gas phase basicity of the 2-pyridone is 212.0 kcal/mol at 298 K and that of the alcohol tautomer is 210.7 kcal/mol. These values lead to  $pK_b$  predictions of 0.0 and 4.5 for the alcohol tautomer and 2-pyridone, respectively in comparison to an experimental value of 0.75.<sup>36</sup> Thus, there is reasonable agreement with the aqueous  $pK_a$  and  $pK_b$  values for the 2-pyridone within 3-4 pK units.

The issue that arises in predicting the  $pK_a$  is whether the adiabatic value is observed or whether the structure resulting from direct ionization is observed. The ground state of the neutral in aqueous solution is trans-6,6'-dhbp lactam and that of the monoanion is the cis-6,6'-lactam.

The corresponding adiabatic gas phase acidity is 319.7 kcal/mol and the vertical value is 324.6 kcal/mol with respective  $pK_a$  values of 8.5 and 11.8. These  $pK_a$  values are in good agreement with the experimental values of 8.5 and 11.7. The actual adiabatic gas phase acidity is for the process trans-6,6'-dhbp pyridinol  $\rightarrow$  cis-6,6'-dhbp lactam<sup>-1</sup> + H<sup>+</sup>

with a value of 326.1 kcal/mol. The vertical gas phase acidity for trans-6,6'-dhbp pyridinol is 335.6 kcal/mol.

In aqueous solution, the lowest energy trans-6,6'-dhbp lactam adds a proton to give the lowest energy trans-6,6'-dhbp lactam<sup>+1</sup> so the solution adiabatic and vertical processes are the same. The gas phase basicity of this process is -205.1 kcal/mol and the p*K*<sub>b</sub> is 4.1. The gas phase basicity for the most stable gas phase isomer trans-6,6'-dhbp pyridinol is -214.0 kcal/mol for the vertical process and is -219.6 kcal/mol for the adiabatic process (trans-6,6'-dhbp pyridinol + H<sup>+</sup> → cis-6,6'-dhbp pyridinol<sup>+1</sup>).

Removal of a proton from the most stable monoanion cis-6,6'-dhbp lactam<sup>-1</sup> in solution gives a p*K*<sub>a2</sub> of 12.2 going to the cis-6,6'-dhbp pyridinol<sup>-2</sup> which is the most stable structure in solution. Addition of a proton to the cation yields a p*K*<sub>b2</sub> of ~ 11.

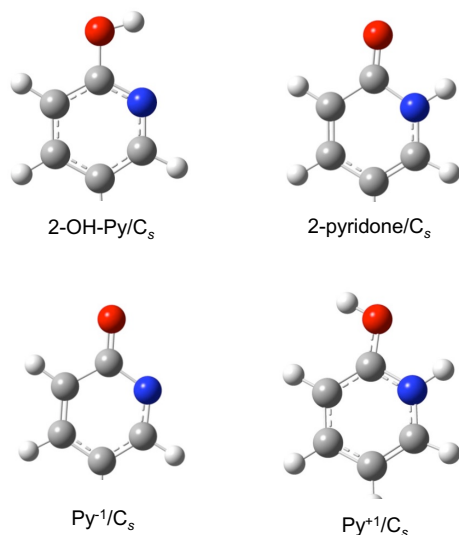


*Figure 2.8.* Optimized structures for isomers and protonation states (-1 to +1) for pyridin-2-ol.

Table 2.5. G3(MP2) gas phase acidities (kcal/mol) and pK<sub>a</sub> values.<sup>a</sup>

Molecule	$\Delta H_{\text{gas}}$	$\Delta G_{\text{gas}}$	$\Delta G_{\text{solv}}$	$\Delta G_{\text{aq}}$	pK <sub>a</sub> /pK <sub>b</sub>
[cis-6,6'-dhbp lactam] <sup>-1</sup> → [trans-6,6'-dhbp pyridinol] <sup>-2+</sup> + H <sup>+</sup>	417.3	410.5	-384.4	26.1	19.2
[trans-6,6'-dhbp lactam] <sup>-1</sup> → [trans-6,6'-dhbp pyridinol] <sup>-2+</sup> + H <sup>+</sup>	412.9	405.7	-384.0	21.7	15.9
[cis-6,6'-dhbp lactam] <sup>-1</sup> → [cis-6,6'-dhbp pyridinol] <sup>-2+</sup> + H <sup>+</sup>	423.6	418.3	-401.7	16.6	12.2
trans-6,6'-dhbp pyridinol → [trans-6,6'-dhbp pyridinol] <sup>-1+</sup> + H <sup>+</sup>	343.5	335.6	-323.3	12.3	9.0
cis-6,6'-dhbp pyridinol → [cis-6,6'-dhbp pyridinol] <sup>-1+</sup> + H <sup>+</sup>	345.4	337.2	-327.4	9.9	7.3
trans-6,6'-dhbp pyridinol → [cis-6,6'-dhbp lactam] <sup>-1</sup> + H <sup>+</sup>	334.4	326.1	-321.9	4.2	3.0
trans-6,6'-dhbp lactam → [cis-6,6'-dhbp lactam] <sup>-1+</sup> + H <sup>+</sup>	328.0	319.7	-308.1	11.6	8.5
trans-6,6'-dhbp lactam → [trans-6,6'-dhbp lactam] <sup>-1+</sup> + H <sup>+</sup>	332.4	324.6	-308.5	16.0	11.8
cis-6,6'-dhbp lactam → [cis-6,6'-dhbp lactam] <sup>-1+</sup> + H <sup>+</sup>	326.8	318.6	-307.8	10.9	8.0
cis-6,6'-dhbp pyridinol + H <sup>+</sup> → [cis-6,6'-dhbp pyridinol] <sup>+1</sup>	-230.7	-223.6	222.4	-1.2	-0.9
trans-6,6'-dhbp pyridinol + H <sup>+</sup> → trans-6,6'-dhbp pyridinol <sup>+1</sup>	-221.1	-214.0	215.7	1.8	1.3
trans-6,6'-dhbp lactam + H <sup>+</sup> → [trans-6,6'-dhbp lactam] <sup>+1</sup>	-212.4	-205.5	211.1	5.6	4.1
trans-6,6'-dhbp pyridinol + H <sup>+</sup> → [cis-6,6'-dhbp pyridinol] <sup>+1</sup>	-226.8	-219.6	219.0	-0.7	-0.5
cis-6,6'-dhbp lactam + H <sup>+</sup> → [cis-6,6'-dhbp lactam] <sup>+1</sup>	-216.9	-209.8	216.2	6.4	4.7
[trans-6,6'-dhbp lactam] <sup>+1</sup> + H <sup>+</sup> → [trans-6,6'-dhbp pyridinol] <sup>+2</sup>	-156.9	-148.6	163.6	15.0	11.0
[trans-6,6'-dhbp lactam] <sup>+1</sup> + H <sup>+</sup> → [cis-6,6'-dhbp pyridinol] <sup>+2</sup>	-155.1	-147.6	162.7	15.5	11.1
[cis-6,6'-dhbp pyridinol] <sup>+1</sup> + H <sup>+</sup> → [trans-6,6'-dhbp pyridinol] <sup>+2</sup>	-136.0	-128.1	141.9	13.8	10.1
2-OH-Py → Py <sup>-1</sup> + H <sup>+</sup>	348.9	341.3	-328.0	13.2	9.7
2-pyridone → Py <sup>-1</sup> + H <sup>+</sup>	347.5	340.0	-320.2	19.8	14.5
2-OH-Py + H <sup>+</sup> → Py <sup>+1</sup>	-218.2	-210.7	210.7	0.0	0.0
2-pyridone + H <sup>+</sup> → Py <sup>+1</sup>	-219.6	-212.0	218.6	6.6	4.8

<sup>a</sup> pK<sub>a</sub> values were obtained from gas phase G3(MP2) free energies plus COSMO with water as the solvent.

### 2.3 Conclusion

The 6,6'-dhbp protonated and deprotonated conformers and tautomers were optimized at the DFT level and their aqueous solution behavior was studied. The presence of the solvent stabilized the lactam over the pyridinol for the neutral 6,6'-dhbp species, in agreement with experiments, and the trans conformer of the lactam was lower in energy with the cis conformer less than 1 kcal/mol higher in energy. The solvent does not change the relative energies for the monoanion species with cis-lactam being the lowest energy structure in both gas phase and aqueous solution. Similarly, no change in energy ordering in the gas phase and in solution was predicted for the +2 or -1 6,6'-dhbp structures. For the -2 pyridinols, the gas phase trans dianion structure is more stable but in aqueous solution the cis dianion becomes more stable by 9.5 kcal/mol. The <sup>1</sup>H-NMR confirms the solution behavior for the anion and dianion. The predicted gas phase UV-vis spectra for the 6,6'-dhbp monoanion, neutral and dianion were not in good agreement with experiment. However, the TD-DFT calculations in aqueous solution are in much better agreement. The calculations predicted a small blue shift for the neutral molecule and for the dianion and a much larger red shift for the monoanion.

Starting with 6,6'-dihydroxy-2,2'-bipyridine in aqueous solution the most stable species is actually the trans-lactam. In performing the synthesis of a metal complex from 6,6'-dhbp, the first step is to form the pyridinol tautomer and rotate about the central C-C bond to form the cis-pyridinol isomer (relative energy = +7.9 kcal/mol as compared to the trans-lactam). Cis to trans rotation can occur before metal chelation or it can occur after monodentate binding of one pyridinol ring to one metal with the trans conformer. Understanding the thermodynamic landscape gives us some idea of why synthetic procedures to make 6,6'-dhbp metal complexes have employed reflux conditions (in

DMF, methanol, water or other solvents)<sup>1, 17-18</sup> or have employed alternate routes with protection and deprotection strategies for installing the OH group.<sup>2-3</sup> An alternative may be to add base and access the singly or doubly deprotonated cis conformations. These conformers can more readily bind to a metal at room temperature. Thus, the use of base suggests lower energy pathways towards metal complex formation that can be applied to metals that are stable and soluble in mildly basic aqueous solvents (pH > 8.5). These results should be applicable to the synthesis of new catalysts and the determination of their formation constants and stability as a function of pH.

## **2.4 Experimental**

*2.4.1 Materials and Experimental Methods.* All chemicals and reagents were purchased from chemical vendors and were used without further purification. 6,6'-dhbp was synthesized according to the literature procedure.<sup>1</sup> Purified water was obtained from a Synergy UV Millipore system. IR spectra were measured on a Jasco FT/IR-4100 spectrometer with a Pike MIRacle ATR or a Mettler-Toledo ReactIR. UV-vis spectra were obtained on a Perkin-Elmer Lambda 35 UV-vis spectrometer. pH measurements were performed using an Accumet AB150 pH meter calibrated with standard buffer solutions.

*2.4.2 Computational Methods.* The geometries were optimized using density functional theory (DFT)<sup>37</sup> with the hybrid B3LYP exchange-correlation functional<sup>38,39</sup> and the DZVP2 basis sets.<sup>40</sup> Harmonic vibrational frequencies were calculated to ensure that the optimized structures were minima. The DFT geometries were then used as starting points for composite correlated molecular orbital theory calculations at the G3(MP2)

level<sup>41</sup> to obtain improved energetics as the G3(MP2) method represents a good compromise between cost and accuracy and the energetics are in good agreement with higher level calculation or/and experiment where available. These calculations were done with the Gaussian 09 program system.<sup>42</sup>

## 2.5 Author Contribution

I was the intellectual lead on all of the experimental aspects and performed all of the experimental work included in this chapter. I was also the lead author on the paper resulting from this project.

## 2.6 References

1. Nieto, I.; Livings, M. S.; Sacci, J. B.; Reuther, L. E.; Zeller, M.; Papish, E. T. *Organometallics*, **2011**, *30*, 6339-6342.
2. Conifer, C. M.; Taylor, R. A.; Law, D. J.; Sunley, G. J.; White, A. J. P.; Britovsek, G. J. P. *Dalton Trans.*, **2011**, *40*, 1031-1033.
3. Conifer, C. M.; Law, D. J.; Sunley, G. J.; Haynes, A.; Wells, J. R.; White, A. J. P.; Britovsek, G. J. P. *Eur. J. Inorg. Chem.*, **2011**, *2011*, 3511-3522.
4. Dubreuil, D. M.; Pipelier, M. G.; Pradere, J. P.; Bakkali, H.; Lepape, P.; Delaunay, T.; Tabatchnik, A. Pyridazine and Pyrrole Compounds, Processes for Obtaining Them and Uses. WO2008012440A2, 2008.
5. Umemoto, T.; Nagayoshi, M.; Adachi, K.; Tomizawa, G. *J. Org. Chem.*, **1998**, *63*, 3379-3385.
6. Moore, C. M.; Dahl, E. W.; Szymczak, N. K. *Current Opinion in Chemical Biology*, **2015**, *25*, 9-17.
7. Moore, C. M.; Szymczak, N. K. *Chemical Communications*, **2013**, *49*, 400-402.
8. Seo, J.; Ali, A. K.; Rose, M. J. *Comments Inorg. Chem.*, **2014**, *34*, 103-113.
9. Seo, J.; Sotman, T. E.; Sullivan, E. R.; Ellis, B. D.; Phung, T.; Rose, M. J. *Tetrahedron*, **2017**, *73*, 4519-4528.

10. Wang, W.-H.; Hull, J. F.; Muckerman, J. T.; Fujita, E.; Himeda, Y. *Energy Environ. Sci.*, **2012**, *5*, 7923-7926.
11. Siek, S.; Burks, D. B.; Gerlach, D. L.; Liang, G.; Tesh, J. M.; Thompson, C. R.; Qu, F.; Shankwitz, J. E.; Vasquez, R. M.; Chambers, N. S.; Szulczewski, G. J.; Grotjahn, D. B.; Webster, C. E.; Papish, E. T. *Organometallics*, **2017**, *36*, 1091-1106.
12. Gerlach, D. L.; Siek, S.; Burks, D. B.; Tesh, J. M.; Thompson, C. R.; Vasquez, R. M.; White, N. J.; Zeller, M.; Grotjahn, D. B.; Papish, E. T. *Inorg. Chim. Acta*, **2017**, *466*, 442-450.
13. Suna, Y.; Ertem, M. Z.; Wang, W.-H.; Kambayashi, H.; Manaka, Y.; Muckerman, J. T.; Fujita, E.; Himeda, Y. *Organometallics*, **2014**, *33*, 6519-6530.
14. Badiei, Y. M.; Wang, W.-H.; Hull, J. F.; Szalda, D. J.; Muckerman, J. T.; Himeda, Y.; Fujita, E. *Inorg. Chem.*, **2013**, *52*, 12576-12586.
15. Wang, W.-H.; Xu, S.; Manaka, Y.; Suna, Y.; Kambayashi, H.; Muckerman, J. T.; Fujita, E.; Himeda, Y. *ChemSusChem*, **2014**, *7*, 1976-1983.
16. Kawahara, R.; Fujita, K.-i.; Yamaguchi, R. *J. Am. Chem. Soc.*, **2012**, *134*, 3643-3646.
17. DePasquale, J.; Nieto, I.; Reuther, L. E.; Herbst-Gervasoni, C. J.; Paul, J. J.; Mochalin, V.; Zeller, M.; Thomas, C. M.; Addison, A. W.; Papish, E. T. *Inorg. Chem.*, **2013**, *52*, 9175-9183.
18. Gerlach, D. L.; Bhagan, S.; Cruce, A. A.; Burks, D. B.; Nieto, I.; Truong, H. T.; Kelley, S. P.; Herbst-Gervasoni, C. J.; Jernigan, K. L.; Bowman, M. K.; Pan, S.; Zeller, M.; Papish, E. T. *Inorg. Chem.*, **2014**, *53*, 12689-12698.
19. Marelius, D. C.; Bhagan, S.; Charboneau, D. J.; Schroeder, K. M.; Kamdar, J. M.; McGettigan, A. R.; Freeman, B. J.; Moore, C. E.; Rheingold, A. L.; Cooksy, A. L.; Smith, D. K.; Paul, J. J.; Papish, E. T.; Grotjahn, D. B. *Eur. J. Inorg. Chem.*, **2014**, *2014*, 676-689.
20. Hufziger, K. T.; Thowfeik, F. S.; Charboneau, D. J.; Nieto, I.; Dougherty, W. G.; Kassel, W. S.; Dudley, T. J.; Merino, E. J.; Papish, E. T.; Paul, J. J. *J. Inorg. Biochem.*, **2014**, *130*, 103-111.
21. Qu, F.; Park, S.; Martinez, K.; Gray, J. L.; Thowfeik, F. S.; Lundeen, J. A.; Kuhn, A. E.; Charboneau, D. J.; Gerlach, D. L.; Lockart, M. M.; Law, J. A.; Jernigan, K. L.; Chambers, N.; Zeller, M.; Piro, N. A.; Kassel, W. S.; Schmehl, R. H.; Paul, J. J.; Merino, E. J.; Kim, Y.; Papish, E. T. *Inorg. Chem.*, **2017**, *56*, 7519-7532.
22. Zhang, T.; Wang, C.; Liu, S.; Wang, J.-L.; Lin, W. *J. Am. Chem. Soc.*, **2014**, *136*, 273-281.
23. Murguly, E.; Norsten, T. B.; Branda, N. *J. Chem. Soc. Perkin Trans. 2*, **1999**, 2789-2794.

24. Manbeck, G. F.; Muckerman, J. T.; Szalda, D. J.; Himeda, Y.; Fujita, E. *J. Phys. Chem. B.*, **2015**, *119*, 7457-7466.
25. Note that equation 5 was written as forming the dication of 6,6'-dhbp in reference 14. However, in view of the pKa values determined herein, it is more realistic that at pH just below 4 we should form the monocation rather than the dication with the free ligand.
26. Schwederski, B.; Kaim, W. *Inorg. Chim. Acta*, **1992**, *195*, 123-126.
27. Pallavicini, P. S.; Perotti, A.; Poggi, A.; Seghi, B.; Fabbrizzi, L. *J. Am. Chem. Soc.*, **1987**, *109*, 5139-5144.
28. Tomasi, J.; Mennucci, B.; Cammi, R. *Chem. Rev.*, **2005**, *105*, 2999-3093.
29. Klamt, A.; Schüürmann, G. *J. Chem. Soc. Perkin Trans.*, **1993**, *2*, 799-805.
30. Klamt, A., *Quantum Chemistry to Fluid Phase Thermodynamics and Drug Design*. Elsevier: Amsterdam, 2005.
31. Gaussian 03, Revision E.01, Frisch, M. J.; Trucks, G. W.; Schlegel, H. B.; Scuseria, G. E.; Robb, M. A.; Cheeseman, J. R.; Montgomery, Jr., J. A.; Vreven, T.; Kudin, K. N.; Burant, J. C.; et al., Gaussian, Inc., Wallingford CT, 2004
32. Bauernschmitt, R.; Ahlrichs, R. *Chem. Phys. Lett.*, **1996**, *256*, 454-464.
33. Casida, M. E.; Jamorski, C.; Casida, K. C.; Salahub, D. R. *J. Chem. Phys.*, **1998**, *108*, 4439-4449.
34. Schäfer, A.; Horn, H.; Ahlrichs, R. *J. Chem. Phys.*, **1992**, *97*, 2571-2577.
35. Wolinski, K.; Hinton, J. F.; Pulay, P. *J. Am. Chem. Soc.*, **1990**, *112*, 8251-8260.
36. pKa Data Compiled by R. Williams.  
[http://research.chem.psu.edu/brpgroup/pKa\\_compilation.pdf](http://research.chem.psu.edu/brpgroup/pKa_compilation.pdf) (accessed 7/1/2017).
37. Parr, R. G.; Yang, W., *Density-Functional Theory of Atoms and Molecules*. Oxford University Press: New York, 1989.
38. Becke, A. D. *J. Chem. Phys.*, **1993**, *98*, 5648-5652.
39. Lee, C.; Yang, W.; Parr, R. G. *Phys. Rev. B*, **1988**, *37*, 785-789.
40. Godbout, N.; Salahub, D. R.; Andzelm, J.; Wimmer, E. *Can. J. Chem.*, **1992**, *70*, 560-571.
41. Curtiss, L. A.; Redfern, P. C.; Raghavachari, K.; Rassolov, V.; Pople, J. A. *J. Chem. Phys.*, **1999**, *110*, 4703-4709.

42. Gaussian 09, Frisch, M. J.; Trucks, G. W.; Schlegel, H. B.; Scuseria, G. E.; Robb, M. A.; Cheeseman, J. R.; Scalmani, G.; Barone, V.; Mennucci, B.; Petersson, G. A.; et al. Gaussian, Inc., Wallingford CT, 2009.
43. Conifer, C. M.; Taylor, R. A.; Law, D. J.; Sunley, G. J.; White, A. J.; Britovsek, G. J. *Dalton Trans*, **2011**, 40, 1031-3.
44. Zhang, T.; Wang, C.; Liu, S.; Wang, J. L.; Lin, W. *J. Am. Chem. Soc.*, **2014**, 136, 273-81.

## 2.7 Supporting Information

Infrared spectroscopy was used to investigate which of the two tautomers, pyridinol or amide, was preferred. Infrared spectroscopy can show the presence or absence of a carbonyl. The IR spectrum of dhbp in the solid state shows a peak at  $1634\text{ cm}^{-1}$ , corresponding to a carbonyl peak (Figure 2.S1). This suggests that the amide form is favored in the solid state. The IR spectrum of dhbp was also measured in the liquid state in DMSO (Figure 2.S2-2.S3). In DMSO, the IR spectrum also shows a carbonyl peak at  $1665\text{ cm}^{-1}$ , so the amide form is also favored in DMSO. This is consistent with the literature<sup>1, 3, 43-44</sup> but is inconsistent with the predicted favored tautomer from our computations.

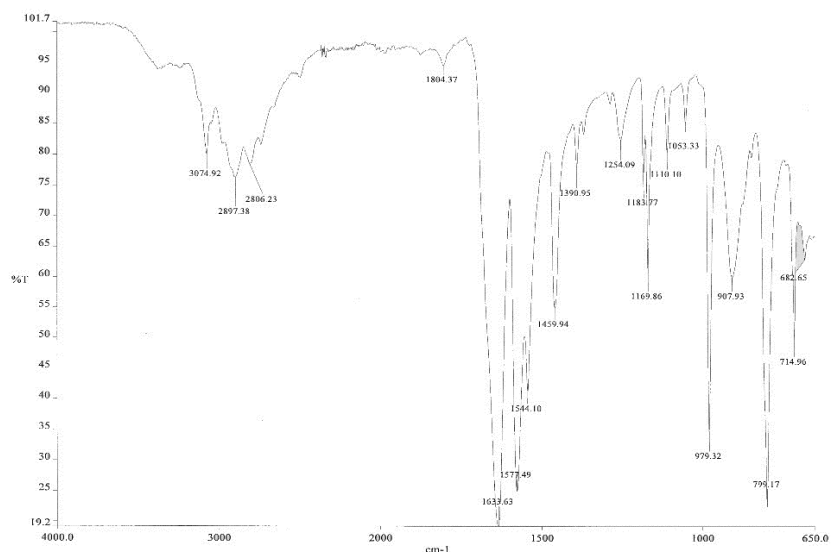


Figure 2.S1. ATR-FTIR spectrum of 6,6'-dhbp in the solid state.

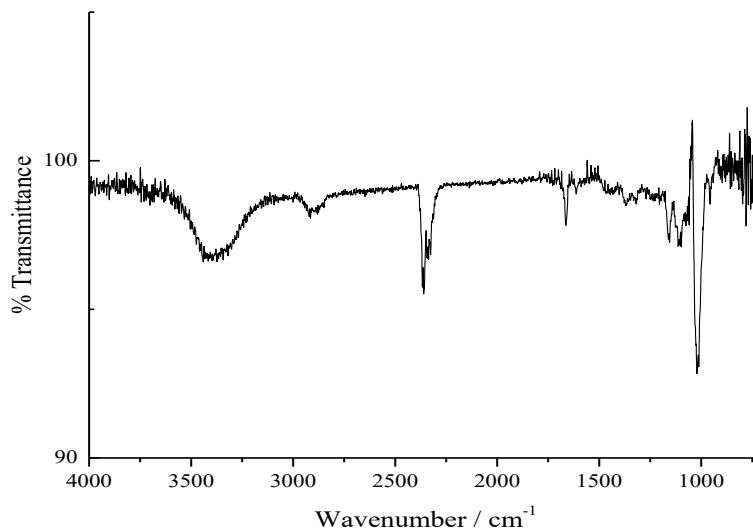


Figure 2.S2. ATR-FTIR spectrum of 6,6'-dhbp in DMSO.

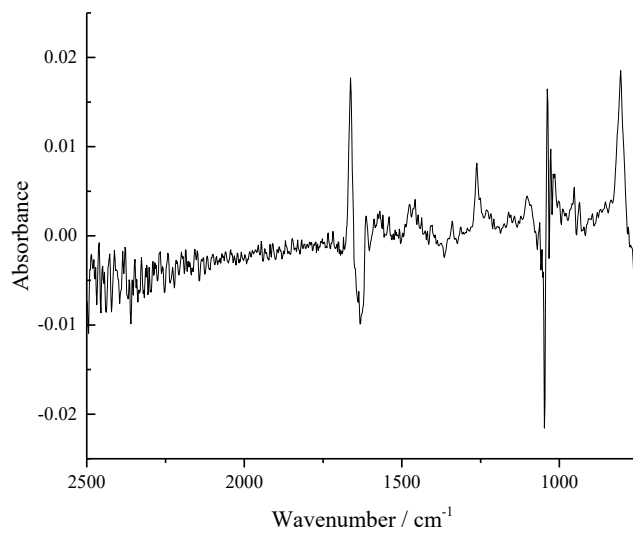
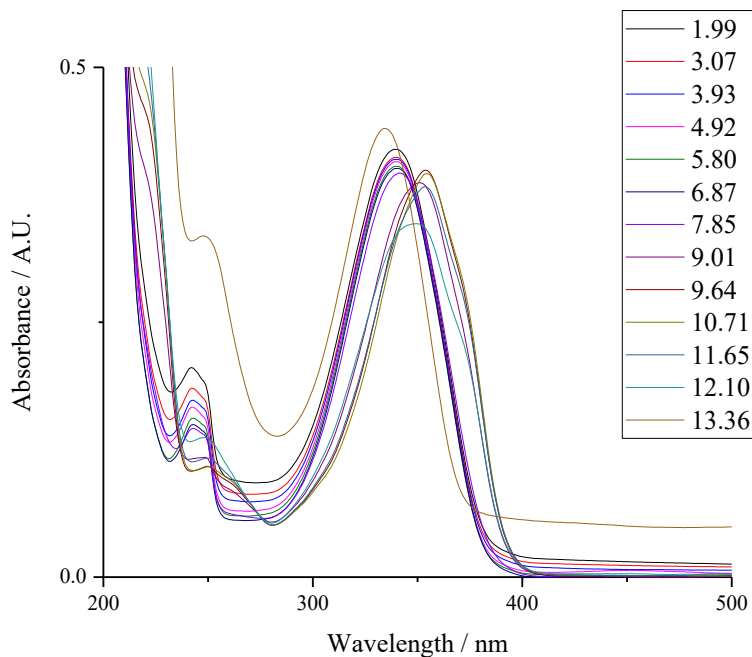
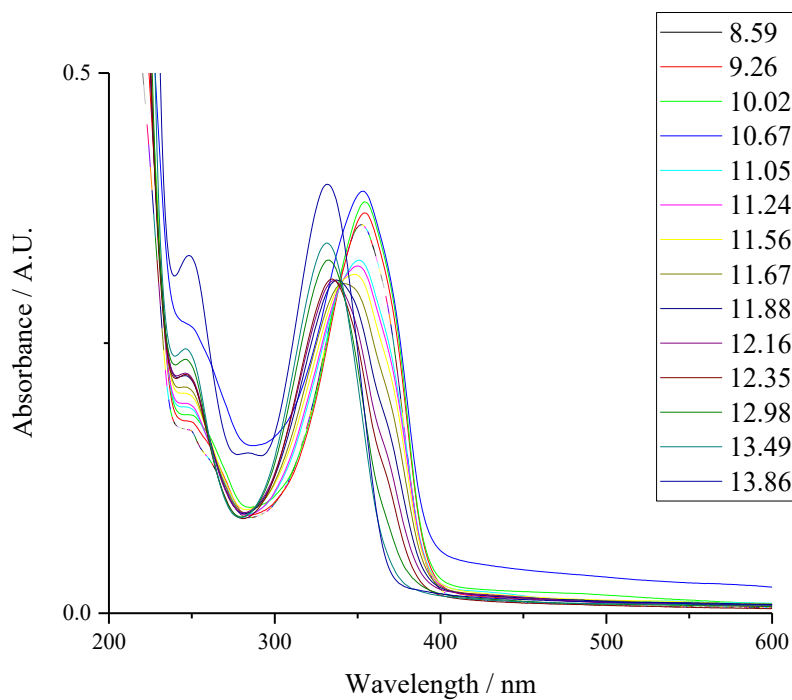


Figure 2.S3. IR spectrum of 6,6'-dhbp in anhydrous DMSO.



*Figure 2.S4.* UV-vis spectra of an aqueous solution of 6,6'-dhbp from 200-500 nm and pH of  $\sim 2$  to  $\sim 13.5$ . The pH was adjusted with aqueous solutions of NaOH or H<sub>2</sub>SO<sub>4</sub>.



*Figure 2.S5.* UV-vis spectra of an aqueous solution of 6,6'-dhbp from 200-600 nm and pH of  $\sim 8.5$  to  $\sim 14$ . The pH was adjusted with aqueous solutions of NaOH or H<sub>2</sub>SO<sub>4</sub>.

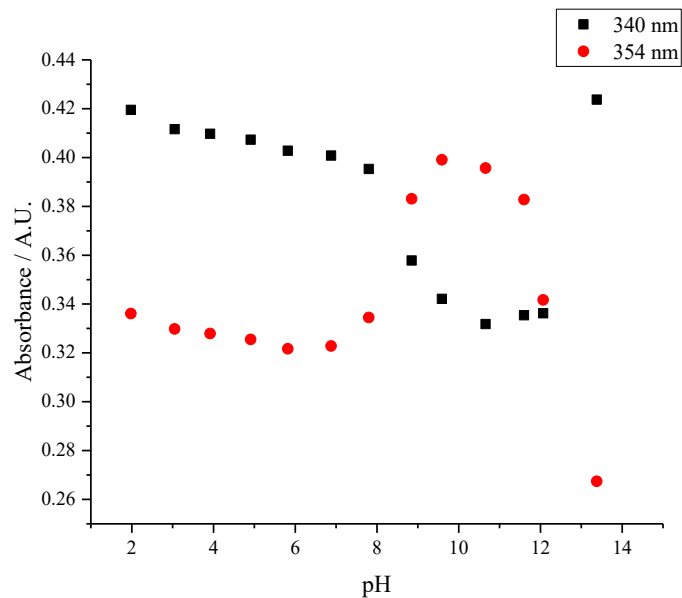


Figure 2.S6. The UV-vis absorbance values of 6,6'-dhbp at 340 nm (black squares) and 354 nm (red circles) with the pH changing from 2 to 14.

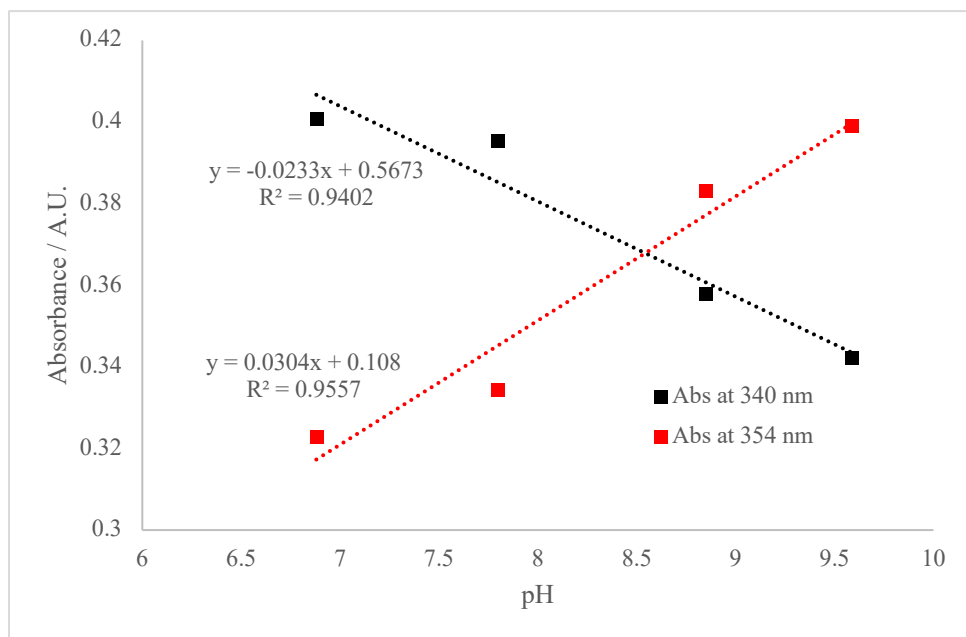


Figure 2.S7. Linear fits of the linear region of Figure 2.S6, approximately pH 7 to 10, for both the absorbance values at 340 nm (black) and 354 nm (red). The  $pK_a$  was determined as the point where the two lines intersect. From the linear fits, the  $pK_a$  was determined to be  $8.5 \pm 1.4$ .

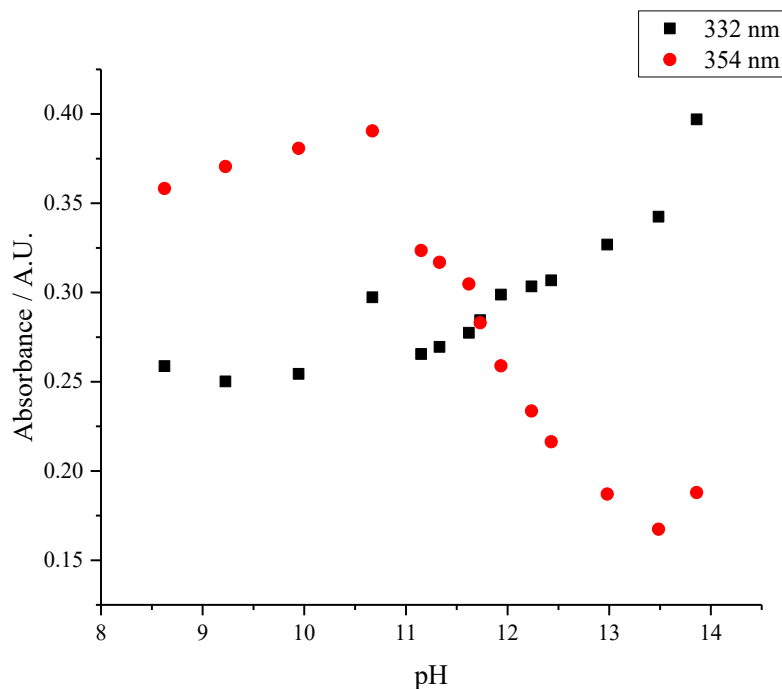


Figure 2.S8. The UV-vis absorbance values of 6,6'-dhbp at 332 nm (black squares) and 354 nm (red circles) with the pH changing from 8.5 to 14.

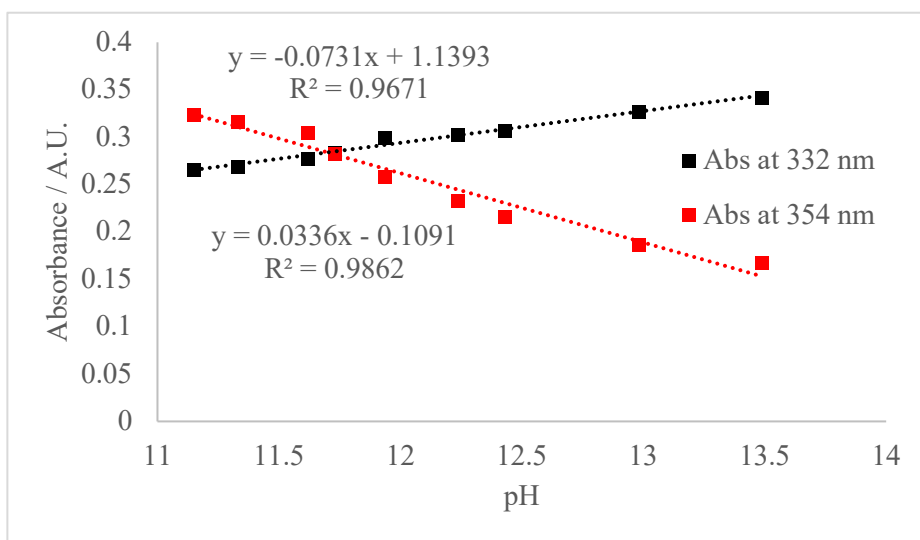


Figure 2.S9. Linear fits of the linear region of Figure S8, approximately pH 11 to 13.5, for both the absorbance values at 332 nm (black) and 354 nm (red). The  $pK_{eq}$  was determined as the point where the two lines intersect. From the linear fits, the  $pK_{eq}$  was determined to be  $11.7 \pm 0.84$ .

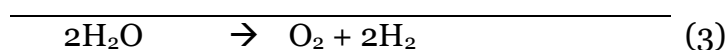
## CHAPTER 3:

### STUDIES OF THE PATHWAYS OPEN TO COPPER WATER OXIDATION CATALYSTS CONTAINING PROXIMAL HYDROXY GROUPS DURING BASIC ELECTROLYSIS

Adapted from Gerlach, D. L.; Bhagan, S.; Cruce, A. A.; Burks, D. B.; Nieto, I.; Truong, H. T.; Kelley, S. P.; Herbst-Gervasoni, C. J.; Jernigan, K. L.; Bowman, M. K.; Pan, S.; Zeller, M.; Papish, E. T. *Inorg. Chem.*, 2014, 53, 12689-12698.

#### 3.1 Introduction

A sustainable energy economy (eqs 1-3) is attainable by mimicking the catalytic efficiency of the oxygen evolving complex in photosystem II (PS II).<sup>1</sup> The active site of the oxygen evolving complex in PS II contains hydrogen bonding residues near its Mn<sub>4</sub>Ca cluster which play a role in proton shuttling to facilitate the kinetically challenging water oxidation reaction (eq 1).<sup>2,3</sup>



Significant developments utilizing metals such as Ru,<sup>4</sup> Ir,<sup>5-6</sup> Mn,<sup>7</sup> Fe,<sup>8</sup> Co,<sup>9-10</sup> Ni,<sup>11</sup> and Cu<sup>12-15</sup> as water oxidation catalysts (WOCs) have been reported. However, water oxidation catalysts with low overpotentials remain elusive and are a major goal of

contemporary research. Lower overpotentials can be achieved by catalysts that facilitate proton coupled electron transfer (PCET) and stabilize key intermediates.<sup>4, 16</sup> We postulated that the recently designed ligand, 6,6'-dihydroxybipyridine (6,6'-dhbp),<sup>17-20</sup> could perform both of these functions with copper, and the results to support this hypothesis are described herein.

Previously, the Papish group reported iridium water oxidation catalysts featuring 6,6'-dihydroxybipyridine (6,6'-dhbp) and 4,4'-dhbp ligands. These catalysts show that initial rates of water oxidation can be increased by a factor of ~100 simply by changing pH from 3 to 6.<sup>21</sup> Our studies demonstrated that enhanced rates for water oxidation catalysis are due to ligand deprotonation which facilitates metal complex oxidation.<sup>21</sup> Parallel water oxidation studies with ruthenium complexes of 6,6'-dhbp and 6,6'-dimethoxybipyridine (6,6'-dmbp) have illustrated that methoxy and hydroxy groups near the metal form hydrogen bonds (including with Ru bound aqua substrate) and such interactions may stabilize reactive intermediates.<sup>22</sup> Thus, 6,6'-dhbp ligands have interesting, pH sensitive properties,<sup>18, 23</sup> and our group and others have shown that metal complexes thereof catalyze several different types of reactions,<sup>17, 19-20</sup> including both oxidative<sup>24</sup> and reductive<sup>18, 25</sup> processes.

We now extend the study of dihydroxy- and dimethoxy-bipyridine ligand series to copper (II) complexes. Recently, others have shown that *in situ* prepared 1:1 mixtures of copper (II) salts and 6,6'-dhbp ligands form a coordination polymer in the crystal phase and exhibit electrocatalytic water oxidation.<sup>26</sup> In our study, monomeric copper (II) complexes exhibiting primarily 2:1 ligand to metal ratios are investigated as water oxidation catalysts. Equilibrium constants are determined for deprotonation events and provide insight into catalytically relevant changes at the metal center. ENDOR and

HYSORE spectroscopy herein demonstrate the continuous ligation of the 6,6'-dhbp ligand to the copper(II) ion through the pH range where water oxidation is tested. The activity of catalysts containing hydrogen bonding OH/O<sup>-</sup> groups near and far from the metal center (in 4,4'-dhbp and 6,6'-dhbp) and hydrogen bond accepting methoxy groups (in 6,6'-dmbp) is investigated.

### 3.2 Results and Discussion

Inspired by copper WOCs using bipy ligands,<sup>12</sup> a series of copper(II) complexes using 6,6'-dhbp and closely related derivatives were synthesized, shown schematically in Figure 3.1 with non-coordinating anions omitted. Monomeric copper-ligand complexes were formed from copper (II) nitrate (**3**) and copper (II) sulfate (**1**, **2**, **4**) to demonstrate the significant influence of varying anions and solvents. Additionally, a well characterized monomeric zinc analogue was prepared as a control (**5**). Metal to ligand ratios are 1:1 in **4** and 1:2 in **1**, **2**, **3**, and **5**. Structural diversity in the array of dxbp (x = hydroxy or methoxy) derived divalent copper and zinc complexes are first discussed and subsequently thermodynamic acidities and water oxidation studies on selected compounds are described.

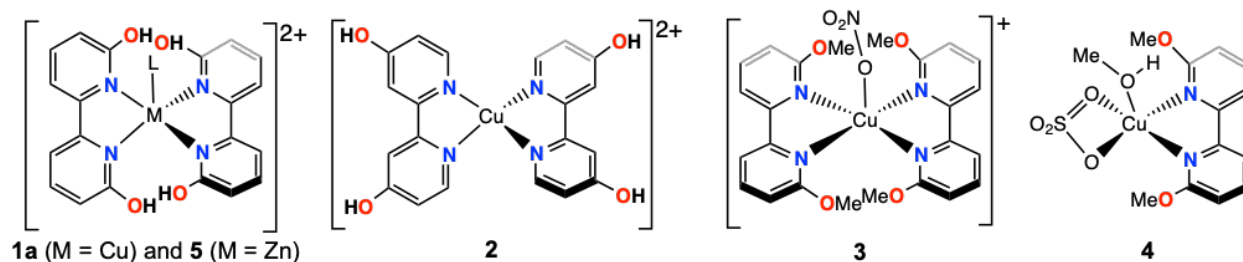


Figure 3.1. Structural diversity of complexes (1 – 5) prepared for this study.

### 3.2.1 Synthesis and Structural Studies

All syntheses were performed by Deidra Gerlach (DLG) and Salome Bhagan (SB), with preliminary synthetic work by Ismael Nieto, Hai Truong, and Corey Herbst-Gervasoni, and crystal structures were solved and refined by Steven Kelley and Matt Zeller.

Treating copper (II) sulfate with 6,6'-dhbp in ethylene glycol resulted in the clean formation of complexes with a 2:1 ratio of ligand to metal which were fully characterized (see Experimental Section and SI). Two different protonation states of [(6,6'-dhbp)<sub>2</sub>Cu]<sup>n+</sup> (**1**) were obtained as brown crystals and green crystals, from a single sample by slow evaporation from methanol. X-ray crystallography was used to identify the brown crystals as the fully protonated, penta-coordinate copper bis(6,6'-dhbp) methanol sulfate salt, [(6,6'-OH-bpy)<sub>2</sub>Cu(CH<sub>3</sub>OH)]SO<sub>4</sub> (**1a**), Figure 3.2. The green crystals were identified as doubly deprotonated tetra-coordinate copper bis(6,6'-dhbp) [(6-OH-6'-O-bpy)<sub>2</sub>Cu]•(CH<sub>3</sub>OH)<sub>2</sub> (**1c**), Figure 3.3. Complexes **1a**, **1c**, and the other protonation states for **1** (**1b**, **1d** (not observed), **1e**) are shown in Scheme 1.

Complex **1a** (Figure 3.2) features a distorted trigonal bipyramidal copper center with  $\tau = 0.697$ .<sup>27</sup> The coordinated methanol has a Cu-O bond distance of 2.340 Å and the 6,6'-dhbp ligands approach the metal more closely (Cu-N distances ~1.96 to 2.07 Å). Both the bound methanol and the OH groups of all the 6,6'-dhbp ligands are hydrogen bond donors to nearby sulfate counter anions (O...O distances range from ~2.54 to 2.78 Å indicating hydrogen bonds). The crystal packing reveals that the copper complex cations are arranged into sheets divided by interwoven planes of the sulfate anions. Interestingly,  $\pi$  stacking occurs between the 6,6'-dhbp ligands of two molecules opposite an inversion center.

Doubly deprotonated **1c** (Figure 3.3) features a distorted geometry around copper that is intermediate between tetrahedral and square planar. The twist angles between planes that contain each 6,6'-dhbp ligand range from 52 to 55°. The Cu-N bonds are slightly shortened (relative to **1a**) and all are around  $\sim 1.97$  Å. This reflects the negative charge on each ligand and the resulting partial negative charge on N due to resonance. Consistent with this explanation is a slightly decreased C-O distance<sup>28</sup> due to double bond character (1.290(3) Å vs. 1.320(3) Å). Note that each dhbp ligand has one deprotonated and one protonated oxygen. Two crystallographically distinct methanol molecules are hydrogen bonded to the 6,6'-dhbp ligand in the crystal phase, but notably they do not coordinate. Hydrogen bonds exist between OH and O<sup>-</sup> of the dhbp ligands (O2...O1 = 2.488(2) Å) in neighboring molecules in the packing diagram (not shown in Figure 3.3). Also, there are moderate strength hydrogen bonds from O<sup>-</sup> of dhbp to methanol (O2...O1S = 2.713(3) Å). An infinite head-to-tail chain of molecules along the crystallographic b axis results from this hydrogen bonding, as described further in the Supporting Information. Although the coordination number differs between these two structures of the crystalized complex **1** at two protonation states, both metal centers have the capacity for further ligation in the presence of coordinating solvent. Spacefill models of each structure show the copper (II) ion as being accessible to a sixth ligand or fifth ligand for complexes **1a** and **1c**, respectively.

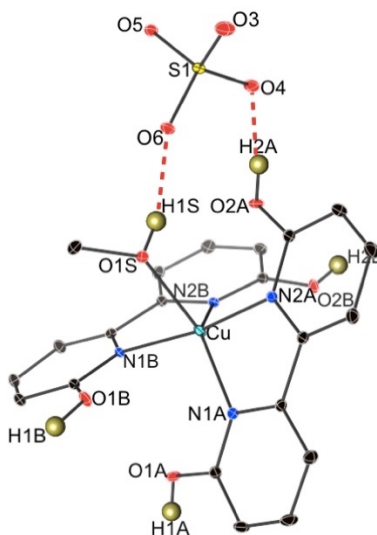


*Figure 3.2.* Structural diagram of the fully protonated complex, [(6,6'-dhbp)<sub>2</sub>Cu(CH<sub>3</sub>OH)]SO<sub>4</sub> (**1a**). This complex features OH to sulfate hydrogen bonds, as shown as red dashed lines. Non-hydrogen atom ellipsoids are shown at 30% probability. Hydrogen atoms are shown as spheres of arbitrary radius. Most hydrogen atoms are omitted for clarity.

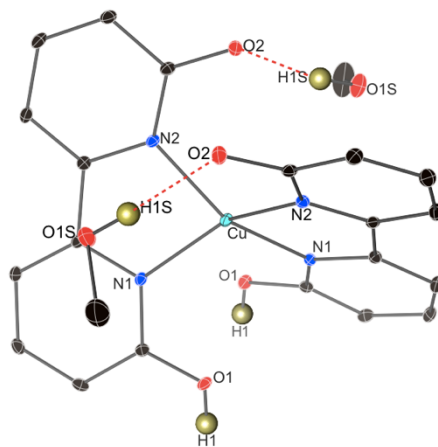


*Figure 3.3.* Structural diagram of the doubly deprotonated complex, [(6-OH-6'-O-bpy)<sub>2</sub>Cu] • (CH<sub>3</sub>OH)<sub>2</sub> (**1c**). This complex features O<sup>-</sup> to methanol hydrogen bonds, as shown with red dashed lines. Non-hydrogen atom ellipsoids are shown at 30% probability. Hydrogen atoms are shown as spheres of arbitrary radius. Most hydrogen atoms are omitted for clarity.

Complex **2** was prepared in a manner analogous to **1** by using 4,4'-dhbp and copper sulfate in a 2:1 ratio. Complex **2** was synthesized to investigate the role of hydroxyl groups far from the copper metal center for water oxidation studies. The light

blue solid was obtained in 82 % yield and characterized by UV-Vis and IR spectroscopy and elemental analysis. Crystals suitable for X-Ray diffraction were not obtained despite several attempts, but complex **2** is likely to have a coordination geometry similar to that of complex **1a** where the possibility of coordination of a fifth ligand L (H<sub>2</sub>O or MeOH) is possible in solution.

Complex **3** was formed from the reaction of 6,6'-dmbp and Cu(NO<sub>3</sub>)<sub>2</sub>•2.5 H<sub>2</sub>O (Figure 3.4). The formula unit obtained by crystallography was [(6,6'-dmbp)<sub>2</sub>Cu(NO<sub>3</sub>)<sub>2</sub>][Cu(NO<sub>3</sub>)<sub>4</sub>] wherein both copper ions are divalent (see supporting information). This structure features a five-coordinate trigonal bipyramidal copper (II) ion ligated by two (N,N) bound 6,6'-dmbp ligands and one κ<sup>1</sup>-nitrate ligand with τ = 0.803. The Cu (II) ion in [Cu(NO<sub>3</sub>)<sub>4</sub>]<sup>2-</sup> binds each nitrate in an asymmetric κ<sup>2</sup> mode with four short Cu-O bonds and four long Cu-O bonds. This anion is rare but has been observed in seven crystal structures in the Cambridge Structural Database.<sup>29-30</sup> However, the poor solubility of this complex (**3**) in basic aqueous solution combined with the presence of two distinct copper environments made this species unsuitable for catalytic water oxidation studies.

In contrast, the reaction of 6,6'-dmbp with copper (II) sulfate using a two-fold excess of the dmbp ligand resulted in isolation of a monomeric copper complex (**4**, Figure 3.5) with a 1:1 ligand to metal ratio. Complex **4** [(6,6'-dmbp)Cu(SO<sub>4</sub>)(CH<sub>3</sub>OH)] was isolated in 75 % yield by recrystallization from methanol and exhibits a square pyramidal geometry around Cu (τ = 0.075) with an apical methanol molecule. Hydrogen bonds between coordinated methanol and neighboring sulfate groups (O5...O7 = 2.671(2) Å) extend along the “a” direction of the unit cell and connect the molecules in a two-dimensional network.

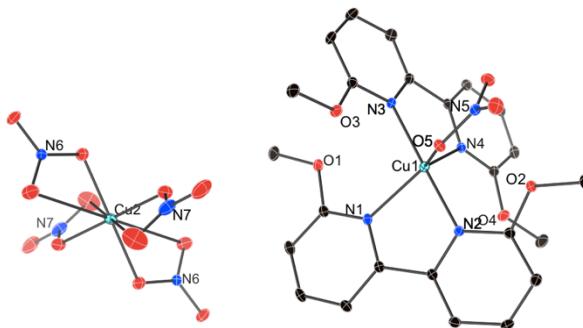


**Figure 3.4.** Copper (II) complex of 6,6'-dimethoxybipyridine (**3**) with the formula unit  $[(6,6'\text{-dmbp})_2\text{Cu}(\text{NO}_3)]_2[\text{Cu}(\text{NO}_3)_4]$ . Ellipsoids are shown at 30% probability. Hydrogen atoms are omitted for clarity and only one  $[(6,6'\text{-dmbp})_2\text{Cu}(\text{NO}_3)]$  unit is shown.

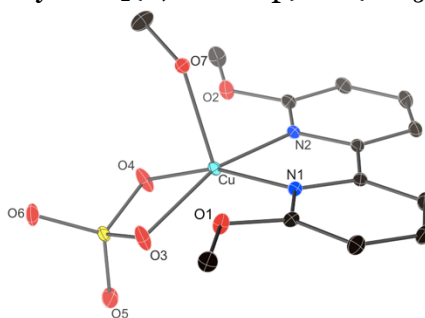


**Figure 3.5.** Structural diagram of  $[(6,6'\text{-dmbp})\text{Cu}(\text{SO}_4)(\text{CH}_3\text{OH})]$  (**4**). This complex features OH of methanol to sulfate hydrogen bonds (not shown), involving neighboring molecules. Ellipsoids are shown at 30% probability. All hydrogen atoms are omitted for clarity.

A zinc complex of 6,6'-dhbp was prepared to determine whether copper is essential for water oxidation (*vide infra*). Treatment of zinc(II) perchlorate hexahydrate with 6,6'-dhbp led to clean formation of  $[(6,6'\text{-dhbp})_2\text{Zn}](\text{ClO}_4)_2$  (**5**) in 29% yield after recrystallization from acetonitrile and hexane (3:1). The crystal structure (Figure 3.6) shows that the geometry around zinc is a nearly perfect tetrahedron (the torsion angle between the planes containing 6,6'-dhbp ligands is  $87\text{-}88^\circ$ ), in contrast to the twisted alignment of ligands in **1c**. Hydrogen bonds are present between all OH groups of 6,6'-dhbp and neighboring disordered perchlorate anions (O...O hydrogen bonding distances range from  $2.680(5)$  to  $2.93(1)$  Å).

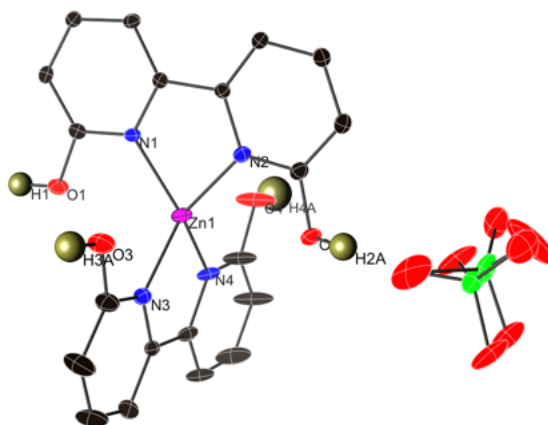


*Figure 3.6.* Structural diagram of  $[(6,6'\text{-dhbp})_2\text{Zn}](\text{ClO}_4)_2 \cdot 3\text{CH}_3\text{CN}$  (**5**). This complex features OH to  $\text{O}^-$  of perchlorate hydrogen bonds. The perchlorate anions are disordered in the crystal (Cl = green and O = red). Non-hydrogen atom ellipsoids are shown at 30% probability. Hydrogen atoms are shown as spheres of arbitrary radius. Most hydrogen atoms are omitted for clarity.

### 3.2.2 Acid-Base Titrations of Complex **1** for Determining Protonation States

The two crystal structures afforded for complex **1** are snapshots of protonation/deprotonation states of this complex. The complex  $[(6,6'\text{-dhbp})_2\text{Cu}(\text{L})]\text{SO}_4$  (**1**) contains four acidic hydrogens from four OH groups of the hydroxypyridine rings, Scheme 1. Further deprotonation events are possible for penta-coordinated complexes of **1** (L = aqua or methanol) as seen in the structure for complex **1a** where methanol is coordinated. The neutral, doubly deprotonated complex  $[(6\text{-OH-}6'\text{-O-bpy})_2\text{Cu}]$  (**1c**) is tetra-coordinate without methanol or water bound in the coordination sphere in the crystal phase (Figure 3.3). Deprotonation of 6,6'-dhbp results in an increase of negative charge on the ligand and as a result binds more strongly to copper. Increasing the negative charge of the ligand supports lower coordination numbers on the metal center through resonance stabilized pyridinolate rings which delocalize the negative charge onto the nitrogen atoms.



12.4 to 13.4 (see SI) affords the elucidation of another inflection point at pH = 12.8. As described below, further experiments show that the inflection points at pH = 5.2, 6.2, and 8.3 are  $pK_a$  values for complex **1**, and the inflection points at 3.9 and 12.8 represent demetallation events occurring in the low and high pH regimes.

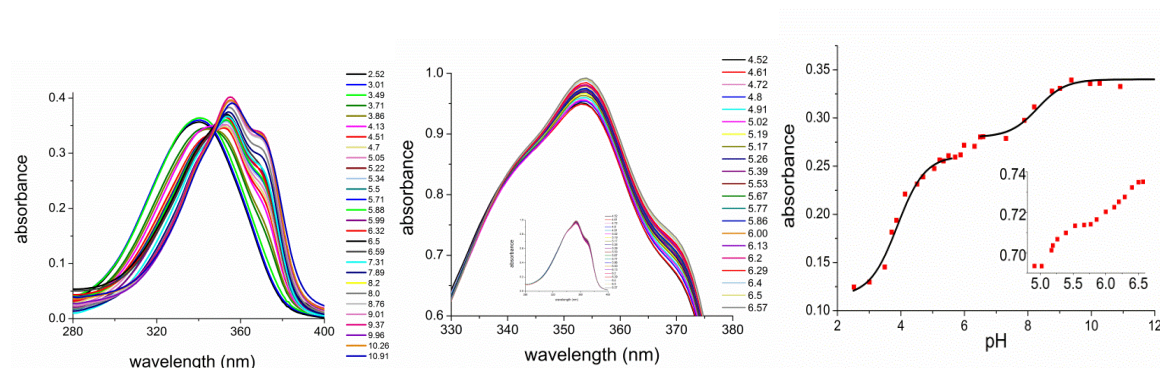


**Figure 3.7.** Left: UV-Vis absorption spectra of aqueous solutions of  $[(6,6'\text{-dhbp})_2\text{Cu}]\text{SO}_4$  (**1**) as a function of pH from pH = 2.5–11 at 25 °C. Middle: Same as left but from pH = 4.5 – 6.5 in 0.1 pH increments, and the inset shows the full peak shape. Right: Plot of absorbance (at  $\lambda = 369$  nm) vs. pH at 25 °C, and the inset shows the same plot from pH 5.0 to 6.5.

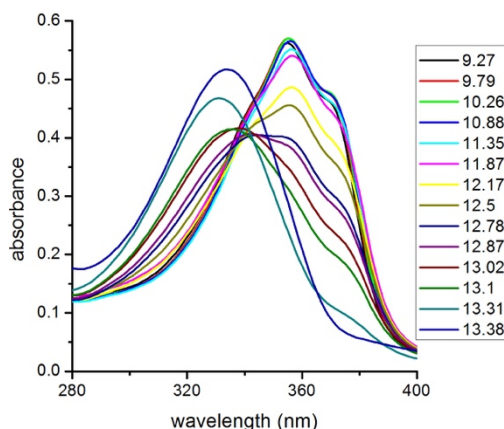


**Figure 3.8.** UV-Vis absorption spectra of aqueous solutions of  $[(6,6'\text{-dhbp})_2\text{Cu}]\text{SO}_4$  (**1**) as a function of pH from pH = 9.3–13.4 at 25 °C.

The  $pK_a$  values of 5.2 and 6.2 are each tentatively each assigned to the removal of one proton from the 6,6'-dhbp ligands (Scheme 1, **1a** goes to **1b** goes to **1c**). Similarly, our studies of  $\text{Ru}^{\text{II}}$  and  $\text{Ir}^{\text{III}}$  complexes of 6,6'-dhbp showed  $pK_a$  values of 5–7.27 and 4.6,

respectively,<sup>18, 21, 23</sup> for removal of ligand protons which are typically more acidic than protons of a metal-bound aqua ligand.<sup>21-22</sup> The last  $pK_a$  value (8.30) is tentatively assigned to the removal of 2 protons (Scheme 1, **1c** goes to **1e**, presumably via **1d**). This value is higher or similar to previously observed values for Ru<sup>II</sup> complexes,<sup>22-23</sup> and this makes sense given the 2- charge associated with complete deprotonation of complex **1** to form **1e**. Deprotonation of Cu(II)-bound aqua ligands to form hydroxide ligands is not supported by the HYSORE evidence (below) until the high pH regime (pH > 12.8). Similarly, studies of Cu(II) bipyridine complexes have shown that the concentration of [Cu(bpy)<sub>2</sub>OH]<sup>+</sup> does not predominate until pH 11.<sup>31</sup>

It should be noted that the absorption event that is most significant at 369 nm is primarily the  $\pi$ - $\pi^*$  of the aromatic dhbp ligand thus the largest change in absorption at this wavelength can be inferred to be a modification of the aromaticity of the ligand with likely minor to no change in absorbance for deprotonation of the possible fifth L ligand (H<sub>2</sub>O or MeOH). The free 6,6'-dhbp ligand alone shows significant change in absorbance and the appearance of a distinct gaussian signal in this region which can be described by loss of aromaticity.

EPR studies on **1**, described below, show significant changes in the coordination geometry (which could include fifth ligand L coordination of water or hydroxide) do not occur until above pH 10. As described below, the EPR data, in particular the HYSORE, was instrumental in identifying that the low and high pH inflection points (pH = 3.9 and 12.8 respectively) are demetallation events for the 6,6'-dhbp ligand. Below pH = 3.9, the 6,6'-dhbp ligand is singly or doubly protonated (most likely), wherein the latter structure would have both oxygen and nitrogen atoms protonated and aromaticity is maintained. At this pH the copper ion will ligate six waters as in the known

$[\text{Cu}(\text{H}_2\text{O})_6]^{2+}$  complex. At pH above 12.8 the 6,6'-dhbp ligand is doubly deprotonated with two phenoxide groups. It is likely that the drive for demetallation of the 6,6'-dhbp ligand at high pH is due to hydroxide out-competing for coordination to the cupric ion.

The distribution of the species **1a-1e** has been plotted as a function of pH, as shown in Figure 3.9 (calculated from the  $\text{p}K_a$  values with Hyperquad Simulation and Speciation software). This shows that from pH 4.5-7 species **1a**, **1b** and **1c** are all present simultaneously, and perhaps this explains the co-crystallization of **1a** and **1c**. Also above pH 9 (i.e. water oxidation conditions, *vide infra*), species **1e** is dominant. Discussion of the speciation above pH 10 is in the EPR section below.

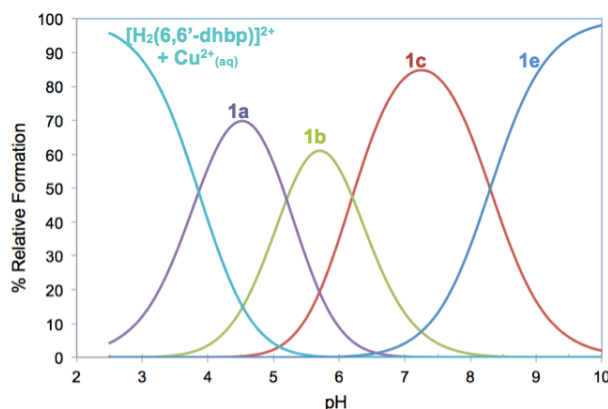


Figure 3.9. Calculated speciation diagram from pH 2.5 to 10 based upon the  $\text{p}K_a$  values for  $[\text{Cu}(6,6'\text{-dhbp})_2]^{2+}$  (**1a**) and the EPR experiments.

Similar acid-base titration studies of  $[(4,4'\text{-dhbp})_2\text{Cu}]^{2+}$  (**2**) by UV-Vis absorption and potentiometric titrations were also performed, and two acid dissociation constants were observed in the range of pH 5 to 8. Studies to assign acid dissociation constants using UV-Vis spectral methods were inconclusive. Thus, exact  $\text{p}K_a$  values could not be obtained for **2** (see SI). Similarly, potentiometric titration of the zinc complex **5** led to

the observation of two  $pK_a$  values (tentatively, each may be the removal of two protons), but exact  $pK_a$  values could not be assigned.

### *3.2.3 EPR Spectroscopy Studies to Determine the Speciation of Complex 1 at Different pH Values*

EPR studies were performed by Alex Cruce and Michael Bowman. The continuous wave (CW) electron paramagnetic resonance (EPR) spectra (combined with electron nuclear double resonance (ENDOR) spectroscopy) can distinguish between N and O ligands on the copper, since hyperfine interactions of the N ligands produce broader resonances. The spectra show that the 6,6'-dhbp ligand(s) are bound to the metal ion throughout pH 5.7 to 12.6 (see the Supporting Information for CW-EPR spectra). This is a wide range that includes the majority of the deprotonation events observed by UV-Vis absorption (*vide supra*) and the water oxidation conditions most extensively studied (*vide infra*). However, the 6,6'-dhbp ligand is not bound to  $Cu^{2+}$  at pH 3.5 and pH 13.3, and these spectra match those observed for  $CuSO_4$  aqueous solutions prepared at the same pH values and correspond with previously noted demetallation events at low and high pH values (inflection points at pH = 3.9 and 12.8, respectively).

The CW spectra taken between pH values 5.7-10.0 are identical (species **A**) and thus the acid dissociation constants (at  $pK_a = 5.2, 6.2$  and  $8.3$ ) reported by UV-Vis spectroscopy are indeed consistent with ligand deprotonation events. A substantial rearrangement at the metal center from pH 5 to 10 would lead to a major change in the EPR spectra. Thus, the data are not consistent with a fifth ligand, e.g.  $H_2O$ , coordinating to any significant extent in this pH regime.

As pH increases from pH 10 to 13.3, the EPR shows that from pH 10 to ~12, species **A** disappears and species **B** and **C** appear, but species **B** dominates the spectrum and species **C** is around 20% of the EPR spectrum from pH 11.5 to 12.6. Species **D** appears at pH 12, and the concentration steadily increases, ultimately becoming the lone species at pH 13.3, with the 6,6'-dhbp ligand completely dissociated (see speciation diagram in the SI). This transformation likely involves coordinating hydroxide ligands as the pH increases. The percentage of each species,  $g$ , and  $A$  values at each pH, is shown in the SI. ENDOR spectroscopy further supports that the same number of 6,6'-dhbp ligands is bound to copper (II) at pH 8.2 and 11, but ligand loss occurs at pH 13.3.

While these EPR spectra do not account for the impact of oxidizing potentials on the complex geometry, at least it is clear that nitrogen ligands are present at pH 10-12.6 wherein water oxidation begins to occur at pH 11.5. At pH 12.6, which is the most frequently studied pH for water oxidation, the mixture is 36% species **B**, 23% species **C**, and 41% species **D** by simulating CW EPR. Thus, at pH 12.6, species **B** and **C** (together 59%) contain 6,6'-dhbp bound to Cu ion from the ENDOR data, but a significant portion of the sample has unligated copper. Spin quantification shows that no significant quantity of EPR silent material is present, thus dinuclear-copper species are unlikely in our pre-catalysts used for water oxidation. This helps to elucidate the nature of the species in solution during water oxidation in our studies (below) and perhaps present in other studies.<sup>26</sup>

Pulsed EPR was utilized to further identify species **A**, **B** and **C**. HYperfine Selective CORrElation Spectroscopy (HYSCORE) is a pulsed EPR technique used to measure ENDOR frequencies, that is, NMR frequencies shifted by hyperfine interactions between the unpaired electron and nuclei near the copper center.

HYSCORE gives a 2D representation of ENDOR frequencies similar to COSY in NMR. HYSCORE spectroscopy has been used to detect axial water protons and axial cysteine protons up to 0.3 nm away from the low-spin, active site heme of cytochrome P450.<sup>32-33</sup> HYSCORE can also detect  $^{13}\text{C}$  up to 0.5 nm from the paramagnetic center.<sup>34</sup> Complex **1** has HYSCORE spectra showing protons from ligated water (pH 10-12.5),  $^{13}\text{C}$  from 6,6'-dhbp ligands (pH 10-12.5), and hydroxide (pH 13.3).

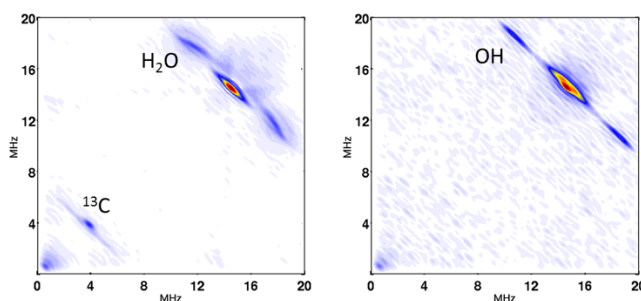


*Figure 3.10.* HYSCORE spectrum at pH 11 of Left) complex **1** and Right)  $\text{CuSO}_4$  in 10% glycol. The intense peak near [14 MHz, 14 MHz] is from protons in solvent surrounding the complexes. The arcs flanking that peak near [18 MHz, 12 MHz] and [12 MHz, 18 MHz] are from protons on water (complex **1**) or hydroxide ( $\text{CuSO}_4$ ) directly coordinated to the copper. Note the tilt of the signals from ligated water on complex **1** (also seen on  $\text{CuSO}_4$  at low pH) compared to the straight lines from copper bound hydroxide in the frozen solution of  $\text{CuSO}_4$  at high pH. The peak near [4 MHz, 4 MHz] is from natural abundance  $^{13}\text{C}$  in the 6,6'-dhbp ligands.

HYSCORE spectra of complex **1**, up to at least pH = 11, have a distinct peak from  $^{13}\text{C}$  along the diagonal near [4 MHz, 4 MHz]. Figure 3.10 shows the spectra at pH 11 for **1** compared to free  $\text{CuSO}_4$  at the same pH with the same solvent conditions. There is a less intense streak running through the diagonal peak from  $^{13}\text{C}$  having hyperfine couplings of as much as 6 MHz. This streak is caused by delocalization of the unpaired electron spin of the copper onto an aromatic ligand where the hyperfine couplings from natural abundance  $^{13}\text{C}$  had a variety of values at the different carbons of the ligand.

The combined evidence includes the acid-base titrations interpreted by UV-Vis spectroscopy and several EPR techniques for aqueous solutions of complex **1**. These experiments elucidate which species are present across a wide range of pH values, including typical water oxidation conditions. Scheme 1 depicts our interpretation of this data, including demetallation events as the pH is lowered below 3.9 and above 12.8. Tentatively, the species labeled as **A**, **B**, and **D** from the EPR data are **1e**, **1e'** (**1e** with aqua ligand coordinated), and a copper hydroxide/aqua complex (Scheme 1). Species **C** is in low abundance so the assignment is uncertain, but it may involve partial ligand loss or hydroxide coordination to the metal center (or both).

#### *3.2.4 Catalytic Water Oxidation Studies*

Electrochemical and electrocatalytic studies were performed by DLG, SB, and myself, with digital simulations and fittings performed by Shanlin Pan. Electrocatalytic studies of copper (II) complexes of 6,6'-dhbp (**1** added as **1a** and **1c**) and 4,4'-dhbp (**2**) were performed in solutions ranging in pH 10 to 14. Cyclic voltammetry (CV) experiments utilized 1 mM of copper catalyst, 0.1 M NaOH/NaOAc aqueous electrolyte, glassy carbon working electrode (dia. 3mm), Ag/AgCl reference electrode (with saturated KCl) and Pt counter electrode. Alkaline solutions of **1** showed irreversible and enhance anodic current that indicates electrocatalytic water oxidation at high pH values, as shown in Figure 3.11. Solutions of **1** used in this study were free from precipitate before potential was applied. CV of complex **1** in dry propylene carbonate with increasing water additions showed no redox activity until alkali water (pH 12.6 with NaOH) was added to the system (see the Supporting Information). Water at high pH is therefore needed to

activate the copper (II) complexes of 6,6'-dhbp in order to observe its redox activities and electrocatalytic water oxidation.

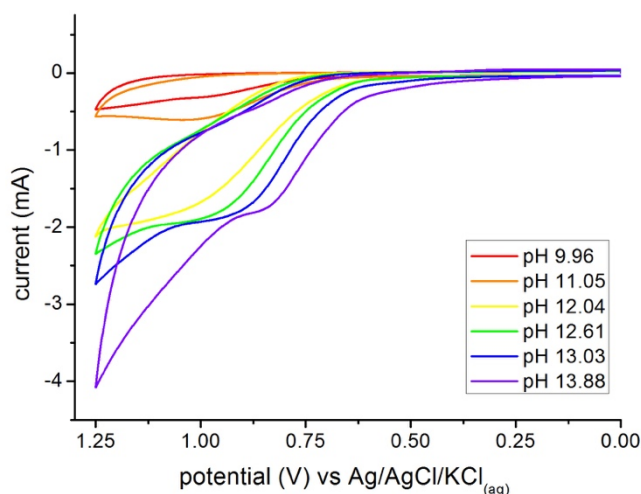


*Figure 3.11.* Cyclic voltammogram (CV) plots (non-background corrected) of 1.0 mM [(6,6'-dhbp)<sub>2</sub>Cu]SO<sub>4</sub> (**1a**) as a function of pH on glassy carbon, scan rate = 100 mV/s in water with 0.1 M NaOAc/NaOH.

The scan rate dependence of CVs of 1.0mM complex **1** at pH 12.6 in aqueous 0.1 M NaOAc/NaOH was obtained (Figure 3.12). At low potential the quasi-reversible reduction of Cu<sup>II/I</sup> is seen at -0.387 V (Figure 3.12). All CVs of complex **1** are fitted using digital simulation to illustrate its electrocatalytic activities as highlighted in Figure 3.13. Although the water oxidation of Cu complex involves multiple steps of proton coupled charge transfer steps,<sup>4, 13-14, 35</sup> the data fitting was done by assuming the Cu complex **1** undergoes a heterogeneous charge transfer step through its aqua-coordinated product [(6,6'-(O)<sub>2</sub>-bpy)<sub>2</sub>Cu(H<sub>2</sub>O)]<sup>2-</sup>, and two following homogenous reactions, including one catalytic water oxidation and an irreversible reaction of the oxidized aqua-coordinated complex **1**. Such data fitting provides an estimate of the charge transfer rate and turnover frequency of the Cu complex, although the true mechanism needs further study to have an improved understanding. From the EPR and HYSORE data for complex **1** at

pH 12.6 it can be inferred that the major copper species present at this pH is the aqua-coordinated  $[(6,6'-(O)_2\text{-bpy})_2\text{Cu}(\text{H}_2\text{O})]^{2-}$  complex (species **B** or **1e'**). An initial oxidation of this complex occurs and is calculated with fitting to be at 0.766 V (vs Ag/AgCl). From this value the overpotential was calculated to be 477 mV. The subsequent water oxidation reaction occurs with an average turn-over rate of  $0.356 \text{ s}^{-1}$ . We also found that an irreversible but non-catalytic pathway of the Cu complex competes with the water oxidation at a faster rate of  $1.082 \text{ s}^{-1}$ , forming some unidentified product (Scheme 2).

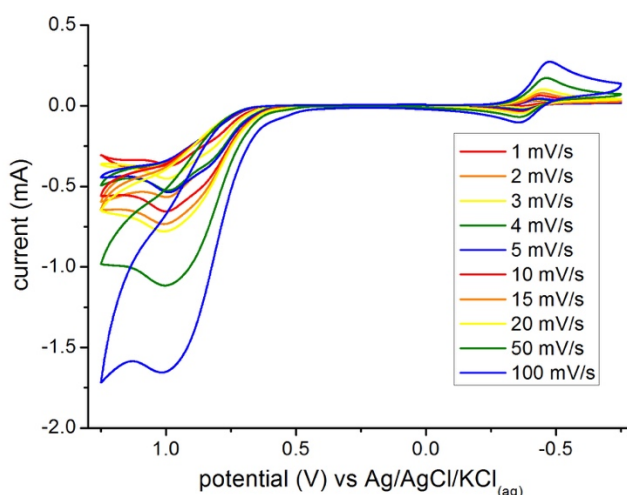


*Figure 3.12.* CV plots as a function of scan rate of for a 1.0 mM pH 12.6 solution of complex **1** on glassy carbon in water with 0.1 M NaOAc/NaOH, corrected for background (see Supporting information for non-background corrected and background scans).

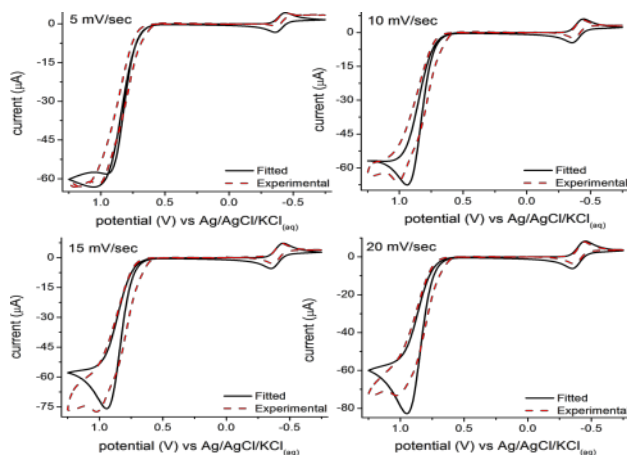
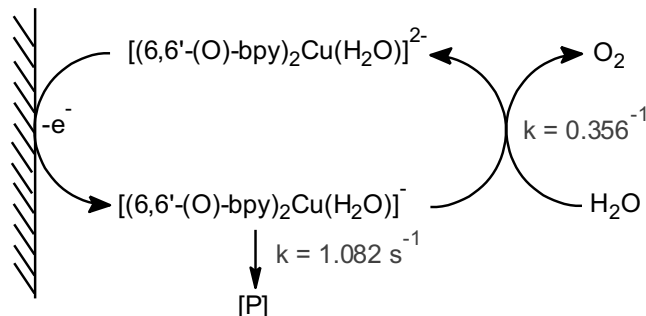


*Figure 3.13.* Simulated CVs of aqueous complex **1** at varied scan rate compared to experimental (Figure 3.11) for the mechanistic fitting of the data.



*Scheme 2.* Schematic view of the fitted water oxidation process occurring in the electrochemical cell for complex **1**.

Bulk electrolysis of 1.0 mM complex **1** at pH 12.6 in aqueous 0.1 M NaOAc at 0.9 V was carried out in an air-tight cell in which the headspace of the vessel was sampled at regular intervals with a gas-tight syringe to be injected for manual sampling of the gas composition via GC-MS. An increase in the relative quantity of oxygen was observed indicating the accumulation of oxygen as positive potential was applied to complex **1** as was expected. Due to the sluggish rate of catalysis by complex **1** to generate oxygen vs. the rate of formation of an unknown inactive product the production of oxygen was not expected to be and was not observed to be dramatic.

Furthermore, the combined data support the catalysis (at pH 12.6) by a 6,6'-dhbp ligated copper complex like **1e'** rather than simple copper salts (e.g. species **D**). Copper sulfate solutions at the same pH show no catalytic current. Also, in our study and another study,<sup>26</sup> both copper(II) and 6,6'-dhbp are necessary for water oxidation at pH 12.6. Other complexes including **4** and **5** (*vide infra*) and the 1:1 complexes of CuSO<sub>4</sub> and 4,4'-dhbp and 4,4'-dmbp are inactive at water oxidation,<sup>26</sup> and this implies that the 6,6'-dhbp plays a role in water oxidation at pH 12.6.

For comparison, CV studies of complexes **1-5** were performed utilizing 1 mM of catalyst, 0.1 M NaOH/NaOAc pH 12.6 electrolyte, glassy carbon working electrode, Ag/AgCl reference electrode and Pt counter electrode, Figure 3.14. Solutions of [(4,4'-dhbp)<sub>2</sub>Cu]<sup>2+</sup> (**2**) did not exhibit any catalytic waves. Complex **3** precipitated when dissolved in electrolyte solution, and water oxidation studies were not performed. Similarly, complex **4** was also insoluble in electrolyte solution; however, water oxidation was attempted. A slightly larger current was obtained for **4** than for electrolyte alone (blank) without the observation of any catalytic waves. Complex **5** was fully soluble in pH 12.6 electrolyte, and a minor oxidative peak (Figure 3.14) was observed which is tentatively assigned to irreversible oxidation of the ligand in complex **5**, as is consistent with similar observations (at E = 1.16 V vs. NHE) for a 1:1 mixture of Zn<sup>II</sup> and 6,6'-dhbp.<sup>26</sup>

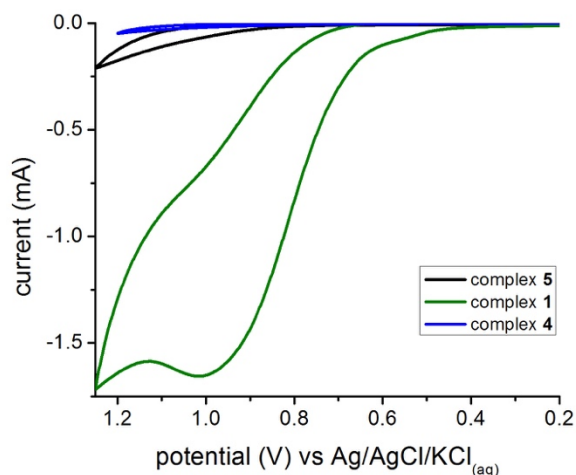


*Figure 3.14.* Comparison of 1 mM solution of complexes **1**, **4**, and **5** at pH 12.6 in 0.1M NaOAc at glassy carbon electrode at 100 mV/s scan rate.

Complex **1** exhibits significantly lower TOF (at 0.356 s<sup>-1</sup>) than other copper catalysts<sup>12, 14</sup> but is similar to the value of 0.4 s<sup>-1</sup> TOF reported for *in situ* prepared 1:1 Cu and 6,6'-dhbp complexes.<sup>26</sup> The over-potential observed (477 mV) for **1** places it at the

low end of copper water oxidation catalysts, lower than reported in two studies (at 640 and 750 mV)<sup>12, 26</sup> but similar to two other studies done at comparable pH values (at 450 and 520 mV).<sup>13-14</sup> At first glance, it appears that the 2:1 ratio of 6,6'-dhbp to copper (in **1**) lowers the over-potential relative to the *in situ* prepared 1:1 ratio of the same components (with overpotential = 750 mV) described in the literature.<sup>26</sup> However, it is also worth noting that there may be an advantage to complexation of the copper (II) prior to dissolution in base, such as preventing formation of Cu(OH)<sub>2</sub> (s) and other insoluble salts. Small amounts of 2:1 complex could conceivably form in previously reported studies<sup>26</sup> and may perhaps be the active catalyst. Likewise, in our study changes may occur to the structure of **1** upon oxidation, which will be the subject of future investigations including computational studies.

### 3.2.5 Mechanistic Possibilities Suggested by these Studies

The structures **1** are biomimetic<sup>3</sup> and show that 6,6'-dhbp can support a network of hydrogen bonds. This provides structural evidence that a high valent copper aqua or hydroxy species (formed from pre-catalyst **1**) could be stabilized by intramolecular hydrogen bonds. This has similarities to how enzymes use hydrogen bonds for O<sub>2</sub> activation and oxygen binding.<sup>36-38</sup> Hydrogen bonds have been shown computationally to facilitate dioxygen activation,<sup>39</sup> and dioxygen activation is the microscopic reverse of water oxidation.

Our evidence (Figure 3.10) presented herein supports that pre-catalyst **1** acts through a mononuclear species. However, **1** is a sluggish catalyst (as are *in situ* prepared 1:1 6,6'-dhbp Cu catalysts<sup>26</sup>). In our case with **1**, O-O bond formation may be the rate-

limiting step. Similarly, with ruthenium catalysts O-O bond formation is often the rate-limiting step and binuclear catalysts have allowed for faster rates.<sup>40</sup>

Lastly, pyridinol rings are also potentially redox non-innocent,<sup>21, 26</sup> and this is a biomimetic strategy<sup>41</sup> for performing multi-electron reactions with first row transition metals.<sup>42</sup> Thus, these combined 6,6'-dhbp ligand features can facilitate PCET and stabilize key intermediates. This provides a reasonable working hypothesis for the relatively low over-potentials observed.

### 3.3 Conclusion

The well-characterized 2:1 complex of  $[(6,6'\text{-dhbp})_2\text{Cu}]^{2+}$  (**1a**) has four acidic protons, and upon removal of these protons with aqueous base, electrocatalytic water oxidation is observed. It is likely that proximal O-/OH groups play a role in shuttling protons and stabilizing proposed high valent copper oxo species, perhaps similarly to the oxygen evolving complex in photosystem II.<sup>2</sup> Furthermore, the crystal structures described herein support the idea that hydrogen bonding interactions observed with 6,6'-dhbp facilitate transformations of the water substrate. Additionally, our prior work<sup>21</sup> showed that 6,6'-dhbp is a non-innocent ligand, and therefore perhaps can mimic the role of tyrosine in photosystem II by accelerating PCET events. While the low overpotential (477 mV) observed for **1** is impressive, the turnover rate was slow ( $0.356\text{ s}^{-1}$ ) and may reflect slow O-O coupling. This work serves to illustrate what productive (water oxidation) and non-productive pathways (competing irreversible oxidation to form a side product) are available to copper complexes of 6,6'-dhbp in basic aqueous solution under electrocatalytic conditions.

### **3.4 Experimental**

#### *3.4.1 General Methods*

The synthesis of 6,6'-dhbp, 6,6'-dmbp and 4,4'-dhbp were adapted from literature.<sup>43-44</sup> All other chemicals were procured from commercial sources. A Fisher Scientific Accumet glass electrode was used to measure pH values and was calibrated with standard buffer solutions. Electronic absorption spectra were recorded with a Perkin Elmer Lambda 35 spectrophotometer. Electrochemical studies were performed on a CHI760C Potentiostat. Additional synthetic schemes, catalytic tables and plots, spectroscopic data, and X-ray single crystal diffraction studies are provided in the Supporting Information. Elemental analyses were performed by Atlantic Microlab, Inc., Norcross, GA.

#### *3.4.2 Acidity Studies*

The  $pK_a$  studies of solutions of complex **2** were performed using concentrated solutions of NaOH and HCl to adjust the pH with negligible change in volume. The pH was monitored before and after the solution absorption measurements.

### **3.5 Author Contribution**

I performed experimental work, including UV/vis measurements,  $pK_a$  studies, and some electrochemical experiments for catalytic testing and contributed to the ideas and writing of the paper resulting from this project.

### **3.6 References**

1. Lewis, N. S.; Nocera, D. G. *Proc. Natl. Acad. of Sci.*, **2006**, *103*, 15729-15735.

2. Umena, Y.; Kawakami, K.; Shen, J.-R.; Kamiya, N. *Nature*, **2011**, *473*, 55-60.
3. Bertini, I.; Gray, H. B.; Stiefel, E. I.; Valentine, J. S., *Biological Inorganic Chemistry*. University Science Books: Sausalito, CA, 2007.
4. Concepcion, J. J.; Jurss, J. W.; Brennaman, M. K.; Hoertz, P. G.; Patrocínio, A. O. T.; Murakami, I. N. Y.; Templeton, J. L.; Meyer, T. J. *Acc. Chem. Res.*, **2009**, *42*, 1954-1965.
5. Blakemore, J. D.; Schley, N. D.; Balcells, D.; Hull, J. F.; Olack, G. W.; Incarvito, C. D.; Eisenstein, O.; Brudvig, G. W.; Crabtree, R. H. *J. Am. Chem. Soc.*, **2010**, *132*, 16017-16029.
6. McDaniel, N. D.; Coughlin, F. J.; Tinker, L. L.; Bernhard, S. *J. Am. Chem. Soc.*, **2008**, *130*, 210-217.
7. Dismukes, G. C.; Brimblecombe, R.; Felton, G. A. N.; Pryadun, R. S.; Sheats, J. E.; Spiccia, L.; Swiegers, G. F. *Acc. Chem. Res.*, **2009**, *42*, 1935-1943.
8. Fillol, J. L.; Codolà, Z.; Garcia-Bosch, I.; Gómez, L.; Pla, J. J.; Costas, M. *Nat Chem*, **2011**, *3*, 807-813.
9. McAlpin, J. G.; Stich, T. A.; Ohlin, C. A.; Surendranath, Y.; Nocera, D. G.; Casey, W. H.; Britt, R. D. *J. Am. Chem. Soc.*, **2011**, *133*, 15444-15452.
10. Reece, S. Y.; Hamel, J. A.; Sung, K.; Jarvi, T. D.; Esswein, A. J.; Pijpers, J. J. H.; Nocera, D. G. *Science*, **2011**, *334*, 645-648.
11. Dinca, M.; Surendranath, Y.; Nocera, D. G. *Proc. Natl. Acad. Sci. U. S. A.*, **2010**, *107*, 10337-10341, S10337/1-S10337/4.
12. Barnett, S. M.; Goldberg, K. I.; Mayer, J. M. *Nat Chem*, **2012**, *4*, 498-502.
13. Chen, Z.; Meyer, T. J. *Angew. Chem., Int. Ed.*, **2012**, *52*, 700-703.
14. Zhang, M.-T.; Chen, Z.; Kang, P.; Meyer, T. J. *J. Am. Chem. Soc.*, **2013**, 2048-2051.
15. Coggins, M. K.; Zhang, M. T.; Chen, Z.; Song, N.; Meyer, T. J. *Angew. Chem., Int. Ed.*, **2014**, *53*, 12226-30.
16. Privalov, T.; Åkermark, B.; Sun, L. *Chem. Eur. J.*, **2011**, *17*, 8313-8317.
17. Papish, E. T.; Nieto, I. *Patent Application Filed with US Patent Office*, **2012**, *PCT/US2012/052518*, Provisionally filed 8/30/11 and final application filed 8/27/12.
18. Nieto, I.; Livings, M. S.; Sacci, J. B.; Reuther, L. E.; Zeller, M.; Papish, E. T. *Organometallics*, **2011**, *30*, 6339-6342.

19. Conifer, C. M.; Law, D. J.; Sunley, G. J.; Haynes, A.; Wells, J. R.; White, A. J. P.; Britovsek, G. J. P. *Eur. J. Inorg. Chem.*, **2011**, *2011*, 3511-3522.
20. Conifer, C. M.; Taylor, R. A.; Law, D. J.; Sunley, G. J.; White, A. J. P.; Britovsek, G. J. P. *Dalton Trans.*, **2011**, *40*, 1031-1033.
21. DePasquale, J.; Nieto, I.; Reuther, L. E.; Herbst-Gervasoni, C. J.; Paul, J. J.; Mochalin, V.; Zeller, M.; Thomas, C. M.; Addison, A. W.; Papish, E. T. *Inorg. Chem.*, **2013**, *52*, 9175-9183.
22. Marelus, D. C.; Bhagan, S.; Charboneau, D. J.; Schroeder, K. M.; Kamdar, J. M.; McGettigan, A. R.; Freeman, B. J.; Moore, C. E.; Rheingold, A. L.; Cooksy, A. L.; Smith, D. K.; Paul, J. J.; Papish, E. T.; Grotjahn, D. B. *Eur. J. Inorg. Chem.*, **2014**, 676-689.
23. Hufziger, K. T.; Thowfeik, F. S.; Charboneau, D. J. N., I.; Dougherty, W. G.; Kassel, W. S.; Dudley, T. J.; Merino, E. J.; Papish, E. T.; Paul, J. J. *Journal of Inorganic Biochemistry*, **2014**, *130*, 103-111.
24. Kawahara, R.; Fujita, K.-i.; Yamaguchi, R. *J. Am. Chem. Soc.*, **2012**, *134*, 3643-3646.
25. Wang, W.-H.; Hull, J. F.; Muckerman, J. T.; Fujita, E.; Himeda, Y. *Energy Environ. Sci.*, **2012**, *5*, 7923.
26. Zhang, T.; Wang, C.; Liu, S.; Wang, J.-L.; Lin, W. *J. Am. Chem. Soc.*, **2014**, *136*, 273-281.
27. Addison, A. W.; Rao, T. N.; Reedijk, J.; Rijn, J. v.; Verschoor, G. C. *J. Chem. Soc., Dalton Trans.*, **1984**, 1349 - 1356.
28. Klein, S.; Dougherty, W. G.; Kassel, W. S.; Dudley, T. J.; Paul, J. J. *Inorg. Chem.*, **2011**, *50*, 2754-2763.
29. Kimblin, C.; Murphy, V. J.; Hascall, T.; Bridgewater, B. M.; Bonanno, J. B.; Parkin, G. *Inorg. Chem.*, **2000**, *39*, 967-974.
30. Su, C.-Y.; Liao, S.; Wanner, M.; Fiedler, J.; Zhang, C.; Kang, B.-S.; Kaim, W. *Dalton Trans.*, **2003**, 189-202.
31. Garribba, E.; Micera, G.; Sanna, D.; Strinna-Erre, L. *Inorg. Chim. Acta*, **2000**, *299*, 253-261.
32. Conner, K. P.; Schimpf, A. M.; Cruce, A. A.; McLean, K. J.; Munro, A. W.; Frank, D. J.; Krzyaniak, M. D.; Ortiz de Montellano, P.; Bowman, M. K.; Atkins, W. M. *Biochemistry*, **2014**, *53*, 1428-1434.
33. Conner, K. P.; Vennam, P.; Woods, C. M.; Krzyaniak, M. D.; Bowman, M. K.; Atkins, W. M. *Biochemistry*, **2012**, *51*, 6441-6457.

34. Hofer, P. *Journal of Magnetic Resonance, Series A*, **1994**, *111*, 77-86.
35. Concepcion, J. J.; Binstead, R. A.; Alibabaei, L.; Meyer, T. J. *Inorg. Chem.*, **2013**, *52*, 10744-10746.
36. Ozaki, S.-i.; Roach, M. P.; Matsui, T.; Watanabe, Y. *Acc. Chem. Res.*, **2001**, *34*, 818-825.
37. Sahu, S.; Widger, L. R.; Quesne, M. G.; de Visser, S. P.; Matsumura, H.; Moënne-Loccoz, P.; Siegler, M. A.; Goldberg, D. P. *J. Am. Chem. Soc.*, **2013**, *135*, 10590-10593.
38. Yang, J.; Kloek, A. P.; Goldberg, D. E.; Mathews, F. S. *Proc. Natl. Acad. Sci. U. S. A.*, **1995**, *92*, 4224-4228.
39. Aullón, G.; Gorun, S. M.; Alvarez, S. *Inorg. Chem.*, **2006**, *45*, 3594-3601.
40. Muckerman, J. T.; Polyansky, D. E.; Wada, T.; Tanaka, K.; Fujita, E. *Inorg. Chem.*, **2008**, *47*, 1787-1802.
41. Gagliardi, C. J.; Vannucci, A. K.; Concepcion, J. J.; Chen, Z.; Meyer, T. J. *Energy Environ. Sci.*, **2012**, *5*.
42. Chirik, P. J.; Wieghardt, K. *Science*, **2010**, *327*, 794-795.
43. Dubreuil, D. M.; Pipelier, M. G.; Pradere, J. P.; Bakkali, H.; Lepape, P.; Delaunay, T.; Tabatchnik, A. Pyridazine and pyrrole compounds, processes for obtaining them and uses. WO2008012440A2, 2008.
44. Himeda, Y.; Onozawa-Komatsuzaki, N.; Sugihara, H.; Kasuga, K. *Organometallics*, **2007**, *26*, 702-712.

### **3.7 Supporting Information**

#### *3.7.1 pH Studies of Complex 1*

Stock solutions of complex 1 was prepared from 10.3 mg dissolved into 10 mL of ethylene glycol, 10 mL of methanol and 30 mL of MP water. Samples for UV-Vis were prepared by dilution of 200  $\mu$ L of the stock solution into 3 mL of MP water.

Adjustments to the pH were made using concentrated solutions of HCl and NaOH. Total addition of acid or base did not exceed 5  $\mu$ L to the UV-Vis ready sample.

Potentiometric titration of complex **1** was also attempted in pure water. A suitable titration curve was not obtained by this method. As the pH is lowered, complex **1** becomes increasingly less soluble.

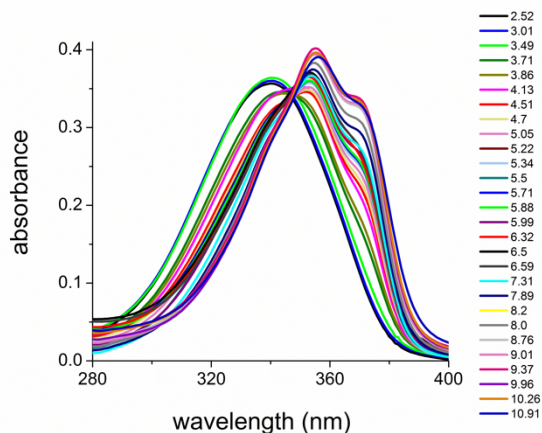


*Figure 3.S1.* Titration of complex **1** using UV/vis from pH 2.5 to 10.9.

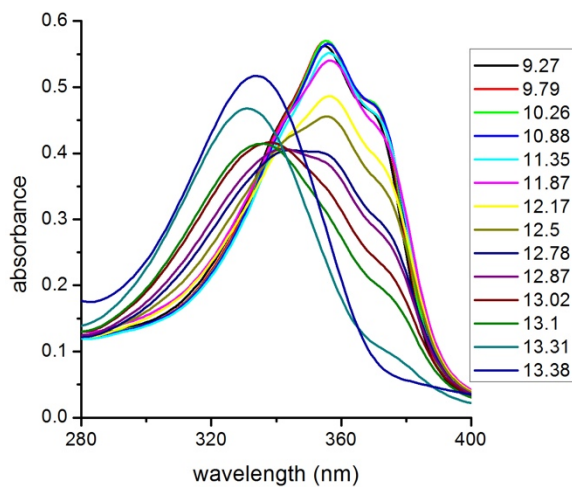


*Figure 3.S2.* Titration of complex **1** using UV/vis from pH 9.3 to 13.4.

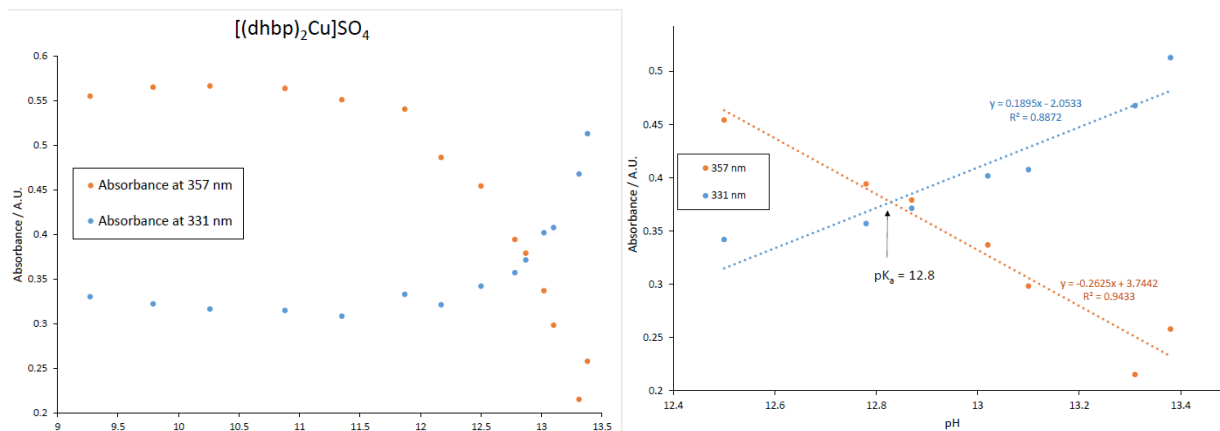


Figure 3.S3. (Left) Plot of absorbance at 357 and 331 nm vs pH from above titration experiment (Figure S2). (Right) Expanded view of absorbance vs pH plot for determining the pH at which 50 % of complex **1** has lost the 6,6'-dhbp ligand.

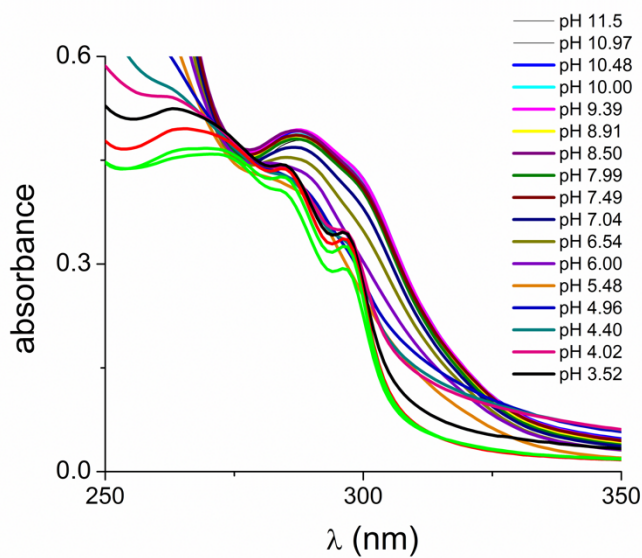


Figure 3.S4. Titration of complex **2** using UV/vis from pH 3.5 to 11.5.

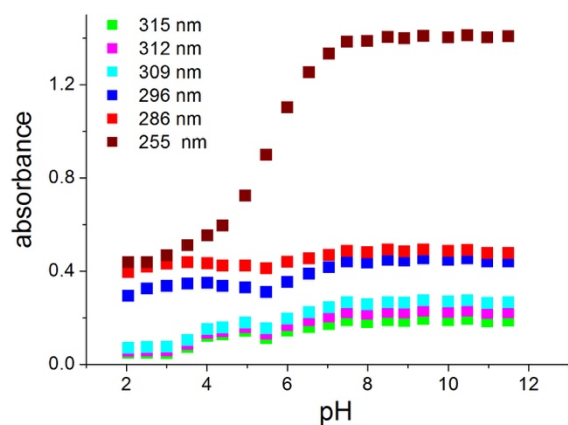


Figure 3.S5. Plot of absorbance vs pH for complex **2** from above titration.

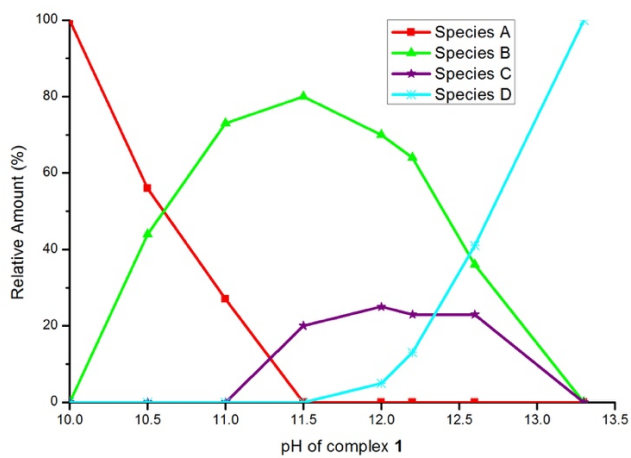
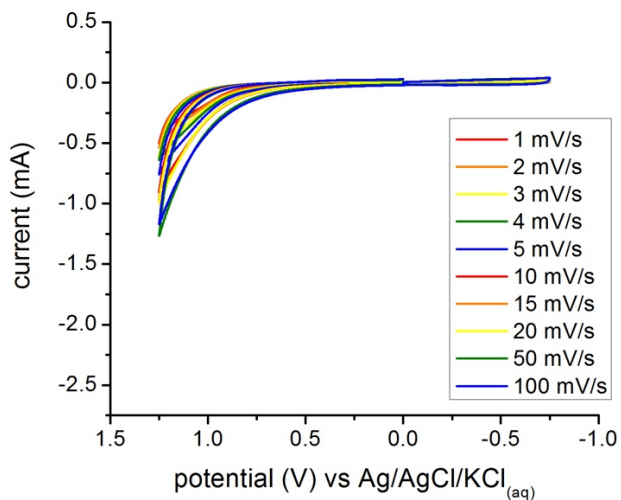


Figure 3.S6. Speciation diagram showing the relative amount of Species **A-D** via CW simulations of complex **1** ranging from pH 10 to 13.3.



*Figure 3.S7.* Cyclic voltammogram of the scan rate dependence of blank electrolyte NaOAc. A solution of aqueous 0.1 M NaOAc at pH 12.6 (NaOH) with a glassy carbon working electrode, Pt counter electrode, and aqueous Ag/AgCl/KCl<sub>(sat)</sub> reference electrode was utilized.

CHAPTER 4:  
IRIDIUM AND RUTHENIUM COMPLEXES OF N-HETEROCYCLIC CARBENE- AND  
PYRIDINOL-DERIVED CHELATES AS CATALYSTS FOR AQUEOUS CARBON  
DIOXIDE HYDROGENATION AND FORMIC ACID DEHYDROGENATION:  
THE ROLE OF THE ALKALI METAL

Adapted from Siek, S.; Burks, D. B.; Gerlach, D. L.; Liang, G.; Tesh, J. M.; Thompson, C. R.; Qu, F.; Shankwitz, J. E.; Vasquez, R. M.; Chambers, N.; Szulczewski, G. J.; Grotjahn, D. B.; Webster, C. E.; Papish, E. T.; et al., *Organometallics*, 2017, 36, 1091-1106.

#### **4.1 Introduction**

Ligands that contain protic functional groups near the metal center can accelerate proton transfer events in many different types of reactions. Our research groups<sup>1-4</sup> and others<sup>5-6</sup> have pioneered the use of 6,6'-dihydroxybipyridine (6,6'-dhbp) ligands (Chart 1) for the formation of metal complexes that catalyze both oxidative and reductive reactions. The hydroxy groups near the metal center lead to a change in ligand charge upon deprotonation, and thereby the electron density at the metal is altered. The ability to instantly modulate the character of the ligands and change from L<sub>2</sub> (6,6'-dhbp, neutral) to LX (monoanionic) and to X<sub>2</sub> (dianionic) can explain the catalytic rate enhancements that are seen upon deprotonation of the metal complexes.<sup>2</sup> Under oxidizing conditions, the Papish group and other groups have shown that both iridium

(e.g. **4Ir**,<sup>2</sup> and its Ir-aqua analog, Chart 1)<sup>7-8</sup> and copper complexes of 6,6'-dhbp undergo decomposition reactions in solution.<sup>4</sup> Furthermore, the Papish group has also shown that Cu(II) complexes of 6,6'-dhbp undergo ligand loss at both high (>13) and low (<4) pH in aqueous solution.<sup>4</sup> Therefore, there is a strong interest in affixing a strong donor to the pyridinol ring to counteract the labile nature of the 6,6'-dhbp ligand.

Carbon dioxide hydrogenation is studied here because 6,6'-dhbp complexes and other pyridinol based complexes of Ir(III) are especially effective at promoting this reaction and (de)hydrogenation in general.<sup>6, 9-11</sup> Other highly efficient CO<sub>2</sub> hydrogenation homogeneous catalysts include several different iridium pincer complexes from Nozaki;<sup>12</sup> Brookhart and Meyer;<sup>13</sup> Bernskoetter, Hazari and Palmore;<sup>14</sup> and others.<sup>15</sup> For formic acid dehydrogenation, a reusable highly active iridium catalyst with a P,N ligand was reported by Williams;<sup>16</sup> other groups have performed formic acid dehydrogenation in the course of methanol dehydrogenation.<sup>17-18</sup> Most of these (de)hydrogenation catalysts perform ionic hydrogenation, which is the sequential transfer of H<sup>+</sup> and H<sup>-</sup>; other transition metal based catalysts for ionic hydrogenation have been reported.<sup>19-27</sup>

The iridium(III) complexes based on 6,6'-dhbp and related ligands are noteworthy for how rapidly they catalyze both CO<sub>2</sub> hydrogenation and the reverse reaction.<sup>6, 11</sup> The rate accelerations seen with 6,6'-dhbp have been attributed to electron donor ability which is enhanced upon deprotonation and proximal OH/O- groups facilitating the transfer of H<sup>+</sup> via a metal-ligand bifunctional catalysis mechanism.<sup>1, 28-31</sup> However, in this paper methoxy substituents are as effective as hydroxy groups at enhancing dehydrogenation rates in some cases. This is evident from comparing 6,6'-dhbp and 6,6'-dimethoxybipyridine (6,6'-dmbp) complexes of iridium and ruthenium.

In addition, importantly, the role of alkali metals in hydrogenation reactions is elucidated for the first time with the 6,6'-dhbp scaffold.

*N*-Heterocyclic carbene (NHC) ligands are strong sigma donors that form stable metal-carbon bonds.<sup>32-34</sup> NHCs have been used in chelates before with pyridine rings (e.g. **A**, Chart 1),<sup>35-37</sup> including in Re, Mn, and Ni catalysts for electrochemical CO<sub>2</sub> reduction,<sup>38-41</sup> but never with pyridinol as a protic ligand. A bidentate ligand containing an NHC and a pyridinol ring could offer a protic group on the metal center in the presence of a strong donor ligand (Chart 1, NHC-py<sup>OH</sup>). These ligands could be tuned by deprotonation (producing OH/O<sup>-</sup> variants) while also containing strong metal-carbon bonds. Herein, the NHC-py<sup>OH</sup> ligand and related ethers, the Ir(III) complexes thereof, and the use of these new metal complexes towards the catalysis of CO<sub>2</sub> hydrogenation and the reverse dehydrogenation reaction are reported.

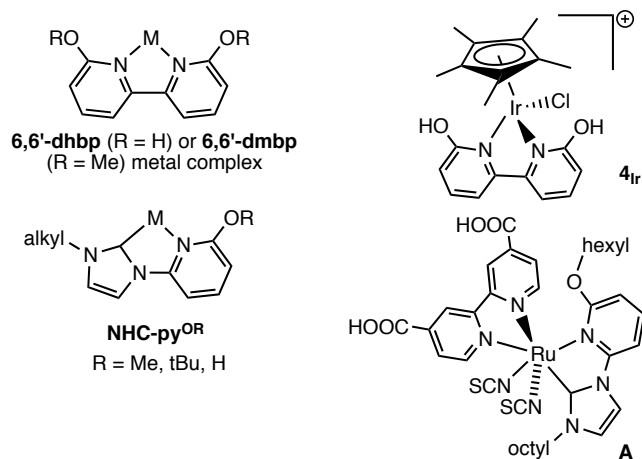


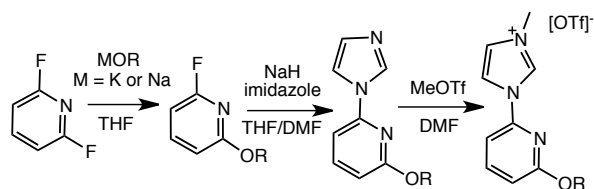
*Chart 1.* Bidentate ligands with proximal protic functional groups and similar metal complexes in the literature.

## 4.2 Results and Discussion

### 4.2.1 Synthesis and Characterization of the Ligands and the Metal Complexes

Syntheses of the *N*-heterocyclic carbene-pyridinol derived ligands (NHC-py<sup>OR</sup>) and the metal complexes of these ligands were performed by Papish group members Deidra Gerlach (DLG) and Sophie Siek (SS). The NHC-py<sup>OR</sup> ligands are easily synthesized as the OR = *O*<sup>t</sup>Bu, OH, or OMe derivatives wherein *O*<sup>t</sup>Bu serves as a protected form for making the OH derivatives. After chelation with the desired metal, moderate heat can drive the deprotection of the *t*-butyl group to produce the hydroxy-substituted ligand with the elimination of isobutene. OR = OMe is a control for comparison of hydrogen bond donor (OH) vs. hydrogen bond acceptor (OMe) properties of the ligand.

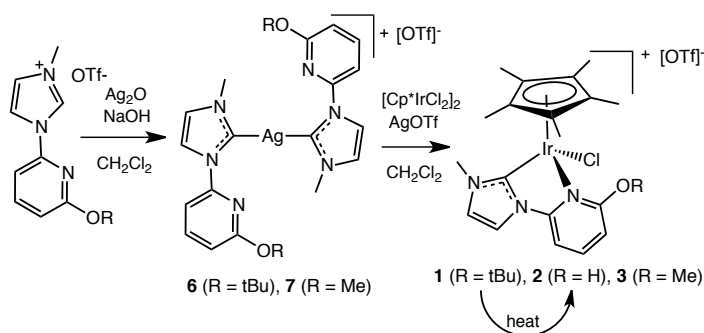
Treating 2,6-difluoropyridine with excess of sodium alkoxide (NaO<sup>t</sup>Bu or NaOMe)<sup>42-44</sup> afforded 2-fluoro-6-alkoxypyridines with replacement of only one fluoride (Scheme 1). Further reaction with sodium imidazolate replaced the remaining fluoride to yield 2-alkoxy-6-(*N*-imidazolyl)pyridines (Im-py<sup>OR</sup>). Alkylation with methyl triflate generated the imidazolium precursors to the NHC ligands, (Im<sup>Me</sup>-py<sup>OR</sup>)OTf.



*Scheme 1.* The synthesis of the imidazolium precursors to the NHC-py<sup>OR</sup> ligands (R = *t*Bu, Me)

The carbene ligand was conveniently formed by deprotonation of the imidazolium salt precursor. This deprotonation is readily achieved with mild base, and the acidity of the C-2 proton is evident by observing H/D exchange in the <sup>1</sup>H-NMR spectra in deuterated protic solvent. Silver bis(carbene) complexes (**6** and **7**) were formed quantitatively through reaction of the imidazolium salts with Ag<sub>2</sub>O and NaOH (Scheme 2) (see Chart 2 for our numbering scheme).<sup>45</sup> The crystal structures of

$[\text{Ag}(\text{NHC-py}^{\text{OtBu}})_2]\text{OTf}$  (**6**) and  $[\text{Ag}(\text{NHC-py}^{\text{OMe}})_2]\text{OTf}$  (**7**) show that the two NHC-py<sup>OR</sup> ligands are monodentate with the pyridinol nitrogen atoms not coordinated. The silver ions are two-coordinate with two carbene ligands arranged with approximately linear C-Ag-C angles (172-174°).



*Scheme 2.* The synthesis of NHC-py<sup>OR</sup> metal complexes **1**, **2**, **3**, **6** and **7**.

Transmetallation of the silver bis(carbene) complexes **6** and **7** with the iridium dimer  $[\text{Cp}^*\text{IrCl}_2]_2$  and one equivalent of AgOTf afforded the chelate complexes  $[\text{Cp}^*\text{IrCl}(\text{NHC}^{\text{Me}}\text{-py}^{\text{OR}})]\text{OTf}$ , complexes **1** and **3** with R = tBu and Me, respectively. The hydroxyl derivative (NHC-py<sup>OH</sup> in **2**) was synthesized by deprotection of complex **1** via superheating a CH<sub>2</sub>Cl<sub>2</sub> solution or reflux of a MeCN solution. Similar to the synthesis of **1** and **3**, the complex  $[\text{Cp}^*\text{IrCl}(6,6'\text{-dmbp})]\text{OTf}$  (**5<sub>Ir</sub>**) was obtained by adding two equivalents of free 6,6'-dmbp ligand and AgOTf to one equivalent of  $[\text{Cp}^*\text{IrCl}_2]_2$ . All of these complexes are yellow and readily recrystallize by evaporation of acetonitrile or by diffusion with diethyl ether.

*Chart 2.* The numbering scheme for the compounds herein.<sup>a</sup>

Compound	Formula
<b>1</b>	$[\text{Cp}^*\text{IrCl}(\text{NHC-py}^{\text{OtBu}})]\text{OTf}$
<b>2</b>	$[\text{Cp}^*\text{IrCl}(\text{NHC-py}^{\text{OH}})]\text{OTf}$
<b>3</b>	$[\text{Cp}^*\text{IrCl}(\text{NHC-py}^{\text{OMe}})]\text{OTf}$
<b>4<sub>Ir</sub></b>	$[\text{Cp}^*\text{IrCl}(6,6'\text{-dhbp})]\text{OTf}$
<b>5<sub>Ir</sub></b>	$[\text{Cp}^*\text{IrCl}(6,6'\text{-dmbp})]\text{OTf}$
<b>4<sub>Ru</sub></b>	$[(p\text{-cymene})\text{RuCl}(6,6'\text{-dhbp})]\text{OTf}$

<b>5<sub>Ru</sub></b>	[( <i>p</i> -cymene)RuCl(6,6'-dmbp)]OTf
<b>6</b>	[Ag(NHC-py <sup>O<sup>t</sup>Bu</sup> ) <sub>2</sub> ]OTf
<b>7</b>	[Ag(NHC-py <sup>OMe</sup> ) <sub>2</sub> ]OTf

<sup>a</sup>Note that ' designates the corresponding metal-aqua complex; e.g. **3'** = [Cp\*Ir(OH<sub>2</sub>)(NHC-py<sup>OMe</sup>)]<sup>2+</sup> as formed in solution by adding AgOTf to **3**.

Complex **2** is protic, and the p*K*<sub>a</sub> value was determined by myself to be 4.9(1), which is similar to the values of 4.6 and 5 previously measured for **4<sub>Ir</sub>** and **4<sub>Ru</sub>** with the diprotic 6,6'-dhbp ligand bound to Ir(III) and Ru(II), respectively (Table 4.1).<sup>1-2</sup> As is typically seen, complexation to the metal lowers the p*K*<sub>a</sub> value by several units (6,6'-dhbp has a p*K*<sub>a</sub> value of 8.5).<sup>46-47</sup>

*Table 4.1.* Thermodynamic acidity (p*K*<sub>a</sub>) values for the protic metal complexes (**2**, **4<sub>Ru</sub>**, **4<sub>Ir</sub>**) studied herein and the free ligand, 6,6'-dhbp.

<b>Compound</b>	<b>p<i>K</i><sub>a</sub></b>	<b>Reference</b>
<b>2</b>	4.9(1)	this work
<b>4<sub>Ir</sub></b>	4.6(1)	2
<b>4<sub>Ru</sub></b>	5	1
6,6'-dhbp	8.5	46

The UV-vis spectrum of each compound was measured in aqueous solution by myself. The yellow Ir(III) complexes **2** and **4<sub>Ir</sub>** have similar absorption features in the UV-visible spectrum, as seen in Figure 4.1, with the majority of absorption occurring in the UV region by π to π\* transitions of the aromatic groups of the ligands and weaker charge transfer (CT) and d-d transitions between 300 and 400 nm. The electronic state of complexes **1** and **3** are shown to be nearly identical by UV-vis whereas deprotection of the O<sup>t</sup>Bu to give OH in complex **2** introduces a second CT absorption feature at ~355 nm comparable to the CT absorption features observed for complex **4<sub>Ir</sub>**. There is little change in the absorption features of the halide bound complex **3** vs. the aqua bound complex **3'** (Figure 4.S2) suggesting that the Ir(NHC-py<sup>OR</sup>) complexes have similar

electronic properties, regardless of whether a halide or aqua ligand fills the coordination sphere.

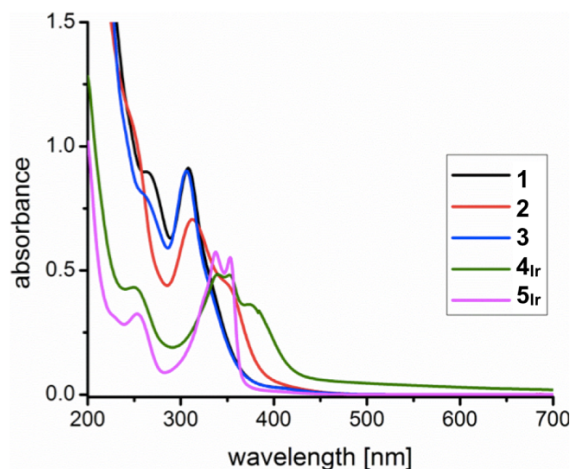


*Figure 4.1.* The aqueous UV/visible absorption spectra of the yellow complexes **1**, **2**, **3**, **4<sub>Ir</sub>** and **5<sub>Ir</sub>** show absorptions primarily in the UV region.

The similarity of the electronic states of these complexes is again found through the electrochemical investigation of non-aqueous solutions by cyclic voltammetry. Cyclic voltammetry was performed by DLG and myself. For all of the complexes **1**, **2**, **3**, **4<sub>Ir</sub>**, and **5<sub>Ir</sub>** an initial irreversible reduction event is observed below -1 V (all values are reported vs. SCE) forming some complex that has a return oxidation event at a more positive potential which is only observed if the initial complex first undergoes the irreversible reduction event. Aprotic complexes **1** and **3** have nearly identical irreversible reduction events at approximately -1.60 V; on scanning to more positive potentials, new irreversible oxidation events at -0.90 V in MeCN were seen. Complex **5<sub>Ir</sub>** with a 6,6'-dmbp ligand exhibits similar behavior, with initial reduction at -1.25 V and, on return to more positive potential, a new oxidation at -0.83 V. However, when the OR group of the pyridine is deprotected to form the protic hydroxyl group, as in the case of

complexes **2** and **4<sub>Ir</sub>**, the return oxidation events occur at a much larger difference in potential than for the complexes in which the hydroxyl group is protected. Due to the lower solubility of complex **4<sub>Ir</sub>**, the CV was performed in DMF. The initial irreversible reduction event occurred at -1.60 V in MeCN and -1.55 V in DMF for complex **2** and at -1.40 V in DMF for complex **4<sub>Ir</sub>** whereas the return oxidation events occur at 0.36 V, 0.33 V and 0.95 V, respectively. The corresponding  $\Delta_p$  between the irreversible reduction and oxidation events are 1.96 V in MeCN and 1.88 V in DMF for complex **2** and 2.35 V for complex **4<sub>Ir</sub>**. Recently, Re complexes with aprotic NHC-py ligands have been reported which similarly show a large difference in the initial irreversible reduction event followed by a “delayed” irreversible oxidation event; the reduction was ascribed to pyridyl ligand forming a radical anion (Py<sup>-</sup>).<sup>38</sup> In the case of both complex **2** and **4<sub>Ir</sub>**, the addition of base forced reduction to occur at more negative potentials, as could be expected from formation of an alkoxide substituent, and diminished the current of the return irreversible oxidation event.

#### *4.2.2 Catalytic CO<sub>2</sub> hydrogenation: Enhancing Activity*

The new NHC-py<sup>OR</sup> complexes along with bipy complexes were tested for the catalysis of the hydrogenation of CO<sub>2</sub> to formate (Table 4.2) by SS and myself. The TON values after 18 h for catalysts **1-5** are used in this paper, but in the SI the pressure drop as a function of time for these catalysts is reported (Figures 4.S5-25). The rate of pressure drop is approximately constant over the course of the 18 h for all of these catalysts (Figure 4.S26). A control reaction was performed with [Cp\*IrCl<sub>2</sub>]<sub>2</sub> (0.15 mM of dimer, or 0.30 mM in iridium) tested as a catalyst, and this produced 0.686 mmol of formate, corresponding to 180 TON (entry 1, Table 4.2). Hence [Cp\*IrCl<sub>2</sub>]<sub>2</sub> is 11.2-12.6 times less

active than the most active catalysts tested (**3** and **4<sub>Ir</sub>**) implicating a significant role of the organic ligands. No other CO<sub>2</sub> reduction products besides formate were observed in these reactions.

Table 4.2. Catalytic hydrogenation of CO<sub>2</sub> with **1-5**.<sup>a</sup>

Entry	Catalyst	Catalyst used as is		Cl <sup>-</sup> removed <i>in situ</i>	
		TON	TOF (h <sup>-1</sup> )	TON	TOF (h <sup>-1</sup> )
1	[Cp*IrCl <sub>2</sub> ] <sub>2</sub>	180 (20)	10	--	
2	<b>1</b>	1090 (20)	60.6	740 (30)	41
3	<b>2</b>	910 (60)	51	860 (100)	48
4	<b>3</b>	2020 (90)	112	2090 (60)	116
5	<b>4<sub>Ir</sub></b>	2270 (90)	126	2400 (70)	130
6	<b>5<sub>Ir</sub></b>	410 (220) <sup>b</sup>	29	290 (60)	16
7	<b>4<sub>Ru</sub></b>	1070 (20)	59.4	2270 (100)	126
8	<b>5<sub>Ru</sub></b>	890 (330)	49	1220 (30)	67.8

<sup>a</sup>Conditions: The reactions were performed in 25 mL of an aqueous solution of 0.3 mM catalyst and 1 M NaHCO<sub>3</sub> at 115 °C and 300 psig of H<sub>2</sub>/CO<sub>2</sub> (1:1). All TON are calculated after 18 hours and are an average of at least 3 experiments (estimated standard deviations are in parentheses). TOF values are for the full 18-hour period (TOF = TON/18h). Data are reported to at most three significant figures based on the measurements. Shaded cells indicate the studies done with OH containing catalysts (**2** with NHC-py<sup>OH</sup> and **4<sub>Ir</sub>**, **4<sub>Ru</sub>** with 6,6'-dhbp). The non-shaded cells used alkoxy-substituted catalysts (**1** with NHC-py<sup>OtBu</sup>, **3** with NHC-py<sup>OMe</sup>, or **5<sub>Ir</sub>**, **5<sub>Ru</sub>** with 6,6'-dmbp). <sup>b</sup> Gave highly variable TON; may be forming nanoparticles.

For the new NHC-py<sup>OR</sup> derivatives, the order of activity is **3** > **1** ≈ **2**, with **3** being almost twice as active as either **1** or **2**. Compounds **1**, **2**, and **3** are best considered to be pre-catalysts, as they all undergo significant transformations in solution (see below). The trend is different with complexes of the dxbp type ligands. The hydroxy dxbp complexes (**4<sub>Ir</sub>** or **4<sub>Ru</sub>**) are more active than the methoxy complexes (**5<sub>Ir</sub>** or **5<sub>Ru</sub>**). These hydrogenation experiments were run in 1 M NaHCO<sub>3</sub>, under basic conditions (pH = 8.5) where the hydroxy groups are deprotonated to give the more electron-donating oxyanions that are proposed to enhance catalysis.<sup>48</sup> Comparing metals, in literature

examples, iridium complexes are generally more active than ruthenium complexes, and this trend holds true here for dhbp complexes ( $4_{\text{Ir}} > 4_{\text{Ru}}$ ) but not for the dmbp analogs ( $5_{\text{Ir}} < 5_{\text{Ru}}$ ). However, the results for both  $5_{\text{Ir}}$  and  $5_{\text{Ru}}$  were inconsistent and suggest catalyst modification.

Comparing monodentate ligands (chloride, triflate, or water) at the catalyst active site, it has been shown that the presence of halide can poison a (de)hydrogenation catalyst, presumably by favorable binding to the active site.<sup>17</sup> Therefore, the bound chloride was removed by adding silver triflate to the catalyst solution; the precipitated silver chloride was easily removed by filtration. The filtrate was then used directly for catalysis without isolation (*in situ* halide removal in Table 4.2). For pre-catalysts **1**, **2**, and **3**, the removal of the chloride does not increase the catalytic activity; silver-triflate-treated **1** and **2** even decrease slightly in activity. However, when treated,  $4_{\text{Ru}}$  (with 6,6'-dhbp bound to Ru) shows a large increase in activity, which more than doubles with the removal of the chlorides (to 95% of the activity of  $4_{\text{Ir}}$ , the Ir analog). Notably, ruthenium is 10 times cheaper than iridium, and although Ru complex  $4_{\text{Ru}}$  was reported in 2011<sup>1</sup> it had not previously been used for CO<sub>2</sub> hydrogenation.

The base used in CO<sub>2</sub> hydrogenation, NaHCO<sub>3</sub>, provides a Lewis acid (Na<sup>+</sup>), which can potentially impact the rate of the reaction. To test this hypothesis, I varied the base and used KHCO<sub>3</sub>, CsHCO<sub>3</sub> and (NH<sub>4</sub>)HCO<sub>3</sub>, which were chosen as commercially available bicarbonate salts (Table 4.3). The K<sup>+</sup> and Cs<sup>+</sup> salts give similar or higher pH values for the resulting solution (see third column of Table 4.3), but the pH does drop slightly with the NH<sub>4</sub><sup>+</sup> salt (pH = 7.8). The Na, K, and Cs bicarbonate salts all resulted in similar TON values with  $4_{\text{Ir}}$ , while the ammonium bicarbonate salt resulted in a significantly lower TON. Similarly, when the pressure is monitored over time (Figures

4.S27-S30), the rate of pressure drop is similar with the alkali metals over the entire course of the reaction; it is much slower with  $\text{NH}_4^+$ . In Table 4.3, the almost 3-fold greater TON seen in entries 1-3 than in entry 4 is a fact whose mechanistic implications will be discussed in the section below on computations.

Table 4.3. Effect of the Lewis acid on  $\text{CO}_2$  hydrogenation with **4<sub>Ir</sub>**.<sup>a</sup>

Entry	M <sup>+</sup>	pH	TON
1	Na <sup>+</sup>	8.1	1430 (70)
2	K <sup>+</sup>	8.3	1410 (50)
3	Cs <sup>+</sup>	8.4	1390 (50)
4	NH <sub>4</sub> <sup>+</sup>	7.8	500 (80)

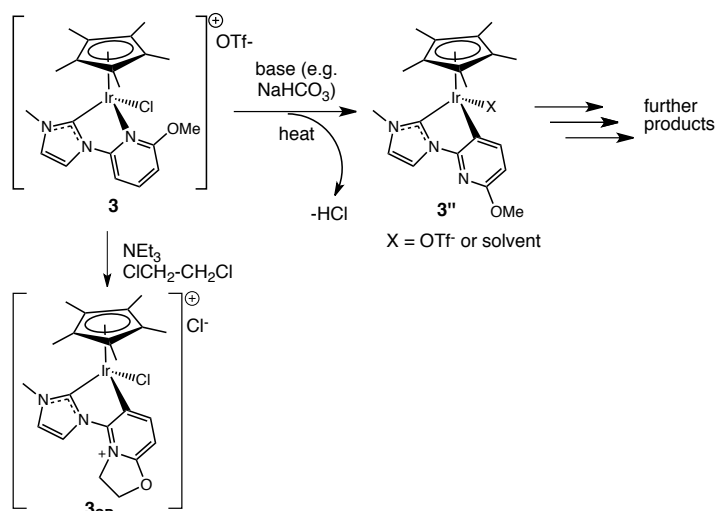
<sup>a</sup>Conditions: The reactions were performed in 25 mL of an aqueous solution of 0.3 mM catalyst and 0.5 M  $\text{MHCO}_3$  (M = Na, K, Cs, or  $\text{NH}_4$ ) at 115 °C and 300 psig of  $\text{H}_2/\text{CO}_2$  (1:1). All TON are calculated after 18 hours and are an average of at least 3 experiments (estimated standard deviations are in parentheses).

#### 4.2.3 Catalytic $\text{CO}_2$ hydrogenation: Pre-Catalyst Transformations

Interestingly, UV-vis absorption spectroscopy of complex **4<sub>Ir</sub>** shows that the catalyst remained mostly unchanged after hydrogenation, yet for **5<sub>Ir</sub>** significant bleaching of the CT features was observed (Figure 4.S4). In short, the robust nature of **4<sub>Ir</sub>** as compared to **5<sub>Ir</sub>** is a main factor for the higher TON observed in Table 4.2. Significant color changes were observed visually for the NHC-py<sup>OR</sup> complexes **1-3** after hydrogenation, which was quantitated by measuring UV-vis absorption (Figure 4.S3). The CT absorption features for the starting complexes bleached leaving only significant absorption in the UV range.

SS performed experiments to elucidate the transformations of complex **3**. <sup>1</sup>H NMR spectral evidence after hydrogenation shows that some **3** remains, but some has been converted into a cyclometallated product, **3''**, as shown in Scheme 3. Complex **3''**

is formed by treating **3** with our hydrogenation conditions or by heating **3** in an inert solvent with base (e.g. treating **3** with Na<sub>2</sub>CO<sub>3</sub> in CH<sub>2</sub>Cl<sub>2</sub> ).



*Scheme 3.* Top: the formation of the cyclometallated **3''** and further products under hydrogenation conditions. Bottom: when **3** is treated with dichloroethane and base the product **3<sub>SP</sub>** results.

While SS was unable to recrystallize **3''**, SS did trap a cyclometallated species by treating **3** with triethylamine in dichloroethane. The resulting product **3<sub>SP</sub>** was isolated in 48% yield, characterized by <sup>1</sup>H-NMR and MS methods, and recrystallized by slow diffusion of ether into acetonitrile. As shown in Scheme 3, the product **3<sub>SP</sub>** appears to result from an S<sub>N</sub>2 reaction between **3''** and dichloroethane, along with surprising loss of the methyl group from the methoxy substituent. In **3<sub>SP</sub>**, the bidentate CC ligand is best described as a zwitterion with a cationic N and an anionic C of the C-bound pyridyl ligand. The metal is still Ir(III), and the complex is cationic. The metrical parameters including Ir-C(NHC) = 1.996(5) Å and Ir-C(Py) = 2.054(7) Å are similar to Ir(III) complexes in the literature.<sup>21</sup> Although **3<sub>SP</sub>** is not the same as the cyclometallated product **3''** obtained under hydrogenation conditions, the pattern of signals in <sup>1</sup>H NMR

spectra of **3''** and **3<sub>SP</sub>** does confirm that the transformation of **3** involves cyclometallation of the pyridine ring.

There is precedent in the literature for cyclometallation of bidentate NHC-pyridine ligands on iridium<sup>37</sup> and rhodium.<sup>49</sup> Cyclometallation has also been reported for 6,6'-dmbp complexes of gold, palladium and platinum,<sup>49-50</sup> but cyclometallation of the dxbp complexes was not observed herein.

After 18 h under basic CO<sub>2</sub> hydrogenation conditions, **3** is converted to a blue solid mixture that appears to contain **3''** and new, unidentified products. The elemental makeup of this water-soluble blue solid was determined from XPS and EDS; reduced C and loss of Cl, F, and S but retention of Ir, N, and O suggest that perhaps Cp\* loss occurs from **3''** after cyclometallation.<sup>51</sup>

#### *4.2.4 Formic acid dehydrogenation*

Dehydrogenation of formic acid was performed with complexes **1-5** by Jamie Tesh (JMT), Courtney Thompson (CRT), SS, and myself. In each trial, 1.02 M formic acid with 0.29 mM of catalyst was heated at 60 °C for 3 h (Table 4).

All three iridium complexes of the new NHC-py<sup>OR</sup> ligands (**1**, **2** and **3**) were found to be active precatalysts (Entries 1-3). These precatalysts can also be compared to iridium and ruthenium complexes of 6,6'-dhbp and 6,6'-dmbp (entries 4-7), of which the iridium complexes of 6,6'-dxbp are by far the most active. The estimated standard deviations in TON values are higher for **1-3** (as compared with **4** and **5**) and may reflect variables related to the transformation of the NHC-py<sup>OR</sup> complexes **1-3**. Since the complexes **4** and **5** appear to be robust catalysts, they are the focus here.

Notably, when 6,6'-dhbp is replaced with 6,6'-dmbp in [Cp\*Ir(6,6'-dmbp)Cl]OTf (**5<sub>Ir</sub>**) we see that the catalyst has comparable activity (Entry 5). Significantly, the

literature on **4<sub>Ir</sub>** describes how hydroxy groups are needed for a metal-ligand bifunctional mechanism,<sup>9</sup> but the similar reactivity of **5<sub>Ir</sub>** and **4<sub>Ir</sub>** suggests that other effects are at work. Our groups provided evidence from X-ray crystallography and reactivity studies of the dmbp complex [(terpy)Ru(6,6'-dmbp)(H<sub>2</sub>O)](OTf)<sub>2</sub> that the methoxy group can *accept* a hydrogen bond from the coordinated aquo ligand,<sup>3</sup> and thus hydrogen bond acceptance by the oxygenated substituents of **5<sub>Ir</sub>** and **4<sub>Ir</sub>** during catalysis may play a role. Formic acid dehydrogenation is performed under acidic conditions (pH = 1.9); hence, none of the OH groups are deprotonated (pK<sub>a</sub> = 4.6 and 5 for **4<sub>Ir</sub>**, and **4<sub>Ru</sub>**, respectively),<sup>1-2</sup> and they may behave similar to methoxy groups as hydrogen bond acceptors and electron-donating groups. Upon replacing the iridium with ruthenium in **4<sub>Ru</sub>** (with 6,6'-dhbp) and **5<sub>Ru</sub>** (with 6,6'-dmbp), the resulting catalysts are far less active (Entries 6 and 7).

Table 4.4. Dehydrogenation of formic acid by catalysts **1-5**.<sup>a</sup>

Entry	Catalyst	Catalyst used as is		Cl <sup>-</sup> removed <i>in situ</i>	
		TON	TOF (h <sup>-1</sup> )	TON	TOF (h <sup>-1</sup> )
1	<b>1</b>	130 (30)	44	200 (40)	66
2	<b>2</b>	90 (50)	31	140 (30)	47
3	<b>3</b>	180 (60)	59	80 (20)	27
4	<b>4<sub>Ir</sub></b>	>3500 <sup>b</sup>	>1200	>3500 <sup>b</sup>	>1200
5	<b>5<sub>Ir</sub></b>	>3500 <sup>b</sup>	>1200	>3500 <sup>b</sup>	>1200
6	<b>4<sub>Ru</sub></b>	45 (12)	15	46 (6)	15
7	<b>5<sub>Ru</sub></b>	140 (10)	45	16 (2)	5

<sup>a</sup>Conditions: Aqueous formic acid (1.02 M) was treated with catalysts **1-5** (0.29 mM) at 60 °C for 3 h. In the right two columns, chloride was removed by treating with silver salts *in situ*. See the experimental section for further details. Turnover numbers (TON) and turnover frequency (TOF) values were calculated to two significant figures at the end of the three hour period by measuring the gas generated (assuming 1:1 of CO<sub>2</sub> : H<sub>2</sub>). TON values are an average of at least 3 experiments (estimated standard deviations are in parentheses). Shaded cells indicate the studies done with OH containing catalysts (**2** with NHC-py<sup>OH</sup> and **4<sub>Ir</sub>**, **4<sub>Ru</sub>** with 6,6'-dhbp). The non-shaded cells used alkoxy-substituted catalysts (**1** with NHC-py<sup>OBu</sup>, **3** with NHC-py<sup>OMe</sup>, or **5<sub>Ir</sub>**, **5<sub>Ru</sub>** with 6,6'-dmbp).<sup>b</sup>These experiments went to 99.8-100% conversion of formic acid to gaseous products; in addition to measuring gas formation we also double checked these values

by  $^1\text{H}$  NMR spectroscopic analysis of an aliquot of the solution phase and these reactions only leave 0 to 0.2% of formic acid unconsumed.

The shaded cells in Table 4.4 show the reactivity of OH substituted catalysts, from which it is readily apparent (Entries 2 and 4) that 6,6'-dhbp ligated catalysts are far more active than the complexes of the NHC-py<sup>OH</sup> ligand. The lesser reactivity may be caused by transformation(s) of the NHC-py<sup>OR</sup> ligated complexes.

The catalyst  $[\text{Cp}^*\text{IrCl}(6,6'\text{-dmbp})]\text{OTf}$  (**5<sub>Ir</sub>**) was further studied over a longer time course as a highly active species of novel structure. The longevity of **5<sub>Ir</sub>** was studied by adding substrate (formic acid) after each reaction cycle was complete (every 3 h). UV-vis absorption spectra of the catalytic mixtures before and after dehydrogenation show that the complexes are unaltered. Complete conversion of formic acid to gaseous products occurs quantitatively (~100% yield) for five cycles over 3 d. Only after gentle heating at 60 °C for 3 d without added substrate does catalyst deactivation occur. Thereafter when formic acid is added a decrease in TOF was observed. A maximal TON of 21,000 was observed at this point (after 8 d) but the ultimate value would be higher because the catalyst is still active. A  $^1\text{H}$  NMR spectrum acquired after concentrating the same reaction mixture shows that the major component is still the original catalyst (Figure 4.S88).

A lower loading of catalyst **5<sub>Ir</sub>** (0.0028 mole % catalyst or 10 times lower relative to the conditions of Table 4.5) was also investigated. Here, the TOF is ~2.8 times faster at ~3300 h<sup>-1</sup> with only 29% conversion at 3 h. For comparison, the TOF values over 3 h are ~1200 h<sup>-1</sup> at 0.028 mole % of **5<sub>Ir</sub>**. A ten fold increase in turnover frequency was anticipated with dropping the catalyst loading, but it appears that at the low catalyst loading the reaction occurs more slowly due to the saturation of all the catalyst sites, or

that catalyst decomposition interferes. At 0.0028 mole % of catalyst **5<sub>Ir</sub>** loading, the reaction does go to 94% conversion (TON = 33,000) after 24 h; thus, if given enough time the yield of product is nearly quantitative, even at very low catalyst loadings.

#### 4.2.5 Computational Study of Catalytic CO<sub>2</sub> Hydrogenation

Computational studies were performed by the Webster group at Mississippi State University. Hydrogenation reactions described herein using 6,6'-dhbp are proposed to proceed via a metal-ligand bifunctional mechanism. It is expected that the OH/O- groups will play a role in transferring protons. This mechanism will be illustrated using **4<sub>Ir</sub>**, which was the most active catalyst for hydrogenation. **4<sub>Ir</sub>** is compared computationally with **5<sub>Ir</sub>**, the 6,6'-dmbp complex, which was considerably less active. The anionic oxygen of the deprotonated 6,6'-dhbp ligand can bind Na<sup>+</sup> to activate CO<sub>2</sub> and hold the substrate near the metal center. Interactions between alkali metals and substrates have literature precedent, and the identity of the alkali metal can greatly impact the rates.<sup>52-57</sup> While [Cp\*Ir(OH<sub>2</sub>)(6,6'-dhbp)]<sup>2+</sup>, **4<sub>Ir</sub>'**, has been computationally studied for CO<sub>2</sub> hydrogenation,<sup>58</sup> the mechanism proposed here is unique in describing the role of the alkali metal and in contrasting dxbp complexes **4<sub>Ir</sub>** and **5<sub>Ir</sub>**. Under the typical hydrogenation conditions (Table 4.2), [Na<sup>+</sup>] = 1 M and [H<sup>+</sup>] = 3.2×10<sup>-9</sup> M at pH 8.5. Thus, Na<sup>+</sup> is used rather than H<sup>+</sup> (as used by Ertem *et al.*<sup>58</sup>) under basic conditions.

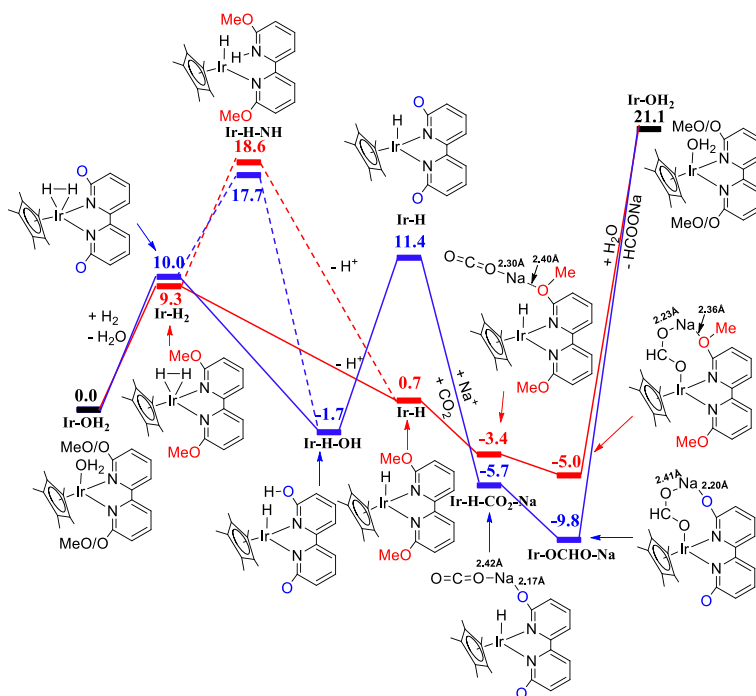


**Figure 4.2.** Diagram of minima with relative energies (solvent corrected energies in kcal/mol) of CO<sub>2</sub> hydrogenation catalyzed by **4Ir** and **5Ir** with the assistance of Na<sup>+</sup> ion. The blue bar with blue solid line represents the pathway of **4Ir** and red bar with red solid line represents the pathway of **5Ir**. The dashed line represents the pathway via the Ir-hydride with protonated pyridine species.

The computed mechanisms of CO<sub>2</sub> hydrogenation catalyzed by **4Ir** and **5Ir** with and without the assistance of Na<sup>+</sup> ion are shown in Figure 4.2. Hydrogenation reactions were run in aqueous base (pH = 8.5), and thus for **4Ir**, the 6,6'-dhbp ligand will first be deprotonated to form the species with the dianionic ligand (6,6'-bobp, 6,6'-bis-O-bipyridine). The activation of dihydrogen leads to **Ir-H<sub>2</sub>**, a  $\sigma$  complex, as the first intermediate. The acidic dihydrogen complex can transfer a proton two ways. With **5Ir**, proton transfer to solvent occurs directly leading to **Ir-H**. With **4Ir**, the O of the dianionic ligand can be protonated to give the **Ir-H-OH** species before loss of a proton and formation of **Ir-H** (water may assist this process).<sup>58</sup> [The formation of a protonated pyridine species (**Ir-H-NH**) is energetically unfavorable for both **4Ir** and **5Ir** (17.7 and

18.6 kcal/mol, respectively).] After the formation of **Ir-H**, one CO<sub>2</sub> molecule could be involved with the assistance of Na<sup>+</sup> ion to form the **Ir-H-CO<sub>2</sub>-Na** species. The **Ir-H-CO<sub>2</sub>-Na** species could then be converted to the Ir-formate species (**Ir-OCHO-Na**), which then would generate the final product **HCOO<sup>-</sup>**. The species thus formed would be lower-energy with the Na<sup>+</sup> interacting with the dianionic 6,6'-bobb ligand as compared with the dmbp ligand (for **4<sub>Ir</sub>** and **5<sub>Ir</sub>** respectively: **Ir-H-CO<sub>2</sub>-Na** at -5.7 and -3.4 kcal/mol, **Ir-OCHO-Na** at -9.8 and -5.0 kcal/mol). The weaker stabilization of Na<sup>+</sup> ion with **5<sub>Ir</sub>** as compared to **4<sub>Ir</sub>** was also confirmed by the longer Na-OMe distances in the **Ir-H-CO<sub>2</sub>-Na** (2.40 *vs* 2.17 Å) and **Ir-OCHO-Na** species (2.36 *vs* 2.20 Å). Thus, **4<sub>Ir</sub>** is predicted to have better catalytic activity than **5<sub>Ir</sub>** in CO<sub>2</sub> hydrogenation with alkali metals present, as is experimentally observed. Without Na<sup>+</sup> ion, a much higher-energy intermediate is observed (**Ir-OCHO** at 18.8 and 12.4 kcal/mol for **4<sub>Ir</sub>** and **5<sub>Ir</sub>**, respectively). This shows the importance of the Lewis acid (Na<sup>+</sup>) in CO<sub>2</sub> hydrogenation.

The related transition states (proceeding from **Ir-H-CO<sub>2</sub>** to **Ir-OCHO**) were located in Figure 4.3 to verify the importance of Na<sup>+</sup> ion in the CO<sub>2</sub> insertion step of the hydrogenation reaction. The transition state free energies are much higher without the assistance of a sodium ion (22.8 and 25.6 kcal/mol for **4<sub>Ir</sub>** and **5<sub>Ir</sub>**, respectively). With Na<sup>+</sup> ion present, CO<sub>2</sub> insertion into the **Ir-H** of **4<sub>Ir</sub>** was achieved by two lower-energy intermediate Na<sup>+</sup>-ion stabilized species (**Ir-HCOO-Na** at 0.7 kcal/mol with a weak Ir--H interaction and **Ir-HCOO-Na** at -7.9 kcal/mol with no Ir to H interaction). The turnover-limiting step in CO<sub>2</sub> insertion process catalyzed by **4<sub>Ir</sub>** with the assistance of Na<sup>+</sup> ion gave a much lower Gibbs free energy compared to that without the assistance of Na<sup>+</sup> ion (3.2 *vs* 22.8 kcal/mol). Similar results were also observed for the **5<sub>Ir</sub>** (6.1 *vs* 25.6 kcal/mol). These related transition states during the CO<sub>2</sub> hydrogenation reaction

catalyzed by **4<sub>Ir</sub>** and **5<sub>Ir</sub>** show the important role of Na<sup>+</sup> ion in the stabilization of reaction intermediates and also demonstrate that **4<sub>Ir</sub>** is predicted to have better catalytic activity than **5<sub>Ir</sub>** in CO<sub>2</sub> hydrogenation. (It is proposed that the use of NH<sub>4</sub><sup>+</sup> would give activation barriers slightly higher than that observed for Na<sup>+</sup> based upon Table 4.4; ammonium can still donate hydrogen bonds but it is a weaker Lewis acid than Na<sup>+</sup>.)

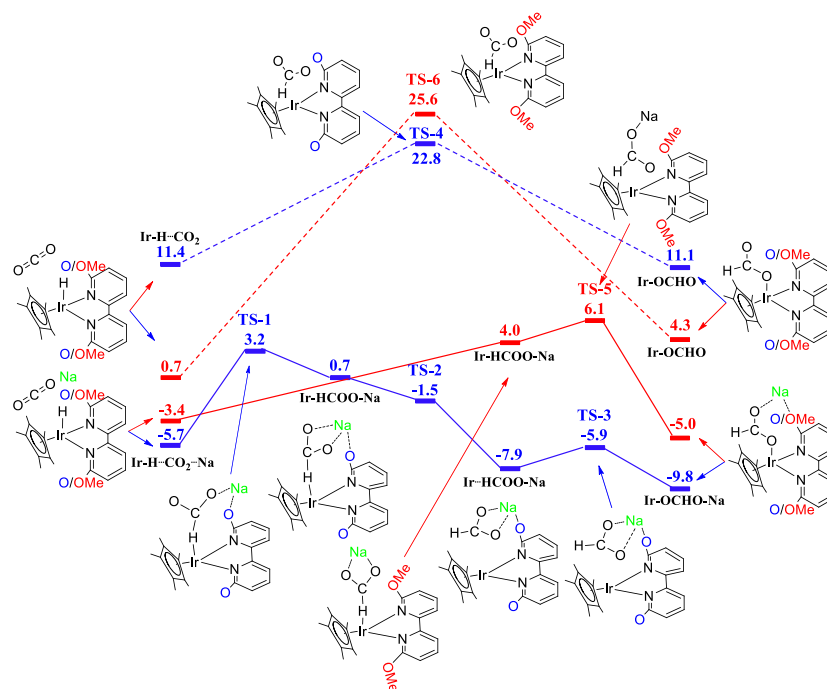


**Figure 4.3.** The free energy diagram (solvent corrected energies in kcal/mol) of CO<sub>2</sub> insertion into the iridium hydride of **4<sub>Ir</sub>** and **5<sub>Ir</sub>** with and without the assistance of a Na<sup>+</sup> ion. The blue bar with solid line represents the pathway of **4<sub>Ir</sub>** and red bar with solid line represents the pathway of **5<sub>Ir</sub>**. The dashed line represents the pathways without the assistance of Na<sup>+</sup> ion.

The H<sub>2</sub> cleavage process catalyzed by **4<sub>Ir</sub>** demonstrates that the pathway from **Ir-H<sub>2</sub>** σ complex to Ir-hydride with hydroxy group species (**Ir-H-OH**) was more favorable than the pathway from **Ir-H<sub>2</sub>** σ complex to Ir-hydride with protonated pyridine species (**Ir-H-NH**) (11.0 vs 28.7 kcal/mol). It is worth noting that an Ir-dihydride species (**Ir-2H**) was observed for the H<sub>2</sub> cleavage process catalyzed by **5<sub>Ir</sub>**. The transition state of

the conversion between the **Ir-H<sub>2</sub>**  $\sigma$  complex and **Ir-2H** dihydride species has not yet been located; however, this process will be facile. The free energy of activation for the conversion between **Ir-2H** dihydride and Ir-hydride with protonated pyridine species (**Ir-H-NH**) of **5<sub>Ir</sub>** was much higher than that of **4<sub>Ir</sub>** (33.9 vs 28.7 kcal/mol).

Computations of the CO<sub>2</sub> insertion process with the assistance of Na<sup>+</sup> ion and H<sub>2</sub> cleavage process were consistent with the experimental observation that **4<sub>Ir</sub>** has better catalytic activity than **5<sub>Ir</sub>** in CO<sub>2</sub> hydrogenation.

In summary, the computed mechanism invokes a role for the oxyanion of dhhp and explains why the dhhp complexes are more active than the dmbp complexes for CO<sub>2</sub> hydrogenation at basic pH. Remarkably, the important role of the secondary coordination sphere in hydrogenation may help explain why the activity of **4<sub>Ru</sub>** is 95% of that seen with **4<sub>Ir</sub>**. In this manner, a less expensive metal (ruthenium) can work nearly as well as iridium when paired with an appropriate ligand.

### *5.2.6 Computational Study of Formic Acid Dehydrogenation*

Recall that OH and OMe groups in dxbp complexes (**4<sub>Ir</sub>** and **5<sub>Ir</sub>**) produced similar rates of dehydrogenation. Under acidic conditions (pH = 1.9 for dehydrogenation of aqueous formic acid) the OH groups in dhhp will not be deprotonated and will behave similarly to OMe groups. Again, the dehydrogenation of formic acid has been studied previously with **4<sub>Ir</sub>'**,<sup>58</sup> but our study is unique in comparing the role of OH vs. OMe groups.

The possible mechanisms of formic acid dehydrogenation catalyzed by **4<sub>Ir</sub>** and **5<sub>Ir</sub>** with intramolecular or intermolecular proton transfer (Figures 4.4 and 4.5) were also explored. Formic acid can first bind to Ir via the hydroxyl group (**Ir-HOCHO**) under acidic aqueous conditions. Then, a lower energy species is formed by conversion to the

species (**Ir-HCOOH**) with formic acid's OH hydrogen bonded species to the OH or OMe of the dxbp ligand. The hydrogen bonds between OH of **Ir-HCOOH** and N of the dxbp and the following intramolecular proton transfer lead to the formation of an Ir-formate species with protonated pyridine (**Ir-HCOO-NH**). Subsequent  $\beta$ -hydride elimination produces  $\text{CO}_2$  and the Ir-hydride species with protonated pyridine (**Ir-H-NH**). The iridium hydride can be protonated intra-molecularly by the NH to form an  $\eta^2\text{-H}_2$   $\sigma$  complex (**Ir-H<sub>2</sub>**), which finally releases an  $\text{H}_2$  molecule. The relatively small differences of the values of reaction energies in formic acid dehydrogenation process catalyzed by **4<sub>Ir</sub>** and **5<sub>Ir</sub>** with intramolecular proton transfer is consistent with the observed similar catalytic activities. Figure 4.5 focuses on intermolecular proton transfers, for example that of HCOOH directly to solvent as it binds to Ir to give the Ir-formate species (**Ir-OCHO**). Here, the dhbp analog is stabilized relative to the dmbp complex by intramolecular hydrogen bonds. In contrast, subsequent minima differ by no more than  $3.5 \text{ kcal mol}^{-1}$  as a function of bipy substituent, consistent with operation of intermolecular proton transfer pathways in formic acid dehydrogenation process catalyzed by **4<sub>Ir</sub>** and **5<sub>Ir</sub>**.

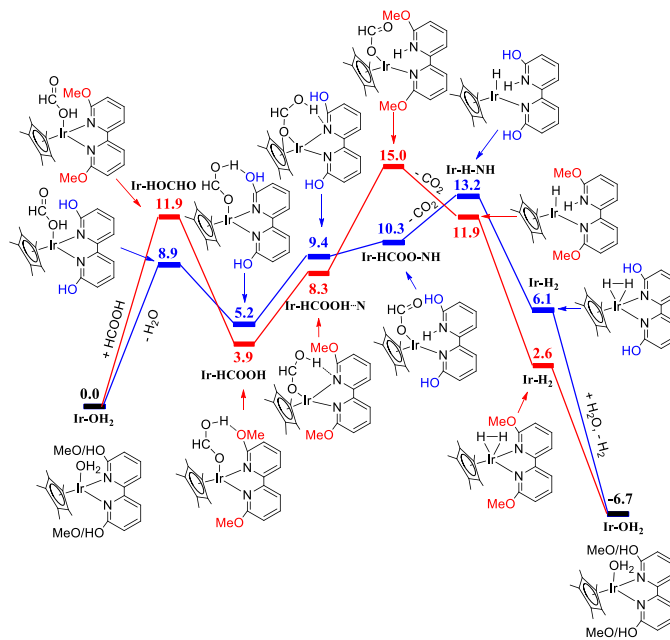


Figure 4.4. Diagram of minima with relative energies (solvent corrected energies in kcal/mol) of intramolecular proton transfer involved formic acid dehydrogenation catalyzed by **4Ir** and **5Ir**. The blue bar with solid line represents the pathway of **4Ir** and red bar with solid line represents the pathway of **5Ir**.

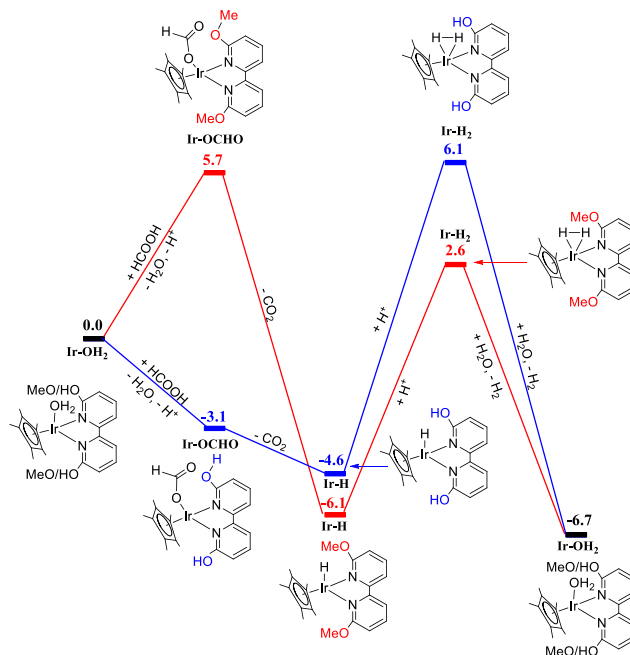


Figure 4.5. Diagram of minima with relative energies (solvent corrected energies in kcal/mol) of intermolecular proton transfer involved formic acid dehydrogenation catalyzed by **4Ir** and **5Ir**. The blue bar with solid line represents the pathway of **4Ir** and red bar with solid line represents the pathway of **5Ir**.

### 4.3 Conclusion

In summary, a new bidentate ligand with an NHC ring bound to a pyridinol ring has been synthesized. The resulting NHC-py<sup>OR</sup> complexes of iridium(III) are moderately active precatalysts for the hydrogenation of CO<sub>2</sub>. Low activity is observed when these NHC-py<sup>OR</sup> complexes (**1-3**) are used for formic acid dehydrogenation. The NHC-pyridinol derived ligands appear to undergo a cyclometallation reaction under basic conditions, and a cyclometallated product was trapped and characterized.

In contrast, the 6,6'-dhbp ligands and complexes thereof are more stable, and products of further transformations are not observed. The iridium 6,6'-dhbp complexes have been used for CO<sub>2</sub> hydrogenation in the literature,<sup>6,9</sup> and similarly we observe that these are highly active catalysts for both hydrogenation and dehydrogenation. However, this work was extended towards ruthenium and 6,6'-dmbp ligands. Our groups and others have described the secondary coordination sphere influence of 6,6'-dhbp and its benefits towards reductive catalysis, specifically CO<sub>2</sub> reduction.<sup>1,6,9,52,59-60</sup> Not surprisingly, under basic conditions, catalysts for hydrogenation with the diprotic ligand 6,6'-dhbp are 5 to 8 times more active than catalysts using the aprotic analog 6,6'-dmbp. Remarkably, ruthenium (**4<sub>Ru</sub>**) is nearly (95%) as active as iridium (**4<sub>Ir</sub>**) with 6,6'-dhbp, and this can be rationalized in terms of the secondary coordination sphere having a big impact on catalysis despite the difference in metal. Computationally, this assertion is supported by observing how binding Na<sup>+</sup> near the metal (in **4<sub>Ir</sub>**) serves to lower the free energy barriers for CO<sub>2</sub> hydrogenation.

However, the secondary coordination sphere is not as important for dehydrogenation under acidic conditions. Here, iridium is more active than ruthenium

and methoxy and hydroxy perform similarly (in **5<sub>Ir</sub>** and **4<sub>Ir</sub>**, respectively). Thus the nature of x in dxbp does not matter if the pH is such that the OH groups are not deprotonated. Electronically, OH and OMe groups are similar and both can accept hydrogen bonds.<sup>3</sup> Computationally this similarity is explained in terms of similar energy barriers for dehydrogenation of formic acid with **4<sub>Ir</sub>** and **5<sub>Ir</sub>**.

In summary, subtle ligand changes can influence the reactivity and the stability of iridium catalysts for CO<sub>2</sub> hydrogenation and formic acid dehydrogenation. These studies also help to determine when the secondary coordination sphere influences the activity of the catalysts (and when it does not). With iridium complexes of dxbp-type ligands as (de)hydrogenation catalysts, hydroxy groups perform better than methoxy groups when the oxyanions can form, but when hydroxy groups remain neutral, they behave similar to methoxy substituents.

## **4.4 Experimental**

### *4.4.1 General Procedures*

All ligand and metal complex syntheses were performed under a nitrogen atmosphere in a glove box or by utilizing standard Schlenk line techniques with oven dried glassware.

<sup>1</sup>H-, <sup>13</sup>C- NMR spectra were acquired at room temperature on a Bruker AV360 360 MHz or AV500 500 MHz spectrometer, as designated, and referenced to the solvent peak.

Mid-IR spectra were collected on a Bruker Alpha ATR-IR spectrometer. Mass spectrometric data were collected on a Waters AutoSpec-Ultima NT spectrometer with electron ionization method. Elemental analyses were performed by NuMega Resonance Labs, Inc., San Diego, CA. Electronic spectra were measured on a Perkin Elmer Lambda 35 UV-visible spectrometer. Cyclic voltammetry experiments were conducted in a 0.1 M

solution of  $\text{Bu}_4\text{NPF}_6$  in acetonitrile (MeCN) or  $N,N'$ -dimethylformamide (DMF) with a glassy carbon working electrode, a Pt counter electrode and a Ag/AgCl reference electrode on a CHI760C Potentiostat. The redox potentials are calibrated to Fc/Fc<sup>+</sup> and reported vs. SCE. A Fisher Scientific accumet glass electrode calibrated with standard buffer solutions was used to measure pH values. Pressurized gas reactions were performed in a Parr reaction vessel. SEM data were collected with a JEOL 7000F Field Emission Gun (FEG) for secondary and backscattered electron images. EDS data were collected using an Oxford system with Silicon Drift Detector (SDD) with Aztec software. XPS data were collected using a Kratos AXIS 165 XPS with a Mono (A1)(144W) anode, 50.0 meV step, 1000 ms dwell time, and hybrid lens mode with resolution of pass energy 20.

#### 4.4.2 Materials

Dry solvents were obtained via the Glass Contour Solvent System built by Pure Process Technology, LLC. All reagents were used as purchased and degassed under vacuum as needed. The compounds 6,6'-dmbp,<sup>61</sup> 6,6'-dhbp,<sup>61</sup> [(*p*-cym)RuCl(6,6'-dmbp)]Cl (**5<sub>Ru</sub>**),<sup>1</sup> [(*p*-cym)RuCl(6,6'-dhbp)]Cl (**4<sub>Ru</sub>**),<sup>1</sup> [Cp\*IrCl(6,6'-dhbp)]Cl (**4<sub>Ir</sub>**),<sup>2</sup> and [Cp\*IrCl(6,6'-dmbp)]Cl<sup>2</sup> were prepared according to previously published procedures. High purity grade (> 97%) formic acid was used as purchased from AMRESCO, Inc. The compressed gases CO<sub>2</sub> and 50/50 vol CO<sub>2</sub>/H<sub>2</sub> were purchased from Airgas and used without further purification.

#### 4.4.14 Procedure for Catalytic Hydrogenation of CO<sub>2</sub>

Catalyst solution (0.3 mM, 25 mL) in 1 M NaHCO<sub>3(aq)</sub> were added to a Parr high-pressure vessel. The vessel was purged at least 3 times and then pressurized to 300 psig with 50/50 CO<sub>2</sub>/H<sub>2</sub>. The vessel was heated at 115 °C, while stirred, for 18 h. After the reaction time, the vessel was cooled to room temperature and the pressure was released. The amount of formate produced was determined by <sup>1</sup>H NMR spectroscopy in D<sub>2</sub>O with isonicotinic acid as an internal standard.

*Halide removal in situ for hydrogenation:* Silver triflate (1 equiv for catalysts of formula [Cp\*IrCl(L)]OTf and 2 equiv for catalysts with formula [Cp\*IrCl(L)]Cl and [(p-cym)RuCl(L)]Cl) was added to the freshly prepared stock solution of aqueous catalyst (0.3 mM, 50 mL) and allowed to stir at room temperature in the absence of light for at least 6 h. The reaction mixture was filtered over Celite with suction. A 25 mL portion of the filtrate was used without further characterization according to the catalytic hydrogenation procedure previously stated.

#### *4.4.15 Procedure for Catalytic Dehydrogenation of Formic Acid*

A stock solution of catalyst (0.3 mM, 100 mL) was freshly prepared in water. Three simultaneous trials were run by transferring 25 mL (0.075 mmol, ~0.003 mole % catalytic loading) of stock solution to three separate 100 mL Schlenk flasks each with tubing to an upturned water filled graduated cylinder in a water basin. The reaction flasks were heated to constant temperature of 60 °C with stirring, and high purity formic acid (1.00 mL, 26.5 mmol) was added to each reaction flask. The dehydrogenation reactions were monitored for 3 h for all reactions and for longer times as indicated. The evolved gas was measured, and the TON was calculated based on the number of moles

of the catalyst used divided by the moles of CO<sub>2</sub> produced (calculated from the volume of gas measured and the van der Waals equation).

*Halide removal in situ for dehydrogenation:* Silver triflate (1 equiv for catalysts of formula [Cp\*IrCl(L)]OTf and 2 equiv for catalysts with formula [Cp\*IrCl(L)]Cl and [(*p*-cym)RuCl(L)]Cl) was added to the freshly prepared stock solution of aqueous catalyst (0.3 mM, 100 mL) and allowed to stir at room temperature in the absence of light. After 12 h of stirring, the reaction mixture was filtered over Celite with suction and used without further characterization according to the catalytic dehydrogenation procedure previously stated.

#### 4.4.16 Computational Methods

The mechanisms were proposed via DFT computations using Gaussian 09 (Revision E01)<sup>62</sup>. Gas phase geometry optimizations were carried out with PBE/PBE<sup>63-64</sup> functional and basis set 1 (BS1). In BS1, iridium utilized the Couty and Hall modified-LANL2DZ<sup>65-67</sup> basis set and the associated LANL2DZ effective core potential, and all other atoms (C, O, N, Na, and H) used the 6-31G (*d'*)<sup>68-70, 71</sup> basis sets. Harmonic vibrational frequency computations were performed to verify the nature of all stationary points. In order to approximate the solvation effect in aqueous condition, the self-consistent reaction field (SCRF) single-point computations with the SMD solvation model<sup>72</sup> on gas-phase optimized geometries were performed. Non-default self-consistent field (SCF) convergence (10<sup>-6</sup>) and density fitting approximation (with AUTO keyword)<sup>73-74</sup> were used in geometry optimizations and single-point SMD solvation computations. Spherical harmonic *5d* and *7f* functions and a pruned integration grid containing 75 radial shells and 302 angular points per shell were used for all computations. Free

energy corrections were determined at 1 atm and 298.15 K. The experimental value of proton solvation energy in water ( $-265.9 \text{ kcal mol}^{-1}$ )<sup>75-76</sup> and experimental Gibbs free energy of proton ( $-6.28 \text{ kcal mol}^{-1}$ )<sup>77-78</sup> were used to calculate the relative reaction energy of the proposed mechanisms.

#### 4.5 Author Contribution

I performed catalytic testing for both CO<sub>2</sub> hydrogenation and formic acid dehydrogenation including data with Lewis acids and pressure data from CO<sub>2</sub> hydrogenation experiments, pK<sub>a</sub> measurement of **2**, and UV/vis measurements of the complexes and reaction solutions. I also advised a group of students that performed catalytic testing for formic acid dehydrogenation and contributed to the writing of the paper resulting from this project.

#### 4.6 References

1. Nieto, I.; Livings, M. S.; Sacci, J. B.; Reuther, L. E.; Zeller, M.; Papish, E. T. *Organometallics*, **2011**, *30*, 6339-6342.
2. DePasquale, J.; Nieto, I.; Reuther, L. E.; Herbst-Gervasoni, C. J.; Paul, J. J.; Mochalin, V.; Zeller, M.; Thomas, C. M.; Addison, A. W.; Papish, E. T. *Inorg. Chem.*, **2013**, *52*, 9175-9183.
3. Marelius, D. C.; Bhagan, S.; Charboneau, D. J.; Schroeder, K. M.; Kamdar, J. M.; McGettigan, A. R.; Freeman, B. J.; Moore, C. E.; Rheingold, A. L.; Cooksy, A. L.; Smith, D. K.; Paul, J. J.; Papish, E. T.; Grotjahn, D. B. *Eur. J. Inorg. Chem.*, **2014**, *2014*, 676-689.
4. Gerlach, D. L.; Bhagan, S.; Cruce, A. A.; Burks, D. B.; Nieto, I.; Truong, H. T.; Kelley, S. P.; Herbst-Gervasoni, C. J.; Jernigan, K. L.; Bowman, M. K.; Pan, S.; Zeller, M.; Papish, E. T. *Inorg. Chem.*, **2014**, 12689-12698.
5. Fujita, K.; Kawahara, R.; Aikawa, T.; Yamaguchi, R. *Angew. Chem., Int. Ed.*, **2015**, *54*, 9057-60.

6. Wang, W.-H.; Hull, J. F.; Muckerman, J. T.; Fujita, E.; Himeda, Y. *Energy Environ. Sci.*, **2012**, *5*, 7923-7926.
7. Lewandowska-Andralojc, A.; Polyansky, D. E.; Wang, C.-H.; Wang, W.-H.; Himeda, Y.; Fujita, E. *Phys. Chem. Chem. Phys.*, **2014**, *16*, 11976-11987.
8. Zhang, T.; deKrafft, K. E.; Wang, J.-L.; Wang, C.; Lin, W. *Eur. J. Inorg. Chem.*, **2014**, *2014*, 698-707.
9. Wang, W.-H.; Xu, S.; Manaka, Y.; Suna, Y.; Kambayashi, H.; Muckerman, J. T.; Fujita, E.; Himeda, Y. *ChemSusChem*, **2014**, *7*, 1976-1983.
10. Fujita, K.; Tanaka, Y.; Kobayashi, M.; Yamaguchi, R. *J. Am. Chem. Soc.*, **2014**, *136*, 4829-32.
11. Hull, J. F.; Himeda, Y.; Wang, W.-H.; Hashiguchi, B.; Periana, R.; Szalda, D. J.; Muckerman, J. T.; Fujita, E. *Nature Chemistry*, **2012**, *4*, 383-388.
12. Tanaka, R.; Yamashita, M.; Nozaki, K. *J. Am. Chem. Soc.*, **2009**, *131*, 14168-14169.
13. Kang, P.; Cheng, C.; Chen, Z.; Schauer, C. K.; Meyer, T. J.; Brookhart, M. *J. Am. Chem. Soc.*, **2012**, *134*, 5500-5503.
14. Ahn, S. T.; Bielinski, E. A.; Lane, E. M.; Chen, Y.; Bernskoetter, W. H.; Hazari, N.; Palmore, G. T. R. *Chem. Commun.*, **2015**, *51*, 5947-5950.
15. Wang, W.-H.; Himeda, Y.; Muckerman, J. T.; Manbeck, G. F.; Fujita, E. *Chem. Rev.*, **2015**, *115*, 12936-12973.
16. Calaje, J. J. A.; Lu, Z.; Kedzie, E. A.; Terrile, N. J.; Lo, J. N.; Williams, T. J. *Nature Communications*, **2016**, 11308-11313.
17. Bielinski, E. A.; Förster, M.; Zhang, Y.; Bernskoetter, W. H.; Hazari, N.; Holthausen, M. C. *ACS Catal.*, **2015**, *5*, 2404-2415.
18. Hu, P.; Diskin-Posner, Y.; Ben-David, Y.; Milstein, D. *ACS Catal.*, **2014**, *4*, 2649-2652.
19. Hu, Y.; Shaw, A. P.; Guan, H.; Norton, J. R.; Sattler, W.; Rong, Y. *Organometallics*, **2016**, *35*, 39-46.
20. Hu, Y.; Norton, J. R. *J. Am. Chem. Soc.*, **2014**, *136*, 5938-5948.
21. Hu, Y.; Li, L.; Shaw, A. P.; Norton, J. R.; Sattler, W.; Rong, Y. *Organometallics*, **2012**, *31*, 5058-5064.
22. Hu, Y.; Shaw, A. P.; Estes, D. P.; Norton, J. R. *Chem. Rev.*, **2016**, *116*, 8427-8462.
23. Fagan, P. J.; Voges, M. H.; Bullock, R. M. *Organometallics*, **2010**, *29*, 1045-1048.

24. Ledger, A. E. W.; Moreno, A.; Ellul, C. E.; Mahon, M. F.; Pregosin, P. S.; Whittlesey, M. K.; Williams, J. M. J. *Inorg. Chem.*, **2010**, *49*, 7244-7256.
25. Namorado, S.; Antunes, M. A.; Veiros, L. F.; Ascenso, J. R.; Duarte, M. T.; Martins, A. M. *Organometallics*, **2008**, *27*, 4589-4599.
26. Guan, H.; Iimura, M.; Magee, M. P.; Norton, J. R.; Zhu, G. *J. Am. Chem. Soc.*, **2005**, *127*, 7805-7814.
27. Papish, E. T.; Magee, M. P.; Norton, J. R. in *Recent Advances in Hydride Chemistry published by Elsevier*, **2001**, 39-74.
28. Casey, C. P.; Guan, H. *J. Am. Chem. Soc.*, **2009**, *131*, 2499-2507.
29. Casey, C. P.; Johnson, J. B.; Singer, S. W.; Cui, Q. *J. Am. Chem. Soc.*, **2005**, *127*, 3100-3109.
30. Casey, C. P.; Singer, S. W.; Powell, D. R.; Hayashi, R. K.; Kavana, M. *J. Am. Chem. Soc.*, **2001**, *123*, 1090-1100.
31. Shvo, Y.; Czarkie, D.; Rahamim, Y.; Chodosh, D. F. *J. Am. Chem. Soc.*, **1986**, *108*, 7400-7402.
32. Arduengo, A. J. *Acc. Chem. Res.*, **1999**, *32*, 913-921.
33. Ledoux, N.; Allaert, B.; Linden, A.; Van Der Voort, P.; Verpoort, F. *Organometallics*, **2007**, *26*, 1052-1056.
34. Dharmasena, U. L.; Foucault, H. M.; dos Santos, E. N.; Fogg, D. E.; Nolan, S. P. *Organometallics*, **2005**, *24*, 1056-1058.
35. Danopoulos, A. A.; Pugh, D.; Smith, H.; Saßmannshausen, J. *Chem. - Eur. J.*, **2009**, *15*, 5491-5502.
36. Chen, H.-S.; Chang, W.-C.; Su, C.; Li, T.-Y.; Hsu, N.-M.; Tingare, Y. S.; Li, C.-Y.; Shie, J.-H.; Li, W.-R. *Dalton Trans.*, **2011**, *40*, 6765-6770.
37. Specht, Z. G.; Grotjahn, D. B.; Moore, C. E.; Rheingold, A. L. *Organometallics*, **2013**, *32*, 6400-6409.
38. Huckaba, A. J.; Sharpe, E. A.; Delcamp, J. H. *Inorg. Chem.*, **2016**, *55*, 682-690.
39. Stanton, I., Charles J; Machan, C. W.; Vandezande, J. E.; Jin, T.; Majetich, G. F.; Schaefer, I., Henry F; Kubiak, C. P.; Li, G.; Agarwal, J. *Inorg. Chem.*, **2016**, *55*, 3136-3144.
40. Agarwal, J.; Shaw, T. W.; Stanton, I., Charles J; Majetich, G. F.; Bocarsly, A. B.; Schaefer, I., Henry F. *Angewandte Chemie International Edition*, **2014**, *53*, 5152-5155.

41. Thoi, V. S.; Kornienko, N.; Margarit, C. G.; Yang, P.; Chang, C. J. *J. Am. Chem. Soc.*, **2013**, *135*, 14413-14424.
42. Briocche, J.; Michalak, M.; Quiclet-Sire, B.; Zard, S. Z. *Organic Letters*, **2011**, *13*, 6296-6299.
43. Gronnier, C.; Bel, P. F. d.; Henrion, G.; Kramer, S.; Gagosz, F. *Organic Letters*, **2014**, *16*, 2092-2095.
44. Schlosser, M.; Rausis, T. *Helvetica Chimica Acta*, **2005**, *88*, 1240-1249.
45. Wang, H. M. J.; Lin, I. J. B. *Organometallics*, **1998**, *17*, 972-975.
46. Zhang, T.; Wang, C.; Liu, S.; Wang, J.-L.; Lin, W. *J. Am. Chem. Soc.*, **2014**, *136*, 273-281.
47. Burks, D. B.; Vasiliu, M.; Dixon, D. A.; Papish, E. T. *J. Phys. Chem. A*, **2018**, ASAP.
48. Himeda, Y. *E. J. Inorg. Chem.*, **2007**, *2007*, 3927-3941.
49. Ghorai, D.; Dutta, C.; Choudhury, J. *ACS Catal.*, **2016**, *6*, 709-713.
50. Cocco, F.; Cinellu, M. A.; Minghetti, G.; Zucca, A.; Stoccoro, S.; Maiore, L.; Manassero, M. *Organometallics*, **2010**, *29*, 1064-1066.
51. Campos, J.; Hintermair, U.; Brewster, T. P.; Takase, M. K.; Crabtree, R. H. *ACS Catal.*, **2014**, *4*, 973-985.
52. Moore, C. M.; Bark, B.; Szymczak, N. K. *ACS Catal.*, **2016**, *6*, 1981-1990.
53. Dub, P. A.; Henson, N. J.; Martin, R. L.; Gordon, J. C. *J. Am. Chem. Soc.*, **2014**, *136*, 3505-3521.
54. Hartmann, R.; Chen, P. *Angew. Chem., Int. Ed.*, **2001**, *40*, 3581-3585.
55. John, J. M.; Takebayashi, S.; Dabral, N.; Miskolzie, M.; Bergens, S. H. *J. Am. Chem. Soc.*, **2013**, *135*, 8578-8584.
56. Hayes, J. M.; Deydier, E.; Ujaque, G.; Lledós, A.; Malacea-Kabbara, R.; Manoury, E.; Vincendeau, S.; Poli, R. *ACS Catal.*, **2015**, *5*, 4368-4376.
57. O, W. W. N.; Lough, A. J.; Morris, R. H. *Organometallics*, **2012**, *31*, 2152-2165.
58. Ertem, M. Z.; Himeda, Y.; Fujita, E.; Muckerman, J. T. *ACS Catal.*, **2016**, *6*, 600-609.
59. Moore, C. M.; Dahl, E. W.; Szymczak, N. K. *Current Opinion in Chemical Biology*, **2015**, *25*, 9-17.

60. Moore, C. M.; Szymczak, N. K. *Chem. Commun.*, **2013**, 49, 400-402.
61. Dubreuil, D. M.; Pipelier, M. G.; Pradere, J. P.; Bakkali, H.; Lepape, P.; Delaunay, T.; Tabatchnik, A. *Pyridine and Pyrrole Compounds, Processes for Obtaining Them and Uses*. 2008.
62. Frisch, M. J.; Trucks, G. W.; Schlegel, H. B.; Scuseria, G. E.; Robb, M. A.; Cheeseman, J. R.; Scalmani, G.; Barone, V.; Mennucci, B.; Petersson, G. A.; Nakatsuji, H.; Caricato, M.; Li, X.; Hratchian, H. P.; Izmaylov, A. F.; Bloino, J.; Zheng, G.; Sonnenberg, J. L.; Hada, M.; Ehara, M.; Toyota, K.; Fukuda, R.; Hasegawa, J.; Ishida, M.; Nakajima, T.; Honda, Y.; Kitao, O.; Nakai, H.; Vreven, T.; Montgomery Jr., J. A.; Peralta, J. E.; Ogliaro, F.; Bearpark, M. J.; Heyd, J.; Brothers, E. N.; Kudin, K. N.; Staroverov, V. N.; Kobayashi, R.; Normand, J.; Raghavachari, K.; Rendell, A. P.; Burant, J. C.; Iyengar, S. S.; Tomasi, J.; Cossi, M.; Rega, N.; Millam, N. J.; Klene, M.; Knox, J. E.; Cross, J. B.; Bakken, V.; Adamo, C.; Jaramillo, J.; Gomperts, R.; Stratmann, R. E.; Yazyev, O.; Austin, A. J.; Cammi, R.; Pomelli, C.; Ochterski, J. W.; Martin, R. L.; Morokuma, K.; Zakrzewski, V. G.; Voth, G. A.; Salvador, P.; Dannenberg, J. J.; Dapprich, S.; Daniels, A. D.; Farkas, Ö.; Foresman, J. B.; Ortiz, J. V.; Cioslowski, J.; Fox, D. J. *Gaussian 09, Revision D.01*, Gaussian, Inc.: Wallingford, CT, USA, 2013.
63. Perdew, J. P.; Burke, K.; Ernzerhof, M. *Phys. Rev. Lett.*, **1996**, 77, 3865-3868.
64. Perdew, J. P.; Burke, K.; Ernzerhof, M. *Phys. Rev. Lett.*, **1997**, 78, 1396.
65. Couty, M.; Hall, M. B. *J Comput Chem*, **1996**, 17, 1359-1370.
66. Hay, P. J.; Wadt, W. R. *J. Chem. Phys.*, **1985**, 82, 270-283.
67. Hay, P. J.; Wadt, W. R. *J. Chem. Phys.*, **1985**, 82, 299-310.
68. Hehre, W. J.; Ditchfie.R; Pople, J. A. *J Chem Phys*, **1972**, 56, 2257-2261.
69. Harihara.Pc; Pople, J. A. *Theor Chim Acta*, **1973**, 28, 213-222.
70. Foresman, J. B.; Frisch, Æ., *Exploring Chemistry with Electronic Structure Methods*. 2nd ed.; Gaussian, Inc: Pittsburgh, PA, 1996, p 110.
71. The 6-31G(d') basis set has the d polarization functions for C, N, and O taken from the 6-311G(d) basis sets, instead of the original arbitrarily assigned value of 0.8 used in the 6-31G(d) basis sets.
72. Marenich, A. V.; Cramer, C. J.; Truhlar, D. G. *J. Phys. Chem. B*, **2009**, 113, 6378-6396.
73. Dunlap, B. I. *J. Chem. Phys.*, **1983**, 78, 3140-3142.
74. Dunlap, B. I. *J. Mole. Stru. (Theochem)* **2000**, 529, 37-40.

75. Camaioni, D. M.; Schwerdtfeger, C. A. *J. Phys. Chem. A*, **2005**, *109*, 10795-10797.
76. Kelly, C. P.; Cramer, C. J.; Truhlar, D. G. *J. Phys. Chem. B*, **2006**, *110*, 16066-16081.
77. Fifen, J. J.; Dhaouadi, Z.; Nsangou, M., J. . *Phys. Chem. A* **2014**, *118*, 11090-11097.
78. Moser, A.; Range, K.; York, D. M. *J. Phys. Chem. B*, **2010**, *114*, 13911-13921.
79. Widegren, J. A.; Finke, R. G. *Journal of Molecular Catalysis A: Chemical*, **2003**, *198*, 317-341.
80. Bayram, E.; Linehan, J. C.; Fulton, J. L.; Roberts, J. A. S.; Szymczak, N. K.; Smurthwaite, T. D.; Özkar, S.; Balasubramanian, M.; Finke, R. G. *J. Am. Chem. Soc.*, **2011**, *133*, 18889-18902.
81. DePasquale, J.; Kumar, M.; Zeller, M.; Papish, E. T. *Organometallics*, **2013**, *32*, 966-979.

## 4.7 Supporting Information

### 4.7.1 pK<sub>a</sub> Determination of **2**

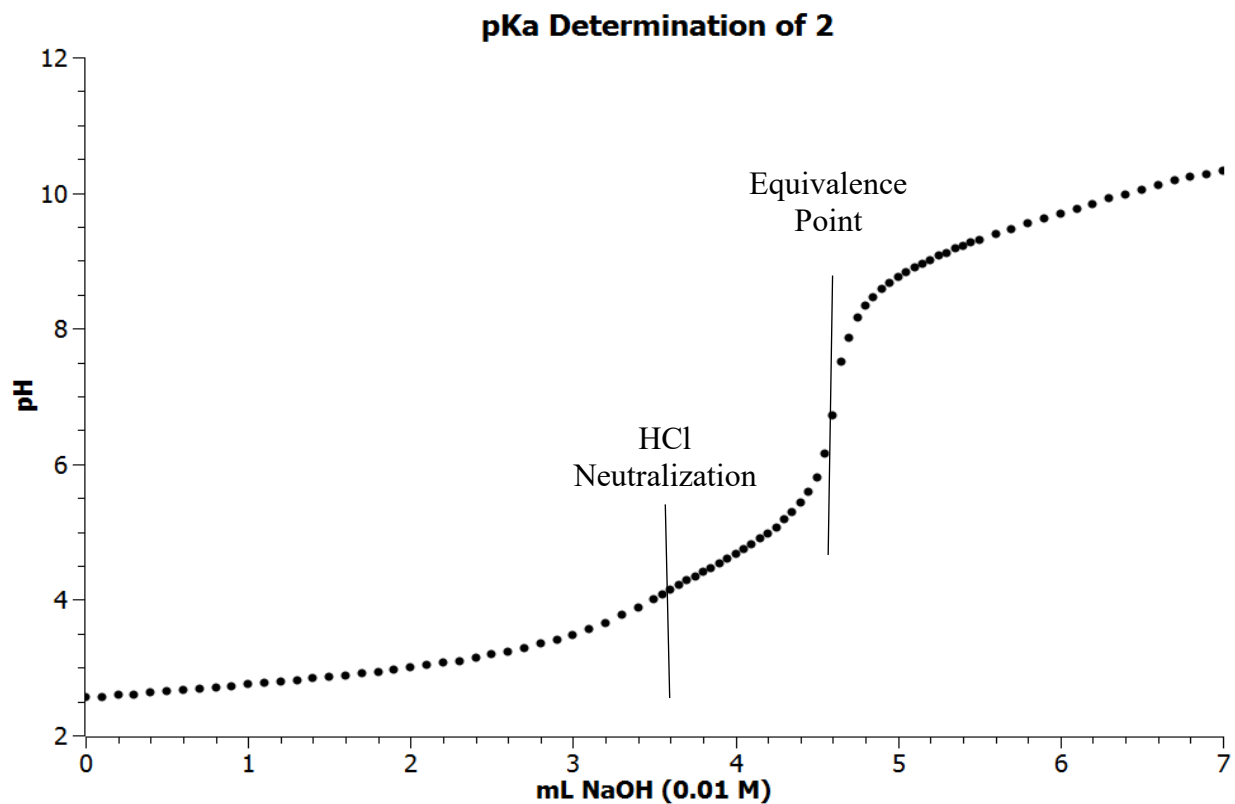


*Figure 4.S1.* Potentiometric titration curve for the pK<sub>a</sub> determination of complex **2**. Complex **2** (10.1 mg, 14.7 μmol) was dissolved in 15 mL of 2.8 mM HCl (aq). To this solution, 0.01 M NaOH (aq) was added in 50 or 100 μL amounts. The pH was measured after each addition. The first sharp increase in the graph is the neutralization of the excess HCl. The second is at the equivalence point.

#### 4.7.2 UV/vis Spectra

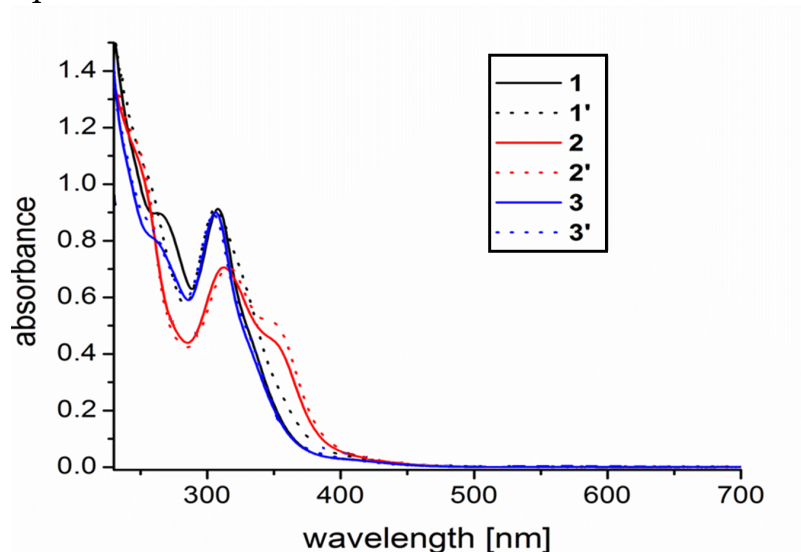


Figure 4.S2. Comparison of aqueous UV/vis absorption spectra of complexes **1-3** to the in situ generation of the aqua bound complexes **1'-3'** with AgOTf shows only minor changes in the absorption spectra with halide removal.

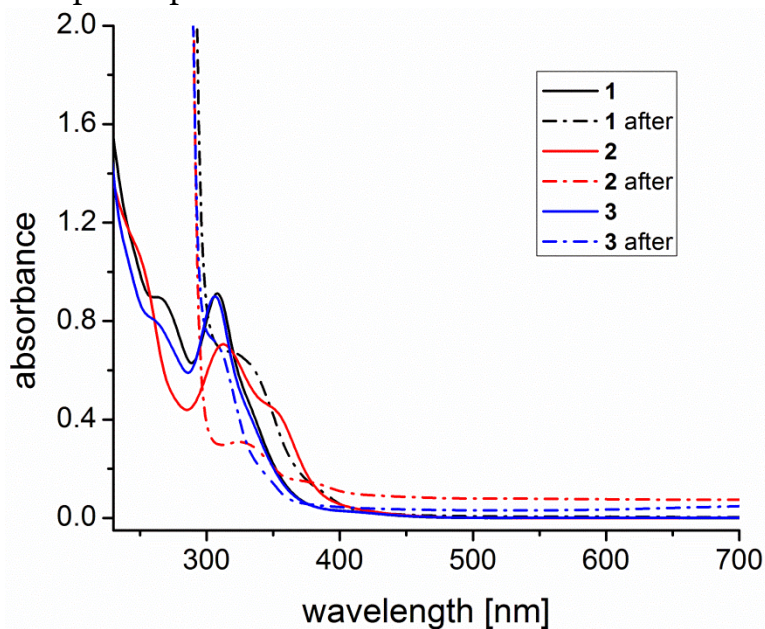
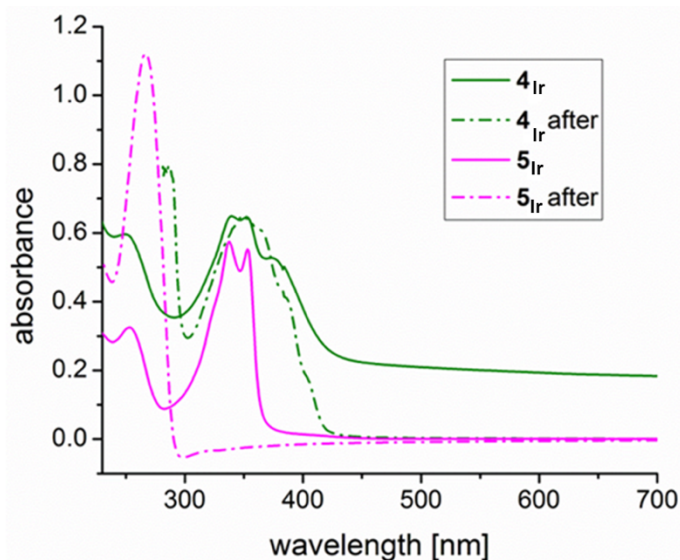


Figure 4.S3. UV/vis absorption spectra of aqueous  $[\text{Cp}^*\text{IrCl}(\text{NHC}^{\text{Me}}\text{-py}^{\text{OR}})]\text{OTf}$  complexes before and after hydrogenation. The spectra before hydrogenation are represented with solid lines, and the spectra after hydrogenation are represented with dash-dot lines. All three complexes have similar absorption spectra after hydrogenation (complex **3'** affords the same absorption spectra as complex **3**).



*Figure 4.S4.* UV/vis absorption spectra of aqueous  $[\text{Cp}^*\text{IrCl}(\text{dxbp})]\text{OTf}$  complexes before and after hydrogenation. The spectra before hydrogenation are represented with solid lines, and the spectra after hydrogenation are represented with dash-dot lines. Complex **4<sub>Ir</sub>** shows little change whereas complex **5<sub>Ir</sub>** has significant change.

#### 4.6.3 Quantitative Poisoning During $\text{CO}_2$ Hydrogenation Reaction

Starting with **3**, we set out to investigate whether the active catalyst was homogeneous or heterogeneous. Various tests have been reported in the literature to probe this issue. As mercury does not form an amalgam with Ir, adding mercury would not be a useful test here.<sup>79</sup> Therefore, quantitative poisoning with 1,10-phenanthroline was utilized.<sup>80-81</sup> A quantitative poison binds strongly to the free sites on the nanoparticle or metal complex and prevents catalysis from occurring.<sup>80</sup> If a catalyst is heterogeneous, there are less metal sites on the surface performing catalysis, so only a small amount of 1,10-phenanthroline (< 1 equiv) is necessary to completely poison the catalyst.<sup>80</sup> For a homogeneous catalyst, there are many more metal sites available to perform catalysis, so more 1,10-phenanthroline (typically 1-5 equiv) is necessary to negatively impact the catalyst.<sup>80</sup> The results of the quantitative poisoning with catalyst **3** are shown in Table 4.S1. There was a

slight decrease in activity with 1 equiv of 1,10-phenanthroline (Entry 2), which is inconsistent with a heterogeneous catalyst that would be completely poisoned. Five equivalents of 1,10-phenanthroline cause a large decrease in catalytic activity (Entry 3), consistent with a homogeneous catalyst. Thus, the catalytically active species here appears to be a molecular species in homogeneous solution. The active catalyst is **3** and/or a molecular species derived from **3**.

As phenanthroline is a bidentate ligand which may not bind effectively to one small free site, different poisons were explored. Quantitative poisoning attempts with several small, monodentate ligands resulted in varying TON with high standard deviations but very little poisoning (Table 4.S2). The data are inconclusive as to whether the active catalyst is homogeneous or heterogeneous. The poisoning ability of pyridine was tested with **4<sub>Ir</sub>**, a known homogeneous catalyst. At the CO<sub>2</sub> hydrogenation reaction conditions, pyridine was unsuccessful as a poison with this homogenous catalyst even at 20 equivalents (Table 4.S2, Entries 5 & 6). We suggest that these poisons listed in Table 4.S2 may impact the rate of decomposition for catalyst **3**. Perhaps these poisons have little impact on **4<sub>Ir</sub>** because it does not undergo transformation since **4<sub>Ir</sub>** is stable under hydrogenation conditions.

*Table 4.S1. Quantitative poisoning of **3** during CO<sub>2</sub> hydrogenation.<sup>a</sup>*

Entry	1,10-phenanthroline : <b>3</b>	TON
1	0:1	2020 (90)
2	1:1	1690 (320)
3	5:1	320 (310)

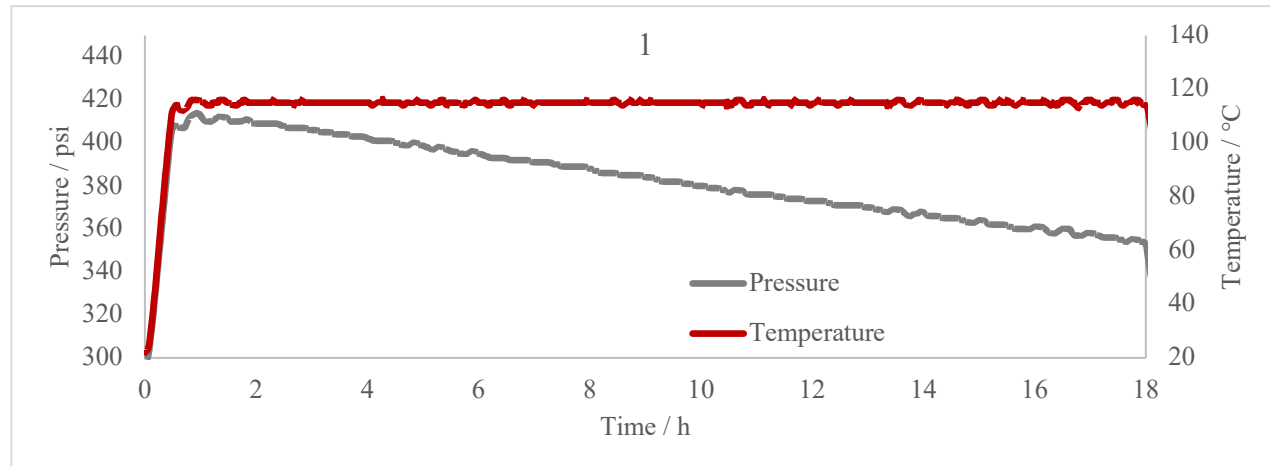
<sup>a</sup>Conditions: The reactions were performed in 25 mL of an aqueous solution of 0.3 mM catalyst and 1 M NaHCO<sub>3</sub> at 115 °C and 300 psig of H<sub>2</sub>/CO<sub>2</sub> (1:1). All TON are calculated after 18 hours and are an average of at least 3 experiments (estimated standard deviations are in parentheses).

Table 4.S2. Quantitative poisoning attempts during CO<sub>2</sub> hydrogenation.<sup>a</sup>

Entry	Catalyst	Additive	Equivalents	TON
1	<b>3</b>	None	0	2020 (90)
2	<b>3</b>	Pyridine	20	1550 (640)
3	<b>3</b>	Dimethylaminopyridine (DMAP)	20	1620 (540)
4	<b>3</b>	Thiophene	20	1670 (480)
5	<b>4Ir</b>	None	0	2270 (90)
6	<b>4Ir</b>	Pyridine	20	2090 (90)

<sup>a</sup>Conditions: The reactions were performed in 25 mL of an aqueous solution of 0.3 mM catalyst and 1 M NaHCO<sub>3</sub> at 115 °C and 300 psig of H<sub>2</sub>/CO<sub>2</sub> (1:1). All TON are calculated after 18 hours and are an average of at least 3 experiments (estimated standard deviations are in parentheses).

#### 4.7.4 Pressure vs. Time Data for Real Time Rates During CO<sub>2</sub> Hydrogenation



*Figure 4.S5.* Plots of pressure vs time (grey) and temperature vs time (crimson) for **1** over the 18 h reaction period of CO<sub>2</sub> hydrogenation, under the standard reaction conditions as listed in the experimental section of the manuscript. The initial sharp increase in temperature and pressure (from 0 to ~1 h) is the vessel heating up to the reaction temperature (115 °C).

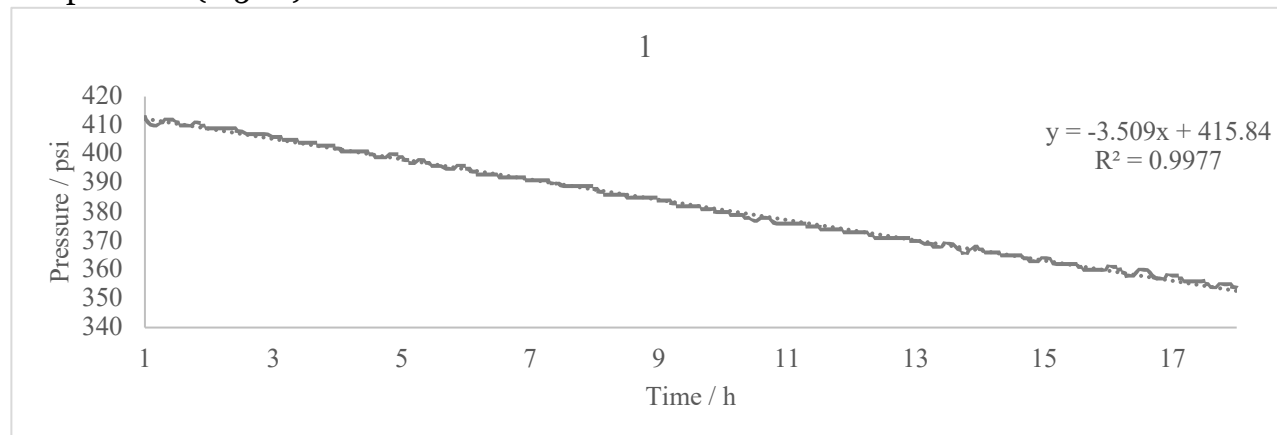


*Figure 4.S6.* Plot of pressure vs time for **1** from 1-18 h with a linear fit of the curve. The equation and R<sup>2</sup> value of the linear fit are shown on the plot.

Time (h)	$k_{\text{obs}}$ (psi/h)
2	3
3	4
4	4
5	4
6	3
7	4
8	3
9	4
10	5
11	2
12	4
13	2
14	4
15	3
16	2
17	4
average	3.4375
slope	3.509

*Table 4.S3.* Table of the calculation of  $k_{\text{obs}}$  for **1** during CO<sub>2</sub> hydrogenation from the pressure vs time data. Each time point is calculated as the change of pressure in the hour centered at the time point (e.g. the 2 h  $k_{\text{obs}}$  is calculated as the change in pressure from 1.5 h to 2.5 h). The average is the average  $k_{\text{obs}}$  of the 16 time points, and the slope is the slope of a linear fit of the pressure vs time plot.

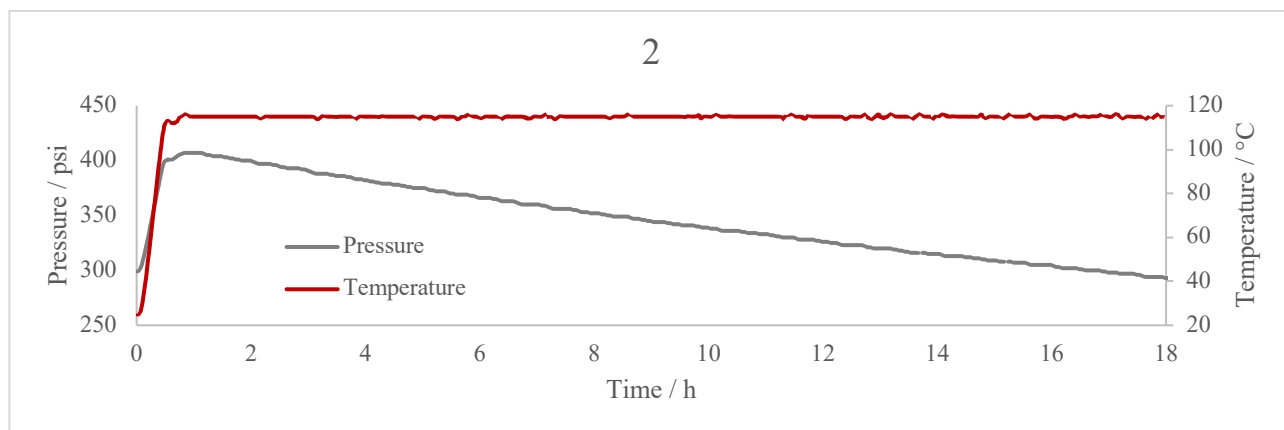


*Figure 4.S7.* Plots of pressure vs time (grey) and temperature vs time (crimson) for **2** over the 18 h reaction period of CO<sub>2</sub> hydrogenation, under the standard reaction conditions as listed in the experimental section of the manuscript. The initial sharp increase in temperature and pressure (from 0 to ~1 h) is the vessel heating up to the reaction temperature (115 °C).

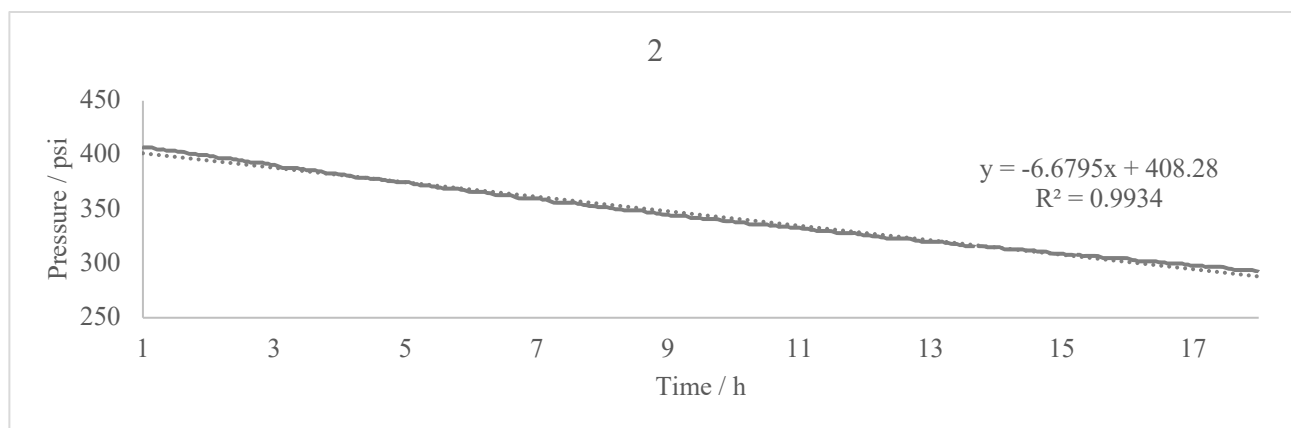


*Figure 4.S8.* Plot of pressure vs time for **2** from 1-18 h with a linear fit of the curve. The equation and R<sup>2</sup> value of the linear fit is shown on the plot.

Time (h)	$k_{\text{obs}}$ (psi/h)
2	9
3	9
4	8
5	8
6	7
7	7
8	7
9	7
10	6
11	7
12	6
13	6
14	5
15	5
16	6
17	5
average	6.75
slope	6.6795

*Table 4.S4.* Table of the calculation of  $k_{\text{obs}}$  for **2** during CO<sub>2</sub> hydrogenation from the pressure vs time data. Each time point is calculated as the change of pressure in the hour centered at the time point (e.g. the 2 h  $k_{\text{obs}}$  is calculated as the change in pressure from 1.5 h to 2.5 h). The average is the average  $k_{\text{obs}}$  of the 16 time points, and the slope is the slope of a linear fit of the pressure vs time plot.

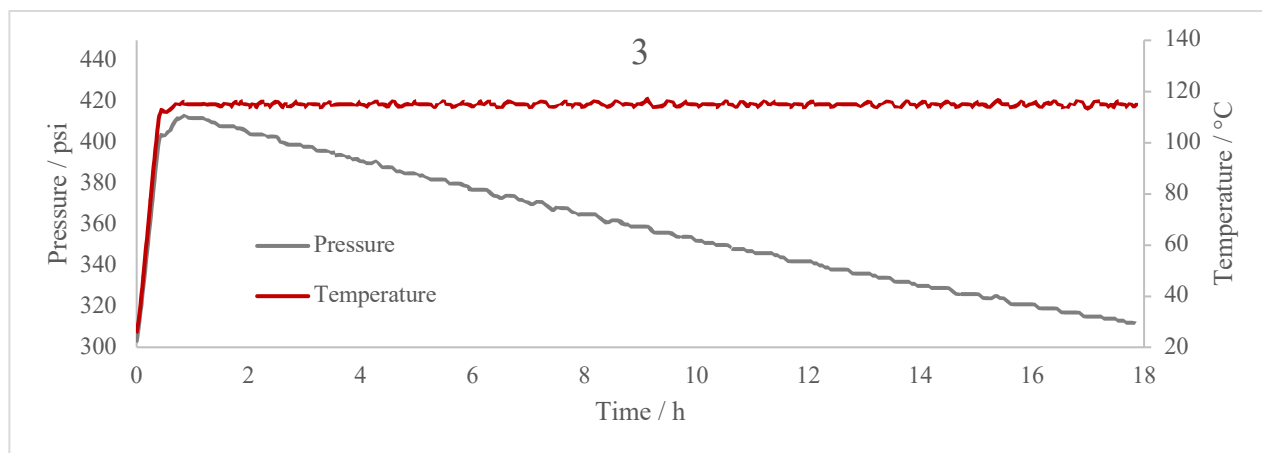


*Figure 4.S9.* Plots of pressure vs time (grey) and temperature vs time (crimson) for **3** over the 18 h reaction period of CO<sub>2</sub> hydrogenation, under the standard reaction conditions as listed in the experimental section of the manuscript. The initial sharp increase in temperature and pressure (from 0 to ~1 h) is the vessel heating up to the reaction temperature (115 °C).

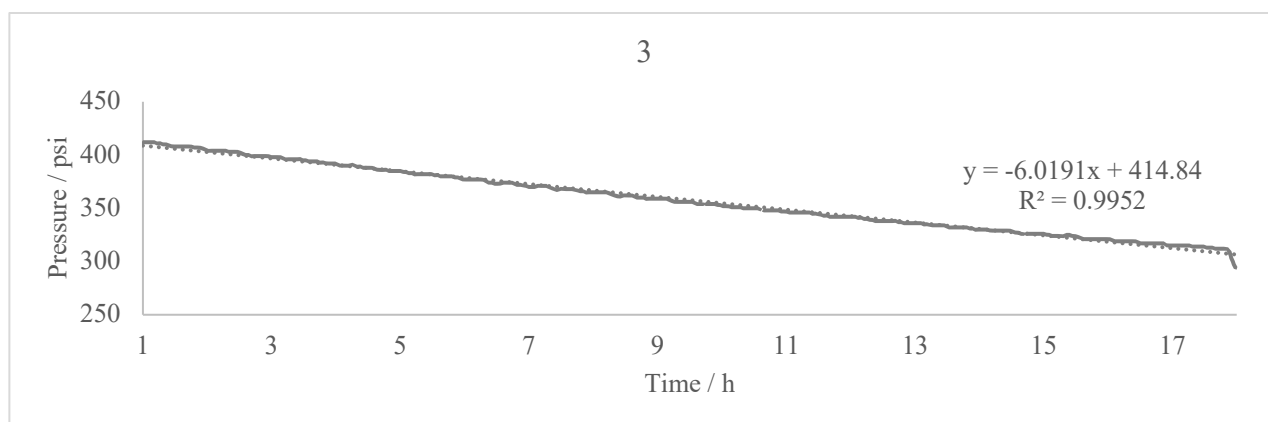


*Figure 4.S10.* Plot of pressure vs time for **3** from 1-18 h with a linear fit of the curve. The equation and R<sup>2</sup> value of the linear fit is shown on the plot.

Time (h)	$k_{\text{obs}}$ (psi/h)
2	5
3	8
4	7
5	6
6	9
7	5
8	6
9	6
10	6
11	6
12	6
13	5
14	4
15	6
16	6
17	3
average	5.875
slope	6.0191

*Table 4.S5.* Table of the calculation of  $k_{\text{obs}}$  for **3** during CO<sub>2</sub> hydrogenation from the pressure vs time data. Each time point is calculated as the change of pressure in the hour centered at the time point (e.g. the 2 h  $k_{\text{obs}}$  is calculated as the change in pressure from 1.5 h to 2.5 h). The average is the average  $k_{\text{obs}}$  of the 16 time points, and the slope is the slope of a linear fit of the pressure vs time plot.

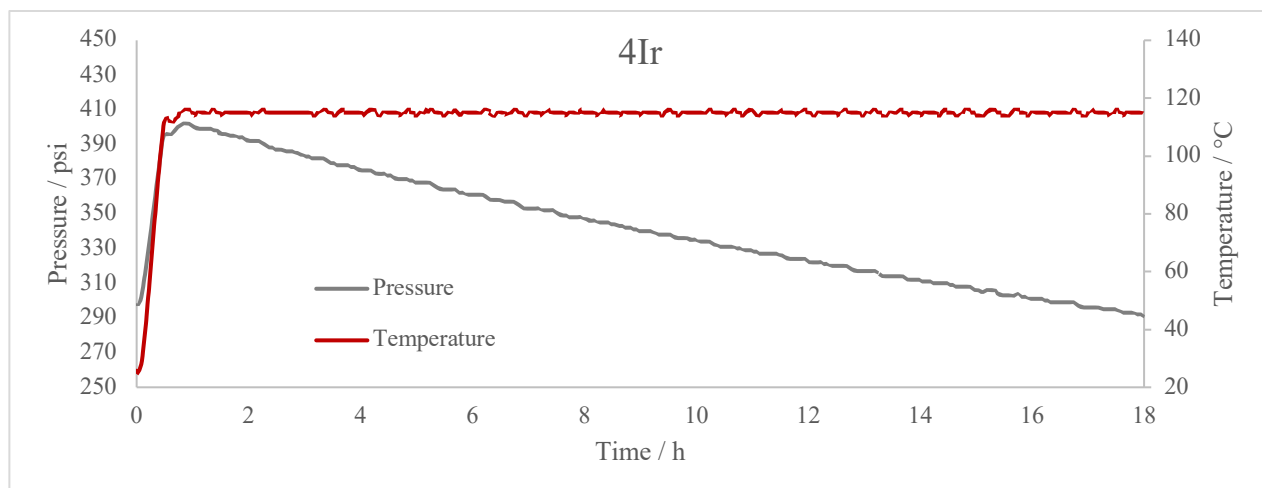


*Figure 4.S11.* Plots of pressure vs time (grey) and temperature vs time (crimson) for **4Ir** over the 18 h reaction period of CO<sub>2</sub> hydrogenation, under the standard reaction conditions as listed in the experimental section of the manuscript. The initial sharp increase in temperature and pressure (from 0 to ~1 h) is the vessel heating up to the reaction temperature (115 °C).

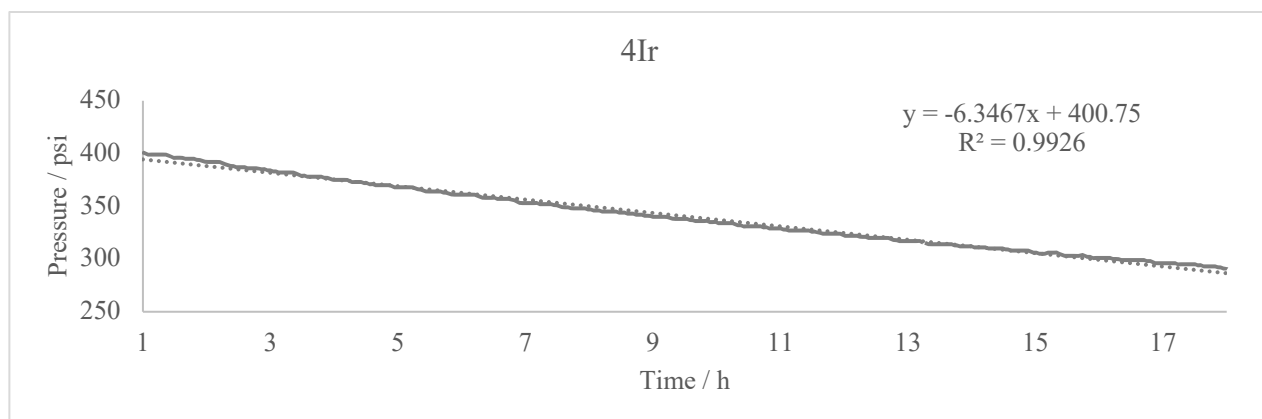


*Figure 4.S12.* Plot of pressure vs time for **4Ir** from 1-18 h with a linear fit of the curve. The equation and R<sup>2</sup> value of the linear fit is shown on the plot.

Time (h)	$k_{\text{obs}}$ (psi/h)
2	9
3	8
4	7
5	8
6	6
7	7
8	7
9	6
10	7
11	5
12	6
13	6
14	4
15	7
16	4
17	4
average	6.3125
slope	6.3467

*Table 4.S6.* Table of the calculation of  $k_{\text{obs}}$  for **4Ir** during CO<sub>2</sub> hydrogenation from the pressure vs time data. Each time point is calculated as the change of pressure in the hour centered at the time point (e.g. the 2 h  $k_{\text{obs}}$  is calculated as the change in pressure from 1.5 h to 2.5 h). The average is the average  $k_{\text{obs}}$  of the 16 time points, and the slope is the slope of a linear fit of the pressure vs time plot.

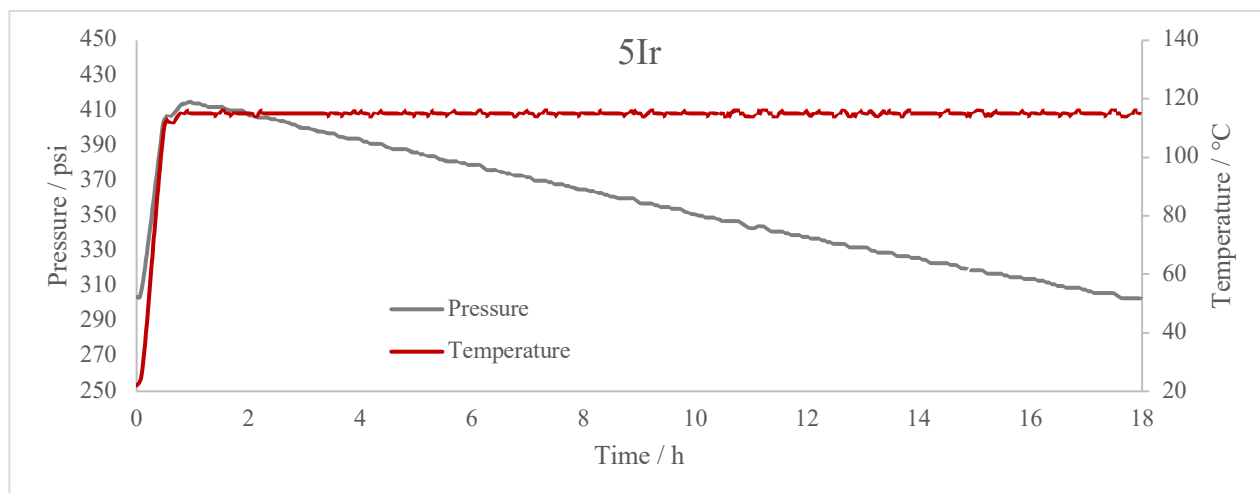


**Figure 4.S13.** Plots of pressure vs time (grey) and temperature vs time (crimson) for **5Ir** over the 18 h reaction period of CO<sub>2</sub> hydrogenation, under the standard reaction conditions as listed in the experimental section of the manuscript. The initial sharp increase in temperature and pressure (from 0 to ~1 h) is the vessel heating up to the reaction temperature (115 °C).

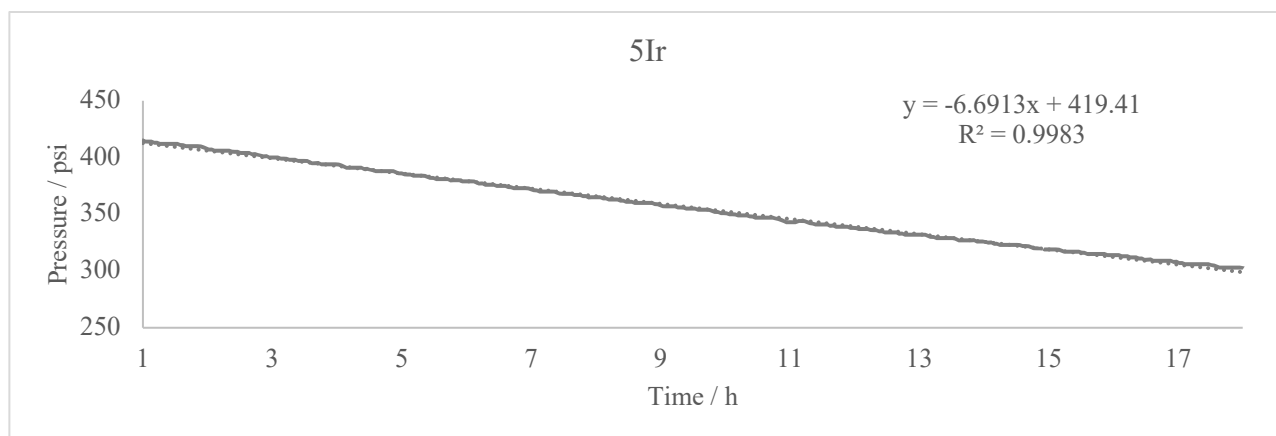


**Figure 4.S14.** Plot of pressure vs time for **5Ir** from 1-18 h with a linear fit of the curve. The equation and R<sup>2</sup> value of the linear fit is shown on the plot.

Time (h)	$k_{\text{obs}}$ (psi/h)
2	8
3	7
4	8
5	7
6	7
7	7
8	7
9	6
10	8
11	6
12	7
13	5
14	6
15	6
16	7
17	4
average	6.625
slope	6.6913

*Table 4.S7.* Table of the calculation of  $k_{\text{obs}}$  for **5r** during CO<sub>2</sub> hydrogenation from the pressure vs time data. Each time point is calculated as the change of pressure in the hour centered at the time point (e.g. the 2 h  $k_{\text{obs}}$  is calculated as the change in pressure from 1.5 h to 2.5 h). The average is the average  $k_{\text{obs}}$  of the 16 time points, and the slope is the slope of a linear fit of the pressure vs time plot.

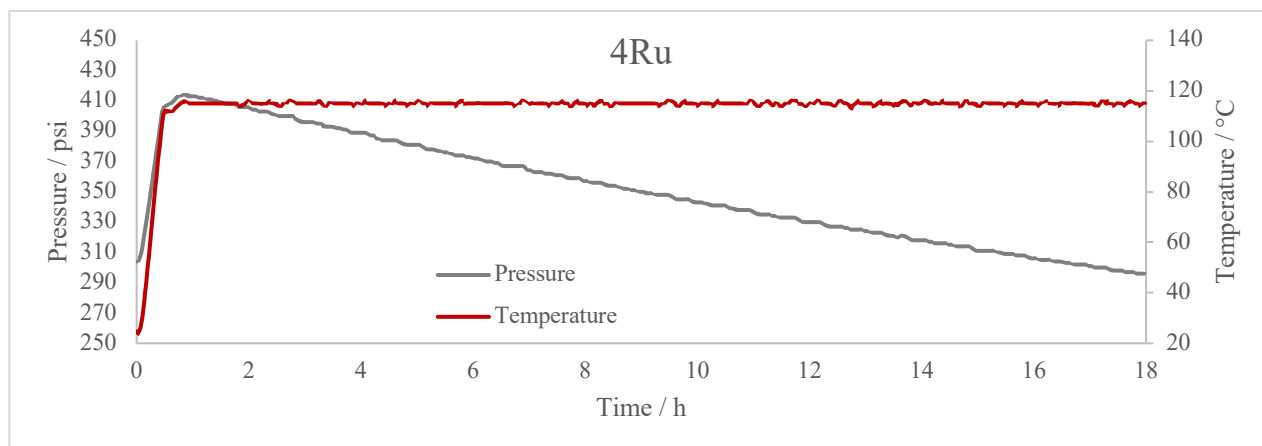


*Figure 4.S15.* Plots of pressure vs time (grey) and temperature vs time (crimson) for **4Ru** over the 18 h reaction period of CO<sub>2</sub> hydrogenation, under the standard reaction conditions as listed in the experimental section of the manuscript. The initial sharp increase in temperature and pressure (from 0 to ~1 h) is the vessel heating up to the reaction temperature (115 °C).

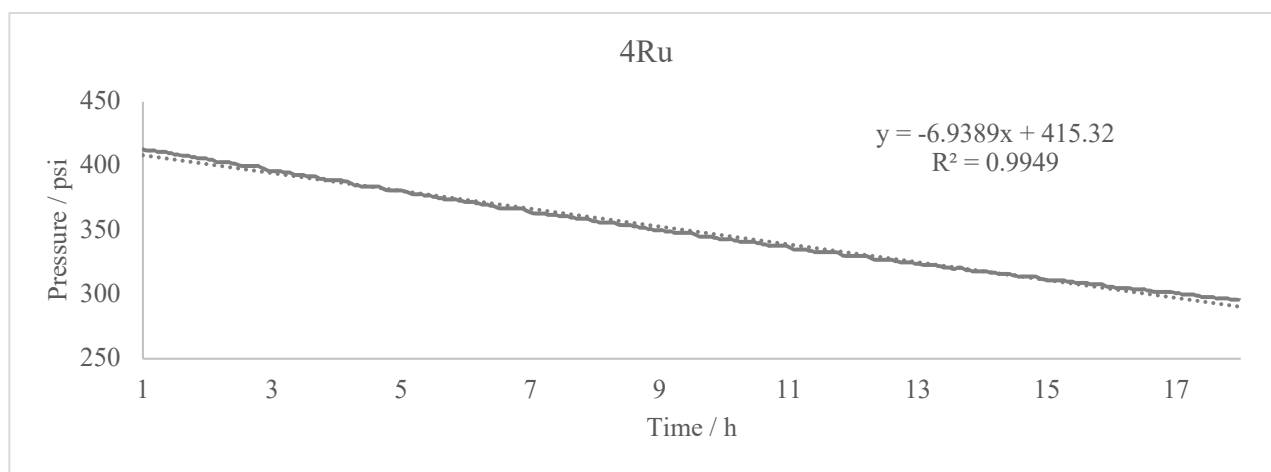


*Figure 4.S16.* Plot of pressure vs time for **4Ru** from 1-18 h with a linear fit of the curve. The equation and R<sup>2</sup> value of the linear fit is shown on the plot.

Time (h)	$k_{\text{obs}}$ (psi/h)
2	8
3	8
4	9
5	8
6	8
7	7
8	7
9	6
10	8
11	7
12	6
13	6
14	6
15	6
16	5
17	6
average	6.9375
slope	6.9389

*Table 4.S8.* Table of the calculation of  $k_{\text{obs}}$  for **4Ru** during CO<sub>2</sub> hydrogenation from the pressure vs time data. Each time point is calculated as the change of pressure in the hour centered at the time point (e.g. the 2 h  $k_{\text{obs}}$  is calculated as the change in pressure from 1.5 h to 2. hr). The average is the average  $k_{\text{obs}}$  of the 16 time points, and the slope is the slope of a linear fit of the pressure vs time plot.

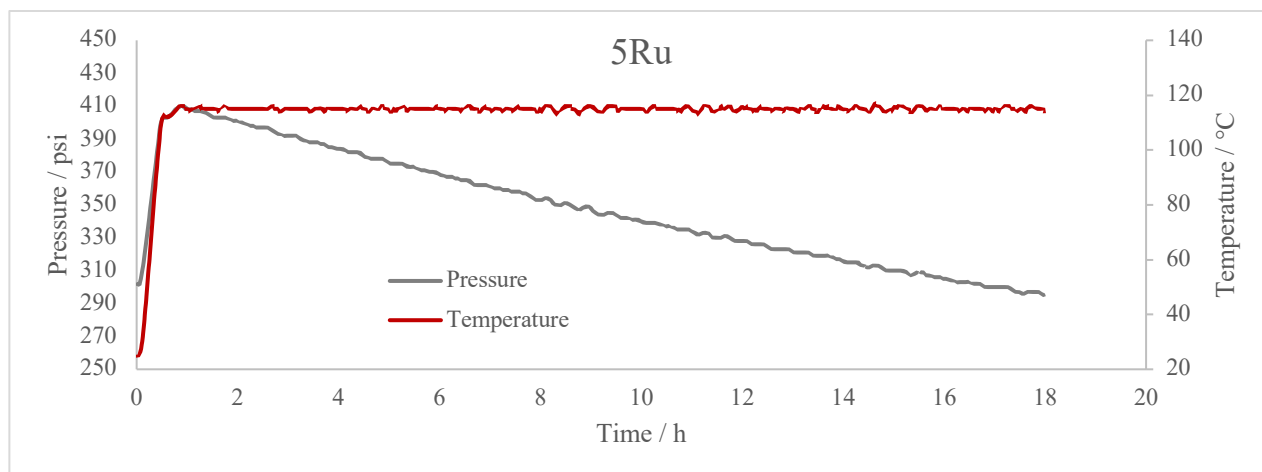


*Figure 4.S17.* Plots of pressure vs time (grey) and temperature vs time (crimson) for **5Ru** over the 18 h reaction period of CO<sub>2</sub> hydrogenation, under the standard reaction conditions as listed in the experimental section of the manuscript. The initial sharp increase in temperature and pressure (from 0 to ~1 h) is the vessel heating up to the reaction temperature (115 °C).

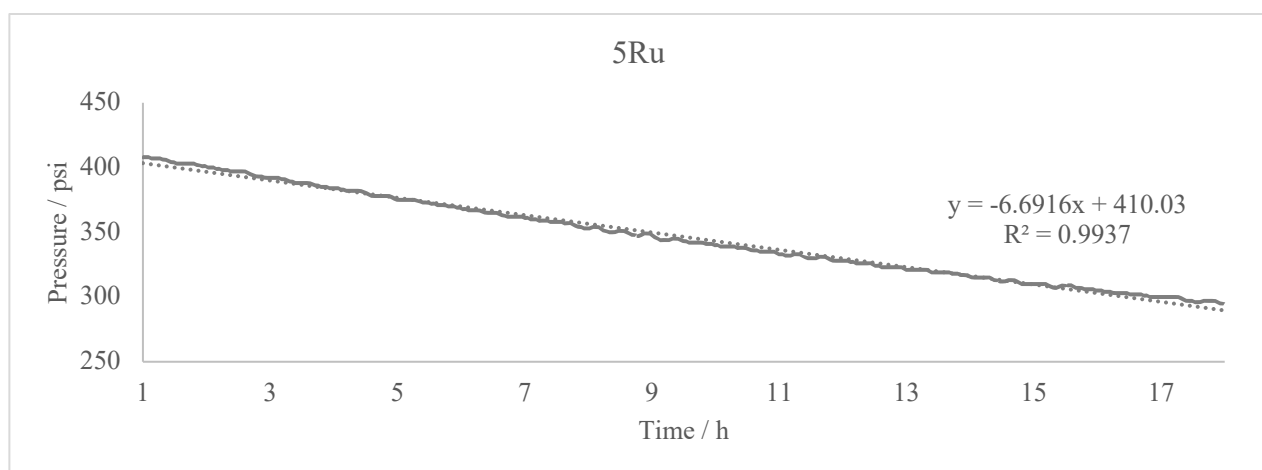


*Figure 4.S18.* Plot of pressure vs time for **5Ru** from 1-18 h with a linear fit of the curve. The equation and R<sup>2</sup> value of the linear fit is shown on the plot.

Time (h)	$k_{\text{obs}}$ (psi/h)
2	7
3	9
4	8
5	8
6	7
7	7
8	7
9	8
10	6
11	7
12	5
13	6
14	7
15	3
16	7
17	5
average	6.6875
slope	6.6916

*Table 4.S9.* Table of the calculation of  $k_{\text{obs}}$  for **5Ru** during CO<sub>2</sub> hydrogenation from the pressure vs time data. Each time point is calculated as the change of pressure in the hour centered at the time point (e.g. the 2 h  $k_{\text{obs}}$  is calculated as the change in pressure from 1.5 h to 2.5 h). The average is the average  $k_{\text{obs}}$  of the 16 time points, and the slope is the slope of a linear fit of the pressure vs time plot.

Catalyst	$k_{\text{obs}}$ / psi/h
<b>1</b>	3.51
<b>2</b>	6.68
<b>3</b>	6.02
<b>4Ir</b>	6.35
<b>5Ir</b>	6.69
<b>4Ru</b>	6.94
<b>5Ru</b>	6.69

*Table 4.S10.* The  $k_{\text{obs}}$ , calculated as the slope a linear fit of pressure vs time for hours 2-18, for all 7 catalysts.

#### 4.6.5 TON Calculated from Pressure Data

Time (h)	TON
2	402
3	453
4	521
5	573
6	642
7	713
8	766
9	839
10	912
11	986
12	1042
13	1099
14	1157
15	1215
16	1273
17	1332
18	1412

Experimental TON      1090

*Table 4.S11.* TON of **1** calculated from the pressure data collected during a standard hydrogenation reaction. TON were calculated using the van der Waals equation and the pressure at each hour. The experimental TON is as calculated in the manuscript after 18 h.

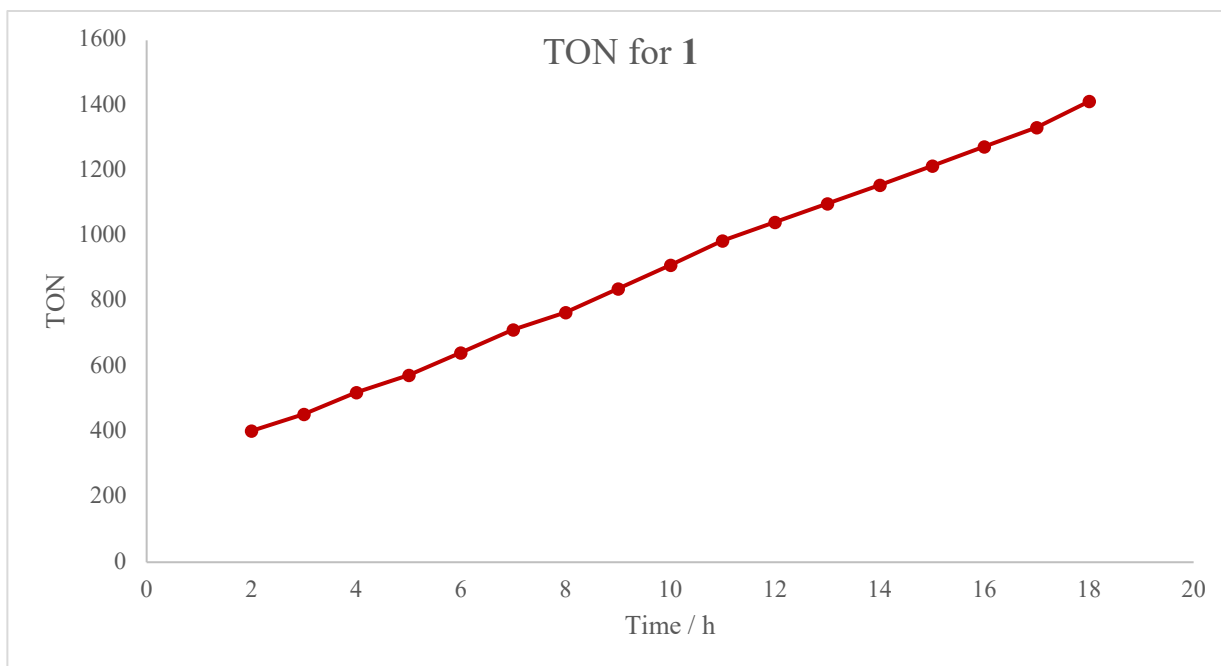


Figure 4.S19. Plot of the pressure-estimated TON vs time for **1**.

Time (h)	TON
2	555
3	713
4	875
5	1005
6	1176
7	1293
8	1453
9	1597
10	1744
11	1851
12	2005
13	2140
14	2255
15	2396
16	2492
17	2663
18	2788
Experimental TON	910

*Table 4.S12.* TON of **2** calculated from the pressure data collected during a standard hydrogenation reaction. TON were calculated using the van der Waals equation and the pressure at each hour. The experimental TON is as calculated in the manuscript after 18 h.

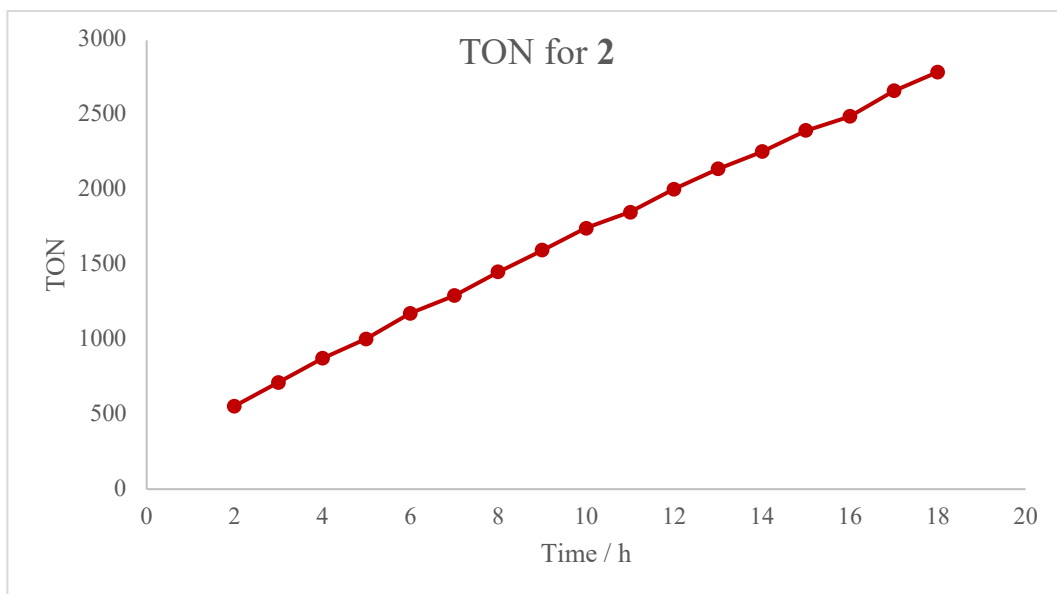


Figure 4.S20. Plot of the pressure-estimated TON vs time for **2**.

Time (h)	TON
2	470
3	590
4	713
5	820
6	967
7	1099
8	1195
9	1313
10	1453
11	1555
12	1659
13	1787
14	1917
15	2005
16	2118
17	2255
18	2325
Experimental TON	2020

*Table 4.S13.* TON of **3** calculated from the pressure data collected during a standard hydrogenation reaction. TON were calculated using the van der Waals equation and the pressure at each hour. The experimental TON is as calculated in the manuscript after 18 h.

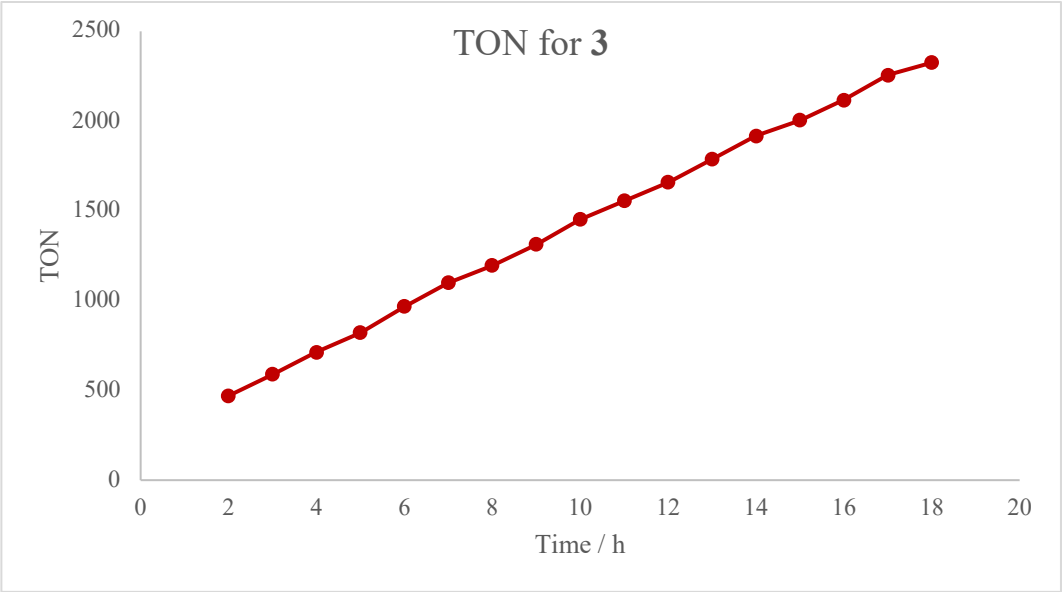


Figure 4.S21. Plot of the pressure-estimated TON vs time for **3**.

Time (h)	TON
2	695
3	839
4	1005
5	1137
6	1273
7	1433
8	1555
9	1701
10	1830
11	1939
12	2073
13	2209
14	2325
15	2468
16	2589
17	2713
18	2839
Experimental TON	2270

*Table 4.S14.* TON of **4<sub>Ir</sub>** calculated from the pressure data collected during a standard hydrogenation reaction. TON were calculated using the van der Waals equation and the pressure at each hour. The experimental TON is as calculated in the manuscript after 18 h.

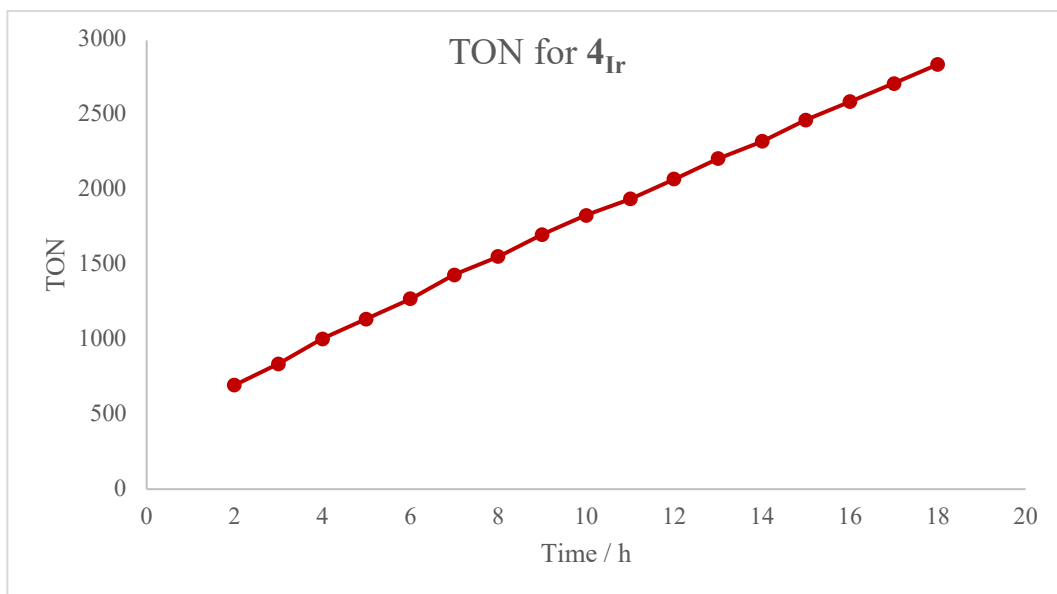


Figure 4.S22. Plot of the pressure-estimated TON vs time for 4<sub>Ir</sub>.

Time (h)	TON
2	436
3	555
4	660
5	802
6	930
7	1061
8	1195
9	1332
10	1473
11	1638
12	1744
13	1873
14	2005
15	2163
16	2279
17	2444
18	2540
Experimental TON	410

*Table 4.S15.* TON of **5<sub>Ir</sub>** calculated from the pressure data collected during a standard hydrogenation reaction. TON were calculated using the van der Waals equation and the pressure at each hour. The experimental TON is as calculated in the manuscript after 18 h.

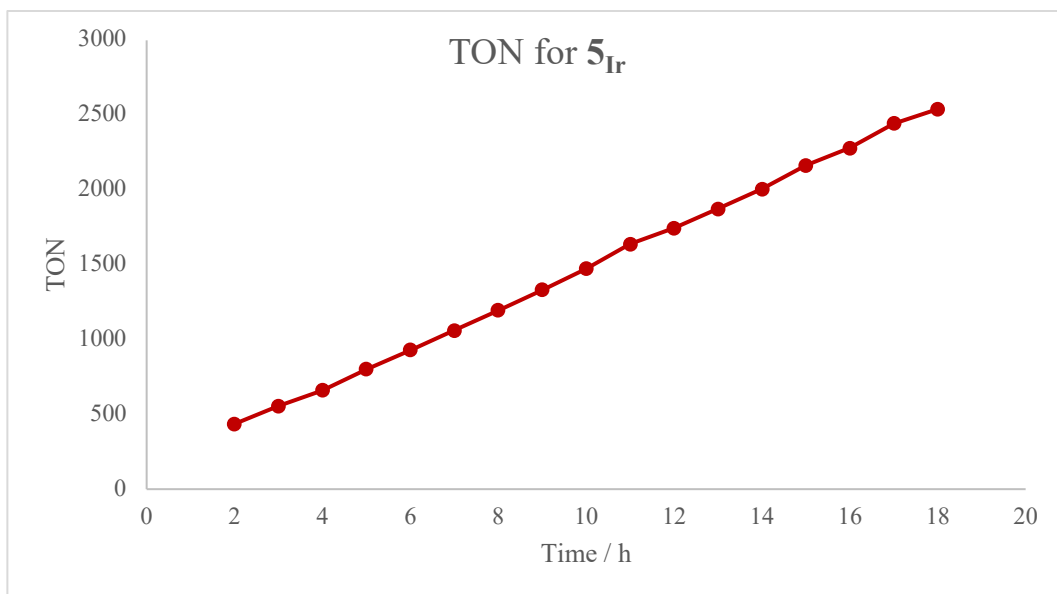


Figure 4.S23. Plot of the pressure-estimated TON vs time for 5<sub>Ir</sub>.

Time (h)	TON
2	453
3	625
4	748
5	893
6	1061
7	1215
8	1352
9	1494
10	1638
11	1765
12	1917
13	2050
14	2186
15	2349
16	2468
17	2589
18	2713
Experimental TON	1070

*Table 4.S16.* TON of **4<sub>Ru</sub>** calculated from the pressure data collected during a standard hydrogenation reaction. TON were calculated using the van der Waals equation and the pressure at each hour. The experimental TON is as calculated in the manuscript after 18 h.

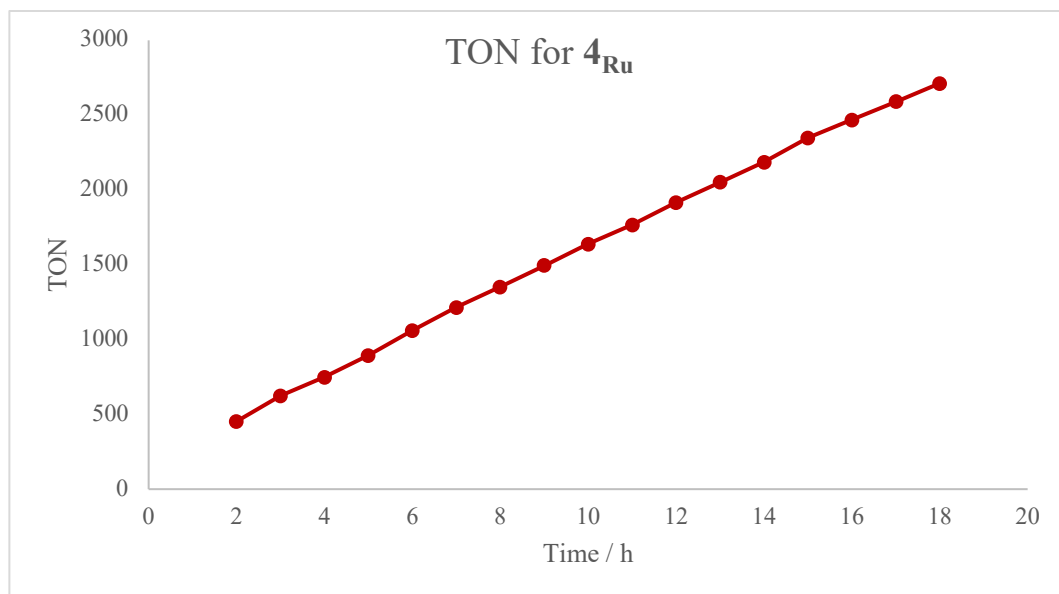


Figure 4.S24. Plot of the pressure-estimated TON vs time for 4<sub>Ru</sub>.

Time (h)	TON
2	555
3	695
4	839
5	1005
6	1118
7	1273
8	1433
9	1535
10	1701
11	1851
12	1961
13	2118
14	2232
15	2373
16	2492
17	2614
18	2738
Experimental TON	890

*Table 4.S17.* TON of **5<sub>Ru</sub>** calculated from the pressure data collected during a standard hydrogenation reaction. TON were calculated using the van der Waals equation and the pressure at each hour. The experimental TON is as calculated in the manuscript after 18 h.

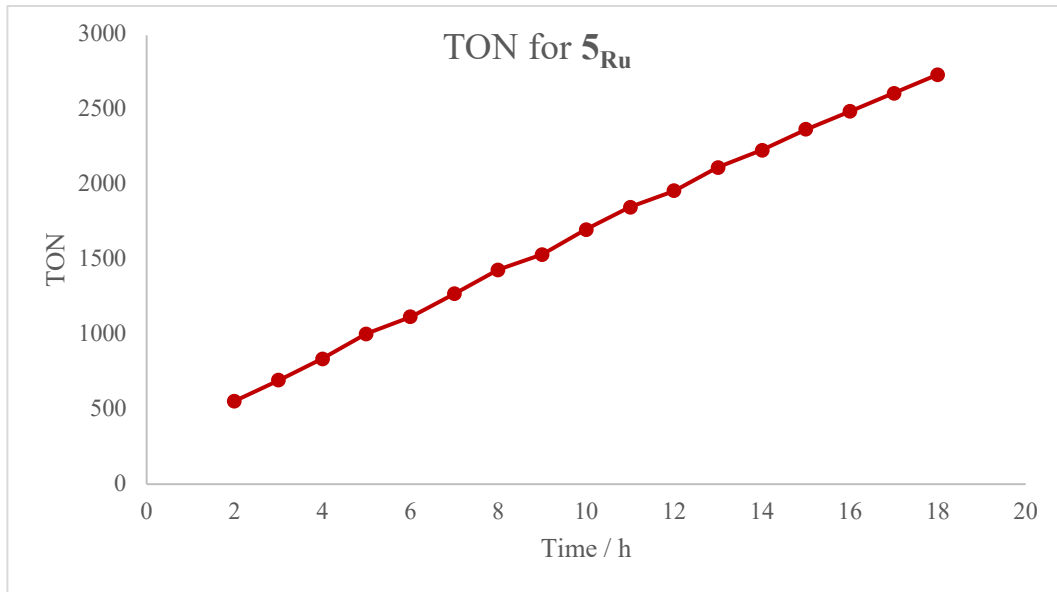


Figure 4.S25. Plot of the pressure-estimated TON vs time for 5<sub>Ru</sub>.

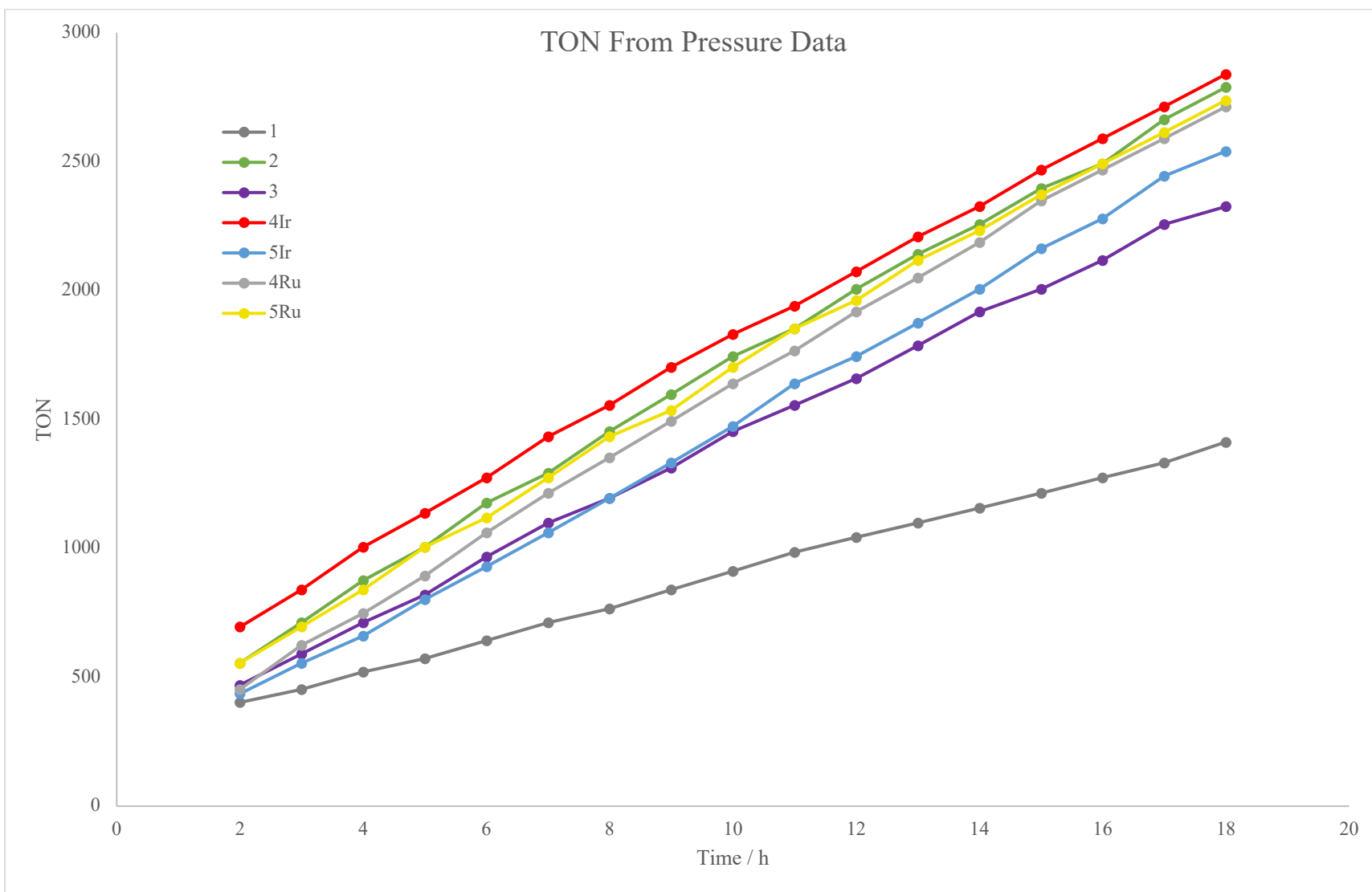
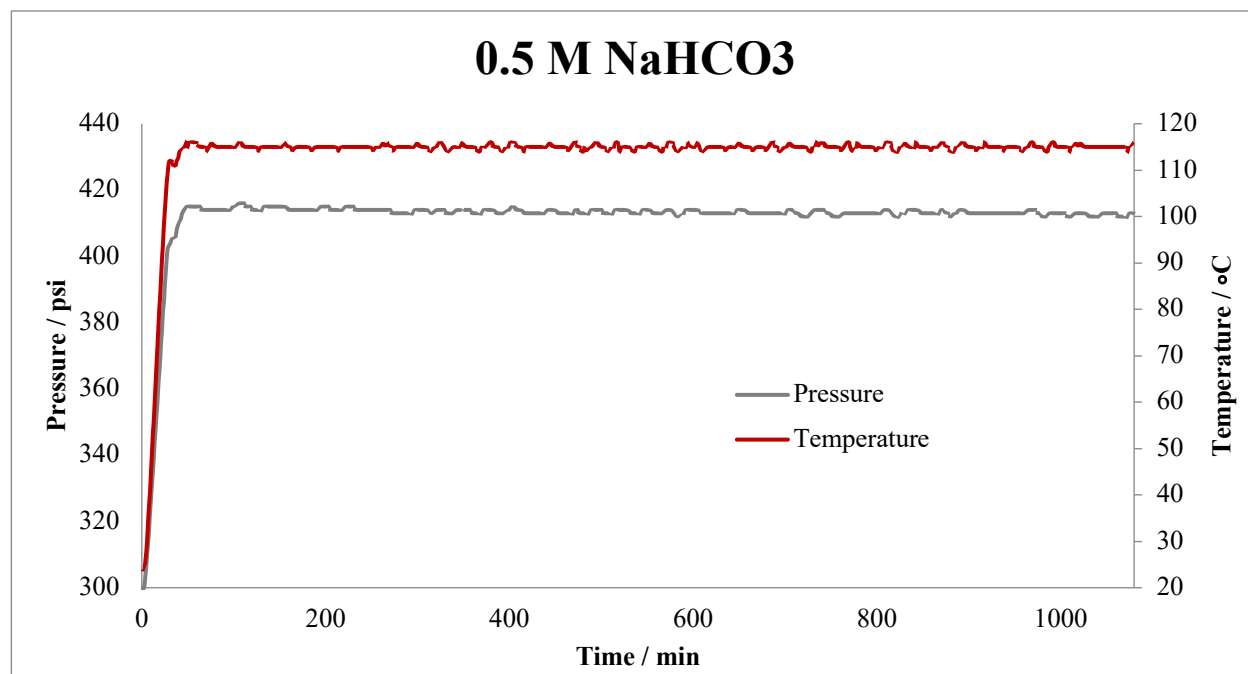


Figure 4.S26. Overlaid plots of the pressure-estimated TON vs time for **1-5**.

Catalyst	Experimental	From Pressure Data	
	TON <sup>a</sup>	TON <sup>b</sup>	% Diff. <sup>c</sup>
<b>1</b>	1090	1412	30%
<b>2</b>	910	2788	206%
<b>3</b>	2020	2325	15%
<b>4<sub>Ir</sub></b>	2270	2839	25%
<b>5<sub>Ir</sub></b>	410	2540	520%
<b>4<sub>Ru</sub></b>	1070	2713	154%
<b>5<sub>Ru</sub></b>	890	2738	208%

*Table 4.S18.* The experimental TON and pressure-estimated TON at 18 h for **1-5**. <sup>a</sup>Experimental TON calculated from NMR of reaction mixture after 18 h with an internal standard, as calculated in the manuscript. <sup>b</sup>TON calculated from the pressure data after 18 h. <sup>c</sup>Percent difference between the experimentally determined TON and the TON calculated from the pressure data. We note that the method of determining TON from formate concentration by <sup>1</sup>H-NMR (2<sup>nd</sup> column) is much more accurate than the method of using pressure changes (3<sup>rd</sup> column). We suspect that the pressure reading is not sensitive enough.



*Figure 4.S27.* Plot of pressure (crimson) and temperature (grey) vs reaction time for CO<sub>2</sub> hydrogenation reaction with **4<sub>Ir</sub>** in 0.5 M NaHCO<sub>3</sub>. The reaction conditions are the same as the standard conditions reported in the manuscript, except with 0.5 M NaHCO<sub>3</sub> (aq) instead of 1 M NaHCO<sub>3</sub> (aq).

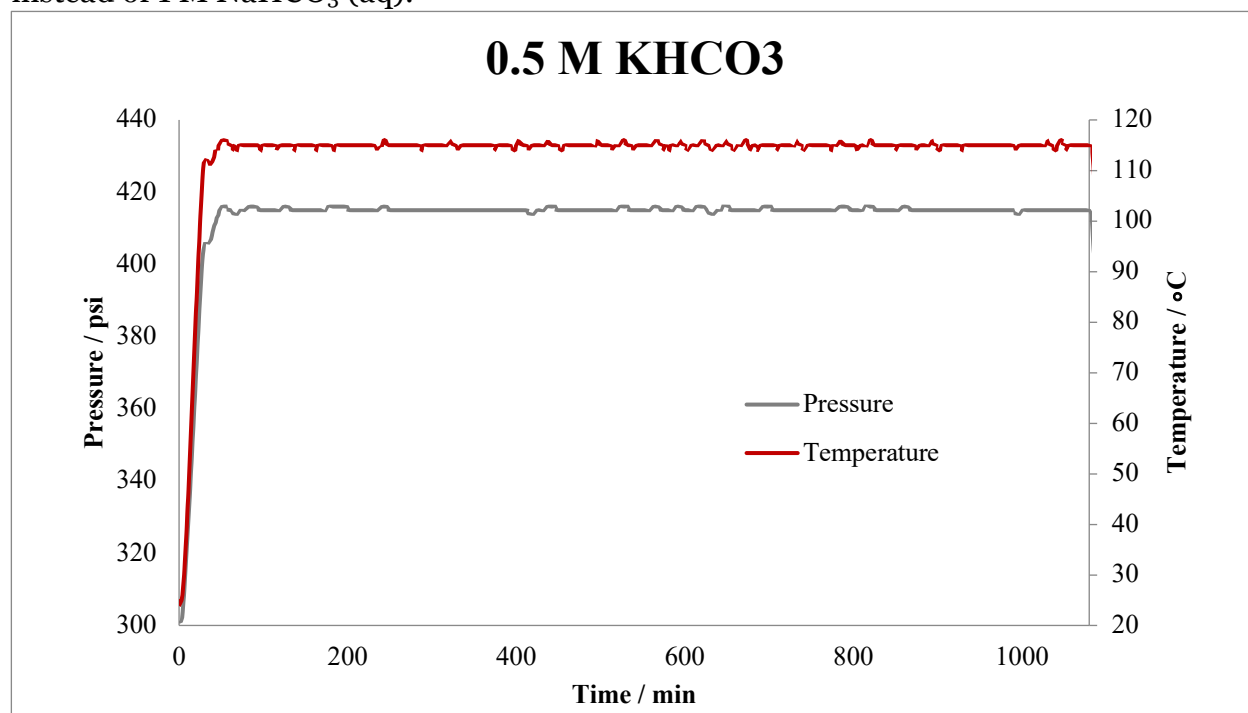


*Figure 4.S28.* Plot of pressure (crimson) and temperature (grey) vs reaction time for CO<sub>2</sub> hydrogenation reaction with **4<sub>Ir</sub>** in 0.5 M KHCO<sub>3</sub>. The reaction conditions are the same as the standard conditions reported in the manuscript, except with 0.5 M KHCO<sub>3</sub> (aq) instead of 1 M NaHCO<sub>3</sub> (aq).

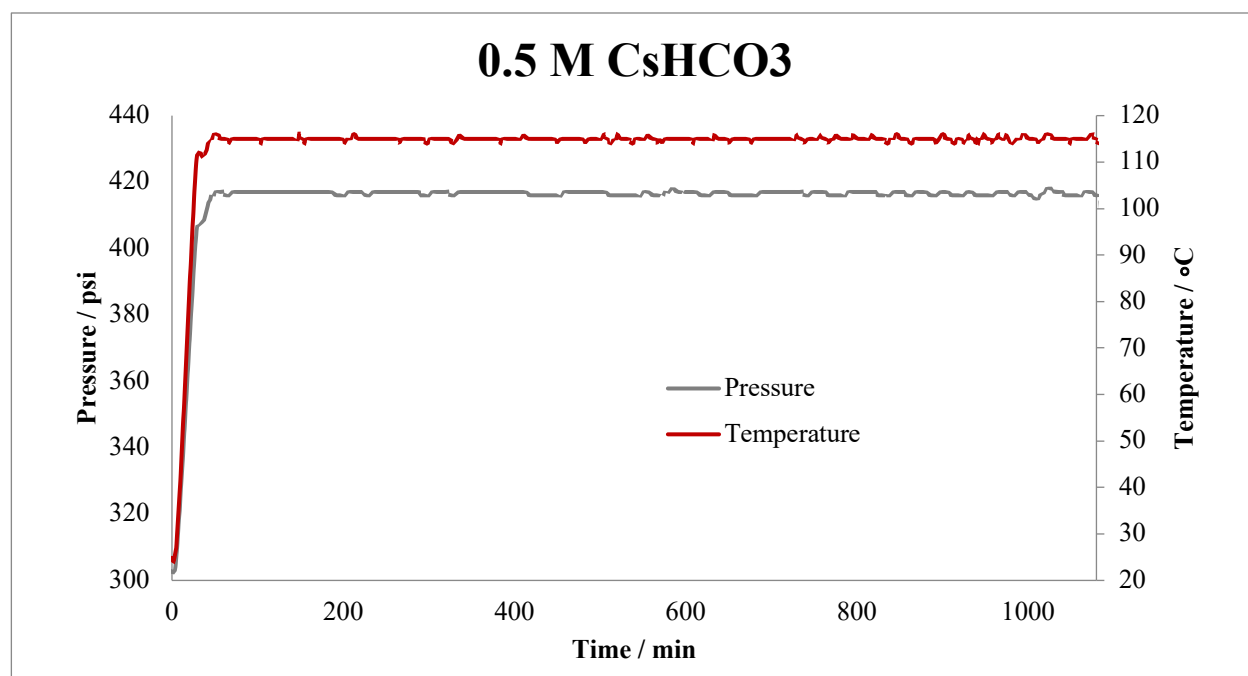


*Figure 4.S29.* Plot of pressure (crimson) and temperature (grey) vs reaction time for CO<sub>2</sub> hydrogenation reaction with **4<sub>Ir</sub>** in 0.5 M CsHCO<sub>3</sub>. The reaction conditions are the same as the standard conditions reported in the manuscript, except with 0.5 M CsHCO<sub>3</sub> (aq) instead of 1 M NaHCO<sub>3</sub> (aq).

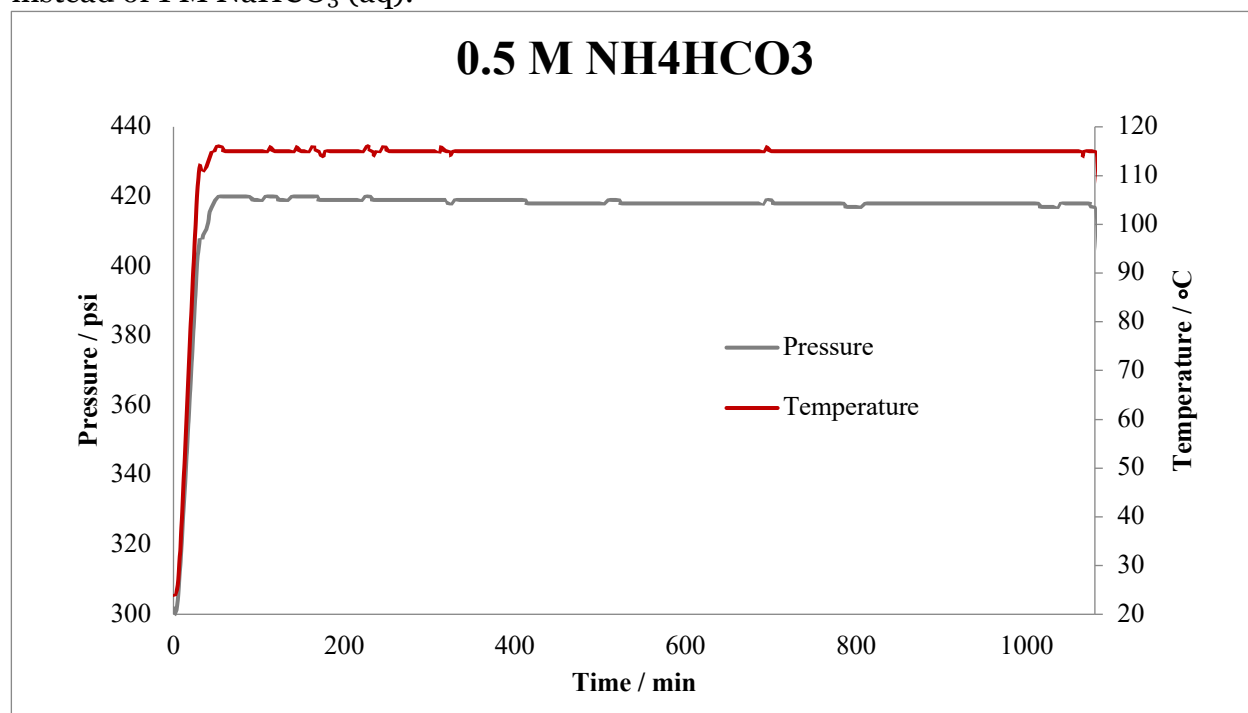


*Figure 4.S30.* Plot of pressure (crimson) and temperature (grey) vs reaction time for CO<sub>2</sub> hydrogenation reaction with **4<sub>Ir</sub>** in 0.5 M NH<sub>4</sub>HCO<sub>3</sub>. The reaction conditions are the same as the standard conditions reported in the manuscript, except with 0.5 M NH<sub>4</sub>HCO<sub>3</sub> (aq) instead of 1 M NaHCO<sub>3</sub> (aq).

CHAPTER 5:  
RUTHENIUM(II) AND IRIDIUM(III) COMPLEXES OF N-HETEROCYCLIC CARBENE  
AND PYRIDINOL DERIVED BIDENTATE CHELATES: SYNTHESIS,  
CHARACTERIZATION, AND REACTIVITY

Adapted from Gerlach, D. L.; Siek, S.; Burks, D. B.; Tesh, J. M.; Thompson, C. R.; Vasquez, R. M.; White, N. J.; Zeller, M.; Grotjahn, D. B.; Papish, E. T. *Inorganica Chimica Acta*, 2017, 466, 442-450.

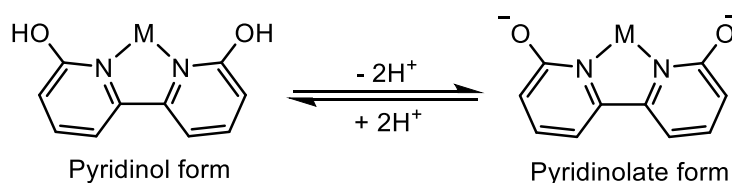
## 5.1 INTRODUCTION

Ruthenium complexes have been instrumental in advancing many fields including medicine and catalysis. Ruthenium is used in medicinal research because many ruthenium complexes are cytotoxic and have anti-proliferative properties. Ruthenium complexes can bind to iron transporters (which are up-regulated in cancer cells) to enhance drug uptake.<sup>1</sup> Thus far, three ruthenium complexes have entered clinical trials and some ruthenium complexes are cytotoxic towards cisplatin resistant cell lines.<sup>2-7</sup> Ruthenium complexes are also known for light harvesting properties. O'Regan and Grätzel pioneered the use of ruthenium complexes as photosensitizers in dye-sensitized solar cells,<sup>8</sup> and Ru-based sensitizers have also been used for artificial photosynthesis, as luminescent molecular probes, as photo responsive molecular devices, and for photocatalysis.<sup>9-17</sup> Furthermore, ruthenium complexes also figure prominently as catalysts for

(de)hydrogenation reactions<sup>18-19</sup> and other types of catalysis (e.g. metathesis).<sup>20-22</sup>

Among hydrogenation reactions, CO<sub>2</sub> is a challenging substrate to activate. Nonetheless, several groups worldwide have achieved CO<sub>2</sub> hydrogenation and the reverse reaction, formic acid dehydrogenation, using transition metals (e.g. Ir, Ru, Fe and others) ligated by N-heterocyclic carbene (NHC) ligands,<sup>23</sup> pyridinol-derived ligands,<sup>24-27</sup> and other ligands.<sup>28-35</sup>

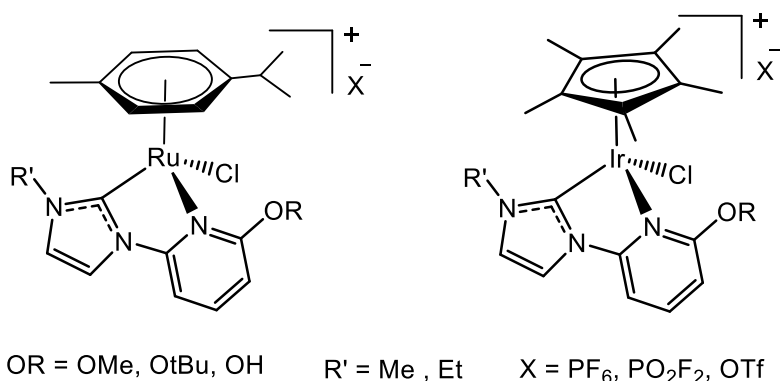
The Papish group and others have previously studied the ligand 6,6'-dihydroxybipyridine (6,6'-dhbp) (Scheme 1) because of its unique advantages. Dhbp is a proton responsive ligand: upon deprotonation of hydroxyl group the electron-donating ability of the ligand is increased. Other pyridinol derived monodentate and chelating ligands have similar proton responsive properties and can form metal-ligand bifunctional catalysts.<sup>36-43</sup> Importantly, the catalytic activity of dhbp metal complexes can be tuned with changes in pH.<sup>44-45</sup> Frequently, the deprotonated metal complexes of 6,6'-dhbp have an enhanced ability to catalyze various reactions including transfer hydrogenation and water oxidation.<sup>44, 46</sup> Ruthenium complexes of 6,6'-dhbp can allow for cancer selective cytotoxicity by low pH triggered photo-dissociation in acidic regions of cancer cells.<sup>47</sup> Thus, in some cases, 6,6'-dhbp ligand can be labile especially when bound to a first row transition metal (e.g. Cu) and under very acidic or basic conditions.<sup>48</sup>



*Scheme 5.1.* Acid-base equilibrium of 6, 6'-dihydroxy-2, 2'-bipyridine (6, 6'-dhbp) complexes.

Likewise, N-heterocyclic carbenes (NHC) are a well-known ligand class that has been used to create many successful homogenous catalysts.<sup>49-54</sup> The stability of the NHC ligand derives from it being a strong  $\sigma$ -donor that can generate a robust M-C bond. Through synthesis, NHCs are readily modified to tune the steric and electronic properties of the ligands.<sup>55-58</sup> Previously, the Papish group designed catalysts containing NHC ligands which catalyzed transfer hydrogenation reactions.<sup>59-60</sup>

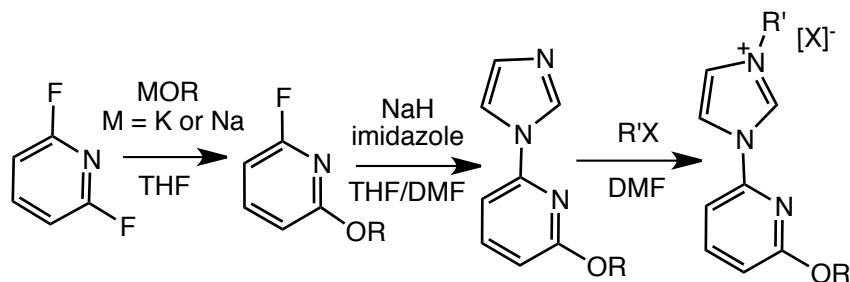
Many ruthenium complexes for the above applications have included pyridine or N-heterocyclic carbene ligands (NHCs). Also, some bidentate and tridentate ligands have combined NHC and pyridine rings on one scaffold.<sup>61-75</sup> However, prior to our recent work, no ligands have combined NHC and pyridinol rings in a chelate.<sup>27</sup> By combining an NHC ring with a pyridinol ring, we would introduce a new ligand class that would combine the strong donor properties of the NHC moiety with the proton responsive pyridinol moiety. Recently, our group has reported new NHC-py<sup>OR</sup> ligands and Ir complexes thereof which serve as pre-catalysts for CO<sub>2</sub> hydrogenation and formic acid dehydrogenation.<sup>27</sup> Here, the synthesis and characterization of the Ru (**8-13**) and Ir (**14-15**) analogues supported by (NHC<sup>R'</sup>-py<sup>OR</sup>) ligands (OR = OMe, OtBu, OH; R' = Me, Et) with different counter anions, (PF<sub>6</sub>)<sup>-</sup> and (OTf)<sup>-</sup>, are reported. The reactivity of these Ru complexes is also briefly described.



Scheme 5.2. General structure of complexes **8-15**.

## 5.2 RESULTS AND DISCUSSION

All syntheses were performed by Deidra Gerlach (DLG), Sophie Siek (SS), Robert Vasquez (RMV), and Nicholas White (NJW). The N-heterocyclic carbene and pyridinol derived ligand precursors ( $\text{Im}^{\text{R}'}\text{-py}^{\text{OR}}\text{X}$ ) (Table 5.1, **1-4**) were readily synthesized by displacement of one *ortho*-fluorine from 2,6-difluoropyridine with NaOR followed by the substitution of the second *ortho*-fluorine with imidazole from sodium imidazolate.<sup>76</sup> The alkylation of the ( $\text{Im-py}^{\text{OR}}$ ) compound with  $\text{CH}_3\text{I}$ ,  $\text{CH}_3\text{OTf}$ , or  $\text{CH}_3\text{CH}_2\text{Br}$  resulted in the formation of imidazolium salts ( $\text{Im}^{\text{R}'}\text{-py}^{\text{OR}}\text{X}$ ), that differ in the R' and OR groups on the imidazole and pyridine ring, respectively, where R' = Me, Et and OR = O<sup>t</sup>Bu, OMe (Table 5.1). Variation in the counter anion gave four compounds: ( $\text{Im}^{\text{Me}}\text{-py}^{\text{OtBu}}\text{I}$ ) (**1**), ( $\text{Im}^{\text{Me}}\text{-py}^{\text{OtBu}}\text{PF}_6$ ) (**2**), ( $\text{Im}^{\text{Et}}\text{-py}^{\text{OMe}}\text{Br}$ ) (**3**), and ( $\text{Im}^{\text{Me}}\text{-py}^{\text{OtBu}}\text{OTf}$ ) (**4**) (Table 5.1). The purpose of the <sup>t</sup>Bu ether moiety was to serve as a protected form for obtaining the OH derivative in the metal complexes. Counter anion exchange was achieved readily by stirring the halide salt (**1**) in  $\text{NH}_4\text{PF}_6$  or  $\text{KPF}_6$  solution to form **2** (Scheme 3), by modifying literature procedures.<sup>61</sup>



Scheme 5.3. The synthesis the imidazolium salts (**1-4**), ( $\text{Im}^{\text{R}'}\text{-py}^{\text{OR}}$ ). OR = <sup>t</sup>Bu, Me; R' = Me, Et; [X]<sup>-</sup> = [I]<sup>-</sup>, [Br]<sup>-</sup>, [OTf]<sup>-</sup>, [PF<sub>6</sub>]<sup>-</sup>. The first two steps were reported previously.<sup>27</sup>

Compound	Formula
<b>1</b>	(Im <sup>Me</sup> -py <sup>OtBu</sup> )I
<b>2</b>	(Im <sup>Me</sup> -py <sup>OtBu</sup> )PF <sub>6</sub>
<b>3</b>	(Im <sup>Et</sup> -py <sup>OMe</sup> )Br
<b>4<sup>a</sup></b>	(Im <sup>Me</sup> -py <sup>OtBu</sup> )OTf
<b>5</b>	[Ag(NHC <sup>Me</sup> -py <sup>OtBu</sup> ) <sub>2</sub> ]PF <sub>6</sub>
<b>6<sup>a</sup></b>	[Ag(NHC <sup>Me</sup> -py <sup>OtBu</sup> ) <sub>2</sub> ]OTf
<b>7<sup>a</sup></b>	[Ag(NHC <sup>Me</sup> -py <sup>OMe</sup> ) <sub>2</sub> ]OTf
<b>8</b>	[(p-cym)Ru(NHC <sup>Me</sup> -py <sup>OMe</sup> )Cl]OTf
<b>9</b>	[(p-cym)Ru(NHC <sup>Me</sup> -py <sup>OtBu</sup> )Cl]OTf
<b>10</b>	[(p-cym)Ru(NHC <sup>Me</sup> -py <sup>OH</sup> )Cl]OTf
<b>11</b>	[(p-cym)Ru(NHC <sup>Me</sup> -py <sup>OtBu</sup> )Cl]PF <sub>6</sub>
<b>12</b>	[(p-cym)Ru(NHC <sup>Et</sup> -py <sup>OMe</sup> )Cl]PF <sub>6</sub>
<b>13</b>	[(p-cym)Ru(NHC <sup>Me</sup> -py <sup>OH</sup> )Cl]PO <sub>2</sub> F <sub>2</sub>
<b>14</b>	[Cp*Ir(NHC <sup>Me</sup> -py <sup>OtBu</sup> )Cl]PF <sub>6</sub>
<b>15</b>	[Cp*Ir(NHC <sup>Me</sup> -py <sup>OH</sup> )Cl]PO <sub>2</sub> F <sub>2</sub>

Table 5.1. Numbering scheme for the compounds studied here. <sup>a</sup>These compounds (**4**, **6**, **7**) were reported in previous work.<sup>27</sup>

The synthesis of NHC<sup>R'</sup>-py<sup>OR</sup> metal complexes **5-15** is shown in Scheme 4. The imidazolium C2 position is readily deprotonated to generate an NHC. Upon treatment of the ligand precursors **2** and **4** with Ag<sub>2</sub>O and NaOH in the absence of light, silver bis(carbene) complexes were formed as [Ag(NHC<sup>Me</sup>-py<sup>OtBu</sup>)<sub>2</sub>]PF<sub>6</sub> (**5**) and [Ag(NHC<sup>Me</sup>-py<sup>OtBu</sup>)<sub>2</sub>]OTf (**6**), respectively. [Ag(NHC<sup>Me</sup>-py<sup>OMe</sup>)<sub>2</sub>]OTf (**7**) was made similarly, as reported previously.<sup>27</sup>

Transmetallation of the silver bis(carbene) complex **5**, **6**, and **7** with the chloro-bridged dimeric ruthenium precursors [(p-cym)RuCl<sub>2</sub>]<sub>2</sub> and one equivalent of AgX afforded the chelate complexes [(p-cym)Ru(NHC<sup>Me</sup>-py<sup>OMe</sup>)Cl]OTf (**8**), [(p-

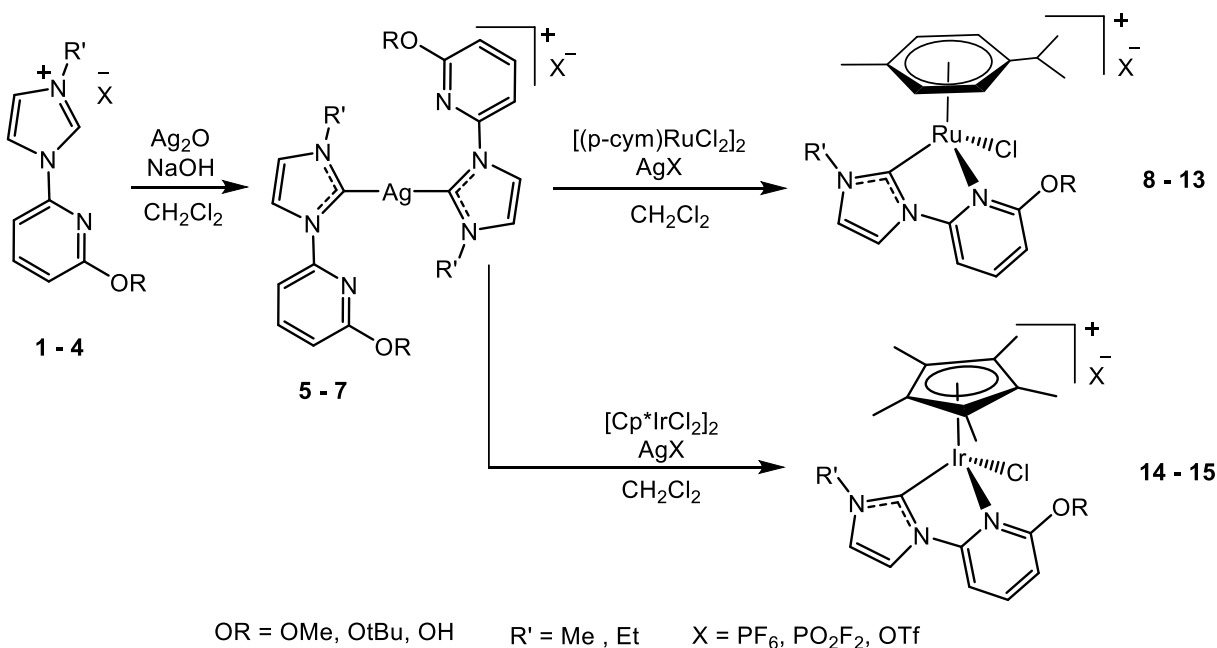
cym)Ru(NHC<sup>Me</sup>-py<sup>OtBu</sup>)Cl]OTf (**9**), and [(*p*-cym)Ru(NHC<sup>Me</sup>-py<sup>OtBu</sup>)Cl]PF<sub>6</sub> (**11**) by use of X = [OTf]<sup>-</sup> or [PF<sub>6</sub>]<sup>-</sup> as appropriate. The complex [(*p*-cym)Ru(NHC<sup>Et</sup>-py<sup>OMe</sup>)Cl]PF<sub>6</sub> (**12**) was made similarly from **3**, but in this case the silver carbene complex was not isolated. The <sup>t</sup>Bu ether deprotection of **9** to form [(*p*-cym)Ru(NHC<sup>Me</sup>-py<sup>OH</sup>)Cl]OTf (**10**) was achieved by superheating a CH<sub>2</sub>Cl<sub>2</sub> solution or reflux of a CH<sub>3</sub>CN solution. The driving force for the deprotection reaction is elimination of isobutene. Finally, for the Ir species, [Cp\*IrCl<sub>2</sub>]<sub>2</sub> was used as our iridium source to obtain [Cp\*Ir(NHC<sup>Me</sup>-py<sup>OtBu</sup>)Cl]PF<sub>6</sub> (**14**).

However, attempts to deprotect complex **11** by a similar procedure led to the isolation of [(*p*-cym)Ru(NHC<sup>Me</sup>-py<sup>OH</sup>)Cl]PO<sub>2</sub>F<sub>2</sub> (**13**). The formation of [PO<sub>2</sub>F<sub>2</sub>]<sup>-</sup> counter anion appears to be due to the hydrolysis of the [PF<sub>6</sub>]<sup>-</sup> anion using adventitious water or the *in situ* formed OH group as a proton source (eq. 1). The hydrolysis of PF<sub>6</sub> was also observed when **14** was de-protected to form [Cp\*Ir(NHC<sup>Me</sup>-py<sup>OH</sup>)Cl]PO<sub>2</sub>F<sub>2</sub> (**15**). For several of these complexes, the hydrolysis of PF<sub>6</sub><sup>-</sup> leads to the appearance of multiple peaks in the <sup>19</sup>F NMR. It is plausible that these peaks represent PO<sub>2</sub>F<sub>2</sub><sup>-</sup> and species on the way to this product.



The literature shows that [PF<sub>6</sub>]<sup>-</sup> can be thermally decomposed to PF<sub>5</sub> and F<sup>-</sup>, and PF<sub>5</sub> can be further transformed to O=PF<sub>3</sub> in the presence of water.<sup>77-79</sup> In our case, it appears that the O=PF<sub>3</sub> was formed *in situ* and reacted further with water to form [PO<sub>2</sub>F<sub>2</sub>]<sup>-</sup> and HF. Others have observed similar reactions.<sup>80-84</sup> While the HF formed in this reaction was not characterized, the glassware appeared to etch after running these

reactions. Due to the hydrolysis of the  $[\text{PF}_6]^-$  anion, the  $[\text{OTf}]^-$  salts were used for reactivity studies.



*Scheme 5.4.* The synthesis of NHC-py<sup>OR</sup> metal complexes **5-15**.

Crystals of these complexes were grown by DLG, SS, and NJW, data sets were collected by DLG and Matthias Zeller (MZ), and structures were solved and refined by DLG (**14-15**), MZ (**10**), and myself (**8-9**, **11-12**). The crystal structures of the complexes **8-12** and **14-15** are shown as molecular diagrams in Figures 5.1, 5.2, and 5.3 with bond lengths and angles in Table 5.2. All of the Ru and Ir complexes were crystallized except for  $[(p\text{-cym})\text{Ru}(\text{NHC}^{\text{Me}}\text{-py}^{\text{OH}})\text{Cl}]\text{PO}_2\text{F}_2$  (**13**). Crystals suitable for X-ray diffraction were typically obtained by layering a solution of dichloromethane with ether. All of the Ru-complexes **8-12** display piano stool structures with the cymene ligand  $\eta^6$  coordinated to the Ru(II) center. The Ru-C<sub>carbene</sub>, Ru-N, and Ru-Cl bond distances are all quite similar to each other and to similar complexes in the literature.<sup>85-90</sup> The C-Ru-N bite angles are all similar and range from  $76.0(1)^\circ$  to  $76.5(1)^\circ$ .

Both complexes **14** and **15** feature a half sandwich structure with the Cp\* ligand  $\eta^5$  coordinated to the Ir(III) metal center. The bond lengths and angles of these complexes are similar to each other (Table 5.2) and to other Ir(III) complexes.<sup>27</sup> The average M-C<sub>carbene</sub> distance is shorter than the M-N bond (despite N (75 pm) having a smaller covalent radius than C (77 pm)) for all of the complexes (**8-15**) due to the strong  $\sigma$  donating and moderate  $\pi$  accepting properties of the NHC ligand.<sup>91</sup>

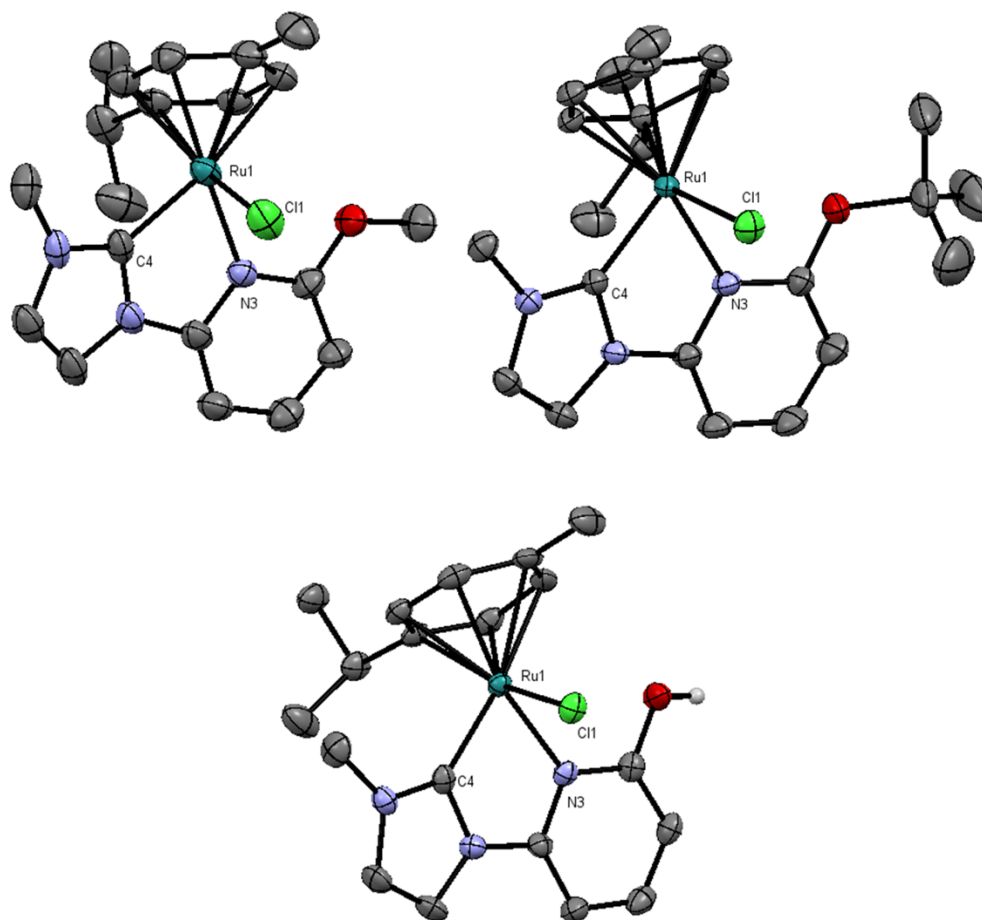


*Figure 5.1.* The ORTEP diagrams with 50% probability ellipsoids of [(*p*-cym)Ru(NHC<sup>Me</sup>-py<sup>OMe</sup>)Cl]OTf **8** (top left), [(*p*-cym)Ru(NHC<sup>Me</sup>-py<sup>OTBu</sup>)Cl]OTf **9** (top right), and [(*p*-cym)Ru(NHC<sup>Me</sup>-py<sup>OH</sup>)Cl]OTf **10** (bottom). Hydrogen atoms (except for the H of the OH group in **10**) and counter anions are omitted for clarity. Atom color codes are carbon (gray) and oxygen (red). These structures are oriented such that the chloride is forward from the plane of the bidentate ligand. Structural parameters are included in the

Supporting Information. Complexes **8** and **10** are disordered with regards to the position of NHC and pyridine rings, and that disorder is omitted here for clarity.

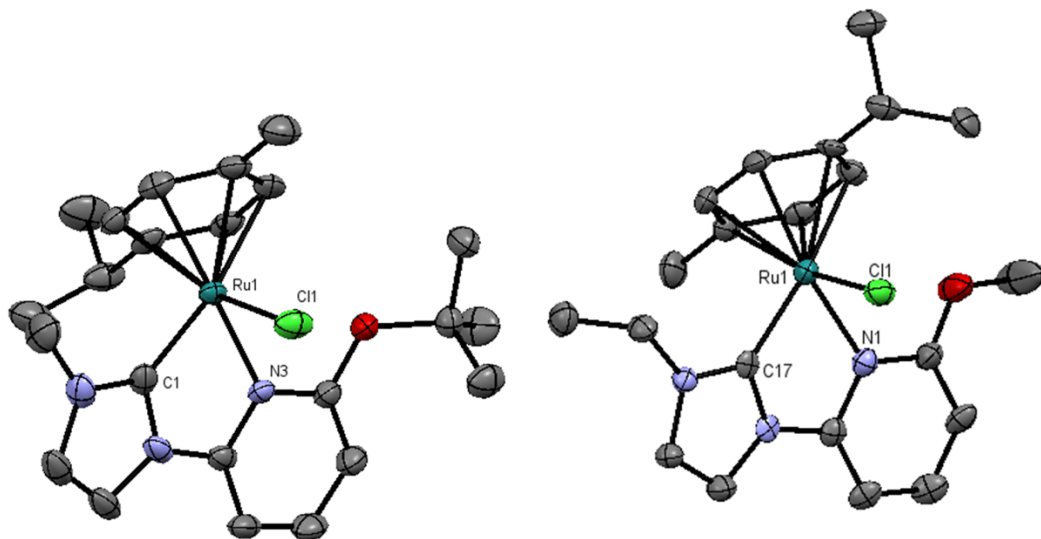


*Figure 5.2.* The ORTEP diagrams with 50% probability ellipsoids of [(*p*-cym)Ru(NHC<sup>Me</sup>-py<sup>OtBu</sup>)Cl]PF<sub>6</sub> **11** (left) and [(*p*-cym)Ru(NHC<sup>Et</sup>-py<sup>OMe</sup>)Cl]PF<sub>6</sub> **12** (right). Hydrogen atoms and counter anions are omitted for clarity. Atom color codes are carbon (gray) and oxygen (red). These structures are oriented such that the chloride is forward from the plane of the bidentate ligand. Structural parameters are included in the Supporting Information. Complex **12** is disordered with regards to the position of the NHC and pyridine rings, and that disorder is omitted here for clarity.

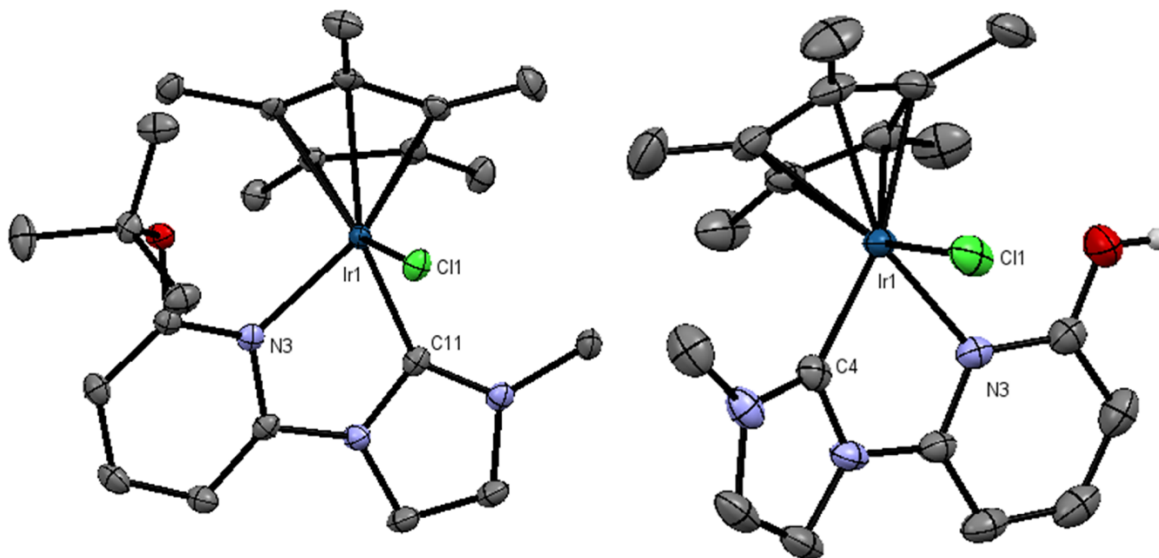


*Figure 5.3.* The ORTEP diagrams with 50% probability ellipsoid of [Cp\*Ir(NHC<sup>Me</sup>-py<sup>OtBu</sup>)Cl]PF<sub>6</sub> **14** (top) and [Cp\*Ir(NHC<sup>Me</sup>-py<sup>OH</sup>)Cl]PO<sub>2</sub>F<sub>2</sub> **15** (bottom). Hydrogen atoms (except for the H of the OH group in **15**) and counter anions are omitted for clarity. Atom color codes are carbon (gray) and oxygen (red). These structures are oriented such

that the chloride is forward from the plane of the bidentate ligand. Structural parameters are included in the Supporting Information.

*Table 5.2.* Selected bond lengths and angles of the complexes **8-15**.

Compound <sup>a</sup>	Bite Angle (°)	Bond Length (Å)		
		Ru-Cl	Ru-N	Ru-C <sub>carbene</sub>
<b>8</b> <sup>b</sup>	76.3(2)	2.398(1)	2.102(4)	2.049(5)
<b>9</b>	76.5(1)	2.407(1)	2.135(1)	2.013(1)
<b>10</b> <sup>c</sup>	76.2(2)	2.402(1)	2.137(4)	2.015(5)
<b>11</b>	76.2(1)	2.404(1)	2.130(3)	2.019(4)
<b>12</b> <sup>d</sup>	76.0(1)	2.415(2)	2.09(2)	2.09(2)
	<b>Avg = 76.2(1)</b>	<b>Avg = 2.405(1)</b>	<b>Avg = 2.119(5)</b>	<b>Avg = 2.037(5)</b>
		Ir-Cl	Ir-N	Ir-C <sub>carbene</sub>
<b>14</b>	76.5(1)	2.409(1)	2.149(3)	2.008(4)
<b>15</b>	75.7(1)	2.408(1)	2.116(2)	2.017(2)
	<b>Avg = 76.1(1)</b>	<b>Avg = 2.408(1)</b>	<b>Avg = 2.133(1)</b>	<b>Avg = 2.013(1)</b>

<sup>a</sup>Compound **8** contains two independent molecules in the unit cell and contains flip disorder of the bidentate ligand, which results in four moieties, A/C and B/D. Compound **10** contains two independent molecules in the unit cell, which results in two moieties, 1/2. Compound **12** contains flip disorder of the bidentate ligand, which results in two moieties, A/B. <sup>b</sup>Bite angle and bond distances are for moiety A. <sup>c</sup>Bite angle and bond distances are for moiety 1. <sup>d</sup>Bite angle and bond distances are for moiety A.

Ruthenium complexes are known to catalyze many reactions including hydrogenation and dehydrogenation.<sup>92-93</sup> We were interested in exploring the reactivity of these ruthenium complexes towards the hydrogenation of CO<sub>2</sub> and the dehydrogenation of formic acid. Complexes **8** and **9** were chosen to study as pre-catalysts because the triflate counter anion is stable and does not undergo unwanted transformations.

CO<sub>2</sub> hydrogenation studies were performed by myself. CO<sub>2</sub> hydrogenation was studied by dissolving the pre-catalysts **8** or **9** (at 0.3mM) in 1.0 M aqueous NaHCO<sub>3</sub> and then pressurizing the vessel with 300 psi of 1:1 CO<sub>2</sub>:H<sub>2</sub> for 18 h at 115 °C. The literature has shown that both CO<sub>2</sub> and NaHCO<sub>3</sub> serve as substrates in this reaction, and removal

of either component decreases the turnover numbers in our experience.<sup>27, 94-96</sup> Indeed, upon dissolving in aqueous solution, carbon dioxide forms  $\text{CO}_3^{2-}$  and  $\text{HCO}_3^-$  as aqueous ions. Sodium bicarbonate also serves as a base to raise the pH of the solution to around 8.5, which enhances the thermodynamic driving force for  $\text{CO}_2$  hydrogenation because the product formed is formate rather than formic acid.<sup>43</sup> The extent of sodium formate production was measured by  $^1\text{H}$  NMR spectroscopy with an internal standard. This allowed for the turnover number (TON) and turnover frequency (TOF) to be calculated (Table 5.3).

Formic acid dehydrogenation studies were performed by SS, Jamie Tesh (JMT), and Courtney Thompson (CRT). For formic acid dehydrogenation, the reaction was performed by heating an aqueous solution of 1.02 M formic acid and 0.29 mM of the pre-catalyst **8** or **9** at 60°C for 3 h. The extent of reaction was determined by measuring the gas collected and using the van der Waals equation to determine TON and TOF by assuming that the products formed are 1:1  $\text{CO}_2$  and  $\text{H}_2$  (Table 5.3).

The order of reactivity for both reactions is that complex **8** is more active than **9**. Both complexes are best considered pre-catalysts as there were significant color changes and a small amount of brown precipitate observed at the end of the reaction. This observation indicates changes that may involve de-coordination of the cymene ligand from the complex.<sup>60, 97-98</sup> Furthermore, recent work has shown that iridium NHC-py<sup>OR</sup> complexes are prone to cyclometallation reactions, and similar transformations may occur here as well.<sup>27</sup> The transformations seen for complexes **8** and **9**, as well as iridium NHC-py<sup>OR</sup> complexes,<sup>27</sup> dissuaded us from undertaking a full study of all the new metal complexes reported herein. Nonetheless, the ligand system NHC-py<sup>OR</sup> may be more promising with a metal less prone to cyclometallation and other side reactions.

Table 5.3. Catalytic CO<sub>2</sub> hydrogenation and FA dehydrogenation of complex **8** and **9**.<sup>a</sup>

Catalyst	Hydrogenation <sup>b</sup>		Dehydrogenation <sup>c</sup>	
	TON	TOF (h <sup>-1</sup> )	TON	TOF (h <sup>-1</sup> )
<b>8</b>	1440 (69)	80	180 (76)	60
<b>9</b>	240 (36)	13	79 (69)	26

<sup>a</sup>All TON were calculated after 18 h for CO<sub>2</sub> hydrogenation and 3 h for FA dehydrogenation and are an average of at least 2 trials. <sup>b</sup>Reaction conditions for hydrogenation: the reaction was performed in 25 mL of an aqueous solution of 0.3 mM pre-catalyst and 1 M NaHCO<sub>3</sub> at 115 °C and 300 psi of H<sub>2</sub>/CO<sub>2</sub> (1:1). <sup>c</sup>Reaction conditions for dehydrogenation: 25 mL of an aqueous solution of formic acid (1.02 M) and pre-catalyst (0.29 mM) was heated at 60 °C.

### 5.3 CONCLUSION

In summary, new NHC<sup>R'</sup>-py<sup>OR</sup> complexes of Ru(II) and Ir(III) with various substituents on the pyridine and NHC rings and two different counter anions, [OTf]<sup>-</sup> and [PF<sub>6</sub>]<sup>-</sup>, were synthesized. [(*p*-cym)Ru(NHC<sup>R'</sup>-py<sup>OR</sup>)Cl]<sup>+</sup> (**8-13**) and [Cp\*Ir(NHC<sup>Me</sup>-py<sup>OR</sup>)Cl]<sup>+</sup> (**14-15**) were synthesized in good yields by transmetallation of the bidentate ligand from [Ag(NHC<sup>Me</sup>-py<sup>OR</sup>)<sub>2</sub>]<sup>+</sup> at room temperature. The deprotection reaction of the *t*-butoxy group to form the hydroxy group shows that the [PF<sub>6</sub>]<sup>-</sup> is unstable under the reaction conditions. The formation of [PO<sub>2</sub>F<sub>2</sub>]<sup>-</sup> is most likely due to the hydrolysis of [PF<sub>6</sub>]<sup>-</sup> by adventitious moisture. A preliminary catalytic reactivity screening indicates that the ruthenium complexes **8** and **9** undergo further transformations when heated. Ruthenium catalysts derived from NHC<sup>R'</sup>-py<sup>OR</sup> appear to be less robust than dhbp complexes.<sup>27</sup>

### 5.4 EXPERIMENTAL

#### 5.4.1 General Procedures

All ligand and metal complex were synthesized under nitrogen atmosphere in a glove box or by utilizing standard Schlenk line techniques with oven dried glassware.  $^1\text{H}$ -,  $^{13}\text{C}$ - and  $^{19}\text{F}$ -NMR spectra were acquired at room temperature on a Bruker AV360 360 MHz or AV500 500 MHz spectrometers, or on Varian 400 or 500 MHz spectrometers, and referenced to the solvent. Mid-IR spectra were collected on a Bruker Alpha ATR-IR spectrometer. Mass spectrometric data were collected on a Waters AutoSpec-Ultima NT spectrometer with electron ionization method. Elemental analyses were performed by NuMega Resonance Labs, Inc., San Diego, CA. Electronic spectra were measured on a Perkin Elmer Lambda 35 UV-visible spectrometer. Pressurized gas reactions were performed in a Parr reaction vessel.

#### 5.4.2 Materials

Dry solvents were obtained via the Glass Contour Solvent System built by Pure Process Technology, LLC. All reagents were used as purchased and degassed under vacuum as needed. The compounds NHC-Py<sup>OR</sup> (R = Me, tBu), [Im<sup>Me</sup>-Py<sup>OtBu</sup>]OTf (**4**), [Ag(NHC<sup>Me</sup>-py<sup>OtBu</sup>)<sub>2</sub>]OTf (**6**), and [Ag(NHC<sup>Me</sup>-py<sup>OMe</sup>)<sub>2</sub>]OTf (**7**) were prepared according to previously published procedures.<sup>27</sup> High purity grade (> 97%) formic acid was used as purchased from AMRESCO, Inc. The compressed gases CO<sub>2</sub> and 50:50 vol CO<sub>2</sub>:H<sub>2</sub> were purchased from Airgas and used without further purification.

#### 5.4.3 Crystal Structures of Complexes **8-15**

Single crystals of complexes **8** – **12**, **14**, and **15** were mounted on a glass filament on a Bruker Apex2 CCD-based X-ray diffractometer<sup>99</sup> equipped with an Oxford N-Helix Cryosystem and a fine focus Mo-target X-ray tube ( $\lambda = 0.71073 \text{ \AA}$ ) operated at 2000 W

power (50 kV, 40 mA). X-ray intensities were measured at 173 K or 100 K with the detector placed at a distance of 6.000 cm from the crystal. The frames were integrated with the Saint<sup>100</sup> software package using a narrow-frame algorithm. Multi-scan absorption corrections were applied using SADABS.<sup>101</sup> The space groups were assigned using XPREP of the Bruker ShelXTL<sup>102</sup> software package. The structures were solved using ShelXT<sup>102</sup> and refined using SHelXL<sup>102</sup> and the graphical user interface ShelXle.<sup>103</sup> All non-hydrogen atoms were refined anisotropically. H atoms on carbon were positioned geometrically and constrained to ride on their parent atom. Additional crystallographic information is provided in the Supplemental Information section. Structures of complexes **8** – **12**, **14**, and **15** were deposited with the Cambridge Crystallographic Database and have reference numbers CCDC 1547999-1548003, 1548004, and 1548005, respectively.

## 5.5 Author Contribution

I performed catalytic testing of complexes **8** and **9** and solved and refined the crystal structures of complexes **8-9** and **11-12**. I was the intellectual lead for the crystallographic work and contributed to the writing of the paper resulting from this project.

## 5.6 REFERENCES

1. Allardyce, C. S.; Dyson, P. J. *Platinum Met. Rev.*, **2001**, *45*, 62-69.
2. Yan, Y. K.; Melchart, M.; Habtemariam, A.; Sadler, P. J. *Chem. Commun.*, **2005**, 4764-4776.
3. Galanski, M.; Arion, V. B.; Jakupec, M. A.; Keppler, B. K. *Curr. Pharm. Des.*, **2003**, *9*, 2078-2089.

4. Heidary, D. K.; Howerton, B. S.; Glazer, E. C. *J. Med. Chem.*, **2014**, *57*, 8936-8946.
5. Wachter, E.; Zamora, A.; Heidary, D. K.; Ruiz, J.; Glazer, E. C. *Chem. Commun.*, **2016**, *52*, 10121-10124.
6. Moucheron, C. *New J. Chem.*, **2009**, *33*, 235-245.
7. Caruso, F.; Rossi, M.; Benson, A.; Opazo, C.; Freedman, D.; Monti, E.; Gariboldi, M. B.; Shaulky, J.; Marchetti, F.; Pettinari, R.; Pettinari, C. *J. Med. Chem.*, **2012**, *55*, 1072-1081.
8. O'Regan, B.; Graetzel, M. *Nature (London)*, **1991**, *353*, 737-40.
9. Wu, W.; Ji, S.; Wu, W.; Shao, J.; Guo, H.; James, T. D.; Zhao, J. *Chem. - Eur. J.*, **2012**, *18*, 4953-4964, S4953/1-S4953/29.
10. Kalyanasundaram, K. *Coord. Chem. Rev.*, **1982**, *46*, 159-244.
11. Gill, M. R.; Garcia-Lara, J.; Foster, S. J.; Smythe, C.; Battaglia, G.; Thomas, J. A. *Nat. Chem.*, **2009**, *1*, 662-667.
12. Chen, W.; Rein, F. N.; Rocha, R. C. *Angew. Chem., Int. Ed.*, **2009**, *48*, 9672-9675, S9672/1-S9672/32.
13. Sun, L.; Burkitt, M.; Tamm, M.; Raymond, M. K.; Abrahamsson, M.; LeGourrierec, D.; Frapart, Y.; Magnuson, A.; Kenez, P. H.; Brandt, P.; Tran, A.; Hammarstroem, L.; Styring, S.; Aakermark, B. *J. Am. Chem. Soc.*, **1999**, *121*, 6834-6842.
14. Gu, J.; Chen, J.; Schmehl, R. H. *J. Am. Chem. Soc.*, **2010**, *132*, 7338-7346.
15. Manner, V. W.; Mayer, J. M. *J. Am. Chem. Soc.*, **2009**, *131*, 9874-9875.
16. Zhao, J.; Ji, S.; Wu, W.; Wu, W.; Guo, H.; Sun, J.; Sun, H.; Liu, Y.; Li, Q.; Huang, L. *RSC Adv.*, **2012**, *2*, 1712-1728.
17. Cao, K.; Lu, J.; Cui, J.; Shen, Y.; Chen, W.; Alemu, G.; Wang, Z.; Yuan, H.; Xu, J.; Wang, M.; Cheng, Y. *J. Mater. Chem. A*, **2014**, *2*, 4945-4953.
18. Himeda, Y.; Onozawa-Komatsuzaki, N.; Sugihara, H.; Arakawa, H.; Kasuga, K. *Organometallics*, **2004**, *23*, 1480-1483.
19. Noyori, R.; Hashiguchi, S. *Acc. Chem. Res.*, **1997**, *30*, 97-102.
20. Samojlowicz, C.; Bieniek, M.; Grela, K. *Chem. Rev.*, **2009**, *109*, 3708-3742.
21. Nguyen, S. T.; Johnson, L. K.; Grubbs, R. H.; Ziller, J. W. *J. Am. Chem. Soc.*, **1992**, *114*, 3974-5.

22. Grubbs, R. H. *Angew. Chem., Int. Ed.*, **2006**, *45*, 3760-3765.
23. Sanz, S.; Azua, A.; Peris, E. *Dalton Trans.*, **2010**, *39*, 6339.
24. Ertem, M. Z.; Himeda, Y.; Fujita, E.; Muckerman, J. T. *ACS Catal.*, **2016**, *6*, 600-609.
25. Hull, J. F.; Himeda, Y.; Wang, W.-H.; Hashiguchi, B.; Periana, R.; Szalda, D. J.; Muckerman, J. T.; Fujita, E. *Nature Chemistry*, **2012**, *4*, 383-388.
26. Wang, W.-H.; Hull, J. F.; Muckerman, J. T.; Fujita, E.; Himeda, Y. *Energy Environ. Sci.*, **2012**, *5*, 7923-7926.
27. Siek, S.; Burks, D. B.; Gerlach, D. L.; Liang, G.; Tesh, J. M.; Thompson, C. R.; Qu, F.; Shankwitz, J. E.; Vasquez, R. M.; Chambers, N. S.; Szulczewski, G. J.; Grotjahn, D. B.; Webster, C. E.; Papish, E. T. *Organometallics*, **2017**, *36*, 1091-1106.
28. Tanaka, R.; Yamashita, M.; Chung, L. W.; Morokuma, K.; Nozaki, K. *Organometallics*, **2011**, *30*, 6742-6750.
29. Tanaka, R.; Yamashita, M.; Nozaki, K. *J. Am. Chem. Soc.*, **2009**, *131*, 14168-14169.
30. Calaje, J. J. A.; Lu, Z.; Kedzie, E. A.; Terrile, N. J.; Lo, J. N.; Williams, T. J. *Nature Communications*, **2016**, 11308-11313.
31. Hu, P.; Diskin-Posner, Y.; Ben-David, Y.; Milstein, D. *ACS Catal.*, **2014**, *4*, 2649-2652.
32. Langer, R.; Diskin-Posner, Y.; Leitun, G.; Shimon, L. J. W.; Ben-David, Y.; Milstein, D. *Angew. Chem., Int. Ed.*, **2011**, *50*, 9948-9952.
33. Liu, Q.; Wu, L.; Güllak, S.; Rockstroh, N.; Jackstell, R.; Beller, M. *Angew. Chem. Int. Ed.*, **2014**, *53*, 7085-7088.
34. Alberico, E.; Sponholz, P.; Cordes, C.; Nielsen, M.; Drexler, H.-J.; Baumann, W.; Junge, H.; Beller, M. *Angew. Chem. Int. Ed.*, **2013**, *52*, 14162-14166.
35. Chakraborty, S.; Bhattacharya, P.; Dai, H.; Guan, H. *Acc. Chem. Res.*, **2015**, *48*, 1995-2003.
36. Royer, A. M.; Rauchfuss, T. B.; Gray, D. L. *Organometallics*, **2010**, *29*, 6763-6768.
37. Fujita, K.; Kawahara, R.; Aikawa, T.; Yamaguchi, R. *Angew. Chem., Int. Ed.*, **2015**, *54*, 9057-60.
38. Kawahara, R.; Fujita, K.-i.; Yamaguchi, R. *J. Am. Chem. Soc.*, **2012**, *134*, 3643-3646.
39. Fujita, K.-i.; Tanino, N.; Yamaguchi, R. *Org. Lett.*, **2007**, *9*, 109-111.

40. Moore, C. M.; Bark, B.; Szymczak, N. K. *ACS Catal.*, **2016**, *6*, 1981-1990.
41. Moore, C. M.; Quist, D. A.; Kampf, J. W.; Szymczak, N. K. *Inorg. Chem.*, **2014**, *53*, 3278-3280.
42. Moore, C. M.; Szymczak, N. K. *Chem. Commun.*, **2013**, *49*, 400-402.
43. Himeda, Y. *E. J. Inorg. Chem.*, **2007**, *2007*, 3927-3941.
44. Nieto, I.; Livings, M. S.; Sacci, J. B.; Reuther, L. E.; Zeller, M.; Papish, E. T. *Organometallics*, **2011**, *30*, 6339-6342.
45. Conifer, C. M.; Taylor, R. A.; Law, D. J.; Sunley, G. J.; White, A. J. P.; Britovsek, G. J. *P. Dalton Trans.*, **2011**, *40*, 1031-1033.
46. DePasquale, J.; Nieto, I.; Reuther, L. E.; Herbst-Gervasoni, C. J.; Paul, J. J.; Mochalin, V.; Zeller, M.; Thomas, C. M.; Addison, A. W.; Papish, E. T. *Inorg. Chem.*, **2013**, *52*, 9175-9183.
47. Hufziger, K. T.; Thowfeik, F. S.; Charboneau, D. J.; Nieto, I.; Dougherty, W. G.; Kassel, W. S.; Dudley, T. J.; Merino, E. J.; Papish, E. T.; Paul, J. J. *J. Inorg. Biochem.*, **2014**, *130*, 103-111.
48. Gerlach, D. L.; Bhagan, S.; Cruce, A. A.; Burks, D. B.; Nieto, I.; Truong, H. T.; Kelley, S. P.; Herbst-Gervasoni, C. J.; Jernigan, K. L.; Bowman, M. K.; Pan, S.; Zeller, M.; Papish, E. T. *Inorg. Chem.*, **2014**, *53*, 12689-12698.
49. Arduengo, A. J., III; Dias, H. V. R.; Harlow, R. L.; Kline, M. *J. Am. Chem. Soc.*, **1992**, *114*, 5530-4.
50. Arduengo, A. J., III; Harlow, R. L.; Kline, M. *J. Am. Chem. Soc.*, **1991**, *113*, 361-3.
51. Crudden, C. M.; Allen, D. P. *Coord. Chem. Rev.*, **2004**, *248*, 2247-2273.
52. Bielawski, C. W.; Grubbs, R. H. *Angew. Chem., Int. Ed.*, **2000**, *39*, 2903-2906.
53. Mizuhata, Y.; Sasamori, T.; Tokitoh, N. *Chem. Rev.*, **2009**, *109*, 3479-3511.
54. Gnanamgari, D.; Sauer, E. L. O.; Schley, N. D.; Butler, C.; Incarvito, C. D.; Crabtree, R. H. *Organometallics*, **2009**, *28*, 321-325.
55. Mata, J. A.; Poyatos, M.; Peris, E. *Coord. Chem. Rev.*, **2007**, *251*, 841-859.
56. Peris, E.; Crabtree, R. H. *Coord. Chem. Rev.*, **2004**, *248*, 2239-2246.
57. Diez-Gonzalez, S.; Nolan, S. P. *Coord. Chem. Rev.*, **2007**, *251*, 874-883.
58. Droege, T.; Glorius, F. *Angew. Chem., Int. Ed.*, **2010**, *49*, 6940-6952.

59. DePasquale, J.; White, N. J.; Ennis, E. J.; Zeller, M.; Foley, J. P.; Papish, E. T. *Polyhedron*, **2013**, *58*, 162-170.
60. DePasquale, J.; Kumar, M.; Zeller, M.; Papish, E. T. *Organometallics*, **2013**, *32*, 966-979.
61. Chen, H.-S.; Chang, W.-C.; Su, C.; Li, T.-Y.; Hsu, N.-M.; Tingare, Y. S.; Li, C.-Y.; Shie, J.-H.; Li, W.-R. *Dalton Trans.*, **2011**, *40*, 6765-6770.
62. Danopoulos, A. A.; Pugh, D.; Smith, H.; Saßmannshausen, J. *Chem. - Eur. J.*, **2009**, *15*, 5491-5502.
63. Downing, S. P.; Danopoulos, A. A. *Organometallics*, **2006**, *25*, 1337-1340.
64. Pugh, D.; Wright, J. A.; Freeman, S.; Danopoulos, A. A. *Dalton Trans.*, **2006**, 775-782.
65. Danopoulos, A. A.; Tsoureas, N.; Wright, J. A.; Light, M. E. *Organometallics*, **2004**, *23*, 166-168.
66. Danopoulos, A. A.; Wright, J. A.; Motherwell, W. B.; Ellwood, S. *Organometallics*, **2004**, *23*, 4807-4810.
67. Danopoulos, A. A.; Tulloch, A. A. D.; Winston, S.; Eastham, G.; Hursthouse, M. B. *Dalton Trans.*, **2003**, 1009-1015.
68. Douthwaite, R. E.; Hauessinger, D.; Green, M. L. H.; Silcock, P. J.; Gomes, P. T.; Martins, A. M.; Danopoulos, A. A. *Organometallics*, **1999**, *18*, 4584-4590.
69. Caramori, G. F.; Ortolan, A. O.; Parreira, R. L. T.; da Silva, E. H. *J. Organomet. Chem.*, **2015**, *799-800*, 54-60.
70. Cheng, Y.; Xu, H.-J.; Sun, J.-F.; Li, Y.-Z.; Chen, X.-T.; Xue, Z.-L. *Dalton Trans.*, **2009**, 7132-7140.
71. Darmon, J. M.; Yu, R. P.; Semproni, S. P.; Turner, Z. R.; Stieber, S. C. E.; DeBeer, S.; Chirik, P. J. *Organometallics*, **2014**, *33*, 5423-5433.
72. Yu, R. P.; Darmon, J. M.; Hoyt, J. M.; Margulieux, G. W.; Turner, Z. R.; Chirik, P. J. *ACS Catal.*, **2012**, *2*, 1760-1764.
73. Yu, R. P.; Darmon, J. M.; Milsman, C.; Margulieux, G. W.; Stieber, S. C. E.; DeBeer, S.; Chirik, P. J. *J. Am. Chem. Soc.*, **2013**, *135*, 13168-13184.
74. Raba, A.; Cokoja, M.; Ewald, S.; Riener, K.; Herdtweck, E.; Poethig, A.; Herrmann, W. A.; Kuehn, F. E. *Organometallics*, **2012**, *31*, 2793-2800.
75. Riener, K.; Bitzer, M. J.; Poethig, A.; Raba, A.; Cokoja, M.; Herrmann, W. A.; Kuehn, F. E. *Inorg. Chem.*, **2014**, *53*, 12767-12777.

76. Schlosser, M.; Rausis, T. *Helv. Chim. Acta*, **2005**, *88*, 1240-1249.
77. Ehlert, T. C.; Hsia, M.-M. *J. Chem. Eng. Data*, **1972**, *17*, 18-21.
78. Rutherford, K. G.; Redmond, W. A. *J. Org. Chem.*, **1963**, *28*, 568-71.
79. Gavritchev, K. S.; Sharpataya, G. A.; Smagin, A. A.; Malyi, E. N.; Matyukha, V. A. *J. Therm. Anal. Calorim.*, **2003**, *73*, 71-83.
80. Fernandezgalan, R.; Manzano, B. R.; Otero, A.; Lanfranchi, M.; Pellinghelli, M. A. *Inorg. Chem.*, **1994**, *33*, 2309-2312.
81. Gibson, D. H.; Ding, Y.; Miller, R. L.; Sleadd, B. A.; Mashuta, M. S.; Richardson, J. F. *Polyhedron*, **1999**, *18*, 1189-1200.
82. Gusev, O. V.; Kalsin, A. M.; Peterleitner, M. G.; Petrovskii, P. V.; Lyssenko, K. A.; Akhmedov, N. G.; Bianchini, C.; Meli, A.; Oberhauser, W. *Organometallics*, **2002**, *21*, 3637-3649.
83. Ino, I.; Zhong, J. C.; Munakata, M.; Kuroda-Sowa, T.; Maekawa, M.; Suenaga, Y.; Kitamori, Y. *Inorg. Chem.*, **2000**, *39*, 4273-4279.
84. Kitagawa, S.; Kawata, S.; Nozaka, Y.; Munakata, M. *Journal of the Chemical Society-Dalton Transactions*, **1993**, 1399-1404.
85. Sanz, S.; Azua, A.; Peris, E. *Dalton Trans.*, **2010**, *39*, 6339-6343.
86. Gandolfi, C.; Heckenroth, M.; Neels, A.; Laurency, G.; Albrecht, M. *Organometallics*, **2009**, *28*, 5112-5121.
87. Hohloch, S.; Suntrup, L.; Sarkar, B. *Organometallics*, **2013**, *32*, 7376-7385.
88. Ogata, K.; Inomata, S.; Fukuzawa, S.-i. *Dalton Trans.*, **2013**, *42*, 2362-2365.
89. Delgado-Rebollo, M.; Canseco-Gonzalez, D.; Hollering, M.; Mueller-Bunz, H.; Albrecht, M. *Dalton Trans.*, **2014**, *43*, 4462-4473.
90. Horn, S.; Gandolfi, C.; Albrecht, M. *Eur. J. Inorg. Chem.*, **2011**, *2011*, 2863-2868.
91. Arduengo, A. J. *Acc. Chem. Res.*, **1999**, *32*, 913-921.
92. Dragutan, V.; Dragutan, I.; Delaude, L.; Demonceau, A. *Coord. Chem. Rev.*, **2007**, *251*, 765-794.
93. Poyatos, M.; Mata, J. A.; Falomir, E.; Crabtree, R. H.; Peris, E. *Organometallics*, **2003**, *22*, 1110-1114.
94. Wang, W.-H.; Himeda, Y.; Muckerman, J. T.; Manbeck, G. F.; Fujita, E. *Chem. Rev.*, **2015**, *115*, 12936-12973.

95. Elek, J.; Nadasdi, L.; Papp, G.; Laurenczy, G.; Joo, F. *Appl. Catal. A* **2003**, *255*, 59–67.
96. Józszai, I.; Joó, F. *J. Mol. Catal. A: Chem.*, **2004**, *224*, 87-91.
97. Castarlenas, R.; Esteruelas, M. A.; Onate, E. *Organometallics*, **2005**, *24*, 4343-4346.
98. Noyori, R.; Yamakawa, M.; Hashiguchi, S. *J. Org. Chem.*, **2001**, *66*, 7931-7944.
99. Bruker Bruker AXS Inc: Madison, Wisconsin USA, 2007.
100. Bruker Bruker AXS Inc: Madison, Wisconsin USA, 2007.
101. Bruker Bruker AXS Inc: Madison, Wisconsin USA, 2001.
102. Sheldrick, G. M. *Acta Cryst.*, **2008**, *A64*, 112-122.
103. Hübschle, C. B.; Sheldrick, G. M.; Dittrich, B. *J. Appl. Cryst.*, **2011**, *44*, 1281-1284.
104. Bruker *Apex2*, Apex2 2013.10-0; Bruker AXS Inc.: Madison, Wisconsin, USA, 2007.
105. Bruker *Saint Plus*, Saint Plus 8.34A; Bruker AXS Inc.: Madison, Wisconsin, USA, 2007.

## 5.7 SUPPORTING INFORMATION

*5.7.1 Single Crystal X-Ray Diffraction Structure Determination for 8 – 12, 14, and 15*  
Single crystals of complexes **8** – **12**, **14**, and **15** were mounted on a glass filament onto the goniometer head of a Bruker ApexII CCD-based X-ray diffractometer<sup>104</sup> equipped with an Oxford N-Helix Cryosystem and a fine focus Mo-target X-ray tube ( $\lambda = 0.71073$  Å) operated at 2000 W power (50 kV, 40 mA). X-ray intensities were measured at 173 K or 100 K with the detector placed at a distance of 6.000 cm from the crystal. Data collections were set up and data were collected using APEX2<sup>1</sup> and frames were integrated with the Saint<sup>105</sup> software package using a narrow-frame algorithm. Scaling was performed and multi-scan absorption corrections were applied using SADABS or TWINABS.<sup>3</sup> The space groups were assigned using XPREP of the Bruker ShelXTL<sup>102</sup> software package. The structures were solved using ShelXT<sup>102</sup> and refined using SHELXL<sup>102</sup> and the graphical user interface ShelXle.<sup>103</sup> All non-hydrogen atoms were refined anisotropically. H atoms on carbon were positioned geometrically and constrained to ride on their parent atom. Structural determination details are listed in the tables below.

The structure of complex **8**, featuring two independent molecules, was found to contain flip disorder of the bidentate, NHC-pyridinol ligand with a ratio of occupation of 0.796(4) to 0.204(4) and 0.754(5) to 0.246(5), respectively. The two moieties were restrained to have similar geometries with SAME command of Shelx.  $U^{ij}$  components of ADPs of disordered atoms were restrained to be similar for atoms closer to each other than 1.7 Å (SIMU command of Shelxl).

The structure of complex **9** contains a methylene chloride solvate molecule disordered around an inversion center. It was freely refined without use of restraints for atom positions or thermal parameters.

The structure of complex **10** was found to be non-merohedrally twinned. The orientation matrices for the two components were identified using the program Cell\_Now,<sup>6</sup> with the two components being related by a 180° rotation around the reciprocal c-axis. The two components were integrated using Saint and corrected for absorption using twinabs, resulting in the following statistics:

3266 data (898 unique) involve domain 1 only, mean I/sigma 24.6

3238 data (871 unique) involve domain 2 only, mean I/sigma 22.9

66638 data (14929 unique) involve 2 domains, mean I/sigma 11.5

36 data (36 unique) involve 3 domains, mean I/sigma 19.4

The exact twin matrix identified by the integration program was found to be:

-1.00000 0.00001 0.00008

-0.00004 -1.00003 0.00054

-0.04225 -0.13674 1.00004

The structure was solved using direct methods with only the non-overlapping reflections of component 1. The structure was refined using the hklf 5 routine with all reflections of component 1 (including the overlapping ones), resulting in a BASF value of 0.45361.

The  $R_{\text{int}}$  value given is for all reflections and is based on agreement between observed single and composite intensities and those calculated from refined unique intensities and twin fractions (TWINABS (Sheldrick, 2012)).

The structure of complex **10** was found to contain a disordered triflate counterion at ~80% occupation. The two moieties were restrained to have similar geometries with the SAME command. A global rigid bond restraint was applied for all atoms (RIGU command of Shelxl).

For complex **11**, the counterion was found to be occupationally disordered, with a  $\text{PO}_2\text{F}_2^-$  anion and a  $\text{PF}_6^-$  anion in a ~53/47 ratio (0.526(5) to 0.474(5)). The  $\text{PO}_2\text{F}_2^-$  was refined by restraining the all equivalent P-X bond lengths to be similar to each other and the X-P-X angles to ideal tetrahedral angles through X...X distance similarity restraints. The disorder in the solvent was refined tentatively as methylene chloride with a minor component of diethyl ether, but the minor solvent was not clearly resolved. For the ether molecule O-C distances were restrained to 1.35(2) Å, C-C distances to 1.54(2) Å, and 1,3 C...C and C...O distances to be each similar.  $U^{ij}$  components of ADPs of  $\text{PO}_2\text{F}_2^-$  and diethyl ether atoms were restrained to be similar for atoms closer to each other than 1.7 Å (SIMU command of Shelxl). The  $\text{CH}_2\text{Cl}_2$  to ether ratio refined to 0.856(5) to 0.144(5).

The structure of complex **12** was found to contain flip disorder of the bidentate, NHC-pyridinol ligand. The two moieties were restrained to have similar geometries using the SAME command of Shelxl. A rigid bond restraint was applied for the disordered atoms (RIGU command of Shelxl), and overlapping atoms C17 and N1B and N1 and C17B were each constrained to have identical ADPs.

Table 5.S1. Single Crystal X-Ray Structure Determination Parameters

	Complex 8	Complex 9	Complex 10
<b>Crystal data</b>			
Chemical formula	[C <sub>20</sub> H <sub>25</sub> ClN <sub>3</sub> ORu](CF <sub>3</sub> SO <sub>3</sub> )	[C <sub>23</sub> H <sub>30</sub> ClN <sub>3</sub> ORu](CF <sub>3</sub> SO <sub>3</sub> ) · CH <sub>2</sub> Cl <sub>2</sub>	[C <sub>19</sub> H <sub>23</sub> ClN <sub>3</sub> ORu](CF <sub>3</sub> SO <sub>3</sub> )
<i>M<sub>r</sub></i>	609.02	693.58	594.99
Space group	Monoclinic, P2 <sub>1</sub> /n	Monoclinic, P2 <sub>1</sub> /n	Triclinic, P1
Temperature (K)	173	173	173
Unit cell dimensions	a = 17.0691 (5) Å b = 12.8560 (4) Å c = 22.0102 (6) Å α = 90° β = 91.331 (1)° γ = 90°	a = 14.3872 (4) Å b = 13.3901 (4) Å c = 16.0189 (5) Å α = 90° β = 109.540 (1)° γ = 90°	a = 7.9823 (4) Å b = 11.9233 (6) Å c = 24.3550 (12) Å α = 87.993 (2)° β = 89.333 (3)° γ = 82.398 (2)°
<i>V</i> (Å <sup>3</sup> )	4828.6 (2)	2908.25 (15)	2296.2 (2)
<i>Z</i>	8	4	4
Radiation type	Mo <i>K</i> α	Mo <i>K</i> α	Mo <i>K</i> α
μ (mm <sup>-1</sup> )	0.90	0.86	0.95
Crystal size (mm)	0.21 x 0.17 x 0.13	0.16 x 0.11 x 0.11	0.52 x 0.09 x 0.04
<b>Data collection</b>			
Diffractometer	AXS SMARTAPEX2 CCD	AXS SMART APEX2 CCD	AXS SMART APEX2CCD
Absorption corr.	Multi-scan SADABS	Multi-scan SADABS	Multi-scan SADABS
<i>T<sub>min</sub></i> , <i>T<sub>max</sub></i>	0.689, 0.746	0.693, 0.747	0.604, 0.747
No. of measured, independent and observed [ <i>I</i> > 2σ( <i>I</i> ) reflections	78949 13315 10868	79536 13657 10709	16720 16720 15462
<i>R<sub>int</sub></i>	0.031	0.027	0.036
(sin θ/λ) <sub>max</sub> (Å <sup>-1</sup> )	0.691	0.833	0.771
<b>Refinement</b>			
<i>R</i> [ <i>F</i> <sup>2</sup> > 2σ( <i>F</i> <sup>2</sup> )]	0.055	0.033	0.051
<i>wR</i> ( <i>F</i> <sup>2</sup> )	0.115	0.088	0.123
<i>S</i>	1.15	1.03	1.15
No. of reflections	13315	13657	16720
No. of parameters	881	368	679
No. of restraints	1056	1	1014
H-atom treatment	Constrained	Constrained	Constrained
Δρ <sub>max</sub> , Δρ <sub>min</sub> (e Å <sup>-3</sup> )	2.35, -1.62	2.06, -0.88	1.44, -1.21

	Complex 11	Complex 12	Complex 14
<b>Crystal data</b>			
Chemical formula	[C <sub>23</sub> H <sub>31</sub> ClN <sub>3</sub> ORu](CF <sub>3</sub> SO <sub>3</sub> ) · CH <sub>2</sub> Cl <sub>2</sub>	[C <sub>21</sub> H <sub>27</sub> ClN <sub>3</sub> ORu](PF <sub>6</sub> )	[C <sub>23</sub> H <sub>32</sub> ClN <sub>3</sub> OIr](PF <sub>6</sub> )
<i>M<sub>r</sub></i>	707.18	618.94	739.13
Space group	Monoclinic, P2 <sub>1</sub> /c	Triclinic, P1	Triclinic, P1
Temperature (K)	173	100	100
Unit cell dimensions	a = 8.8971 (2) Å b = 20.5974 (6) Å c = 16.3311 (4) Å α = 90° β = 102.449 (2)° γ = 90°	a = 7.1127 (12) Å b = 12.621 (2) Å c = 13.872 (2) Å α = 77.748 (8)° β = 79.664 (9)° γ = 88.071 (8)°	a = 8.9448 (10) Å b = 11.6487 (12) Å c = 12.6853 (13) Å α = 81.176 (3)° β = 87.316 (3)° γ = 85.457 (3)°
<i>V</i> (Å <sup>3</sup> )	2922.42 (13)	1197.2 (3)	1301.2 (2)
<i>Z</i>	4	2	2
Radiation type	Mo <i>K</i> α	Cu <i>K</i> α	Mo <i>K</i> α
μ (mm <sup>-1</sup> )	0.89	7.57	5.36
Crystal size (mm)	0.32 x 0.13 x 0.12	0.02 x 0.02 x 0.02	0.24 x 0.20 x 0.07
<b>Data collection</b>			
Diffractometer	AXS SMARTAPEX2 CCD	Bruker AXS Prospector CCD	AXS SMARTAPEX2 CCD
Absorption corr.	Multi-scan SADABS	Multi-scan Apex2	Multi-scan SADABS
<i>T<sub>min</sub></i> , <i>T<sub>max</sub></i>	0.645, 0.746	0.547, 0.753	0.401, 0.736
No. of measured, independent and observed [ <i>I</i> > 2σ( <i>I</i> )] reflections	55025 9436 8288	21127 4158 3384	20580 6471 5902
<i>R<sub>int</sub></i>	0.023	0.111	0.036
(sin θ/λ) <sub>max</sub> (Å <sup>-1</sup> )	0.738	0.597	0.670
<b>Refinement</b>			
<i>R</i> [ <i>F</i> <sup>2</sup> > 2σ( <i>F</i> <sup>2</sup> )]	0.057	0.063	0.026
<i>wR</i> ( <i>F</i> <sup>2</sup> )	0.138	0.152	0.062
<i>S</i>	1.18	1.22	1.04
No. of reflections	9436	4158	6471
No. of parameters	451	426	334
No. of restraints	390	230	0
H-atom treatment	Constrained	Constrained	Constrained
Δρ <sub>max</sub> , Δρ <sub>min</sub> (e Å <sup>-3</sup> )	2.43, -0.70	0.91, -0.79	1.82, -1.95

	Complex 15
<b>Crystal data</b>	
Chemical formula	[C <sub>19</sub> H <sub>24</sub> ClN <sub>3</sub> OIr](PF <sub>2</sub> O <sub>2</sub> )
<i>M<sub>r</sub></i>	639.03
Space group	Monoclinic, P2 <sub>1</sub> /n
Temperature (K)	173
Unit cell dimensions	a = 7.4271 (2) Å b = 13.6185 (4) Å c = 22.2835 (6) Å α = 90° β = 90.793 (1)° γ = 90°
<i>V</i> (Å <sup>3</sup> )	2253.67 (11)
<i>Z</i>	2
Radiation type	Mo Kα
μ (mm <sup>-1</sup> )	6.16
Crystal size (mm)	0.16 x 0.11 x 0.07
<b>Data collection</b>	
Diffractometer	AXS SMARTAPEX2 CCD
Absorption corr.	Multi-scan SADABS
<i>T<sub>min</sub></i> , <i>T<sub>max</sub></i>	0.489, 0.747
No. of measured, independent and observed [ <i>I</i> > 2σ( <i>I</i> ) reflections	57833 9206 7493
<i>R<sub>int</sub></i>	0.032
(sin θ/λ) <sub>max</sub> (Å <sup>-1</sup> )	0.787
<b>Refinement</b>	
<i>R</i> [ <i>F</i> <sup>2</sup> > 2σ( <i>F</i> <sup>2</sup> )]	0.026
<i>wR</i> ( <i>F</i> <sup>2</sup> )	0.058
<i>S</i>	1.02
No. of reflections	9206
No. of parameters	279
No. of restraints	0
H-atom treatment	Mixture of independent and constrained refinement
Δρ <sub>max</sub> , Δρ <sub>min</sub> (e Å <sup>-3</sup> )	1.88, -1.35

CHAPTER 6:  
NICKEL(II) Pincer complexes demonstrate that the remote  
substituent controls catalytic carbon dioxide reduction

Adapted from Burks, D. B.; Davis, S.; Lamb, R. W.; Liu, S.; Rodrigues, R. R.; Liyanage, N. P.; Sun, Y.; Webster, C. E.; Delcamp, J. H.; Papish, E. T., *Chem. Commun.*, 2018, 54, 3819-3822.

### 6.1 Introduction

Solar fuels via CO<sub>2</sub> reduction to form CO are potentially renewable and sustainable, if the problem of designing a robust and active catalyst can be overcome.<sup>1</sup> This work deals with the impact of changes in remote functional groups on catalyst activity. Specifically, we are investigating the role of protic  $\pi$  donors (OH groups) on the activity of nickel(II) complexes. Direct electrocatalytic reduction of CO<sub>2</sub> to CO<sub>2</sub><sup>-•</sup> is an energetically demanding process (-1.99 V vs. SHE in H<sub>2</sub>O at pH 7).<sup>2</sup> In practice, proton coupled electron transfer (PCET) can provide a lower energy pathway to CO formation (CO<sub>2</sub> + 2e<sup>-</sup> + 2H<sup>+</sup> → CO + H<sub>2</sub>O at -0.52 V vs. SHE in H<sub>2</sub>O at pH 7). Importantly, PCET processes can be accelerated by having protic ligands near the metal center of the catalyst.<sup>3</sup> The catalyst also lowers the activation barrier for this reaction and can select for CO formation vs. other multi-electron products (HCO<sub>2</sub>H at -0.61 V, HCHO at -0.49 V, CH<sub>3</sub>OH at -0.38 V and CH<sub>4</sub> at -0.24 V vs SHE in H<sub>2</sub>O at pH 7).<sup>2, 4</sup>

Chemists are still learning how to predict when a change in a remote substituent will greatly impact catalytic rates and catalyst longevity. This is especially true in the area of CO<sub>2</sub> reduction by both electrochemical and photochemical methods. Hydroxy (OH) groups (via covalently attached phenols) have been added to iron porphyrin-based catalysts and have resulted in improved turnover frequencies (TOFs) for electrocatalytic CO<sub>2</sub> reduction due to an increased local concentration of protons.<sup>5</sup> However, in the case of photocatalytic CO<sub>2</sub> reduction using these same phenol substituted iron complexes, these catalysts were prone to decomposition.<sup>6</sup> Similarly, a phenol group on the ligand is beneficial in electrocatalytic CO<sub>2</sub> reduction with a manganese(I) catalyst; again the OH group is thought to facilitate proton transfer and play a key mechanistic role.<sup>7</sup> In contrast, the use of the 4,4'- or 6,6'-dihydroxybipyridine (dhbp) ligand with Re(I) or Ru(II) complexes has illustrated that in this specific case, proximal hydroxyl groups are detrimental to electrocatalytic CO<sub>2</sub> reduction, and in fact the 6,6'-dhbp complexes only gives minimal activity (TON = 1 or less) with competing decomposition.<sup>8-9</sup> Nonetheless, proximal OH groups (in bidentate<sup>10</sup> and tridentate<sup>11</sup> ligands) are generally beneficial in metal catalysts for the hydrogenation of CO<sub>2</sub><sup>12-14</sup> and other substrates. With these studies in mind, it was unclear at the outset of our work herein whether pyridinol derived pincers would enhance or reduce photodriven catalytic CO<sub>2</sub> reduction activity with nickel(II).

N-heterocyclic carbene (NHC) and pyridine rings have been combined to make bidentate, tridentate pincer, and tetradentate ligands for metal catalysts that are highly active for CO<sub>2</sub> reduction<sup>15-19</sup> and other reactions. Focusing on the group 10 metals,<sup>20</sup> tetradentate NCCN ligands bind to Ni(II) and form highly efficient photodriven catalysts for CO<sub>2</sub> reduction to CO.<sup>15</sup> Because pincer ligands often form highly active catalysts with

earth-abundant metals, we aimed to affix a pyridinol-NHC pincer ligand to a Ni metal center. Thus, we can evaluate the effect of modulating electron density at the metal center with a  $\pi$  electron donor group ( $O^-$ ) at the *para* (to  $N_{py}$ ) position.<sup>21</sup> As shown below, this simple change converts inactive complexes to active photocatalytic systems.

Papish et al. recently reported a bidentate ligand that was the first to combine the NHC and pyridinol moieties, and these ligands supported Ir(III) and Ru(II) complexes that were studied for catalytic  $CO_2$  hydrogenation.<sup>12</sup> However, thus far, no one has combined NHC and pyridinol derived rings on a pincer scaffold until our recent report that ruthenium complex **1** (Figure 6.1) is an efficient catalyst for  $CO_2$  reduction to CO. Complex **1** is a robust catalyst with selective formation of CO; in contrast complex **2**, with the unsubstituted pincer, is inactive. These recently reported results illustrate that a remote methoxy group can greatly enhance photocatalysis.<sup>22</sup> In this work, we aimed to use these new CNC pincer ligands with Ni(II), an earth abundant metal.

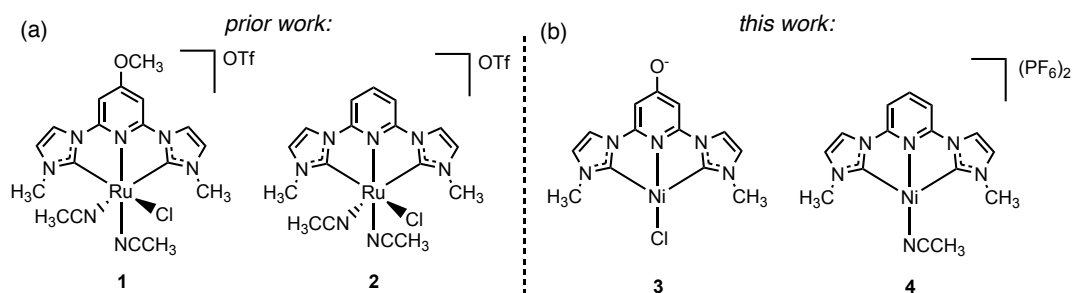
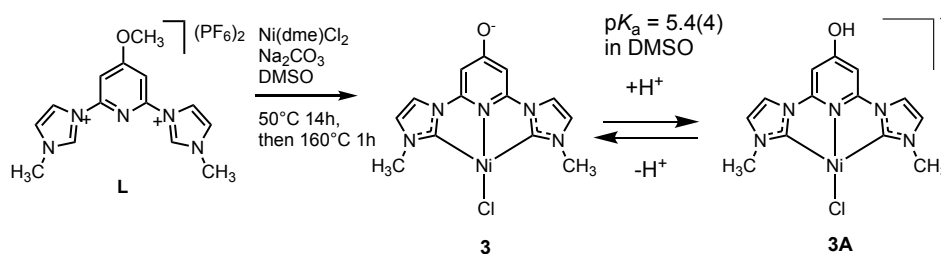


Figure 6.1. (a) Ru(II) photocatalysts (**1**: TON = 250, **2**: TON = 3) for  $CO_2$  reduction<sup>22</sup> and (b) Ni(II) complexes **3** and **4**.<sup>23</sup>

## 6.2 Results and Discussion

The synthesis of the nickel(II) complex **3** begins with the carbene precursor **L** (used here as the  $PF_6^-$  salt) which we recently reported (Scheme 1).<sup>22</sup> The synthesis of Ni(II) pincer complexes typically involves high heat ( $\sim 160$  °C) in several literature procedures.<sup>24</sup> Following these procedures, treatment of **L** with  $Ni(dme)Cl_2$  in the

presence of  $\text{Na}_2\text{CO}_3$  as the base in DMSO resulted in loss of a methyl group to form the  $\text{O}^-$  substituted ligand in 29% yield (Scheme 1). It appears that high heat as well as excess free chloride resulted in methyl loss as methyl chloride, as our reaction conditions resemble known methods for deprotection of phenol derived ethers.<sup>25</sup> Complex **3** is neutral with Ni(II) ligated by a chloride and an anionic pincer. **3** was fully characterized by  $^1\text{H-NMR}$ , IR, MS, and EA. The IR spectrum shows a peak at  $1568\text{ cm}^{-1}$  which is consistent with  $\text{C}=\text{O}$  character. This complex has limited solubility in most solvents, but it can be studied in aprotic organic solvents like DMSO and  $\text{CH}_3\text{CN}$ . Complex **3** can be reversibly protonated to form cation **3A**. For example, in DMSO, triflic acid can protonate **3** and then proton sponge can be used to deprotonate **3A** as followed by UV-vis or  $^1\text{H-NMR}$  spectroscopy (Figure 6.S16 and 6.S23, respectively). Acetic acid ( $\text{p}K_{\text{a}} = 12.3$  in DMSO) appears to be too weak an acid to protonate **3**. These results show that the  $\text{p}K_{\text{a}}$  of **3A** is between zero and  $\sim 10$  in DMSO. With the addition of sulfamic acid ( $\text{p}K_{\text{a}} = 6.5$  in DMSO), an equilibrium between **3** and **3A** is reached as observed by UV-vis spectroscopy (Figure 6.S15). This equilibrium constant was used to calculate the  $\text{p}K_{\text{a}}$  (**3A**) = 5.4(4) (*cf.* computationally we predicted a  $\text{p}K_{\text{a}}$  value of 3.9 in DMSO, see supporting information).



*Scheme 1.* Synthetic route to catalyst **3** and reversible protonation of **3** to give the acidic form, **3A**.

One could reasonably expect that a deprotonated oxygen would allow for a more electron-rich pyridyl ring, which could then donate more electron density to the metal center. Natural atomic orbital (NAO)<sup>26</sup> analysis, performed by the Webster group at Mississippi State University, was used to compare atomic charges between species. Upon deprotonation of **3A** to produce **3**, there is an increase in the negative charge on the O atom (+4%), the N<sub>py</sub> atom (+5%), and the nickel atom (+2%), indicating that the protonation state does have an effect on the charge of the metal center. Along with the change in the atomic charges, the C-O distance decreases from 1.33 Å in **3A** to 1.25 Å in **3**. As expected with this decrease in bond length, the computed harmonic stretching frequency ( $\omega_{\text{CO}}$ ) shifts from 1513 cm<sup>-1</sup> in **3A** to 1609 cm<sup>-1</sup> in **3**, reflecting the increase in the carbonyl C-O bond order. Experimentally the C-O stretch shifts from 1448 cm<sup>-1</sup> in **3A** to 1568 cm<sup>-1</sup> in **3**. The changes in atomic charges and computed  $\omega_{\text{CO}}$  are also reflected in deprotonation of the CNC-Ni fragment.

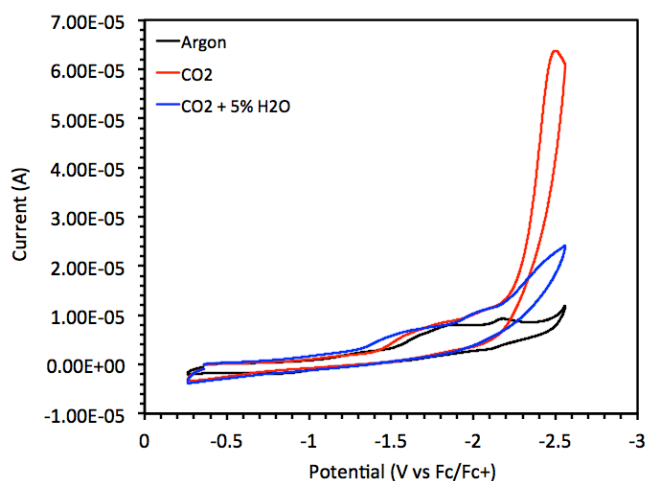


*Figure 6.2.* CVs of **3** under argon, CO<sub>2</sub>, and CO<sub>2</sub> with added water. The electrolyte is 0.1 M Bu<sub>4</sub>NPF<sub>6</sub> in CH<sub>3</sub>CN with a glassy carbon working electrode, Ag/AgCl reference, and Pt counter electrodes. Each CV is a fresh solution of complex **3** (1.0 mM).

Complex **3** was studied for CO<sub>2</sub> reduction, both electrocatalytically and photocatalytically, by the Delcamp group at The University of Mississippi. Complex **3** was evaluated for the electrocatalytic reduction of CO<sub>2</sub> via cyclic voltammetry (CV) experiments to compare with known electrocatalyst **4**.<sup>23</sup> Similar to catalyst **4**, a catalytic current increase was apparent for complex **3** at the third reduction wave (wave onset at -2.2 V vs Fc<sup>+</sup>/Fc;  $i_{\text{cat}}/i_{\text{p}} = 6$ ) when CV scans under argon and CO<sub>2</sub> atmospheres were compared (Figure 6.2). Upon addition of a proton source (H<sub>2</sub>O) the current under CO<sub>2</sub> diminishes substantially, nearing the current observed at the third reduction wave under argon. This result suggests **3** is operating under a reductive disproportionation mechanism to give CO and CO<sub>3</sub><sup>2-</sup> as the products (product analysis below) from CO<sub>2</sub>.

Through the use of a photosensitizer (PS), nickel complexes are known to photocatalytically reduce CO<sub>2</sub>.<sup>15, 27-28</sup> Typically, the PS is first photoexcited to generate a reducing species, which accepts an electron from a sacrificial donor (SD, Figure S6). The reduced PS then can transfer an electron to the Ni catalyst, which may interact with CO<sub>2</sub> before accepting a second electron to reduce CO<sub>2</sub> to CO along with formation of H<sub>2</sub>O or CO<sub>3</sub><sup>2-</sup> (in the presence or absence of H<sup>+</sup>, respectively).

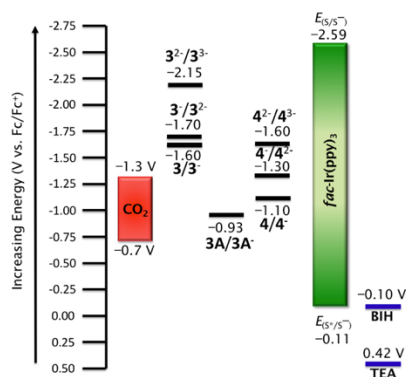
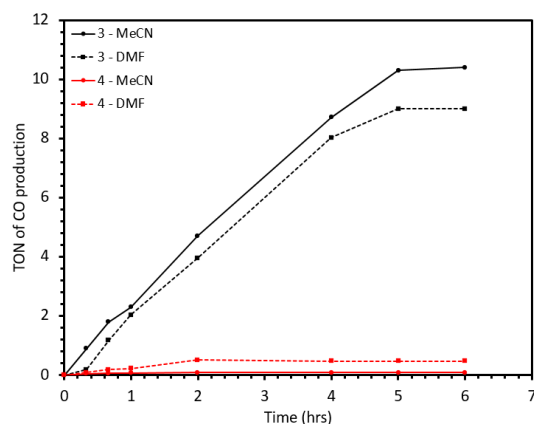


Figure 6.3. An energy level diagram with each catalyst, an estimated reduction potential range for CO<sub>2</sub>, the PS, and each SD. Note: The energy level for **3A/3A<sup>-</sup>** represents the onset of a catalytic wave in the CV in the presence of TfOH.

Specifically, Ir(ppy)<sub>3</sub> [tris(2-phenylpyridine)iridium(III)] was selected as the PS due to its high photostability, reversible reduction and a potent reduction potential (-2.59 V vs. Fc<sup>+</sup>/Fc, Figure 6.3).<sup>19</sup> 1,3-dimethyl-2-phenyl-2,3-dihydro-1H-benzo[d]-imidazole (BIH) was used as a SD because it is readily oxidized and is known to react with Ir(ppy)<sub>3</sub> during photolysis. We note that the Ir(ppy)<sub>3</sub>/BIH system is energetically favourable for the transfer of an electron to the first three reduction potentials of either catalyst **3** or catalysts **4**. However, there is a notable difference in driving force (550 mV) for electron transfer from complex **3** to CO<sub>2</sub> versus from complex **4** to CO<sub>2</sub> from the third catalyst reduction potential. In an acetonitrile solution with Ir(ppy)<sub>3</sub>, BIH, and triethylamine (TEA) saturated with CO<sub>2</sub>, complex **3** gives 10.6 turnovers (TON; moles CO/moles complex) when irradiated with a solar simulator to approximate natural sunlight over a six-hour period (Table 6.1, Figure 6.4). After 6 h of irradiation CO production ceases. Under identical conditions, complex **4** gives a TON of only 0.09. This difference in TON highlights the critical role of a remote O<sup>-</sup> group in allowing for higher catalyst activity. Changing the solvent to DMF lead to a similar TON of 9.0 (Table 6.1, entry 3) for complex **3** and only 0.5 TON for complex **4**. When TEA was removed, the TON value for complex **3** dropped dramatically (Table 6.1, entry 5). TEA may serve multiple roles in the photocatalytic reduction of CO mixture (electron source, proton source after electron transfer, base). However, TEA is thermodynamically poorly positioned to serve as a SD (and thus as proton source) which suggests the primary role of TEA is as a base (Figure 6.3). Proton sponge is a surrogate base with a similar basicity to TEA (pK<sub>a</sub> values are 9.00 and 7.50 in DMSO for the conjugate acids of TEA and proton sponge, respectively), but it has a dramatically higher energy oxidation potential of -0.15 V exceeding that of BIH. Reactions with proton sponge gave a TON of 5.6 with

complex **3**, which suggests one of the primary roles of TEA is to serve as a base because the added electron donation strength of proton sponge did not improve the TON value (Table 6.1, entry 6). To test the effect of acid on photocatalysis with **3**, triflic acid (TfOH) was added as a strong acid and gave low reactivity (0.9 TON, Table 6.1, entry 7). This result highlights the importance of keeping the strongest acid in the solution at a relatively high  $pK_a$  value. The protonated complex **3A** is likely a poor catalyst due to the diminished electron donor strength from the OH group. Negative controls including the removal of Ir(ppy)<sub>3</sub>, BIH, CO<sub>2</sub>, or complex **3** produced <1 TON. Similarly, with **3** in the dark and all reaction components no CO is produced. Thus, all reaction components are needed, and the observed CO is from photocatalytic CO<sub>2</sub> reduction. Additionally, a Hg-poison test shows the active complex is likely homogeneous in nature (Table 6.S10).



*Figure 6.4.* Turnover number versus time plot for photocatalytic reactions with complexes **3** and **4**.

The rate of reactivity of complex **3** was found to consistently give a turnover frequency (TOF; TON/time) of  $\sim 2.2 \text{ h}^{-1}$  for the first 4 hours before CO production slowed at 5 hours and ceased by 6 hours (Figure 6.4). The difference in CO produced in MeCN versus DMF is largely due to  $\sim 30$  additional minutes of sustained catalysis with

MeCN as the initial rates over the first 4 hours are near identical. Providing the active catalyst results from dissociation of the Cl<sup>-</sup> ligand on complex **3**, the similar rates in DMF and MeCN suggest this coordination site is not strongly associated with either solvent.

Entry	Complex	Change <sup>a</sup>	TON <sub>max</sub>
1	<b>3</b>	none	10.6
2	<b>4</b>	none	0.1
3	<b>3</b>	no MeCN, with DMF	9.0
4	<b>4</b>	no MeCN, with DMF	0.5
5	<b>3</b>	no TEA	1.8
6	<b>3</b>	no TEA, with proton-sponge	5.6
7	<b>3</b>	add TfOH, no TEA	0.9
8	<b>3</b>	no Ir	0.6
9	<b>3</b>	no BIH	0.3
10	<b>3</b>	no CO <sub>2</sub> , with N <sub>2</sub>	0.2

*Table 6.1.* Photocatalytic CO<sub>2</sub> reduction under varied conditions. <sup>a</sup>Standard conditions: 0.1 mM Ni-complex, 0.1 mM Ir(ppy)<sub>3</sub>, 11 mM BIH, 0.1 mL TEA, 1.9 mL MeCN, room temperature, and 150 W Xenon Lamp with an AM 1.5G filter for solar simulation.

Computational studies (Figures 6.5, 6.S30, 6.S31, and 6.S33-36) by the Webster group at Mississippi State University show that removal of chloride from **3A<sup>o</sup>** produces fragment **5A** and from **3<sup>-</sup>** produces fragment **5**. After deprotonation of **5A** to produce **5**, there is an increase in the negative charge on the O atom (+6%), the N<sub>py</sub> atom (+6%), and the nickel atom (+6%). Furthermore, because coordination of CO<sub>2</sub> to the metal is a necessary step in catalysis, the relative energies of CO<sub>2</sub> binding to fragments **5A** (protonated) and **5** (deprotonated) were investigated (Figures 6.S34 and 6.S35). Starting with coordinatively unsaturated **5A**, attempts to locate a structure with CO<sub>2</sub> coordinated to the nickel were unsuccessful. The resulting complex, **6A**, is a van der Waals complex (monopole/induced dipole) that has a Ni-C<sub>CO<sub>2</sub></sub> distance of 3.32 Å and a nearly linear OCO bond angle (179.3°). In the case of the analogous deprotonated complex (**5**), the van der Waals complex exists (**6**); however, more importantly, a

structure (**7**) with CO<sub>2</sub> bound to nickel can be located (Ni-C<sub>CO<sub>2</sub></sub> = 2.04 Å). The charge of the CO<sub>2</sub> unit in complex **7**, which has bound CO<sub>2</sub>, is -0.301. Furthermore, the charge of the CO<sub>2</sub> unit in complex **6A** (0.0074) is nearly zero (the sum of the NAO charges in free CO<sub>2</sub>). These results suggest a plausible explanation for how protonation state influences the ability of the catalyst to reduce CO<sub>2</sub> to CO. Furthermore, the pincer ligand is less electron rich in complex **4** (cf. **3A** with OH) because it lacks an electron donor group, which may explain the photocatalytic inactivity. Via CV studies it is clear that the reduction potential of **3A** is dramatically shifted more positive from that of **3** (Figures 6.3 & 6.S8). In contrast **3** (O<sup>-</sup> group) is active with greater electron density supplied from the pincer to Ni.

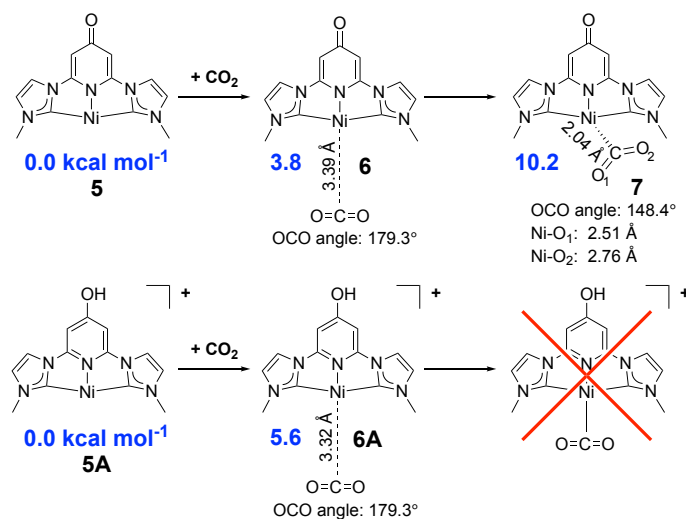


Figure 6.5. Computational study of CO<sub>2</sub> reduction from two different protonation states. Relative energies are in blue.

### 6.3 Conclusion

In summary, a surprising effect from a single remote atom change from a hydrogen (in **4**) to an oxygen anion (in **3**) on the pincer CNC ligand resulted in a dramatic increase in catalyst reactivity, effectively turning on CO<sub>2</sub> reduction. Complex **3** may be a pre-catalyst based on initial complex **3** showing catalytic current on the third reduction wave

initially before a species with catalytic activity on the first reduction wave grows in. Sustained photocatalytic reactivity was observed for complex **3** in the presence of a photosensitizer for the first 6 hours. This study highlights the importance of careful remote substituent selection as a single atom substitution on a ligand can render an active complex completely inactive. Furthermore, these are switchable catalysts that can be “turned off” or “turned on” by manipulating the concentration of protons in solution.

## 6.4 Experimental

### 6.4.1 Synthetic General Methods

All syntheses were performed under inert atmosphere. All reagents were purchased from commercial sources and were used as is, except where noted. All NMR spectra were obtained on a Bruker AV360 360 MHz spectrometer and are calibrated to the residual solvent peak. IR spectra were measured on a Bruker Alpha ATR-IR spectrometer. UV-vis spectra were measured on a Perkin-Elmer Lambda 35 spectrophotometer. Air-free UV-vis samples were prepared under a nitrogen atmosphere; the spectra were measured in an air-free cuvette. Ultra-dry and air free DMSO used in the pK<sub>a</sub> studies was produced by drying anhydrous DMSO over a column of molecular sieves and then distilling at reduced pressure. MS spectra were obtained on a Waters AutoSpec-Ultima NT spectrometer. Elemental analysis was performed by Atlantic Microlab, Inc. The carbene pre-cursor of the pincer ligand was prepared by literature procedure.<sup>22</sup>

### 6.4.2 Synthesis of Complex **3**

96 mg (436.9 μmol) of Ni(dme)Cl<sub>2</sub>, 90.2 mg (851.0 μmol) of Na<sub>2</sub>CO<sub>3</sub>, and 200.5 mg (357.3 μmol) of [MeNHC-Py<sub>OMe</sub>-NHC<sup>Me</sup>][PF<sub>6</sub>]<sub>2</sub> were added to an oven-dried Schlenk

flask. 4 mL of anhydrous DMSO were added to the flask via cannula transfer. The reaction mixture was heated at 50 °C for 14 hr and then heated at 160 °C for 1 hr. After cooling to room temperature, there is a large amount of precipitate from the reaction mixture. The solid was collected by filtration. The collected solid was sonicated in 10 mL of anhydrous methanol for 10 minutes and then filtered through a frit. The filtrate was placed at 10 °C for 12 hr. A light orange solid precipitated out and was collected by filtration. The solid was washed 3 times with 0.5 mL of cold methanol. The solid was dried under vacuum to yield a light orange solid. (36.4 mg, 29 % yield). <sup>1</sup>H-NMR (360 MHz, *d*<sub>6</sub>-DMSO) δ (ppm): 3.87 (6H, s), 6.21 (2H, s), 7.38 (2H, d, *J* = 1.9 Hz), 7.98 (2H, d, *J* = 1.9 Hz). ESI-MS(+) *m/z*: 358.2 ([M+HCOOH]<sup>+</sup>, M = [Ni(<sup>Me</sup>NHC-Py<sub>O</sub>-NHC<sup>Me</sup>)]<sup>+</sup> = [NiON<sub>5</sub>C<sub>13</sub>H<sub>12</sub>]<sup>+</sup> and HCOOH is formic acid from the MS solvent). FT-IR (ATR, solid state) cm<sup>-1</sup>: 3089 (w), 1639 (s), 1563 (m), 1534 (s), 1513 (s), 1481 (m), 1406 (m), 1310 (m), 1282 (m), 1237 (s), 1075 (m), 962 (m), 860 (w), 828 (w), 732 (s), 694 (m), 610 (w), 417 (m). Elem. Anal. Calcd. for [NiClON<sub>5</sub>C<sub>13</sub>H<sub>12</sub>·2H<sub>2</sub>O] = (**3**·2H<sub>2</sub>O): C, 40.61 %; N, 18.22 %; H, 4.19 %. Found: C, 40.29 %; N, 17.83 %; H, 4.01 %. Recrystallized **3** used for EA was the dihydrate (crystallization was done open to air) as confirmed by <sup>1</sup>H NMR.

## 6.5 Author Contribution

I was the intellectual lead and performed most of the experimental work included in this chapter. I was also the lead author on the paper resulting from this project.

## 6.6 References

1. Robert, M. *ACS Energy Lett.*, **2016**, *1*, 281-282.
2. Matsubara, Y.; Grills, D. C.; Kuwahara, Y. *ACS Catal.*, **2015**, *5*, 6440-6452.

3. Zhang, T.; Wang, C.; Liu, S.; Wang, J.-L.; Lin, W. *J. Am. Chem. Soc.*, **2014**, *136*, 273-281.
4. Benson, E. E.; Kubiak, C. P.; Sathrum, A. J.; Smieja, J. M. *Chem. Soc. Rev.*, **2009**, *38*, 89-99.
5. Costentin, C.; Robert, M.; Savéant, J.-M. *Acc. Chem. Res.*, **2015**, *48*, 2996-3006.
6. Bonin, J.; Chaussemier, M.; Robert, M.; Routier, M. *ChemCatChem*, **2014**, *6*, 3200-3207.
7. Agarwal, J.; Shaw, T. W.; Schaefer, I., Henry F; Bocarsly, A. B. *Inorg. Chem.*, **2015**, *54*, 5285-5294.
8. Duan, L.; Manbeck, G. F.; Kowalczyk, M.; Szalda, D. J.; Muckerman, J. T.; Himeda, Y.; Fujita, E. *Inorg. Chem.*, **2016**, *55*, 4582-4594.
9. Manbeck, G. F.; Muckerman, J. T.; Szalda, D. J.; Himeda, Y.; Fujita, E. *J. Phys. Chem. B.*, **2015**, *119*, 7457-7466.
10. Nieto, I.; Livings, M. S.; Sacci, J. B.; Reuther, L. E.; Zeller, M.; Papish, E. T. *Organometallics*, **2011**, *30*, 6339-6342.
11. Moore, C. M.; Bark, B.; Szymczak, N. K. *ACS Catal.*, **2016**, *6*, 1981-1990.
12. Siek, S.; Burks, D. B.; Gerlach, D. L.; Liang, G.; Tesh, J. M.; Thompson, C. R.; Qu, F.; Shankwitz, J. E.; Vasquez, R. M.; Chambers, N. S.; Szulczewski, G. J.; Grotjahn, D. B.; Webster, C. E.; Papish, E. T. *Organometallics*, **2017**, *36*, 1091-1106.
13. Wang, W.-H.; Hull, J. F.; Muckerman, J. T.; Fujita, E.; Himeda, Y. *Energy Environ. Sci.*, **2012**, *5*, 7923-7926.
14. Hull, J. F.; Himeda, Y.; Wang, W.-H.; Hashiguchi, B.; Periana, R.; Szalda, D. J.; Muckerman, J. T.; Fujita, E. *Nature Chemistry*, **2012**, *4*, 383-388.
15. Thoi, V. S.; Kornienko, N.; Margarit, C. G.; Yang, P.; Chang, C. J. *J. Am. Chem. Soc.*, **2013**, *135*, 14413-14424.
16. Thoi, V. S.; Chang, C. J. *Chem. Commun.*, **2011**, *47*, 6578.
17. Agarwal, J.; Shaw, T. W.; Stanton, I., Charles J; Majetich, G. F.; Bocarsly, A. B.; Schaefer, I., Henry F. *Angew. Chem., Int. Ed.*, **2014**, *53*, 5152-5155.
18. Liyanage, N. P.; Dulaney, H. A.; Huckaba, A. J.; Jurss, J. W.; Delcamp, J. H. *Inorg. Chem.*, **2016**, *55*, 6085-94.
19. Huckaba, A. J.; Sharpe, E. A.; Delcamp, J. H. *Inorg. Chem.*, **2016**, *55*, 682.
20. Therrien, J. A.; Wolf, M. O.; Patrick, B. O. *Inorg. Chem.*, **2015**, *54*, 11721-11732.

21. Danopoulos, A. A.; Pugh, D.; Smith, H.; Saßmannshausen, J. *Chem. - Eur. J.*, **2009**, *15*, 5491-5502.
22. Boudreaux, C. M.; Liyanage, N. P.; Shirley, H.; Siek, S.; Gerlach, D. L.; Qu, F.; Delcamp, J. H.; Papish, E. T. *Chem. Commun.*, **2017**, *53*, 11217-11220.
23. Sheng, M.; Jiang, N.; Gustafson, S.; You, B.; Ess, D. H.; Sun, Y. *Dalton Trans.*, **2015**, *44*, 16247-16250.
24. Inamoto, K.; Kuroda, J.-i.; Hiroya, K.; Noda, Y.; Watanabe, M.; Sakamoto, T. *Organometallics*, **2006**, *25*, 3095-3098.
25. Jarowicki, K.; Kocięski, P. *Journal of the Chemical Society, Perkin Transactions 1*, **1999**, *0*, 1589-1616.
26. Reed, A. E.; Weinstock, R. B.; Weinhold, F. *J. Chem. Phys.*, **1985**, *83*, 735-746.
27. Kuehnel, M. F.; Orchard, K. L.; Dalle, K. E.; Reisner, E. *J. Am. Chem. Soc.*, **2017**, *139*, 7217-7223.
28. Hong, D.; Tsukakoshi, Y.; Kotani, H.; Ishizuka, T.; Kojima, T. *J. Am. Chem. Soc.*, **2017**, *139*, 6538-6541.
29. Fei, H.; Sampson, M. D.; Lee, Y.; Kubiak, C. P.; Cohen, S. M. *Inorg. Chem.*, **2015**, *54*, 6821.
30. Sampson, M. D.; Kubiak, C. P. *J. Am. Chem. Soc.*, **2016**, *138*, 1386-1393.
31. Frisch, M. J.; Trucks, G. W.; Schlegel, H. B.; Scuseria, G. E.; Robb, M. A.; Cheeseman, J. R.; Scalmani, G.; Barone, V.; Mennucci, B.; Petersson, G. A.; Nakatsuji, H.; Caricato, M.; Li, X.; Hratchian, H. P.; Izmaylov, A. F.; Bloino, J.; Zheng, G.; Sonnenberg, J. L.; Hada, M.; Ehara, M.; Toyota, K.; Fukuda, R.; Hasegawa, J.; Ishida, M.; Nakajima, T.; Honda, Y.; Kitao, O.; Nakai, H.; Vreven, T.; Montgomery Jr., J. A.; Peralta, J. E.; Ogliaro, F.; Bearpark, M. J.; Heyd, J.; Brothers, E. N.; Kudin, K. N.; Staroverov, V. N.; Kobayashi, R.; Normand, J.; Raghavachari, K.; Rendell, A. P.; Burant, J. C.; Iyengar, S. S.; Tomasi, J.; Cossi, M.; Rega, N.; Millam, N. J.; Klene, M.; Knox, J. E.; Cross, J. B.; Bakken, V.; Adamo, C.; Jaramillo, J.; Gomperts, R.; Stratmann, R. E.; Yazyev, O.; Austin, A. J.; Cammi, R.; Pomelli, C.; Ochterski, J. W.; Martin, R. L.; Morokuma, K.; Zakrzewski, V. G.; Voth, G. A.; Salvador, P.; Dannenberg, J. J.; Dapprich, S.; Daniels, A. D.; Farkas, Ö.; Foresman, J. B.; Ortiz, J. V.; Cioslowski, J.; Fox, D. J. *Gaussian 09*, Gaussian, Inc.: Wallingford, CT, USA, 2009.
32. Lee, C.; Yang, W.; Parr, R. G. *Phys. Rev. B*, **1988**, *37*, 785-789.
33. Becke, A. D. *J. Chem. Phys.*, **1993**, *98*, 5648-5652.
34. Perdew, J. P.; Burke, K.; Ernzerhof, M. *Phys. Rev. Lett.*, **1997**, *78*, 1396-1396.

35. Perdew, J. P.; Burke, K.; Ernzerhof, M. *Phys. Rev. Lett.*, **1996**, *77*, 3865-3868.
36. Dunlap, B. I. *J. Mol. Struct. Theochem*, **2000**, *529*, 37-40.
37. Dunlap, B. I. *J. Chem. Phys.*, **1983**, *78*, 3140-3142.
38. Wadt, W. R.; Hay, P. J. *J. Chem. Phys.*, **1985**, *82*, 284-298.
39. Hay, P. J.; Wadt, W. R. *J. Chem. Phys.*, **1985**, *82*, 299-310.
40. Couty, M.; Hall, M. B. *J. Comput. Chem.*, **1996**, *17*, 1359-1370.
41. Check, C. E.; Faust, T. O.; Bailey, J. M.; Wright, B. J.; Gilbert, T. M.; Sunderlin, L. S. *The Journal of Physical Chemistry A*, **2001**, *105*, 8111-8116.
42. Hehre, W. J.; Ditchfield, R.; Pople, J. A. *J. Chem. Phys.*, **1972**, *56*, 2257-2261.
43. Hariharan, P. C.; Pople, J. A. *Theor. Chim. Acta*, **1973**, *28*, 213-222.
44. Moser, A.; Range, K.; York, D. M. *J. Phys. Chem. B*, **2010**, *114*, 13911-13921.
45. Kelly, C. P.; Cramer, C. J.; Truhlar, D. G. *J. Phys. Chem. B*, **2007**, *111*, 408-422.
46. Panov, A.; Fripiat, J. J. *Langmuir*, **1998**, *14*, 3788-3796.
47. Pretsch; Clerc; Seibl; Simon, *Tables of Spectral Data for Structure Determination of Organic Compounds*. 2 ed.; Springer-Verlag: Heidelberg, New York, 1989.

## 6.7 Supporting Information

### 6.7.1 Photocatalysis General Information

A 150 W Sciencetech SF-150C Small Collimated Beam Solar Simulator equipped with an AM 1.5 filter was used as the light source for the photocatalytic experiments. Head space analysis was performed using a VICI gas tight syringe with stopcock and a custom Agilent 7890B Gas Chromatography instrument equipped with Agilent PorapakQ 6ft, 1/8 O.D. column. Quantitation of CO and CH<sub>4</sub> were made using an FID detector, while H<sub>2</sub> was quantified using a TCD detector. All calibrations were done using standards purchased from BuyCalGas.com.

### 6.7.2 Photocatalysis Procedure

To a 17 mL vial was added BIH (0.005 g, 0.02 mmol), MeCN (6 ml, bulk or anhydrous), and catalyst (0.2 ml from  $1 \times 10^{-3}$  M in MeCN solution). The solution was bubbled vigorously with CO<sub>2</sub> for at least 15 minutes until the solution volume reached 1.9 ml and then 0.1 ml of degassed triethylamine or N,N,N',N'-Tetramethyl-1,8-naphthalenediamine (proton sponge) was added to the mixture. The tube was sealed with a rubber septum and irradiated with a solar simulator. Head space samples were taken and the pressure was adjusted to atmospheric pressure by pressurizing the sample (300  $\mu$ L taken from the headspace then compressed to 250  $\mu$ L) then submerging the sealed gas tight syringe into diethyl ether. The syringe was open and gas was observed exiting the needle tip. The syringe was then sealed, removed from the diethyl ether solution and injected into the GC mentioned above.

### 6.7.3 Cyclic Voltammetry

C-H instruments electrochemical analyzer was used to measure the CV in the presence of Ag/AgCl as the reference electrode, Platinum as the counter electrode and Glassy

carbon was the working electrode and 0.1 M n-Bu<sub>4</sub>NPF<sub>6</sub> as the supporting electrolyte. All electrochemical measurements were taken in anhydrous acetonitrile (or 5% water in anhydrous acetonitrile) at a scan rate of 100 mV/s and minimum exposure to light. For each run concentration of catalyst kept constant at 1 mM. Before each measurement, the solution was degassed with Ar or CO<sub>2</sub> (for ~15 min). To avoid concentration changes for the electrolyte and catalyst, the desired experimental solvent volume and accurate concentrations were added to the electrolysis cell. The solvent height in the cell was marked and, the mixture was then diluted with pure acetonitrile (~2 mL). The mixture was then degassed with Ar or CO<sub>2</sub> until the solvent evaporated and level returned to the marked volume. During cyclic voltammetry scans, the sweep width window was set to approximately 100 mV past the second reduction wave peak. Since the catalyst is not active under dark conditions same experiments ran after exposing the catalyst and electrolyte solution to ambient fluorescent light in different time periods.

#### 6.7.4 <sup>1</sup>H NMR Formate Detection

Our slightly modified procedure is as follows: Upon reaction completion, 0.8 mL of the reaction solution was taken into a syringe and added to a 4 mL vial. To this 36 μL of Verkade's Triisobutyl Superbase (CAS# 331465-71-5; 2,8,9-Triisobutyl- 2,5,8,9-tetraaza-1- phosphabicyclo[3.3.3]undecane). The mixture was sonicated for 10 minutes at room temperature. 1.16 mL of a d<sub>3</sub>-MeCN ferrocene solution (1.19 mM concentration) was added to the mixture. The vial was thoroughly mixed, then an NMR spectrum was taken on a 500 MHz NMR or 300 MHz NMR with an extended D1-delay of 10 seconds and a minimum of 200 scans. The ratio of the formate peak (~8.7 ppm) and the ferrocene peak (~4.2 ppm, see below) were then compared to a calibration curve generated through the analysis of known concentrations of formate (0.0 mM, 0.1 mM, 1.0 mM,

and 10.0 mM solutions). Through this method, the concentration of formate could be evaluated accurately through a trendline having an  $R^2$  value of 0.997 and 0.999 (see below). All NMR spectra were evaluated with MestReNova software to ensure level baselines in the analyte region prior to integrating peaks. This method has been previously described in the literature.<sup>29</sup>

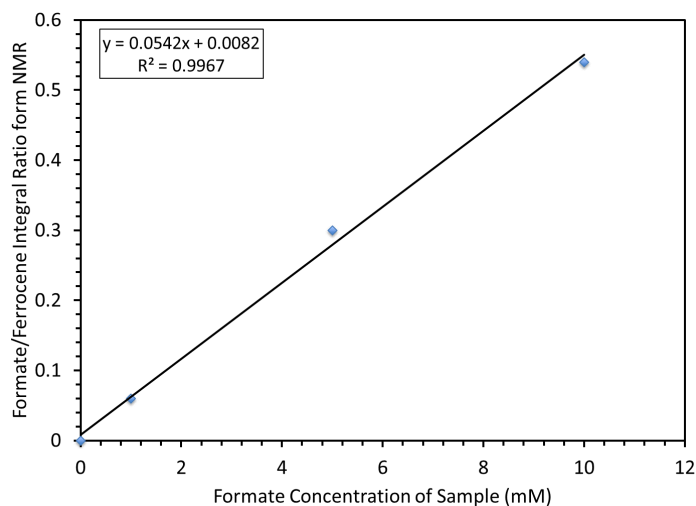


*Figure 6.S1:* NMR formate calibration curve in  $d_3$ -MeCN with ferrocene as an internal standard with Verkade's base.

*GC traces for photocatalytic experiments.*

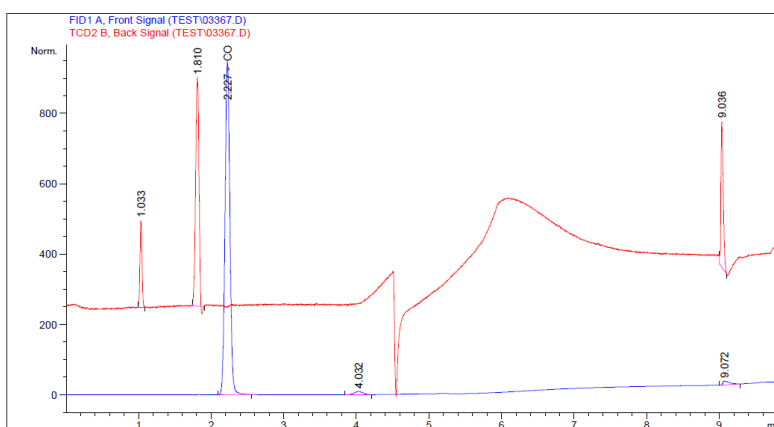


*Figure 6.S2:* Example GC-trace for photocatalytic reaction with **Catalyst 3** after 5hrs. FID detector is the blue trace and can detect CO and CH<sub>4</sub>. Only CO and H<sub>2</sub> is observed. The red trace is the TCD curve which can detect H<sub>2</sub> at ~1.0 minutes (not observed is

substantial quantities). The TCD curve shows peak only as noise in the GC spectrum from the heat ramp cycle, backflush, and trace O<sub>2</sub>. The y-axis is for the FID curve.

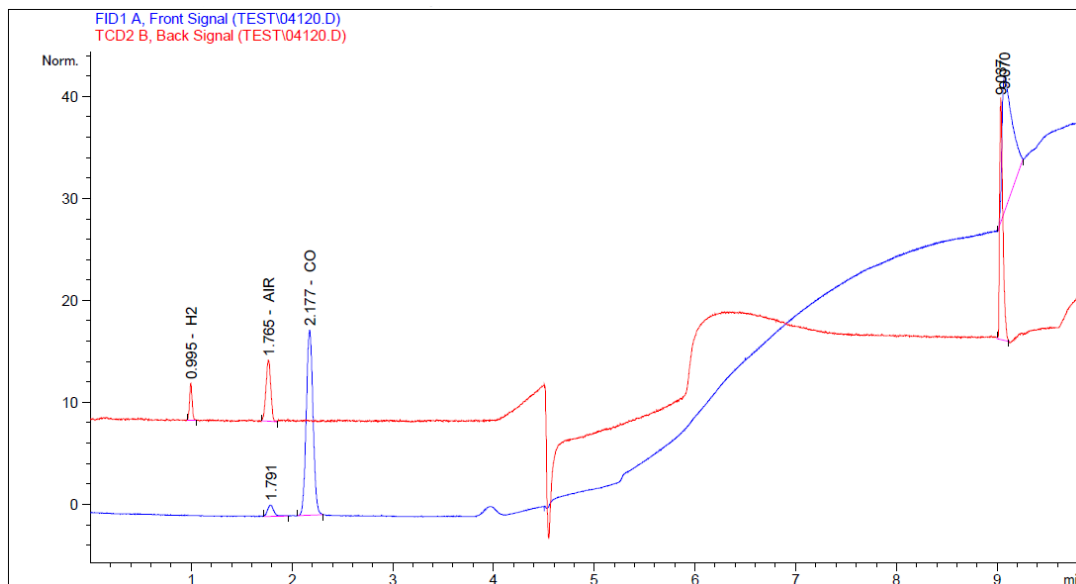


*Figure 6.S3:* Example GC-trace for photocatalytic reaction with **Catalyst 4** after 5hrs. FID detector is the blue trace and can detect CO and CH<sub>4</sub>. Only CO and H<sub>2</sub> is observed. The red trace is the TCD curve which can detect H<sub>2</sub> at ~1.0 minutes (not observed is substantial quantities). The TCD curve shows peak only as noise in the GC spectrum from the heat ramp cycle, backflush, and trace O<sub>2</sub>. The y-axis is for the FID curve.

*6.7.5 For the following CV studies:* Interestingly, the reduction potentials of the catalyst shift significantly over time (Figure S4 and S5). The first reduction wave of **3** under argon shifts from an onset of -1.5 V to -1.1 V, and under CO<sub>2</sub> a current increase at the first reduction wave is apparent. Providing the reductive disproportionation mechanism is active, this represents a negligible estimated overpotential for this process.<sup>30</sup> This dramatic shift under CV conditions suggests a new catalytically competent species is formed over time and which of the two complexes is present during dilute photocatalysis conditions is not obvious. We note the magnitude of the current with this shift is challenging to reproduce presumably due to solubility constraints as the solution does become cloudy over time (see page S28-S29 for a proposed explanation), making direct

study of this species challenging. Over time (~1 hour), a film deposits on the electrodes that explains the drift in potential. Reproducibility does seem to be enhanced with ambient fluorescent light exposure. Attempts to analyze the new species via NMR studies did not yield a noticeable change in the NMR spectrum, which suggests a high concentration of electrolyte might be necessary for this change to occur. However, this issue can be avoided by performing CV on fresh samples each time.

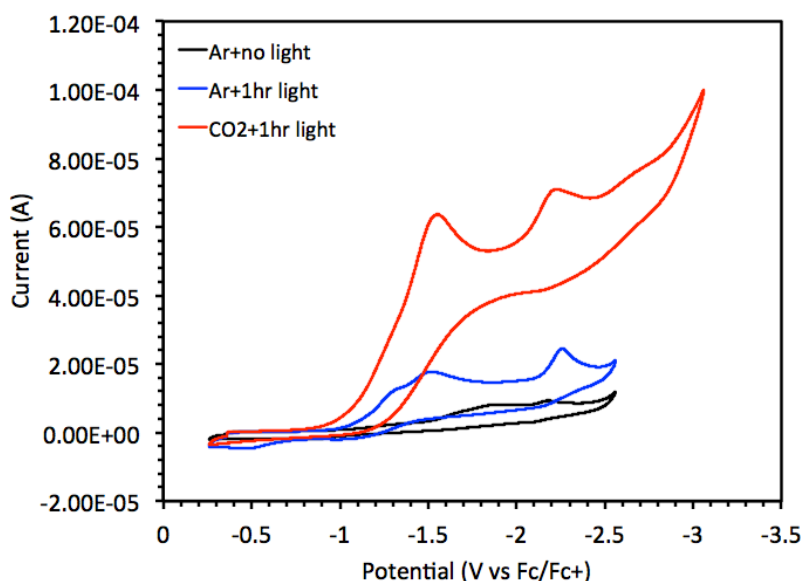


*Figure 6.S4:* Cyclic voltammograms of complex **3** initially under argon (black), after being exposed to ambient light at room temperature for an hour under argon (blue) and under CO<sub>2</sub> (red). CV curves are measured in acetonitrile with 0.1 M Bu<sub>4</sub>NPF<sub>6</sub> electrolyte. Glassy carbon working electrode, Ag/AgCl reference electrode, and platinum counter electrode are used for the measurements with a scan rate of 100 mV/s and ferrocene as the internal standard.

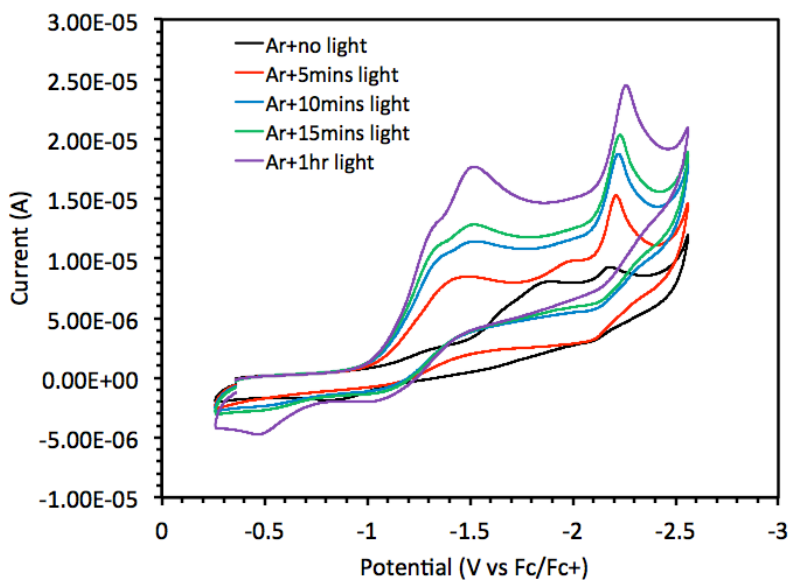


*Figure 6.S5:* Cyclic voltammograms of complex **3** under argon (black), after being exposed to ambient light at room temperature for various times under argon. CV curves are measured in acetonitrile with 0.1 M Bu<sub>4</sub>NPF<sub>6</sub> electrolyte. Glassy carbon working electrode, Ag/AgCl reference electrode, and platinum counter electrode are used for the measurements with a scan rate of 100 mV/s and ferrocene as the internal standard.

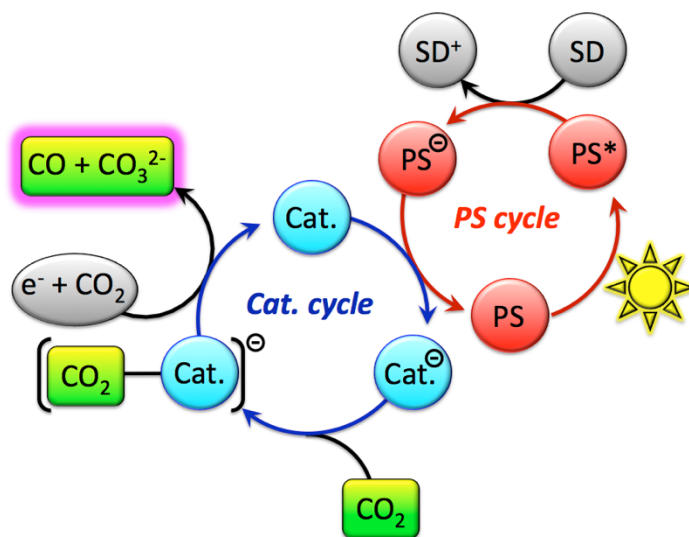


*Figure 6.S6:* A generic photocatalytic cycle for the reductive disproportionation of CO<sub>2</sub> to CO and CO<sub>3</sub><sup>2-</sup>.

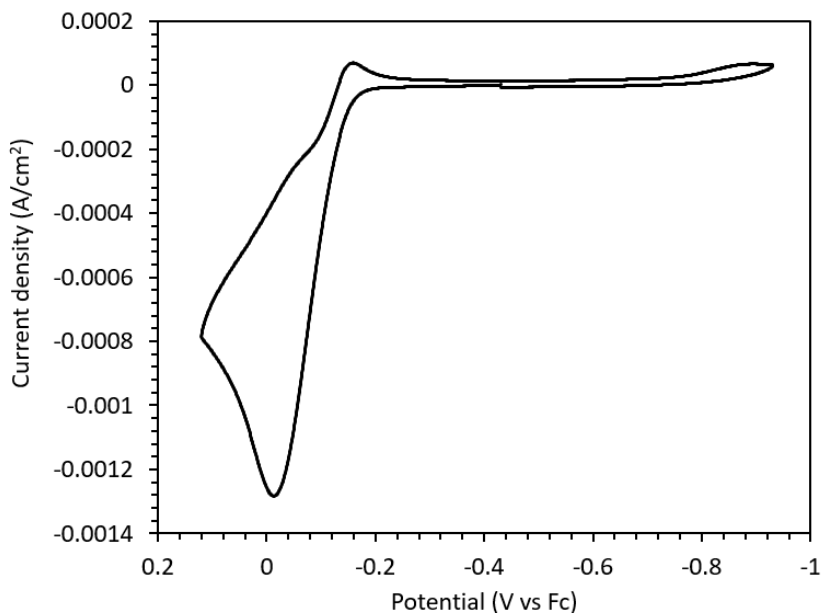


*Figure 6.S7:* CV of proton sponge in MeCN under Ar atmosphere. 0.1 M Bu<sub>4</sub>NPF<sub>6</sub> used as the supporting electrolyte and glassy carbon as the working electrode, and Pt is the counter and pseudo reference electrodes.

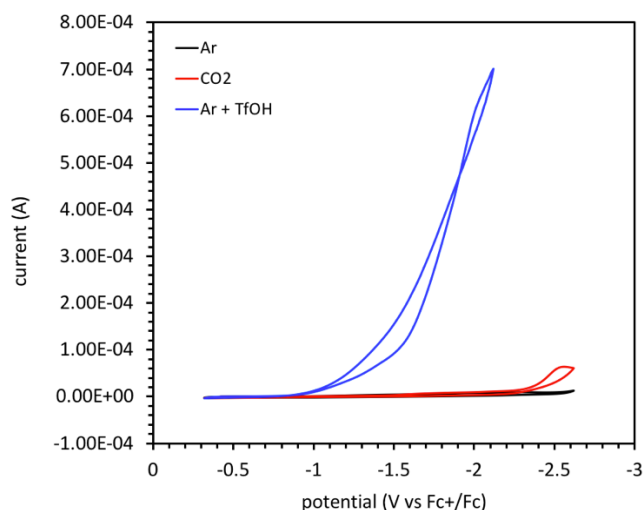


*Figure 6.S8:* CVs of **3** under argon, CO<sub>2</sub> and with TfOH present under argon. The electrolyte is 0.1 M Bu<sub>4</sub>NPF<sub>6</sub> in CH<sub>3</sub>CN with a glassy carbon working electrode, Ag/AgCl reference, and Pt counter electrodes. Each CV is a fresh solution of complex **3** (1.0 mM).

#### 6.7.6 Discussion of Figure S8

To probe the reduction potential of **3A** under the conditions evaluated photocatalytically with added triflic acid, cyclic voltammetry measurements were conducted. The black and red curves are the same curves presented in Figure 2 under

argon and CO<sub>2</sub>, respectively. The added blue curve is a CV collected in the presence of triflic acid (~0.33 M), which clearly shows a large shift in reduction potential to -0.93 V versus ferrocene (compared to -1.60 V in the absence of TfOH). Additionally, a large increase in current is observed which is indicative catalysis relating to H<sub>2</sub> formation. The large shift in reduction potential suggests a significant change in catalyst structure, which is likely due to ligand protonation leading to a dramatically easier reduced complex.

### 6.7.7 Characterization of Complex **3**.

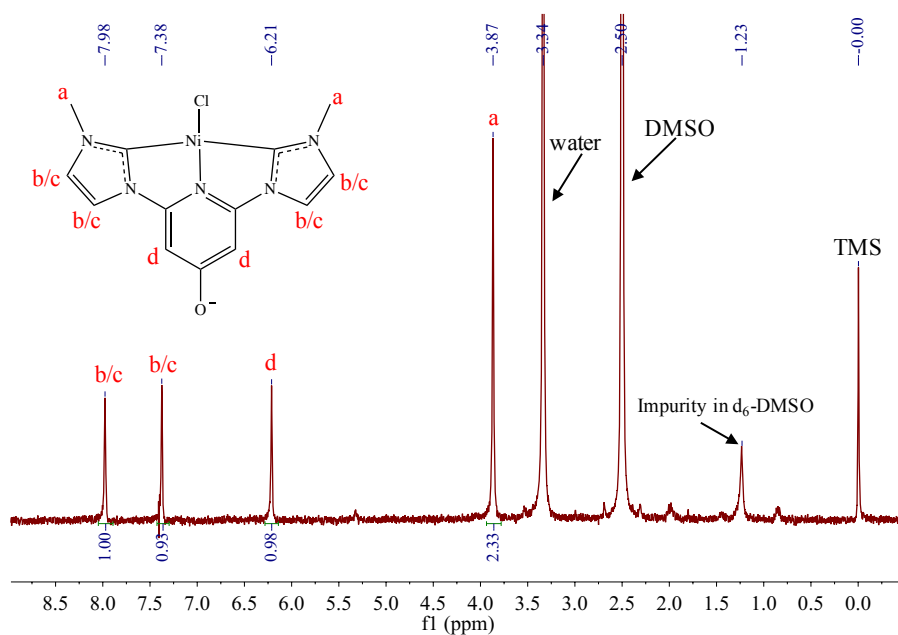


Figure 6.S9. <sup>1</sup>H-NMR (360 MHz) spectrum of complex **3** in *d*<sub>6</sub>-DMSO.

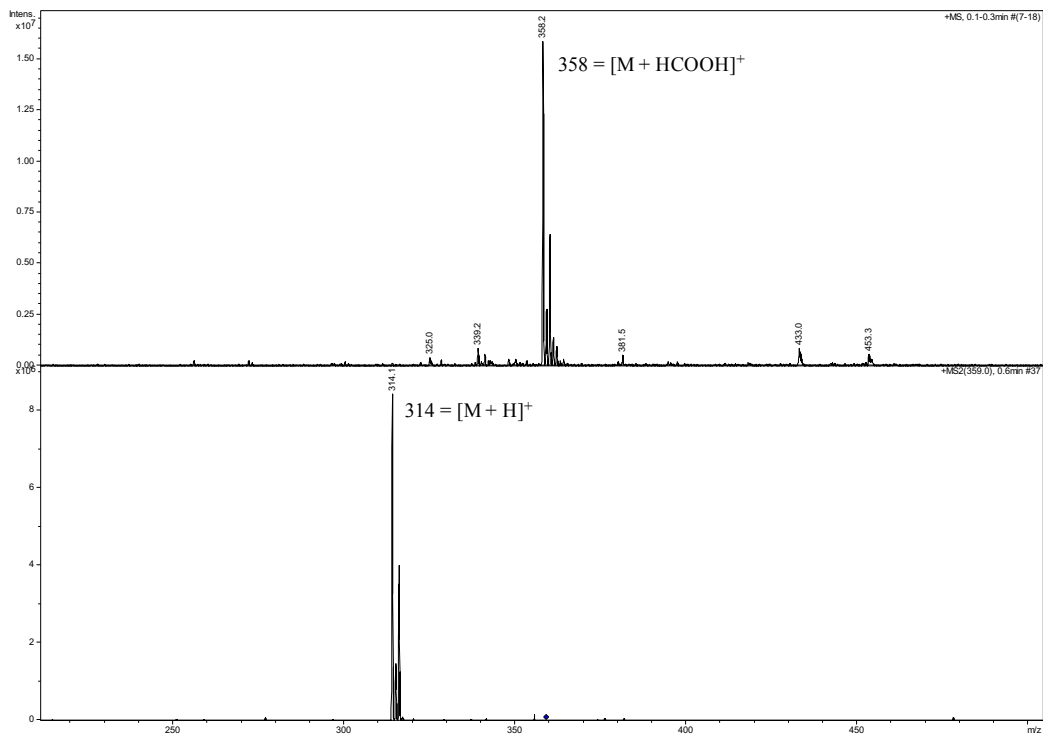


Figure 6.S10. ESI(+)-MS of complex **3** where M is NiON<sub>5</sub>C<sub>13</sub>H<sub>12</sub> and HCOOH is formic acid from the MS solvent. The bottom pane is MS/MS of the peak in the top pane with m/z of 358.

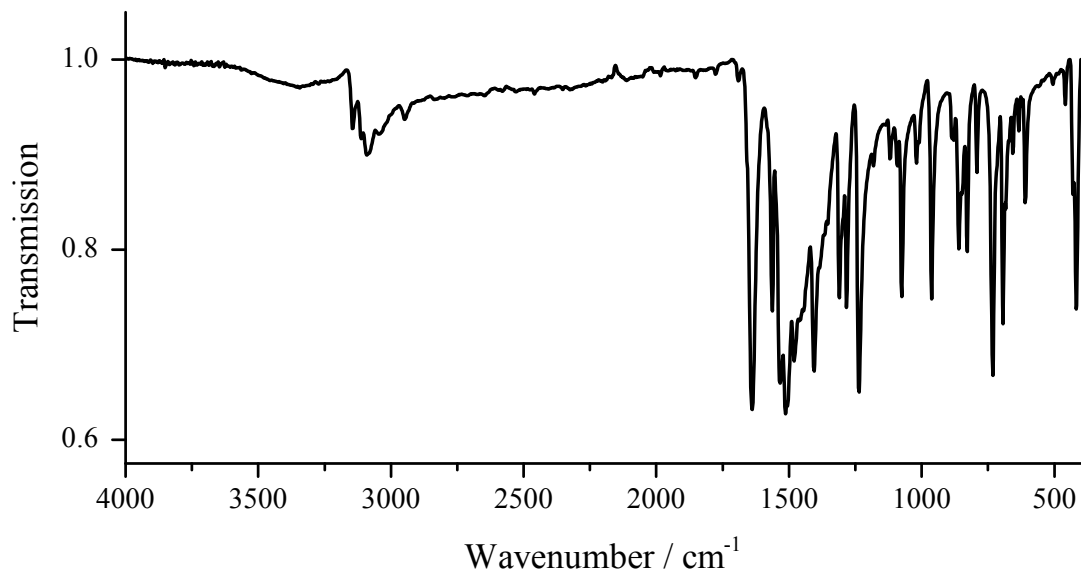


Figure 6.S11. FT-IR (ATR) of complex **3** in the solid state.

6.7.8 Qualitative Tests to Confirm the Presence of a Nickel Bound Inner Sphere Chloride in **3** (vs. an Outer Sphere Chloride).

1. See Figure S12 for the  $^1\text{H}$  NMR spectra from these experiments:

a. Adding a small amount (0.5 equiv) of AgOTf to complex **3** causes the peaks in the  $^1\text{H}$  NMR attributed to the pincer to broaden and decrease in intensity. A precipitate is formed that is presumably AgCl. There is also a peak at  $\sim 10$  ppm which suggests formation of the imidazolium salt, by reprotonating the NHC. We interpret this as a loss of stability upon removing an inner sphere Cl with silver. Removal of an outer sphere Cl would not change the  $^1\text{H}$  NMR spectrum as much, if at all.

b. By adding 1 equiv of AgOTf to **3** we see similar changes to in part a), but they are more pronounced.

c. Adding AgOTf (10 eq) to **3** leads to a precipitate and a shift in all the peaks in the  $^1\text{H}$  NMR. Once again, removal of an inner sphere chloride appears to have occurred. Also, with excess Ag(I) present, the NMR also suggests that a silver pincer complex was formed, the location of the peaks matches that for similar NHC complexes of silver (Papish *et al. Organometallics*, **2017**, *36*, 1091) (Danopoulos *et al. Dalton Trans.* 2008, 1087). Note that the Danopoulos paper had silver(I) displacing Ni(II) to form a silver complex, as we propose here.

2. Adding  $\text{CH}_3\text{CN}$  does not lead to a change of the  $^1\text{H}$  NMR spectrum in DMSO (Figure S13). This suggests that acetonitrile does not readily displace the bound halide ligand. If a water ligand was bound to Ni(II), it might be readily displaced by acetonitrile.

We believe the combined evidence above supports that **3** is [(pincer)NiCl] with an inner sphere chloride.

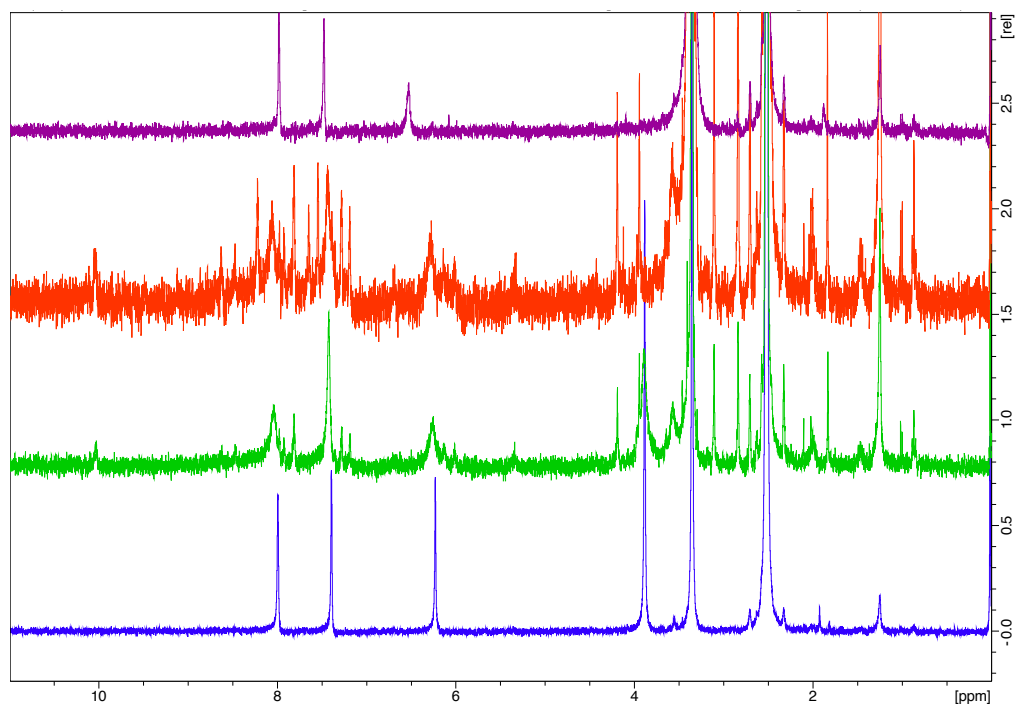


*Figure 6.S12.* <sup>1</sup>H-NMR (360 MHz) spectra of complex **3** in d<sub>6</sub>-DMSO (blue spectrum) with the addition of 0.5 equivalents of AgOTf (green spectrum), 1.0 equivalents of AgOTf (red spectrum), and 10 equivalents of AgOTf (purple spectrum).

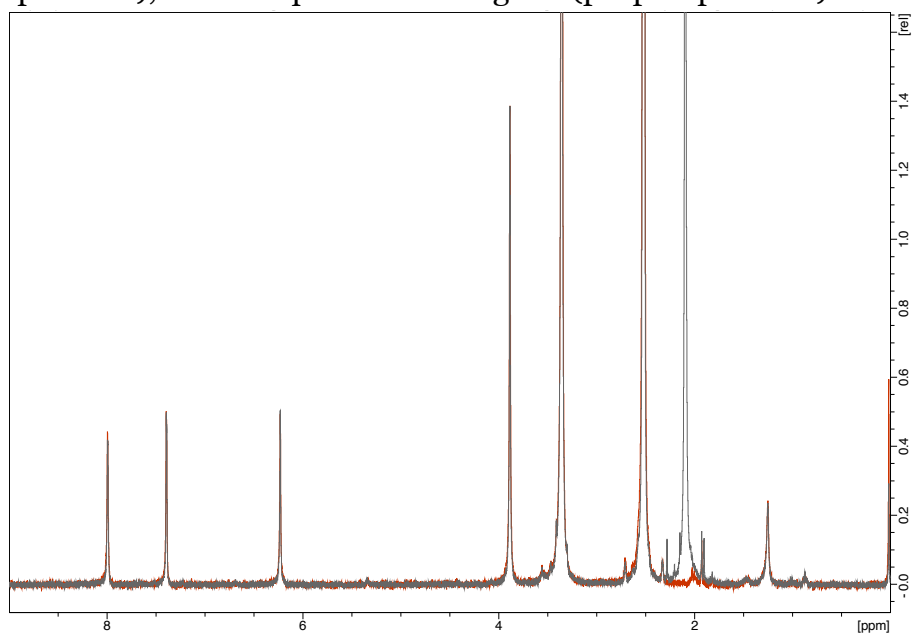


*Figure 6.S13.* <sup>1</sup>H-NMR (360 MHz) spectra of complex **3** in d<sub>6</sub>-DMSO (red spectrum) with the addition of 10 equivalents of acetonitrile (grey spectrum). The additional peak at ~2 ppm is free acetonitrile and there is no evidence of Ni(II) bound acetonitrile.

### 6.6.9 $pK_a$ Studies of Complex **3**.

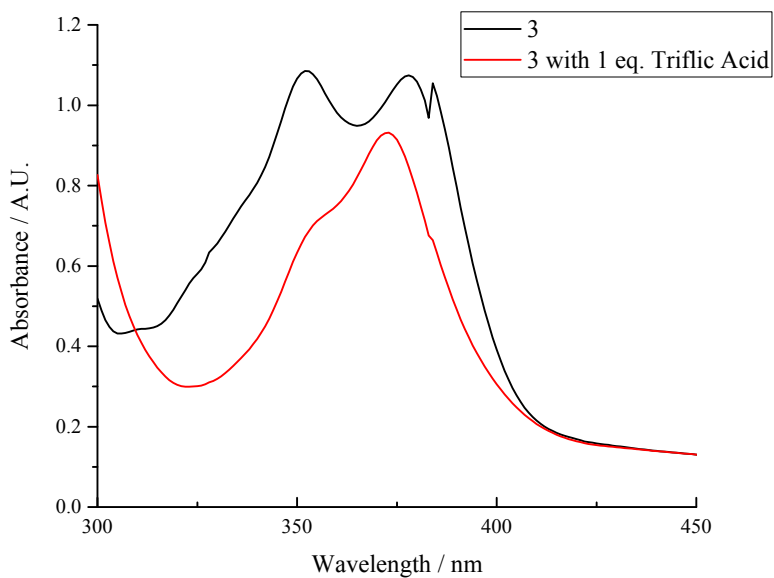


Figure 6.S14. UV-vis spectra of complex **3** (0.26 mM) in DMSO with the addition of a 0.08 M triflic acid solution in DMSO.

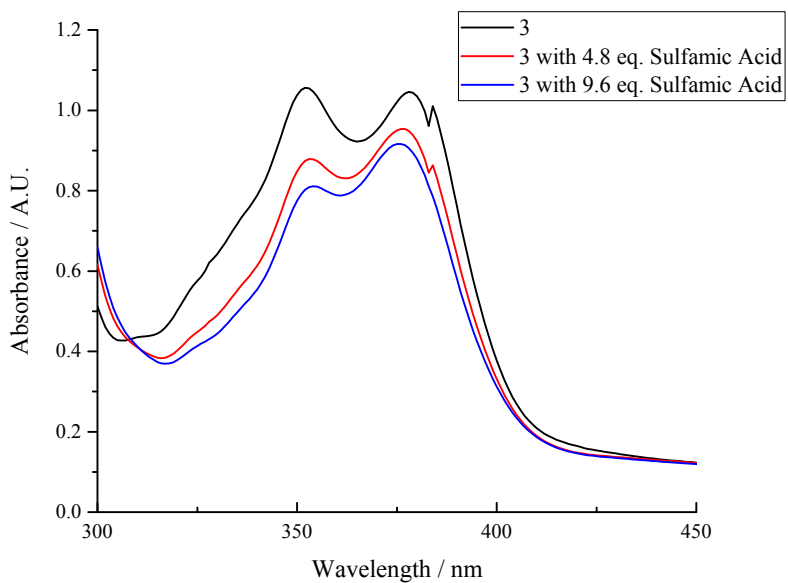
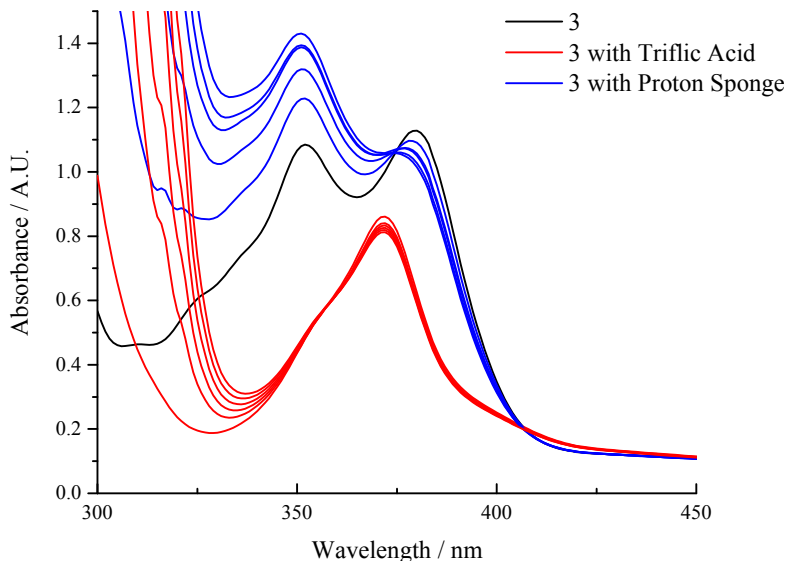
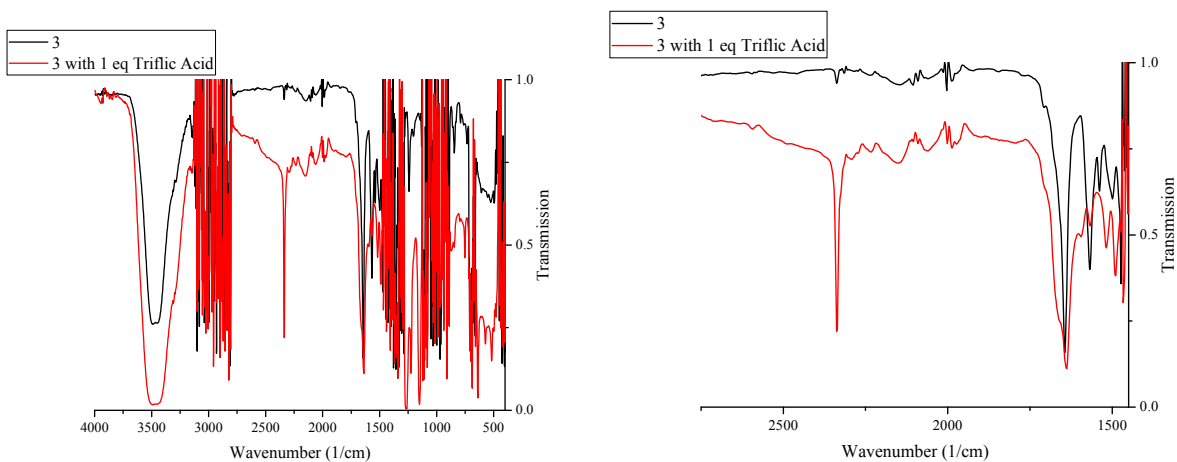


Figure 6.S15. UV-vis spectra of complex **3** (0.26 mM) in DMSO with the addition of a 0.08 M sulfamic acid solution in DMSO.



*Figure 6.S16.* UV-vis spectra of complex **3** (0.28 mM) in DMSO with the alternating addition of triflic acid (1 eq., red spectra) and proton sponge (1 eq., blue spectra), showing the reversibility of the protonation and deprotonation. The increase in intensity of the peak at  $\sim 345$  nm during each cycle is likely due to a slight excess of proton sponge added. (Proton sponge has a strong, broad absorption with a  $\lambda_{\text{max}}$  at 340 nm).



*Figure 6.S17.* FT-IR spectra of complex **3** (8.3 mM) in DMSO (black spectra) with the addition of 1 equivalent of triflic acid (red spectra). The large areas of excessive noise are due to the absorptions of the solvent, DMSO (See Figure S16). The peak at  $1568\text{ cm}^{-1}$ , assigned to the C=O stretch, decreased with the addition of triflic acid, while the peak at  $1638\text{ cm}^{-1}$ , assigned to the C=C stretch, remained approximately unchanged.

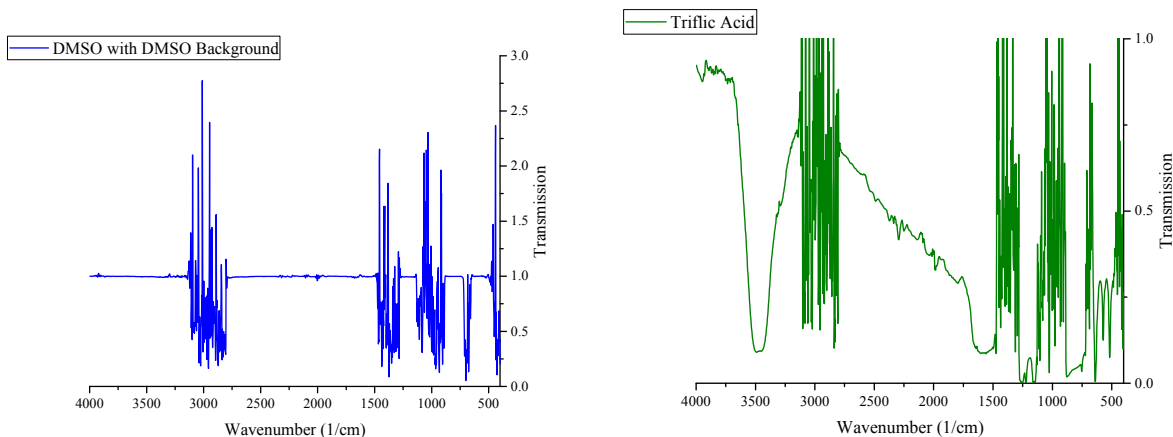


*Figure 6.S18.* (Left) FT-IR spectrum of DMSO after a background of DMSO was taken. (Right) FT-IR spectrum of triflic acid in DMSO.

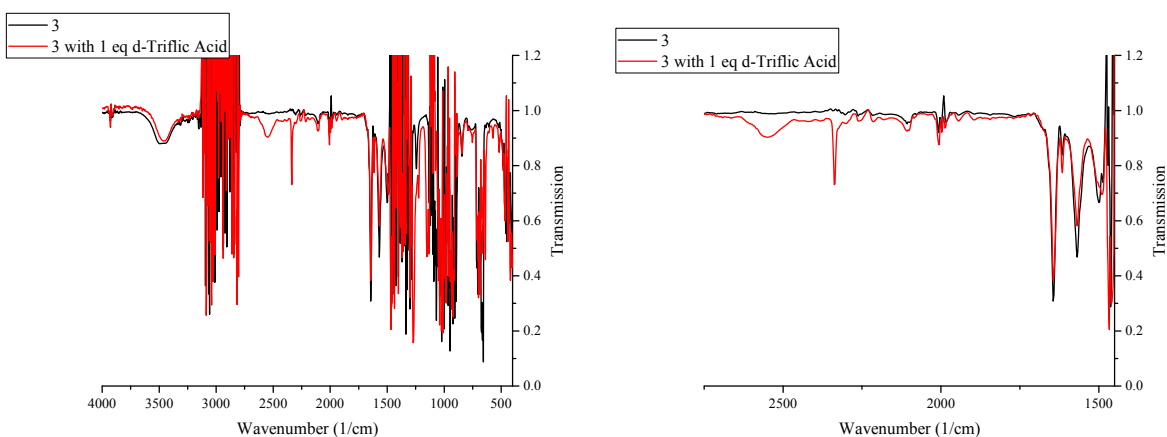


*Figure 6.S19.* FT-IR spectra of complex **3** (5.5 mM) in DMSO (black spectra) with the addition of 1 equivalent of deuterated-triflic acid (red spectra). The large areas of excessive noise are due to the absorptions of the solvent, DMSO (see Figure S16). The peak at 2556  $\text{cm}^{-1}$  is the OD stretch. The peak at 1568  $\text{cm}^{-1}$  also decreased.

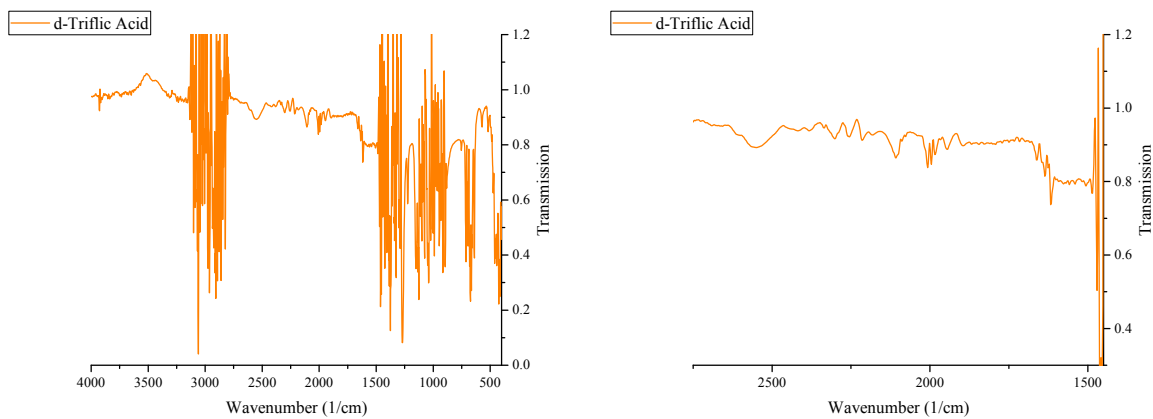


Figure 6.S20. FT-IR spectrum of d-triflic acid in DMSO.

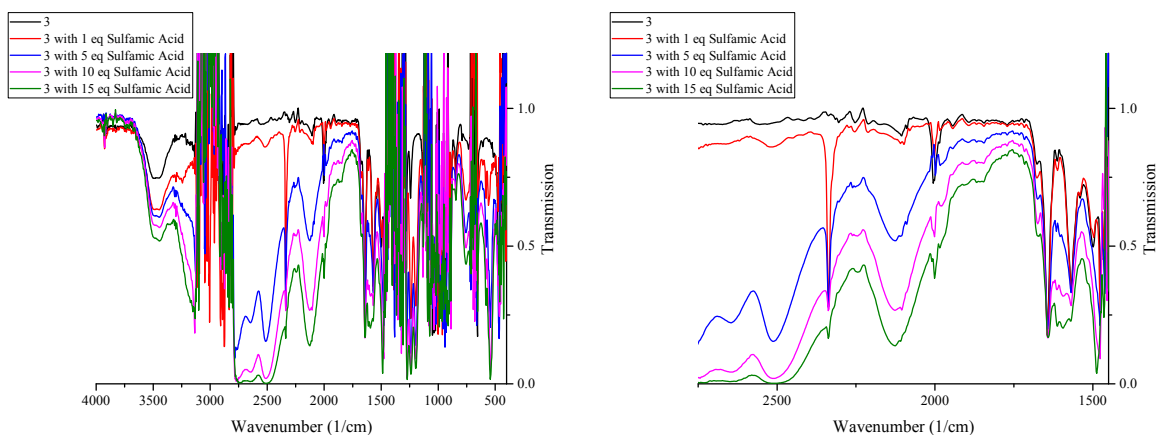


Figure 6.S21. FT-IR spectra of complex **3** (6.5 mM) in DMSO (black spectra) with the addition of multiple equivalents of sulfamic acid. The large areas of excessive noise are due to the absorptions of the solvent, DMSO (See Figure S16). Unfortunately, sulfamic acid has large absorptions in the IR (see Figure S20), so any change in the peak at 1568  $\text{cm}^{-1}$  is obscured.

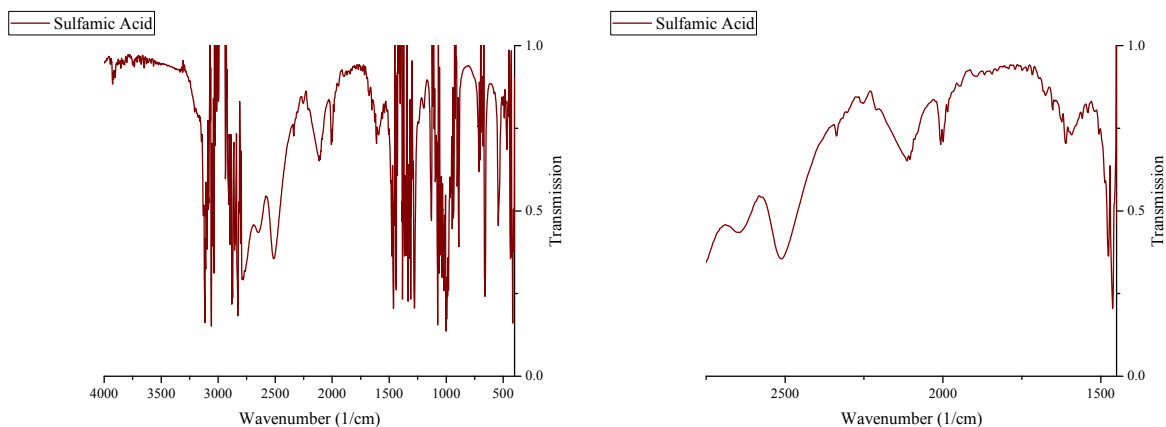


Figure 6.S22. FT-IR spectrum of sulfamic acid in DMSO.

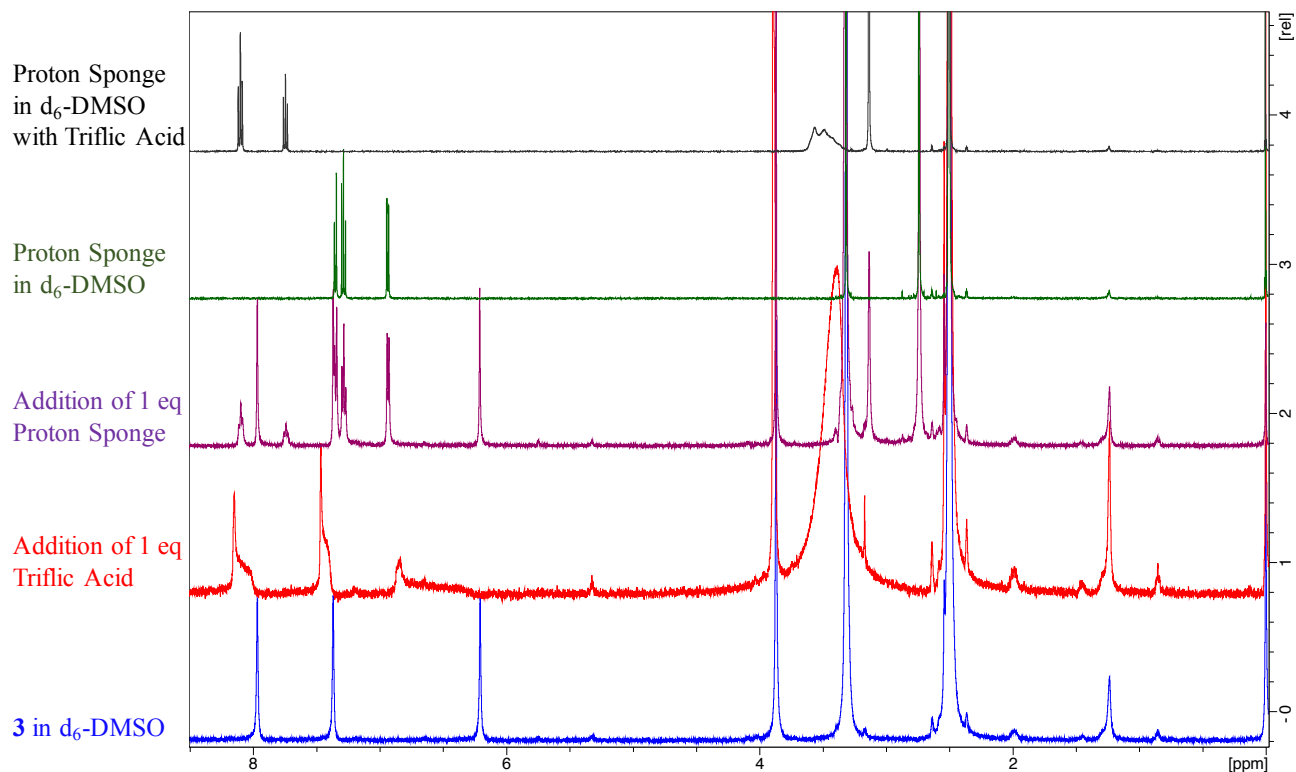
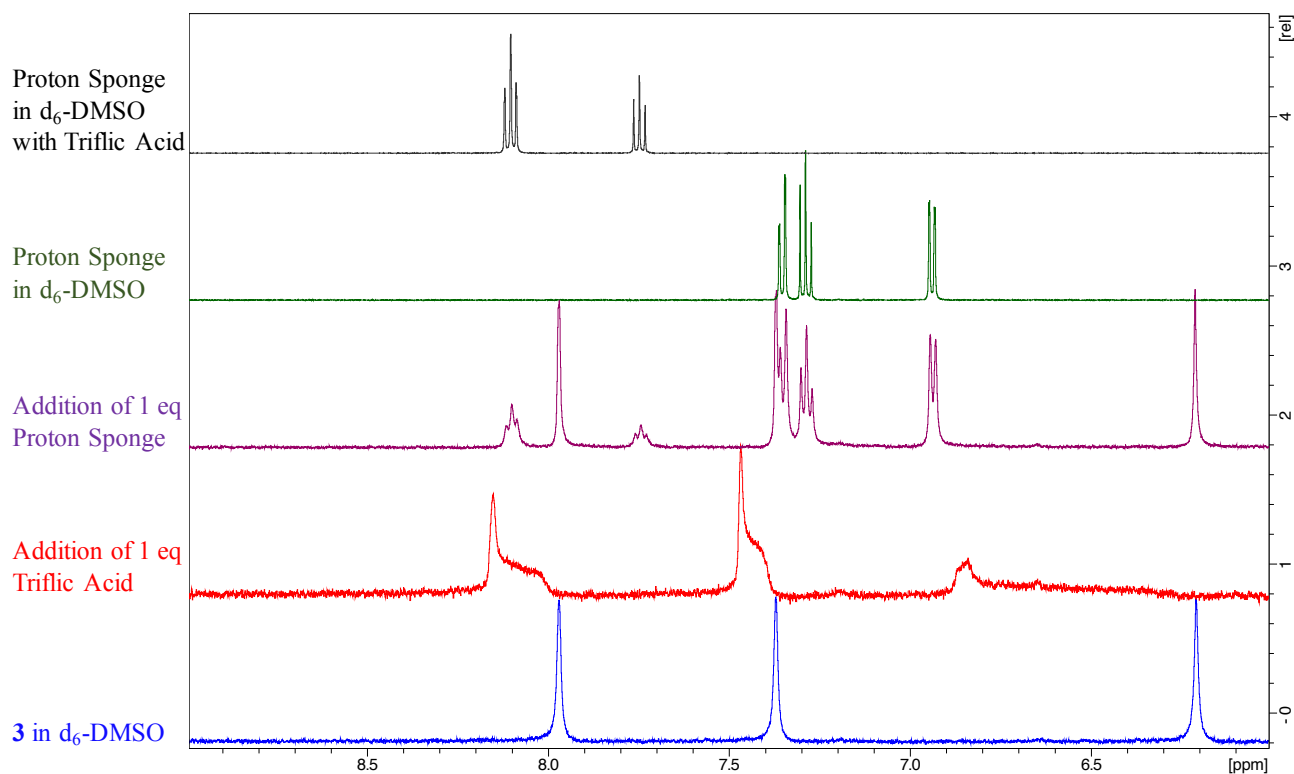


Figure 6.S23a.  $^1\text{H}$ -NMR spectra of a solution of complex **3** in  $\text{d}_6$ -DMSO (blue spectrum) with the addition of 1 equivalent of triflic acid (red spectrum), followed by the addition of 1 equivalent of proton sponge (violet spectrum). The NMR spectra of proton sponge (green spectrum) and proton sponge with the addition of triflic acid (black spectrum) in  $\text{d}_6$ -DMSO are also shown.



*Figure 6.S23b.* The aromatic region of the  $^1\text{H}$ -NMR spectra shown in Figure S21a. Upon the addition of acid (blue spectrum to red spectrum), all of the peaks shift downfield, with the proton of the pyridinol ring shifting the most (6.21 ppm to 6.98 ppm). This is consistent with the proton's environment changing from an alkene in the quinoidal deprotonated form to aromatic in the pyridinol protonated form. With the addition of base to the solution (red spectrum to violet spectrum), the peaks shift back to the original chemical shifts of the deprotonated complex **3**; this demonstrates the reversibility of the protonation and deprotonation.

#### 6.7.10 Isolation and Characterization of Complex 3A.

To a solution of complex **3** (5.8 mg, 17  $\mu\text{mol}$ ) in DMSO (2.0 mL), 1 equivalent of triflic acid was added. The solution immediately changed from light orange to light yellow. After sitting undisturbed for 48 hr, a bright yellow solid had precipitated out of the solution. The solid was collected by filtration and washed 3 times with 0.5 mL of dichloromethane. <1 mg of the solid was recovered. The characterization data of the solid follow.

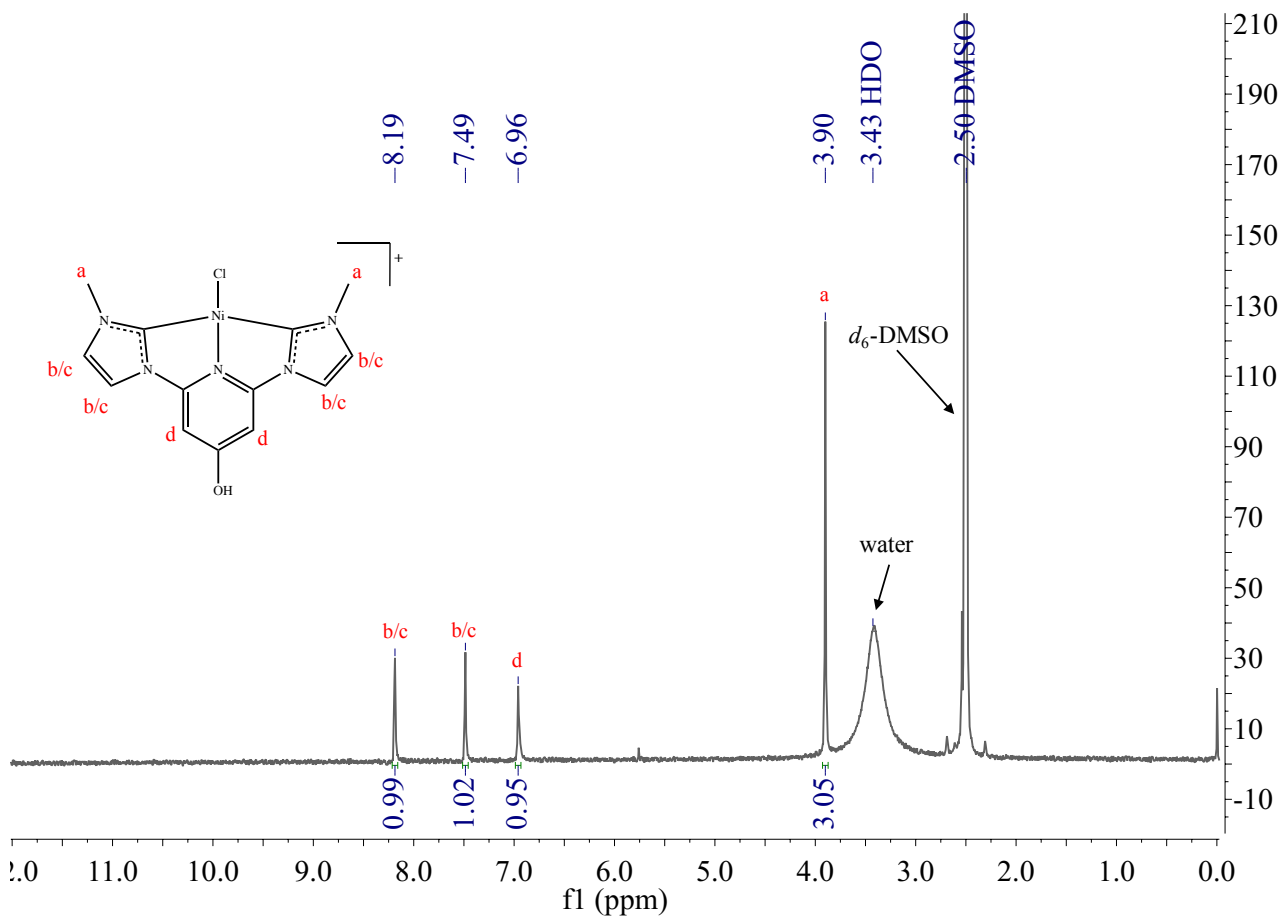
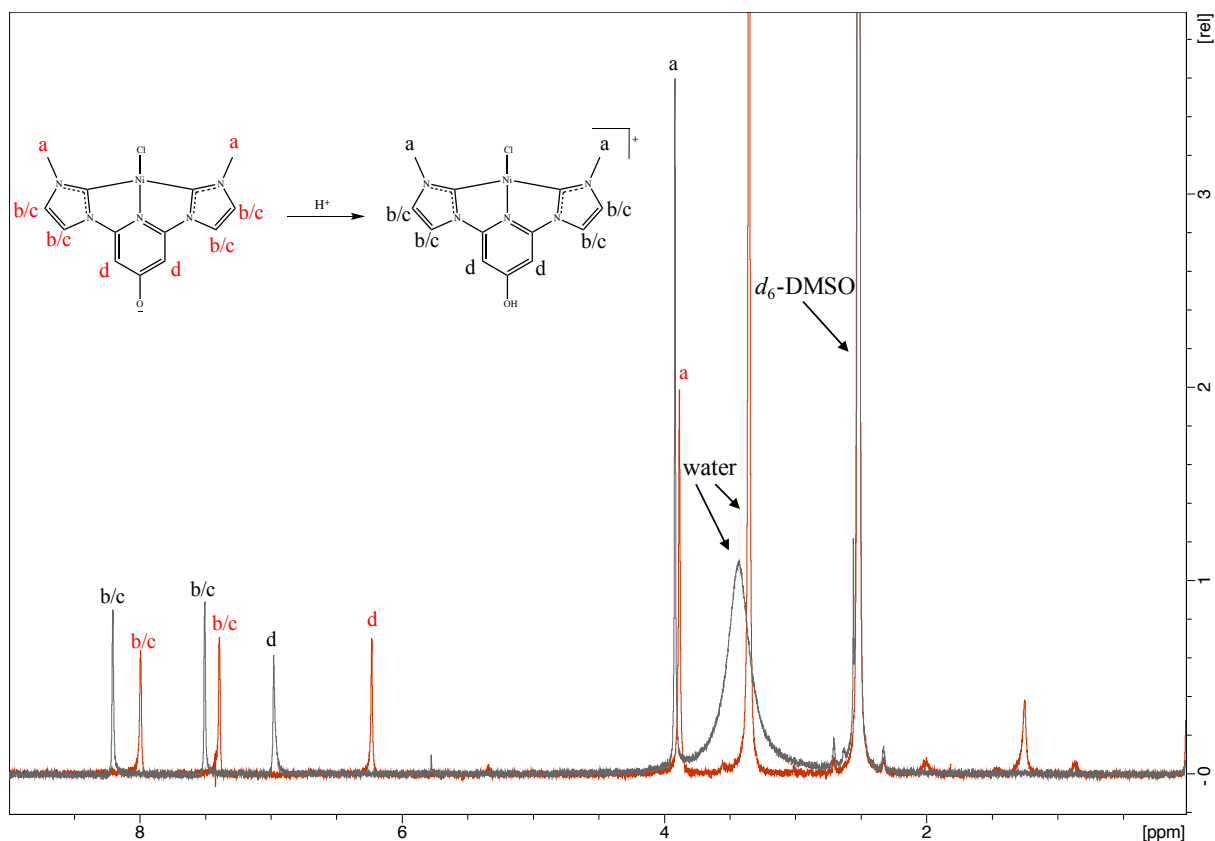


Figure 6.S24.  $^1\text{H-NMR}$  (360 MHz) spectrum of complex **3A** in  $d_6$ -DMSO.



*Figure 6.S25.* Overlaid  $^1\text{H}$ -NMR spectra of complexes **3** (crimson spectrum) and **3A** (grey spectrum) in  $d_6$ -DMSO. As observed with the in situ-generated protonated complex **3A** (Figure S21), all of the proton peaks of complex **3A** are shifted downfield relative to complex **3**. The largest shift is the pyridinol proton (labeled “d”). The residual water peak in the solvent has also broadened significantly in the spectrum of **3A**. This is commonly observed with compounds containing a hydroxyl group.

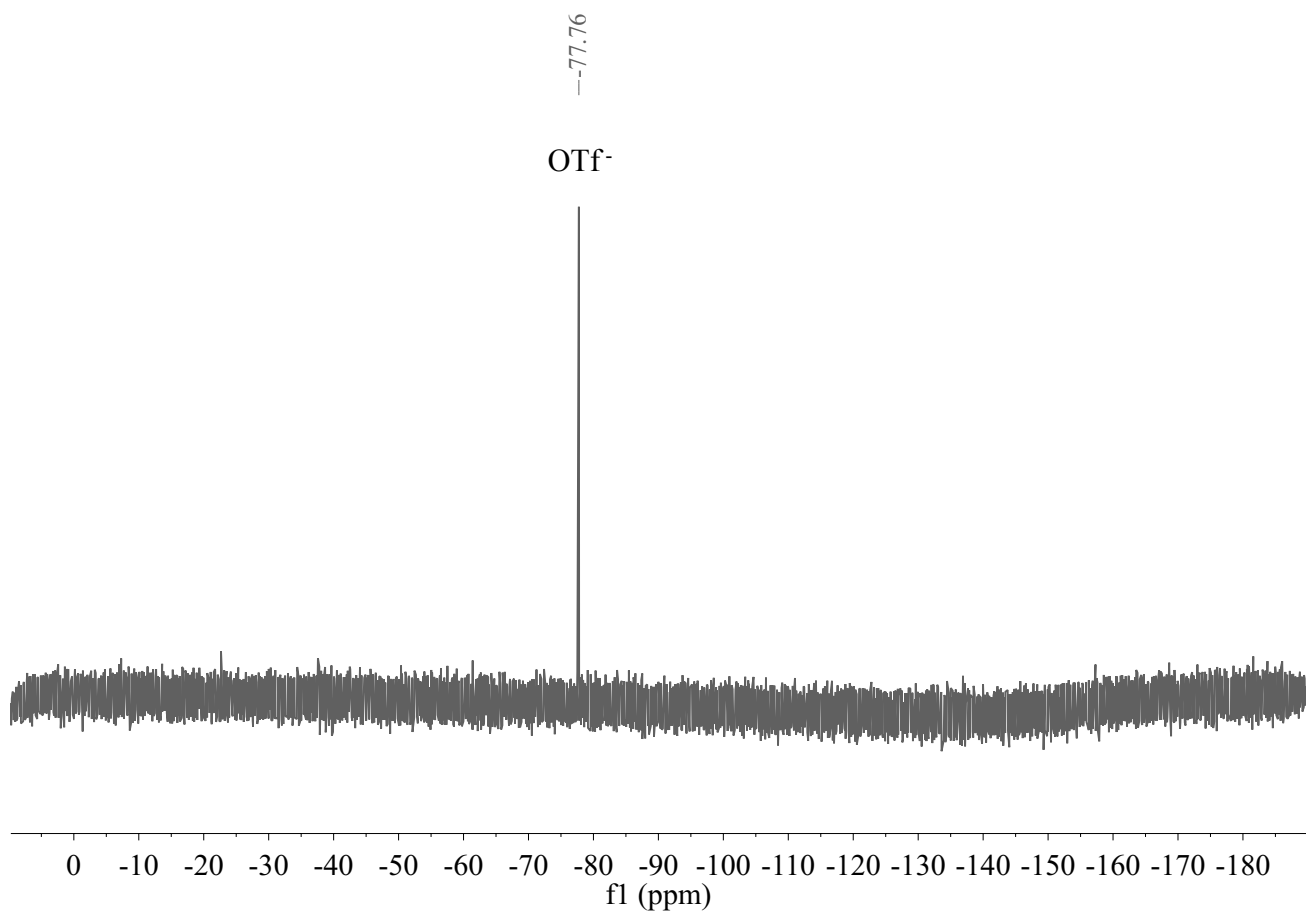


Figure 6.S26.  $^{19}\text{F}$ -NMR (338.8 MHz) spectrum of complex **3A** in  $d_6$ -DMSO.

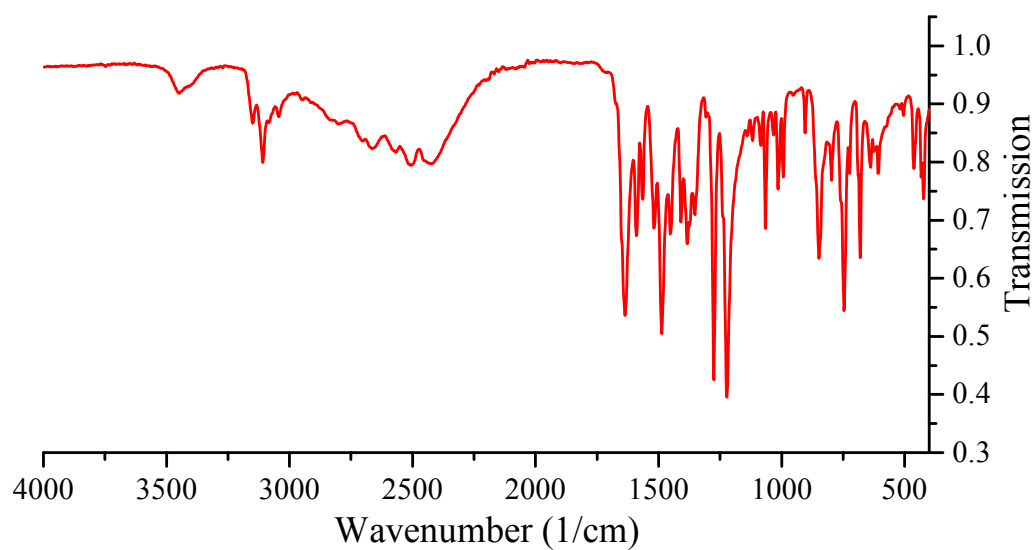
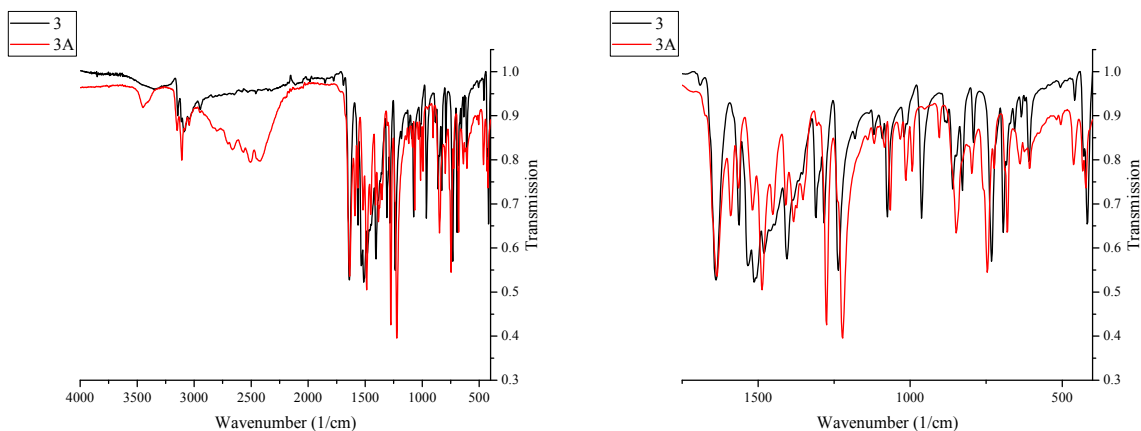
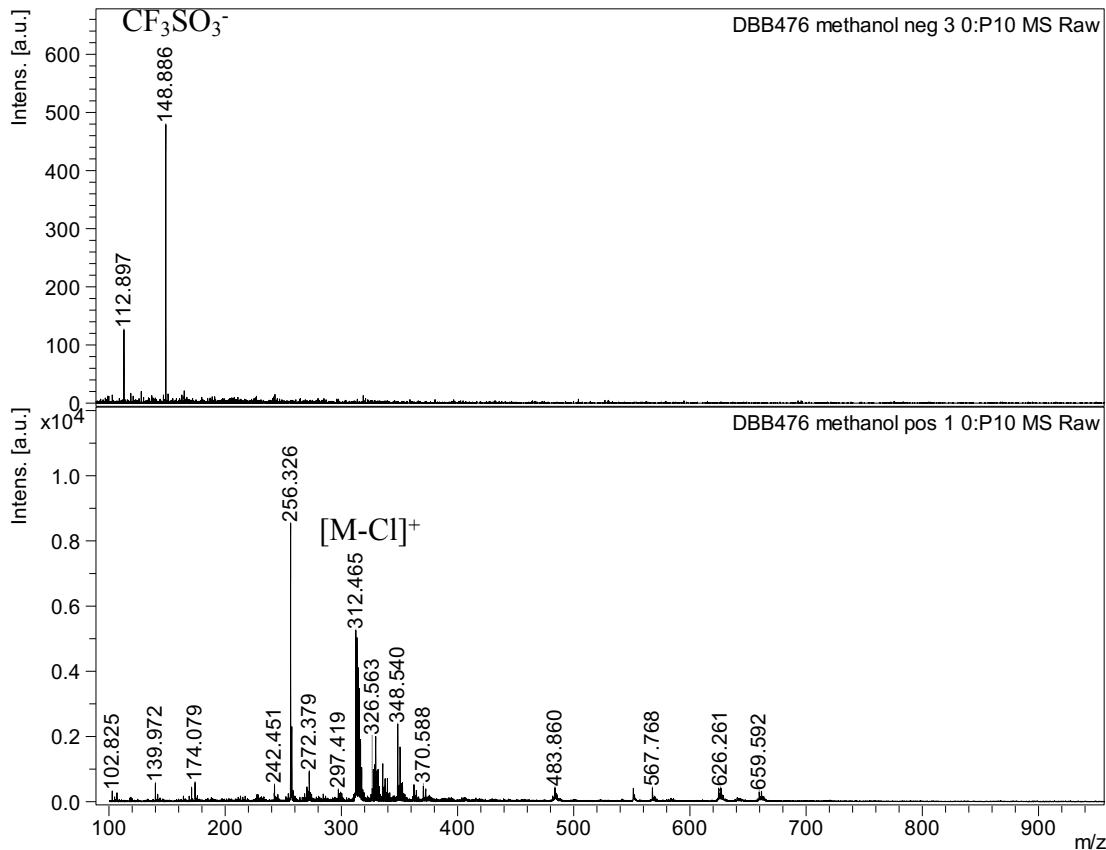


Figure 6.S27. FT-IR (ATR) spectrum of complex **3A** in the solid state.



**Figure 6.S28.** FT-IR (ATR) spectra of complexes **3** (black spectrum) and **3A** (red spectrum) in the solid state. The peak at  $1568\text{ cm}^{-1}$ , assigned to the C=O stretch, is diminished in **3A** compared to **3**. The peak at  $1638\text{ cm}^{-1}$ , assigned to the C=C stretch, remains constant in both spectra. A new peak at  $3455\text{ cm}^{-1}$  appears in the spectrum of **3A**, corresponding to the OH stretch. The broad peaks from  $\sim 2300\text{ cm}^{-1}$  to  $\sim 3000\text{ cm}^{-1}$  in the spectrum of **3A** are probably due to the triflate counterion.



**Figure 6.S29a.** MALDI-MS spectrum of complex **3A**. (Top) Spectrum in negative mode.  $[\text{CF}_3\text{SO}_3]^-$  is the triflate counterion. (Bottom) Spectrum in positive mode. M is  $\text{NiClON}_5\text{C}_{13}\text{H}_{12}$ .

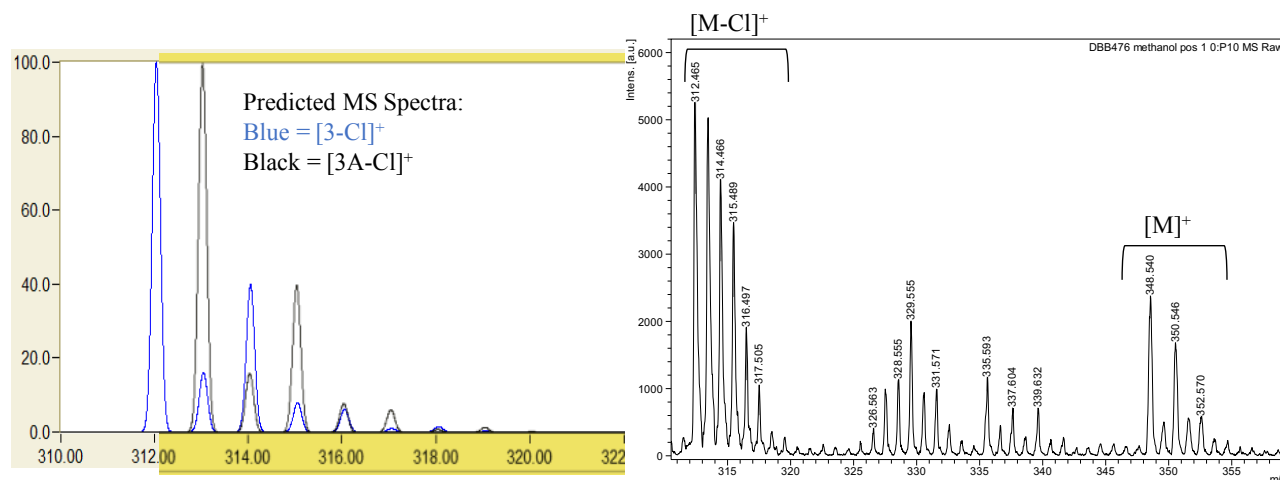


**Figure 6.S29b.** MALDI-MS spectrum of complex **3A**. (Left) Predicted isotopic pattern of a 50:50 mix of **3** and **3A**, with a chloride lost. (Right) MALDI-MS spectrum of **3A**. The  $[M-Cl]^+$  peak corresponds to a ~1:1 ratio of **3** to **3A**, which matches the predicted pattern on the right. Deprotonation of **3A** to yield **3** could occur in the solvent of the MS.

#### 6.7.11 Summary of Data from $pK_a$ Studies.

All of the data presented above are consistent with a reversible protonation of complex **3** upon the addition of triflic acid. The UV-vis spectra reversibly switch back-and-forth upon successive additions of triflic acid and proton sponge. In the IR spectra, the peak at  $1568\text{ cm}^{-1}$ , assigned to the C=O stretch (corroborated by computations, vide infra), decreases in intensity with the addition of triflic acid, both in situ and in the isolated complex **3A**. In the  $^1\text{H-NMR}$  spectra, the peaks all shift downfield with the addition of triflic acid to complex **3**, with the pyridinol proton being the most affected. These changes in the chemical shifts in the  $^1\text{H-NMR}$  are reversible, as observed with the successive additions of triflic acid and proton sponge.

#### 6.7.12 Computational Methods

All computations were carried out using the Gaussian 09<sup>31</sup> implementation of B3LYP<sup>32-33</sup> or PBE/PBE<sup>34-35</sup> (with auto-fitting functions)<sup>36-37</sup>. The basis set for nickel was the Hay

and Wadt basis set (BS) and effective core potential (ECP) combination (LANL2DZ)<sup>38-39</sup> as modified by Couty and Hall<sup>40</sup> where the two outermost p functions have been replaced by a (41) split of the optimized nickel 4p function. The basis set for chlorine was the [LANL2DZ(d,p)]<sup>38-39, 41</sup> basis set (BS) and effective core potential (ECP) combination. The 6-31G(d')<sup>42-43</sup> basis sets were used for all other atoms. Spherical harmonic d functions were used throughout, *i.e.*, there are 5 angular basis functions per d function. This basis set combination is referred to as BS1. All geometries were fully optimized with corresponding analytical frequency computations to ensure a zeroth-order saddle-point was achieved. Solvent optimizations utilized the IEF-PCM solvation model with UAKS radii and parameters consistent with either acetonitrile or DMSO (for determination of p*K*<sub>a</sub> only) as the solvent. The free energy of a proton in DMSO (−280.0 kcal mol<sup>−1</sup>) was determined using the following equation:

$$G_{\text{H}^+}^{\text{soln}} = G_{\text{H}^+}^{\text{gas}} + G_{\text{H}^+}^{\text{solv}}$$

where  $G_{\text{H}^+}^{\text{gas}}$  is the gas-phase free energy of a proton (−6.28 kcal mol<sup>−1</sup>),<sup>44</sup>  $G_{\text{H}^+}^{\text{solv}}$  is the recommended free energy of solvation of a proton in DMSO (−273.7 kcal mol<sup>−1</sup>),<sup>45</sup> and  $G_{\text{H}^+}^{\text{soln}}$  is the solution free energy of a proton.

### 5.6.13 Computational Results

Complex **3** contains a monoanionic pincer that could be formally represented as a phenoxide. Computations with no geometry constraints result in a bonding pattern that is more consistent with a quinonidal resonance form, which contains more C–O double bond character and places the formal negative charge on the N<sub>py</sub> atom. The C–O bond

length is significantly shorter in **3** compared to **3A** (1.25 vs 1.33 Å), indicating that there is increased double-bond character between carbon and oxygen. Reduction events and deprotonation of any species results in increase in negative charge on O, N<sub>py</sub>, and Ni. One-electron reduction from **3A** to **3A<sup>o</sup>** or **3** to **3<sup>-</sup>** results in a gain of a full -1 charge. These reduction events lead to a significant increase in negative charge for the Cl. Other atoms (Ni, N<sub>py</sub>, C, and O) also have increases their negative charge. Dechlorination (**3A<sup>o</sup>** to **5A** or **3<sup>-</sup>** to **5**) results in a significant loss in negative charge for Ni and a small increase in negative charge on N<sub>py</sub>. Dechlorination results in no change in charge for oxygen (**3A<sup>o</sup>** to **5A**) or a decrease in negative charge (**3<sup>-</sup>** to **5**). Dechlorination from **3A<sup>o</sup>** to **5A** results in a loss of a full -1 charge from the complex. However, since the charge of Cl in **3A<sup>o</sup>** is ~-0.79, there is a net loss of ~0.21 units of negative charge from all other atoms in **3A<sup>o</sup>** upon production of **5A**.

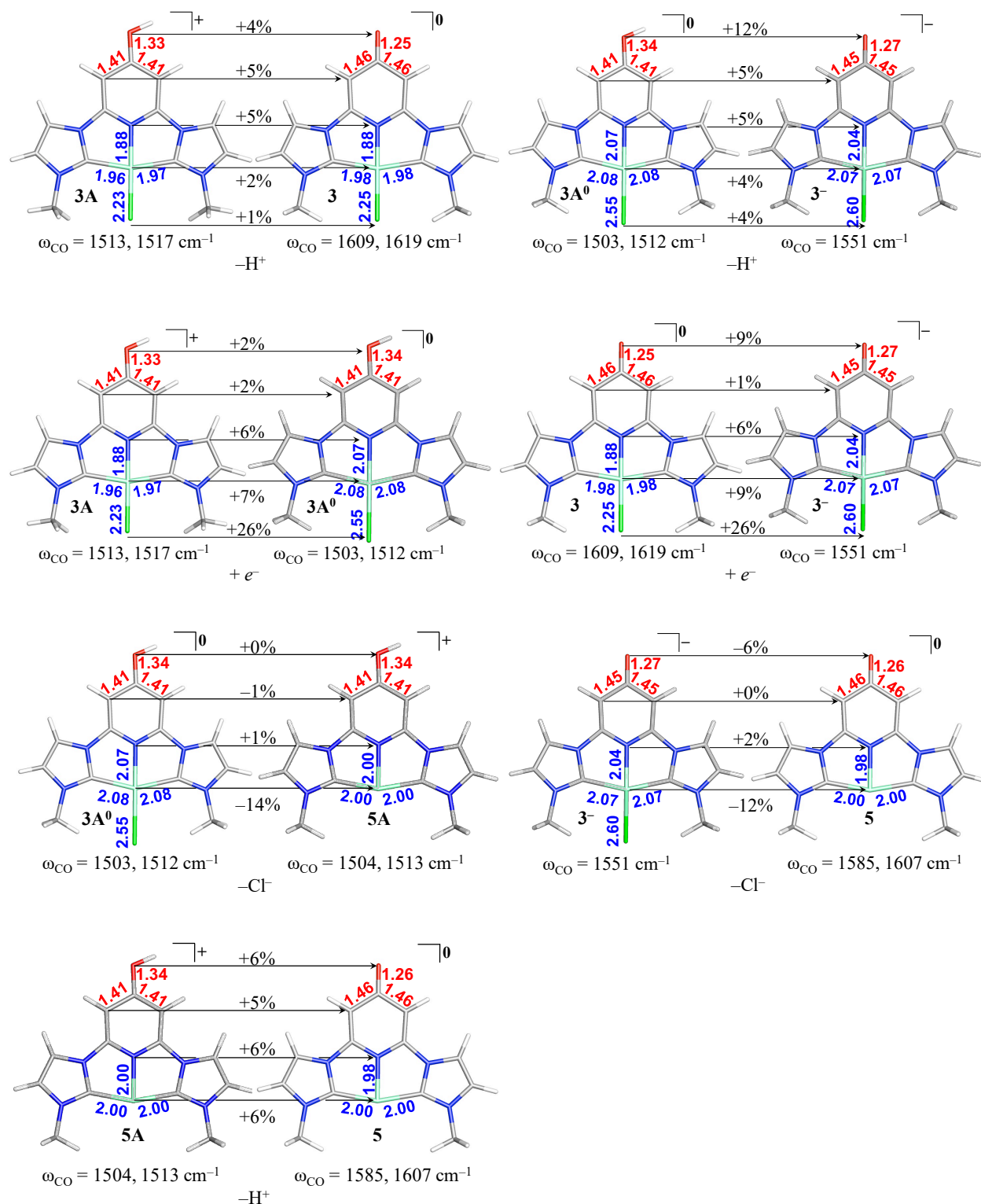
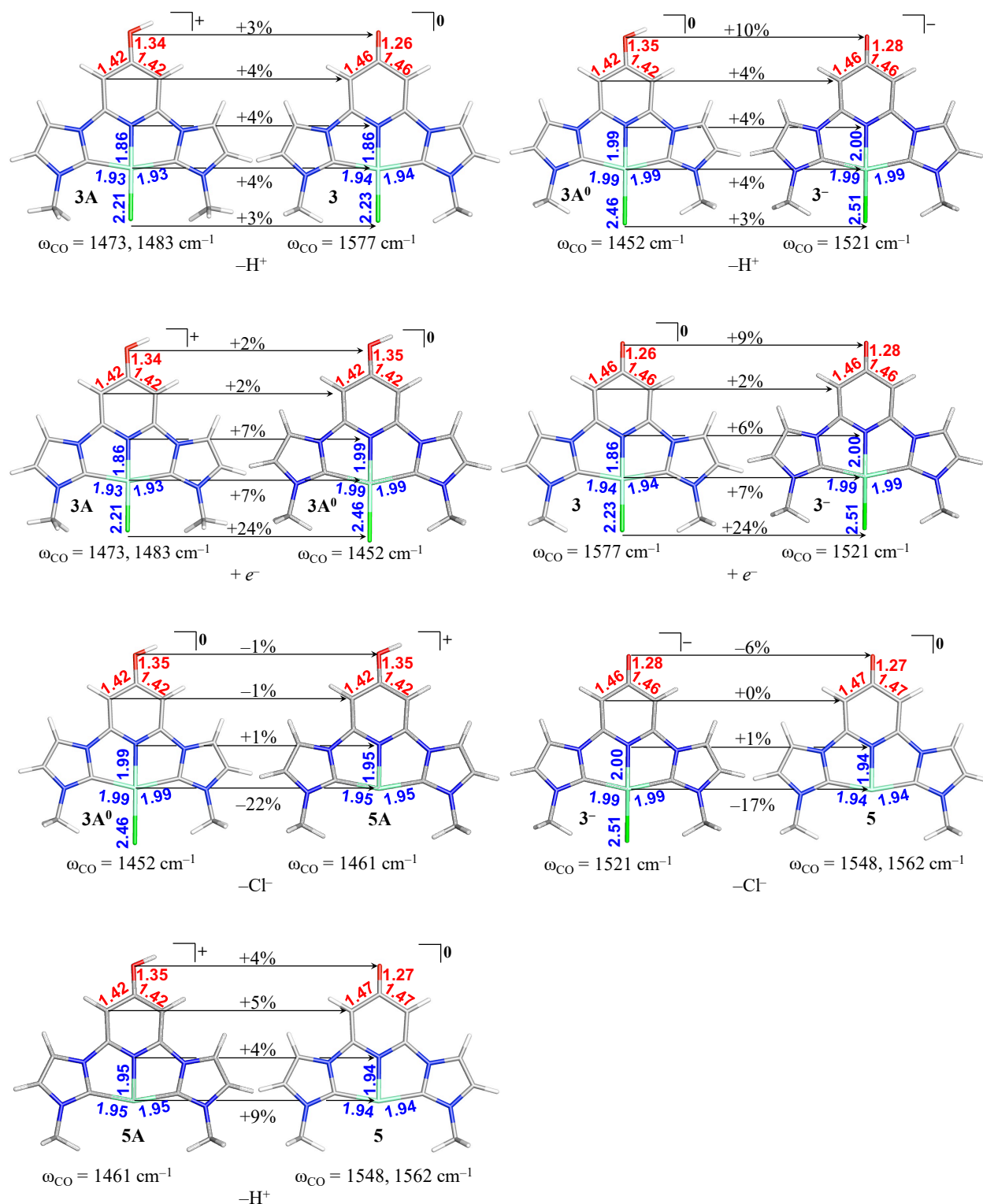


Figure 6.S30: Changes in select bond lengths (Å),  $\omega_{CO}$  ( $\text{cm}^{-1}$ ), and percent change in negative charge, % (as measured by change in NAO charges for protonation, reduction, or chloride dissociation events) with PCM-B3LYP/BS1. Percentages reflect the changes in negative charge for the designated atoms.



**Figure 6.S31:** Changes in select bond lengths (Å),  $\omega_{CO}$  ( $\text{cm}^{-1}$ ), and percent change in negative charge, % (as measured by change in NAO charges for protonation, reduction, or chloride dissociation events) with PCM-PBEPBE-auto/BS1. Percentages reflect the changes in negative charge for the designated atoms.

For the reaction  $\mathbf{3A} \rightleftharpoons \mathbf{3} + \text{H}^+$ ,  $\Delta G_{\text{rxn}}$  is determined from:

$$\Delta G_{\text{rxn}} = (G_{\mathbf{3}} + G_{\text{H}^+}) - (G_{\mathbf{3A}})$$

Using the relationship between  $\Delta G$  and the equilibrium constant,  $K$ :

$$K = e^{(-\Delta G_{\text{rxn}}/RT)}$$

where  $R = 1.9858775 \times 10^{-3} \text{ kcal K}^{-1} \text{ mol}^{-1}$  and  $T = 298.15 \text{ K}$ , the  $\text{p}K_{\text{a}}$  of  $\mathbf{3A}$  in DMSO is computed to be 3.9.

#### 6.6.14 Carbonyl Stretching Frequencies

Table 6.S1 provides the computed  $\omega_{\text{CO}}$  for  $\mathbf{3}$ ,  $\mathbf{3A}$ , and select carbonyl containing compounds from the literature. Including PCM solvation consistently shifts the computed  $\omega_{\text{CO}}$  to lower energy. The computed  $\omega_{\text{CO}}$  of  $\mathbf{3}$  and  $\mathbf{3A}$  are significantly lower in energy compared to other compounds containing the C=O moiety, but the shift to lower energy in a solvent field is consistent throughout. Computed  $\omega_{\text{CO}}$  correlates quite well with experimental  $\nu_{\text{CO}}$  using either B3LYP/BS1 or PCM-B3LYP/BS1 (Figure S30). Results for complex  $\mathbf{3A}$  (which is a monocation) are not included in the plot in Figure S30. We can speculate that ion-pairing effects will significantly alter the observed stretching frequency and no attempt has been made to model those effects in the computations.

Table 6.S1:  $\omega_{\text{CO}}$  and  $\nu_{\text{CO}}$  of **3**, **3A**, and select carbonyl containing compounds (in  $\text{cm}^{-1}$ )<sup>46</sup>

47

Compound	$\omega_{\text{CO}}^{\text{gas}}$		$\omega_{\text{CO}}^{\text{MeCN}}$		$\nu_{\text{CO}}^{\text{Expt}}$
<b>3</b>	1695(1)	1722(919)	1619(804)	1619(859)	1513
<b>3A</b>	1529(86)		1517(341)	1517(338)	1609
<b>3<sup>-</sup></b>	n.d.		1551(1218)		n.d.
<b>3A<sup>o</sup></b>	n.d.		1503(175)	1512(247)	n.d.
acetone	1822(163)		1772(336)		1731
cyclobutanone	1889(284)		1827(562)		1775
cyclopentanone	1844(226)		1787(446)		1750
cyclohexanone	1819(202)		1763(441)		1715
anthrone	1742(194)		1690(510)	1646(239)	1662
2,5-cyclohexadiene-1,4-dione	1756(365)		1716(1092)		1669

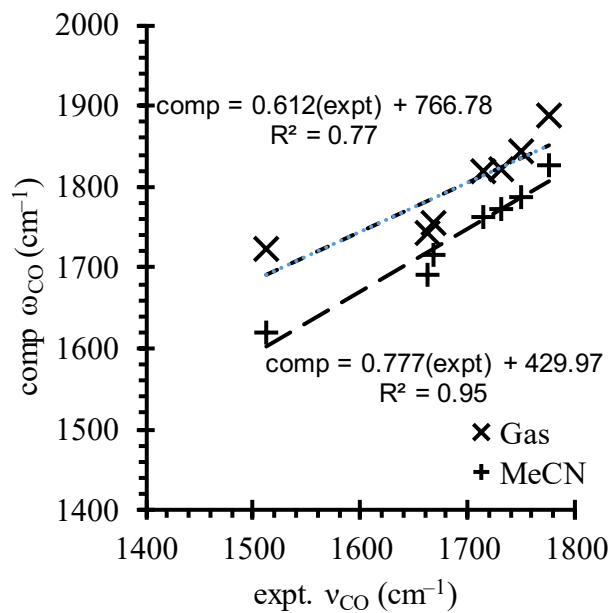
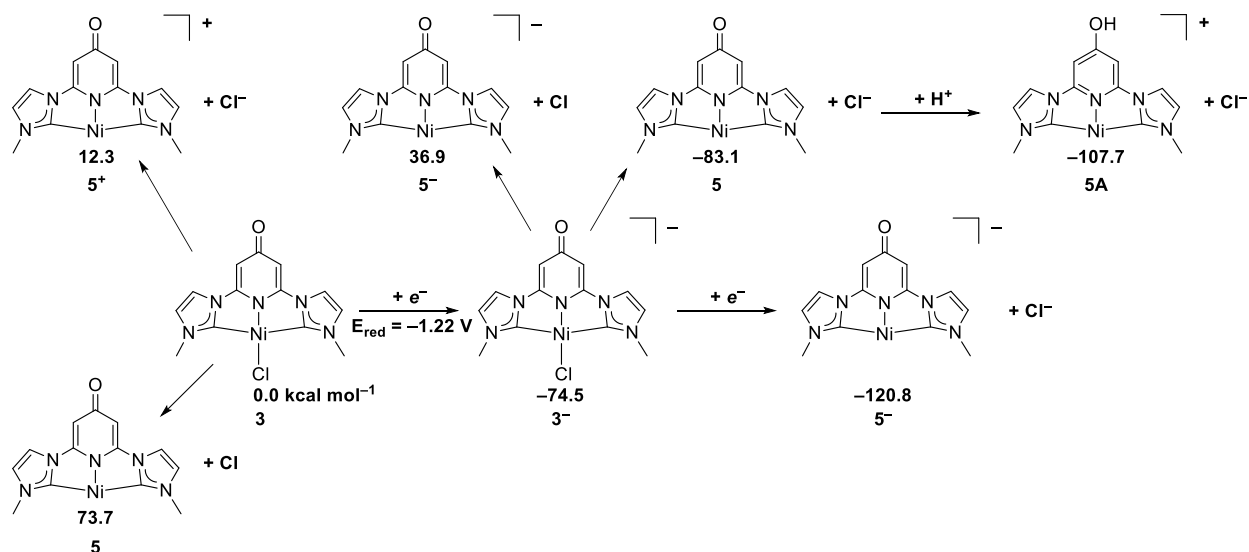


Figure 6.S32: Computed  $\omega_{CO}$  vs experimental  $\nu_{CO}$  for neutral carbonyl containing compounds.<sup>46-47</sup>

### 6.7.15 Generation of Catalyst and Binding CO<sub>2</sub>



**Figure 6.S33:** Possible electrochemical events with **3** for generation of species responsible for catalysis in acetonitrile (PCM-B<sub>3</sub>LYP/BS<sub>1</sub>). Reduction potential is reported vs NHE in acetonitrile.

For one-step reactions involving **3** and **5**, protonation of the O atom is the most favored. In the presence of TfOH acid, some nickel chlorides are known to exchange the chloride ligand for a triflate; this reaction (Figure S32) is nearly thermoneutral. However, simple dissociation of the chloride ligand to form **5**<sup>+</sup> is relatively endergonic ( $\Delta G_{\text{rxn}} = 11.4 \text{ kcal mol}^{-1}$ ), the exchange could also proceed through an associative mechanism (not studied here). Upon formation of the nickel triflate complex, two such complexes can dimerize forming a bond between the O atom of one complex and the nickel atom of a neighboring complex releasing a triflate counterion in the process. This dimerization is exergonic ( $\Delta G = -10.7 \text{ kcal mol}^{-1}$ ) and, based on the thermodynamics, could lead to a polymerization sequence. This could be one explanation for the observed cloudiness of some reaction solutions.

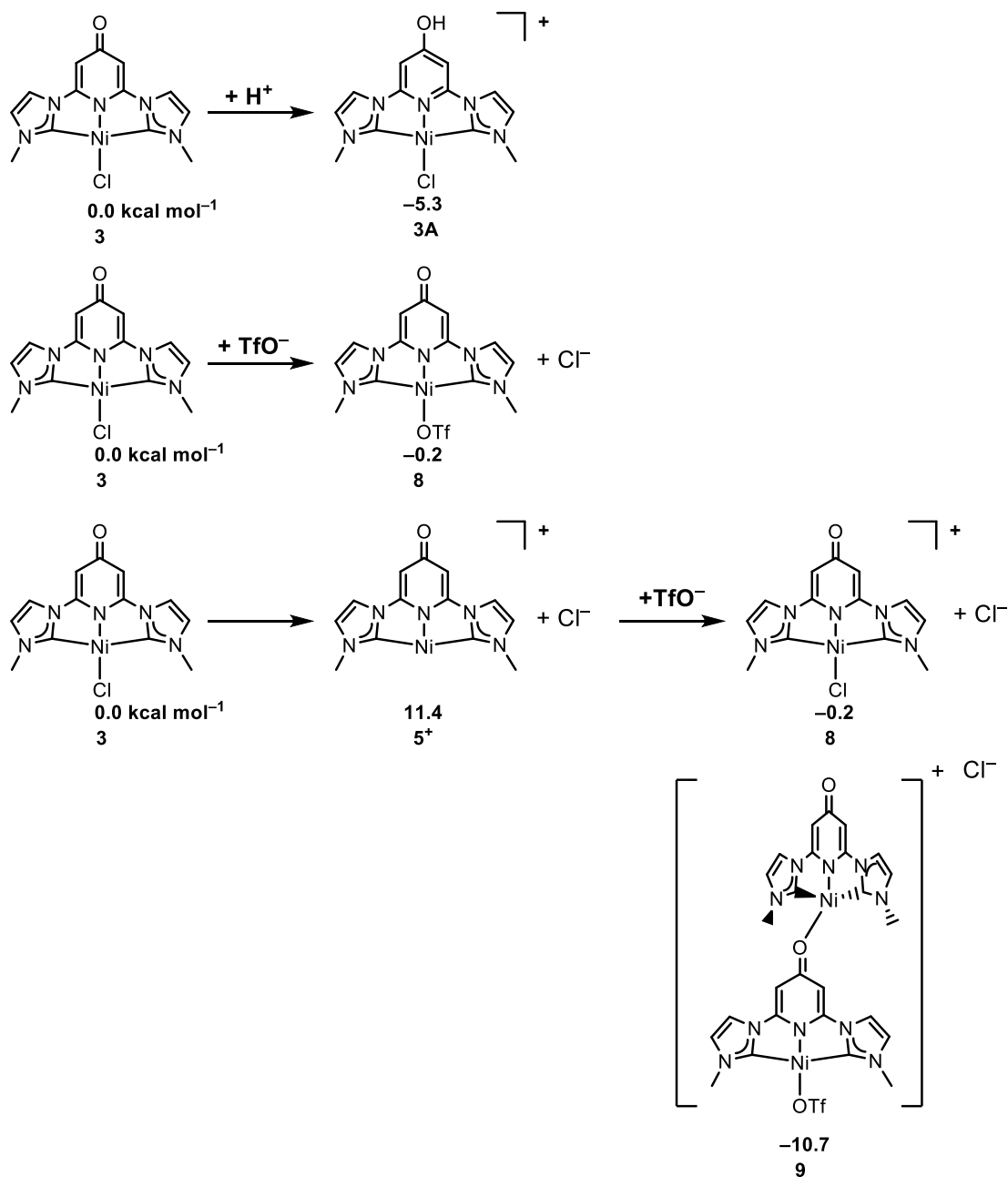


**Figure 6.S34:** Possible reactions of **3** and **5** with triflate in DMSO (PCM-B<sub>3</sub>LYP/BS1). CO<sub>2</sub> binds to complex **5** to produce complex **6**. Attempts to locate bound CO<sub>2</sub> structures with coordinatively unsaturated complex **5A** were unsuccessful. Structure **6A** has an unbound CO<sub>2</sub>; the Ni-C<sub>CO<sub>2</sub></sub> distance is 3.32 Å, and the OCO bond angle is nearly linear (179.3°). In the case of the neutral catalyst, CO<sub>2</sub> does bind to nickel through the carbon atom (Ni-C<sub>CO<sub>2</sub></sub> 2.04 Å) and is free energy for binding CO<sub>2</sub> is endergonic by 10.2 kcal mol<sup>-1</sup>. Inspection of the total spin density on the CO<sub>2</sub> atoms in **7** and **6A** shows that there is a slight net β spin in **7** (-0.0616) and a slight net α spin in **6A** (0.0005) while the Ni has a large α spin in both cases (~0.94).

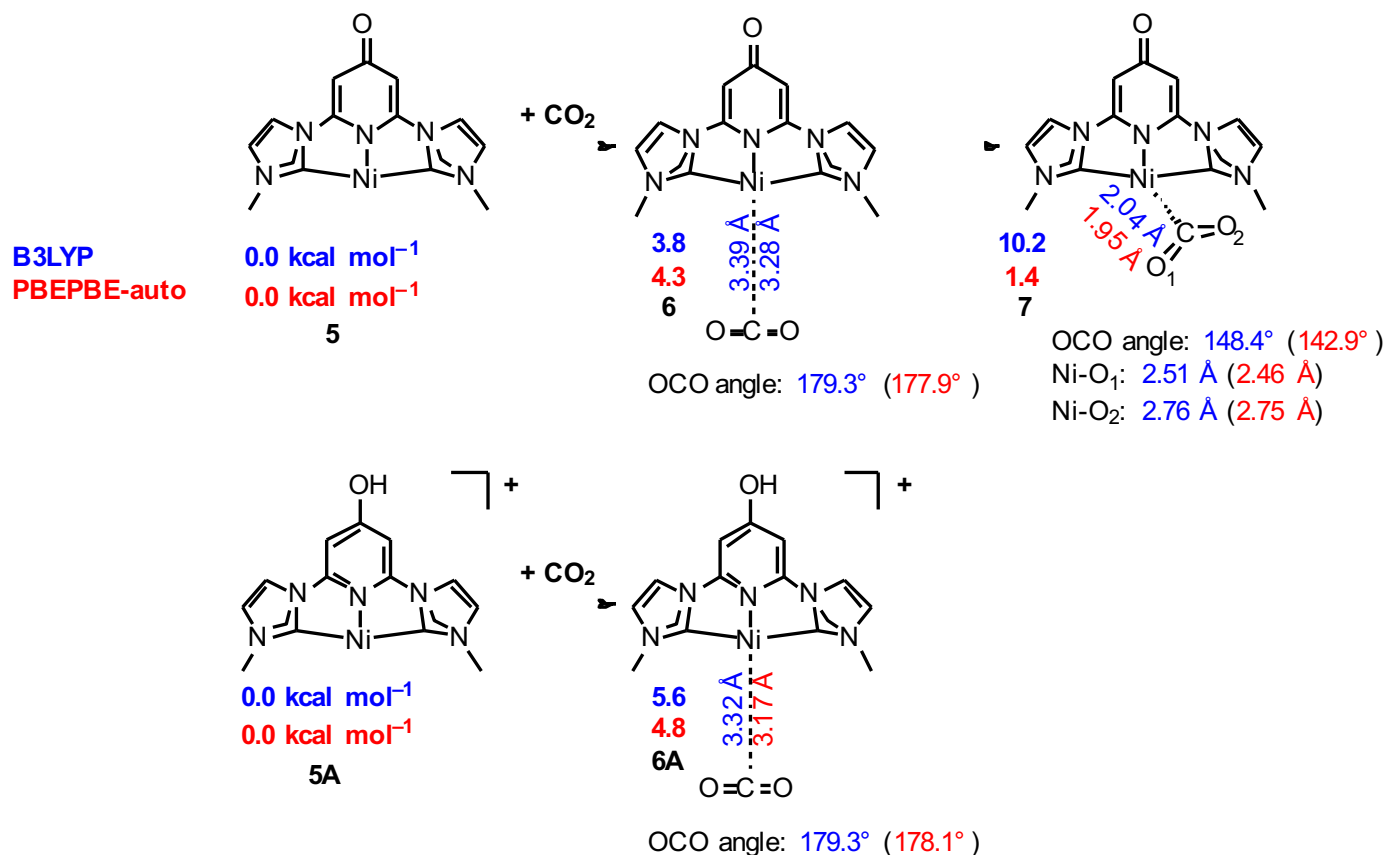


Figure 6.S35: Relative energy (kcal mol<sup>-1</sup>) of binding of CO<sub>2</sub> to the neutral vs. protonated proposed catalyst (PCM-B3LYP/BS1).

### 6.7.16 Mercury Poisoning Tests

Table 6.S10: Photocatalysis in the absence and presence of Hg over time.

Time (hours)	TON without Hg	TON with Hg
0	0	0
0.33	0.9	0.9
0.66	1.8	2.1
1	2.3	2.6*
2	4.7	4.7
4	8.7	9.1
5	10.3	10.4
6	10.4	10.4

\*Indicates the time at which >3000 equiv. of Hg was added to the reaction. Addition of Hg is recommended to be done after the active catalysts has had time to form. See *Journal of Molecular Catalysis A: Chemical* **2003**, 198, 317-341 for further discussion. No appreciable rate difference is observed in the presence of Hg.

CHAPTER 7:  
SPECTROSCOPIC AND MECHANISTIC STUDIES OF RUTHENIUM CNC-PINCER  
COMPLEXES FOR CARBON DIOXIDE REDUCTION CATALYSIS

### 7.1 Introduction

Due to an increase in energy consumption, the detrimental environmental effects of burning nonrenewable fossil fuels, and the finite nature of nonrenewable energy sources, alternative, renewable sources of energy production are desired. The reduction of carbon dioxide to various products has the potential to help alleviate this energy problem.<sup>1</sup> CO<sub>2</sub> can be reduced to various products—e.g. formic acid, methanol, and carbon monoxide—depending upon the number of protons and electrons involved in the reduction; therefore, any catalyst used for CO<sub>2</sub> reduction must be selective for carbon dioxide reduction over proton reduction, which has a more positive reduction potential than CO<sub>2</sub>.<sup>2-3</sup>

Typical photocatalytic CO<sub>2</sub> reduction catalytic systems involve a catalyst, sacrificial donor, and photosensitizer.<sup>4-8</sup> Usually, the photosensitizer is excited and then accepts an electron from the sacrificial donor. The reduced photosensitizer then transfers an electron to the catalyst.<sup>8</sup> The catalyst then reduces CO<sub>2</sub> or undergoes a subsequent reduction before reducing CO<sub>2</sub>. While the identity of the sacrificial donors and photosensitizer can affect the selectivity of catalysis for CO or formate,<sup>6</sup> the catalyst is of great interest to study.

The Papish group has recently reported several catalysts for photocatalytic CO<sub>2</sub> reduction (Figure 7.1).<sup>5-7, 9</sup> All of these catalysts involve a CNC-pincer ligand composed of pyridinol-derivatives and N-heterocyclic carbenes, and most involve a ruthenium center. Interestingly, these ruthenium catalysts are self-sensitized for visible light, which eliminates the need for adding an expensive, precious metal photosensitizer.<sup>9</sup> The turnover numbers (TON) for CO production for the ruthenium-containing catalysts are shown in Table 7.1. The complexes have differing TON values, and **5** has the highest activity with a TON of 55 for CO production under normal reaction conditions. At lower catalyst loading, **5** yields a TON of 33,000 for CO production, which is the highest reported TON for a mononuclear, self-sensitized CO<sub>2</sub> reduction photocatalyst in the literature.<sup>9</sup> The complexes also have varying turnover frequencies (TOF), and complexes **1**, **2**, and **3** have an induction period before catalysis begins, so they are best considered as precatalysts. Since catalyst **5** is the most active and is a true catalyst (rather than a precatalyst), we have focused the most effort on studying the mechanism for this catalyst.

<b>Catalyst</b>	<b>TON for CO<sup>a</sup></b>	<b>Max TOF (h<sup>-1</sup>)</b>
<b>1</b>	45	0.5
<b>2</b>	12	0.2
<b>3</b>	33	7.0
<b>4</b>	15	0.7
<b>5</b>	55	8.3
<b>5<sup>b</sup></b>	33,000	250

*Table 7.1.* Catalyst performance of complexes **1-5** for carbon dioxide reduction to carbon monoxide without a photosensitizer. <sup>a</sup>Standard reaction conditions: 0.1 mM catalyst, 100 mM BIH, and 360 mM TEA in acetonitrile with irradiation from a 150 W xenon lamp solar simulator. <sup>b</sup>Catalyst concentration is 1.0 nM and all other reaction conditions are the same.<sup>9</sup>

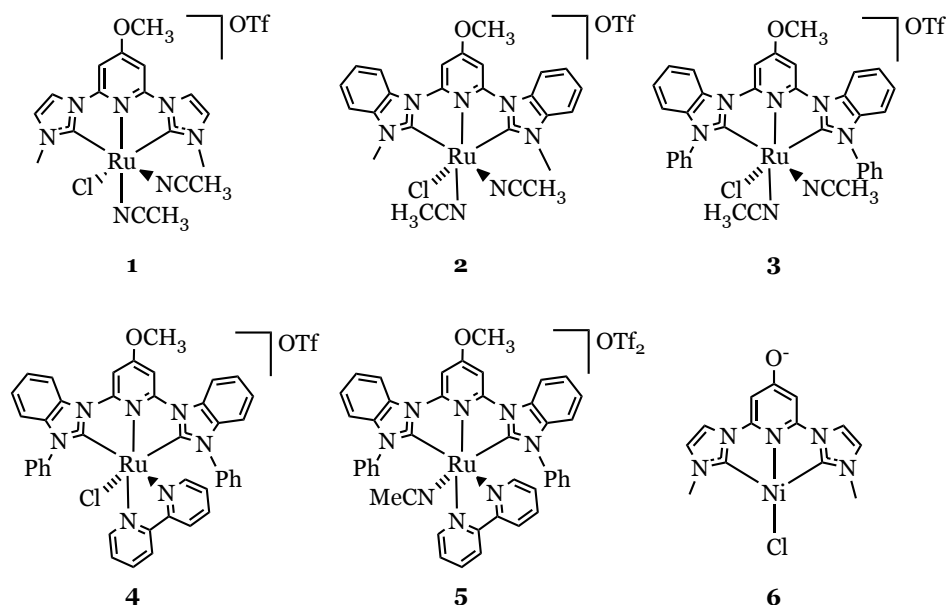


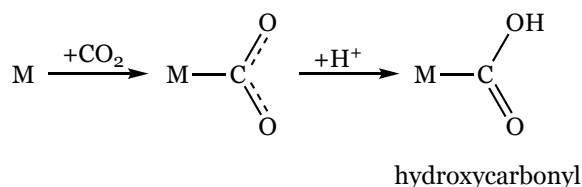
**Figure 7.1.** Structures of CO<sub>2</sub> reduction catalysts studied by the Papish group. **1–5** are studied in this chapter.

All of the catalysts shown in Figure 7.1 have similar ligand scaffolds; however, slight differences in ligand backbone (imidazole vs. benzimidazole), ligand wingtip (methyl vs. phenyl), and identity/denticity of auxiliary ligands (acetonitrile (MeCN) vs. bipyridine (bipy)) have an impact on catalytic rate, catalyst lifetime, and maximum turnover number. Detailed mechanistic and kinetic studies of these catalysts can help in understanding how these catalysts work, which will help in the development of new catalytic systems.

Previous kinetic and mechanistic studies of other carbon dioxide reduction catalysts in the literature have included stopped-flow spectroscopy,<sup>10-12</sup> kinetic isotope effects (KIE),<sup>13-14</sup> and computational methods,<sup>15-16</sup> among other techniques. These studies have resulted in knowledge of reaction rates of different catalysts and of common reaction pathways for carbon dioxide reduction.

While there are multiple pathways for carbon dioxide activation discussed in the literature, there are two pathways that are commonly proposed: binding of CO<sub>2</sub> to the metal followed by protonation (resulting in a hydroxycarbonyl species, M-COOH) or CO<sub>2</sub>-insertion into a metal-hydride bond (resulting in a metalloformate species, M-OCOH) (Figure 7.2).<sup>16-19</sup>

a. CO<sub>2</sub> coordination and protonation



b. CO<sub>2</sub>-insertion into M-H bond

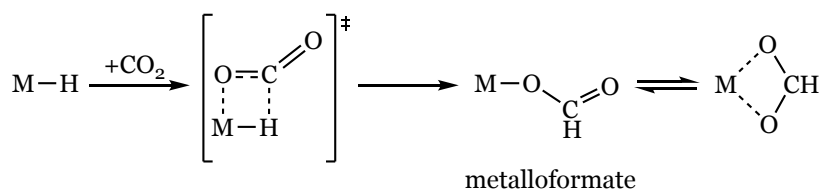


**Figure 7.2.** Pathways for CO<sub>2</sub> reduction by a metal-centered catalyst. M is shown to represent a metal center; other ligands around metal center are omitted for clarity and generality. Charges on the metal-complex are omitted for clarity.

For the first scenario, CO<sub>2</sub> can coordinate to the metal in 3 possible coordination modes: κ<sup>1</sup> through either the C or O or κ<sup>2</sup> through the C and O (Figure 7.3). With electron-rich metal centers, coordination of the C as κ<sup>1</sup> is the preferred coordination mode because the carbon is more electrophilic than the oxygens.<sup>20</sup> This κ<sup>1</sup> coordination through the C allows for the metal center to charge transfer to the antibonding π\* orbital of CO<sub>2</sub>. This increased electron density in the antibonding orbital results in CO<sub>2</sub> becoming bent when bound to the metal center. Once CO<sub>2</sub> is bound as κ<sup>1</sup>-C to the metal, one of the oxygens is protonated, resulting in a hydroxycarbonyl complex (Figure 7.2a).

The hydroxycarbonyl complex then undergoes C-OH bond cleavage to produce water and a metal-carbonyl complex (M-CO).<sup>17</sup>

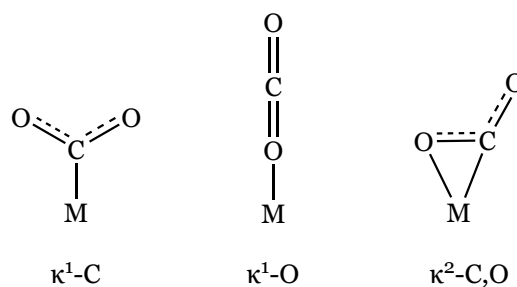


Figure 7.3. Coordination modes of CO<sub>2</sub>.

The second pathway of CO<sub>2</sub> reduction is CO<sub>2</sub>-insertion into a metal-hydride (M-H) bond. In a metal-hydride bond, the metal center bears more of the positive charge and the hydride bears more of the negative charge. Therefore, when CO<sub>2</sub> normally interacts with a M-H bond, the carbon of the CO<sub>2</sub>, which is more electrophilic, will interact with the hydride and one of the oxygens, which are more nucleophilic, will interact with the metal center (Figure 7.2b).<sup>21</sup> This CO<sub>2</sub>-insertion results in the formation of a metalloformate complex. The metalloformate species can either release the formate or promote dehydration of the formate to form carbon monoxide.<sup>18</sup>

While many carbon dioxide reduction catalytic conditions involve the addition of a proton source, carbon dioxide reduction can also occur without an added proton source. In this process, carbon dioxide undergoes a disproportionation of 2 CO<sub>2</sub> molecules to CO and CO<sub>3</sub><sup>2-</sup>.<sup>17, 22</sup>

Herein, complexes **1-5** were studied by UV/vis and IR spectroscopies as they are reduced by a chemical reductant and during the subsequent reaction with CO<sub>2</sub>. Complex **5**—the catalyst with the highest TON for CO<sub>2</sub> reduction to CO—was studied further by real-time IR spectroscopy to observe a ruthenium-hydroxycarbonyl species and a ruthenium-carbonyl species.

## 7.2 Results and Discussion

### 7.2.1 Spectroscopic Studies

To initially begin studying the mechanism of the CO<sub>2</sub> reduction catalysts, the UV/vis spectrum of each complex was monitored to observe changes in the electronic spectra upon reduction (Figures 7.4, 7.S1-S4). Potassium graphite (KC<sub>8</sub>) was chosen as the chemical reducing agent as it has a large negative reduction potential that is sufficient to reduce the ruthenium complexes (e.g. for **1** E = -2.30 V vs Fc/Fc<sup>+</sup>)<sup>5, 9</sup> and lacks absorptions in the UV and visible regions.

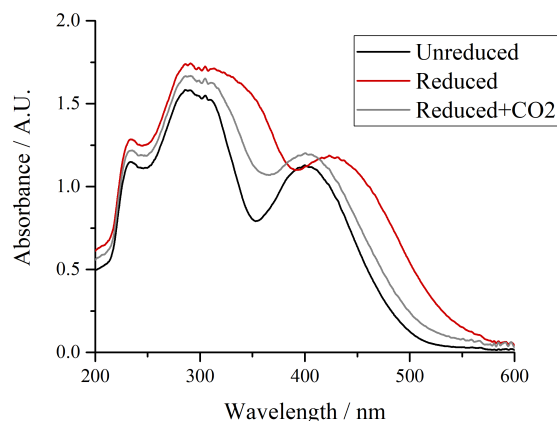


*Figure 7.4.* UV/vis spectra of a 0.15 mM solution of **5** in acetonitrile: unreduced (black), reduced with 2 equivalents of KC<sub>8</sub> (crimson), and reduced with 2 equivalents of KC<sub>8</sub> followed by exposure to CO<sub>2</sub> (grey).

The UV/vis spectrum of each complex features an intense MLCT band in the lower visible region (420-450 nm) (Figures 7.4, 7.S1-S4). This transition results from a metal-to-ligand charge transfer (MLCT). For the Ru(CNC)(bipy) complexes, this transition is from the metal-based HOMO to the bipy-based LUMO.<sup>9, 23</sup> When complexes **1-3** and **5** are reduced, the MLCT band redshifts by 20-30 nm for each complex (Figures 7.4, 7.S1-S3). Complex **4**, however, blueshifts by only a few nm when reduced (Figure 7.S4). The MLCT band of unreduced complex **4** (the only complex with

no MeCN bound to Ru) is at higher wavelength than all of the other complexes, but when it is reduced, the wavelength of the MLCT band is similar to the other reduced complexes. The large absorption features below 350 nm are due to the bound MeCN and  $\pi$ - $\pi^*$  transitions.

Once the complexes were reduced, they could be exposed to CO<sub>2</sub> and monitored by UV/vis spectroscopy for further changes in the spectra. While this is not exactly replicating the photochemical reaction conditions—a proton source and irradiation source are not added and thus will not produce desired products—it is expected that CO<sub>2</sub> will bind to the reduced catalyst, resulting in changes in the spectra; the nature and rate of these changes can give insight into the catalytic cycle.<sup>10</sup> For all of the complexes except **4**, when the reduced complexes are exposed to CO<sub>2</sub> (reduced+CO<sub>2</sub>), the MLCT band blueshifts back toward the wavelength of the starting, unreduced complex (Figures 7.5, 7.S1-S4). This suggests that the electronic states of the unreduced and reduced+CO<sub>2</sub> complexes are similar to each other but different from the reduced complex, potentially due to the transfer of an electron to CO<sub>2</sub>, resulting in a similar electronic state to the unreduced complex.

Because there are changes in the UV/vis spectra when the reduced complexes are exposed to CO<sub>2</sub>, stopped-flow UV/vis spectroscopy was attempted to try to measure the rates of reaction of the reduced complexes with CO<sub>2</sub>; however, these experiments were unsuccessful in obtaining consistent rate data.

To measure the IR spectra of the reduced complexes, the reduced species were isolated as solids (**1<sub>red</sub>** – **5<sub>red</sub>**). KC<sub>8</sub> was added to a solution of the complex in acetonitrile which was then stirred, filtered, and dried under vacuum to yield the reduced complex as a solid. The reduced species with CO<sub>2</sub> was isolated by reducing the complex in

acetonitrile, filtering, and bubbling with CO<sub>2</sub>(g) until the solvent evaporated, yielding the reduced+CO<sub>2</sub> species as a solid (**1<sub>red</sub>**+CO<sub>2</sub> – **5<sub>red</sub>**+CO<sub>2</sub>). Once the solids were isolated, the IR spectrum of each was measured with an ATR-IR under a nitrogen atmosphere (Figures 7.5, 7.S5-S8).

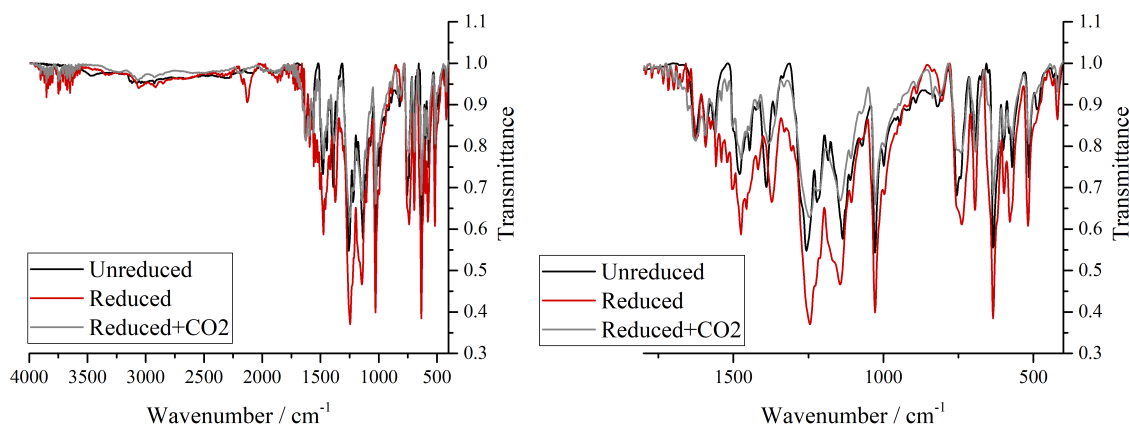


*Figure 7.5.* (Left) ATR-IR spectra in the solid state of unreduced **5** (black), reduced **5** (**5<sub>red</sub>**, reduced with 2 equivalents KC<sub>8</sub>, crimson), and reduced **5** with CO<sub>2</sub> (**5<sub>red</sub>**+CO<sub>2</sub>, grey). (Right) Expanded IR spectra of **5** to show fingerprint region.

When each complex is reduced, the peaks in the fingerprint region remain fairly similar compared to the unreduced complex. This is probably because the structures of the unreduced and reduced complexes are fairly similar; the ligand scaffold, which is responsible for most of the IR stretches, remains consistent when reduced. Likewise, the spectrum of the reduced with CO<sub>2</sub> species is also fairly similar in the fingerprint region.

One of the largest changes for each compound upon reduction is observed in the 2100-2300 cm<sup>-1</sup> region. The peaks here correspond to the nitrile (C≡N) stretch of the bound acetonitrile of the complex. When reduced, the acetonitrile peak increases in intensity and shifts from ~2275 cm<sup>-1</sup> to ~2125 cm<sup>-1</sup>. When the reduced species is exposed to CO<sub>2</sub>, the peak shifts back towards higher wavenumber to ~2165 cm<sup>-1</sup>.

In each of the IR spectra of the reduced complexes with CO<sub>2</sub>, there is a small peak at 1652 cm<sup>-1</sup> (Figures 7.5, 7.S5-S8). This peak is assigned to a C=O stretch, which could be due to a bound carbon dioxide, a hydroxycarbonyl species, or a metalloformate species. The formation of the hydroxycarbonyl or metalloformate species would be due to protonation by adventitious water in the (incompletely) dried acetonitrile.

To further study the changes in the IR spectra, complex **5** was studied by measuring the IR spectrum over time by using a ReactIR instrument which is capable of measuring real-time IR spectra. When a solution of reduced **5** in acetonitrile was exposed to CO<sub>2</sub> and the IR spectra were measured in situ over time, two new peaks at 1652 and 1670 cm<sup>-1</sup> appeared after several minutes of exposure to CO<sub>2</sub> (Figure 7.6). Both of these stretches are potentially C=O stretches. The C=C stretch of the pyridyl of the pincer ligand is still present at 1633 cm<sup>-1</sup> after exposure to CO<sub>2</sub>. This stretch is resilient and remains at the same position independent of reduction or exposure to CO<sub>2</sub>. This C=C stretch is also present at approximately the same wavenumber with other complexes containing similar CNC-pincer ligands.<sup>5, 7, 9</sup>

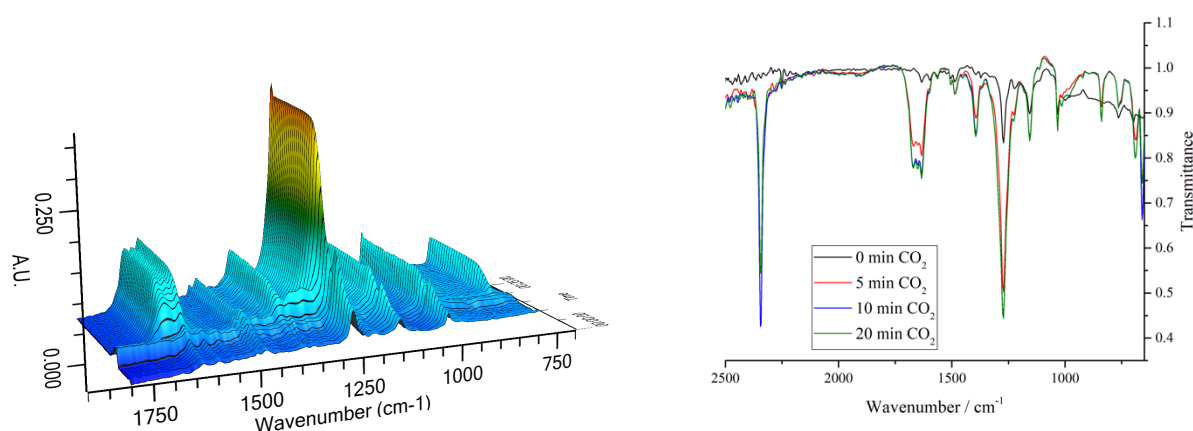


*Figure 7.6.* (Left) ReactIR spectra of **5** (reduced with 2 eq. KC<sub>8</sub>) and CO<sub>2</sub> monitored over a 20 minute period. (Right) Overlaid IR spectra obtained from the ReactIR after 0 minutes (black), 5 minutes (red), 10 minutes (blue), and 20 minutes (green) exposure to CO<sub>2</sub>.

To confirm that these peaks correspond to C=O stretches, the same experiment was repeated using  $^{13}\text{CO}_2$  instead of natural abundance  $\text{CO}_2$  (Figure 7.7). In this case, only one  $^{13}\text{C}=\text{O}$  stretching frequency is observed at  $1596\text{ cm}^{-1}$  (Table 7.2). The use of  $^{13}\text{CO}_2$  also makes it possible to assign the C-O bend of a bound COOH species (Figure 7.8). The C-O bend with  $\text{CO}_2$  is observed at  $839\text{ cm}^{-1}$  and shifts to  $813\text{ cm}^{-1}$  when  $^{13}\text{CO}_2$  is used. The shifts to lower wavenumber are consistent with using heavier carbon-13; the ratios of the frequency with  $^{13}\text{C}$  to the frequency with  $^{12}\text{C}$  are consistent for each of the stretches/bends (Table 7.2). The predicted ratio from Hooke's Law is 0.978.

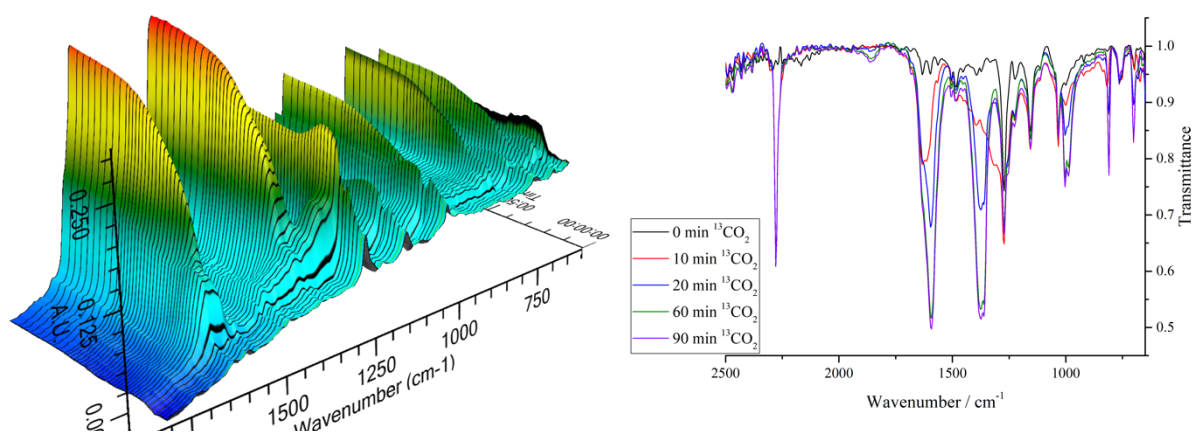


Figure 7.7. (Left) ReactIR spectra of **5** (reduced with 2 eq.  $\text{KC}_8$ ) and  $^{13}\text{CO}_2$  monitored over a 90 minute period. (Right) Overlaid IR spectra obtained from the ReactIR after 0 minutes (black), 10 minutes (red), 20 minutes (blue), 60 minutes (green), and 90 minutes (purple) exposure to  $^{13}\text{CO}_2$ .

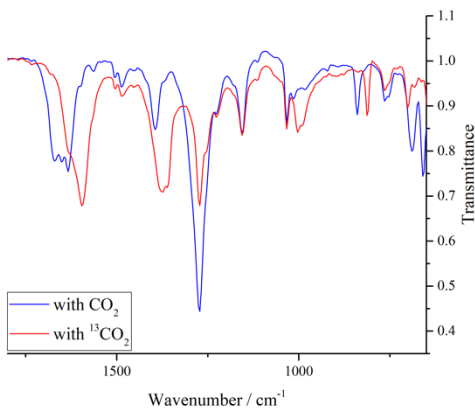


Figure 7.8. Overlaid IR spectra of **5** (reduced with 2 eq.  $\text{KC}_8$ ) after 20 minutes of exposure to  $\text{CO}_2$  (blue) or  $^{13}\text{CO}_2$  (red).

Stretch/Bend	with $\text{CO}_2$ ( $\text{cm}^{-1}$ )	with $^{13}\text{CO}_2$ ( $\text{cm}^{-1}$ )	Ratio $\nu_{13}/\nu_{12}$
$\text{CO}_2$ (dissolved)	2346	2279	0.971
C=O	1652 & 1670	1596	0.966 <sup>a</sup>
C=C	1633	1633	---
C-O	839	813	0.969

Table 7.2. Observed frequencies from the IR spectra of reduced **5** after 20 minutes of exposure to  $\text{CO}_2$  or  $^{13}\text{CO}_2$ . <sup>a</sup>Calculated using  $1652 \text{ cm}^{-1}$  for the  $^{12}\text{C}=\text{O}$  frequency.

From the possible reaction pathways, **5** can bind  $\text{CO}_2$  and then be reduced or **5** can be reduced and then bind  $\text{CO}_2$  (Figure 7.9). The IR spectra of unreduced **5** were measured over time with exposure to  $\text{CO}_2$  or  $^{13}\text{CO}_2$  (Figures 7.10-11). By using natural abundance  $\text{CO}_2$  and  $^{13}\text{CO}_2$ , a C=O stretch was not observed in the IR spectrum. This means that the unreduced complex likely does not bind  $\text{CO}_2$ , and therefore, in the reaction pathway, **5** is reduced before  $\text{CO}_2$  binds to the metal center.

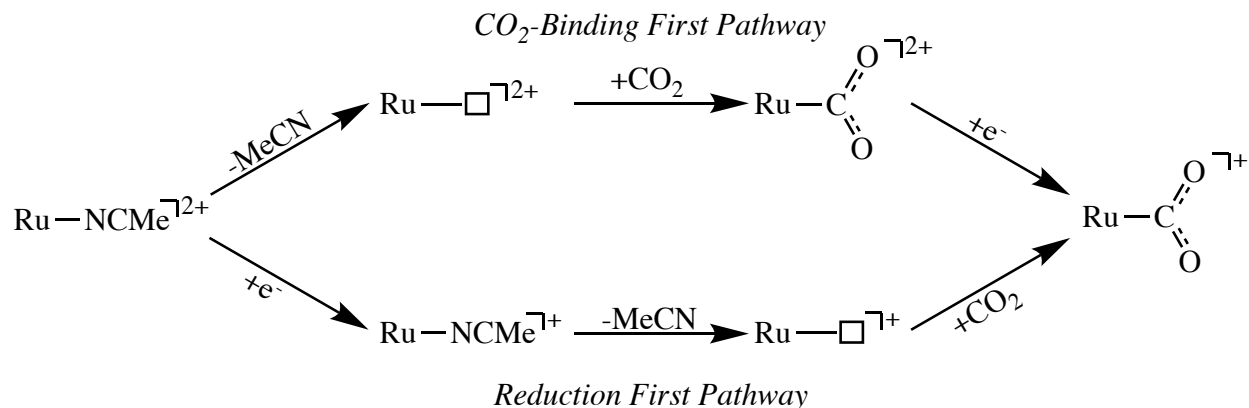


Figure 7.9. Possible binding pathways of CO<sub>2</sub> to **5**.

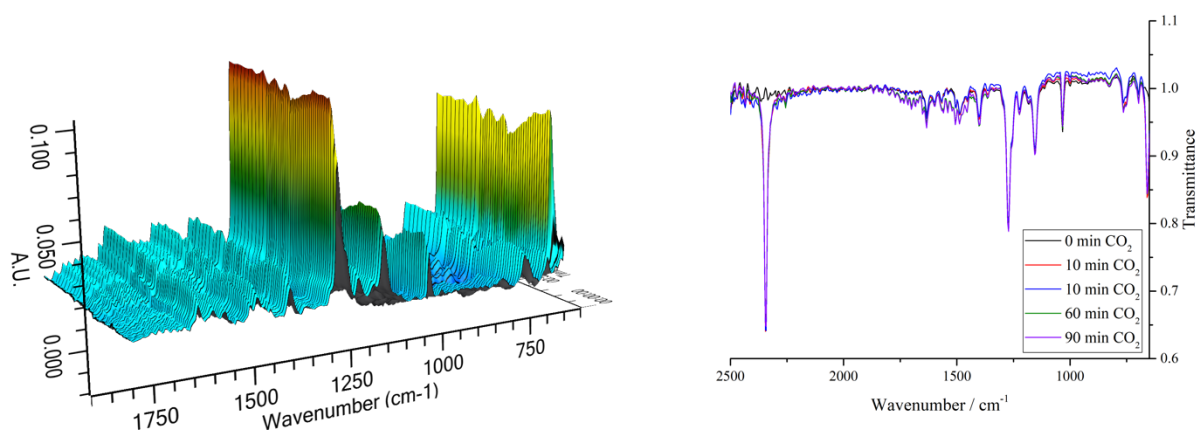


Figure 7.10. (Left) ReactIR spectra of unreacted **5** and CO<sub>2</sub> over a 90 minute period. No major changes were observed. (Right) Overlaid IR spectra obtained from the ReactIR after 0 minutes (black), 10 minutes (red), 20 minutes (blue), 60 minutes (green), and 90 minutes (purple) exposure to CO<sub>2</sub>.

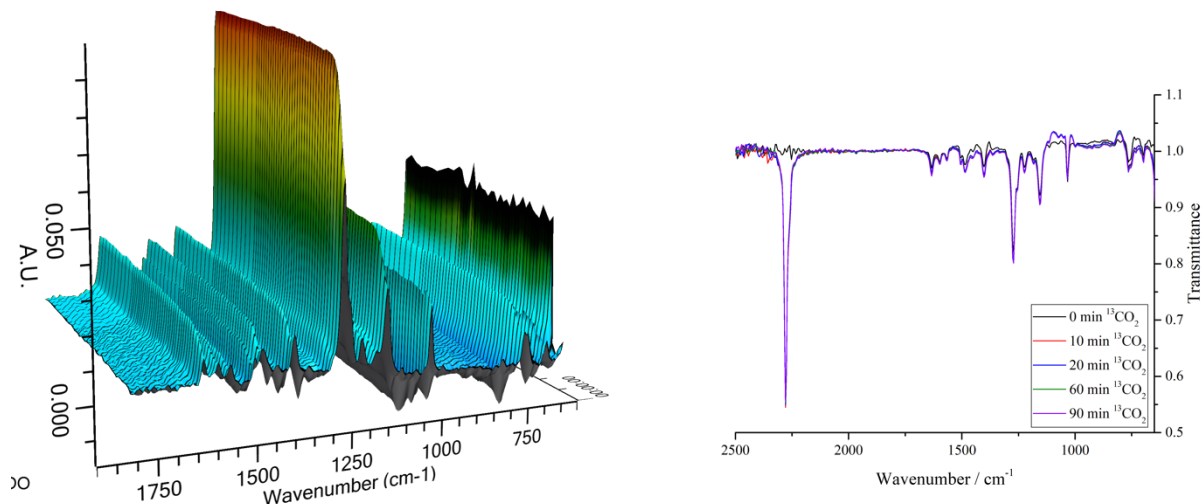
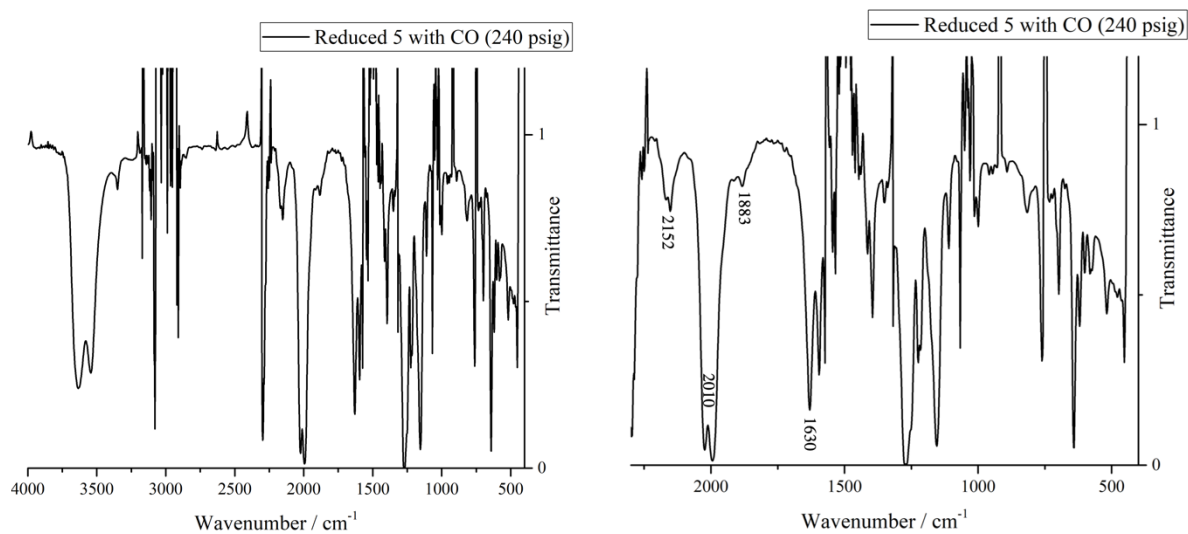


Figure 7.11. (Left) ReactIR spectra of unreacted **5** and <sup>13</sup>CO<sub>2</sub> over a 90 minute period. No major changes were observed. (Right) Overlaid IR spectra obtained from the ReactIR after 0 minutes (black), 10 minutes (red), 20 minutes (blue), 60 minutes (green), and 90 minutes (purple) exposure to <sup>13</sup>CO<sub>2</sub>.

Attempts were made to form a ruthenium-carbonyl (Ru-CO) species in situ. Real-time IR experiments were performed with **5** using natural abundance CO and  $^{13}\text{CO}$  to determine if unreduced or reduced **5** can bind to CO (Figures 7.S15-S17). However, these experiments were hindered by the low solubility of CO(g) in acetonitrile. While the solubility of CO in acetonitrile could not be found in the literature, CO has low solubility in similar solvents such as dimethylsulfoxide, methanol, and water.<sup>24-25</sup> Also, in the IR spectrum of neat acetonitrile purged with CO(g), only a small peak attributable to CO is observed (Figure 7.S18).

To overcome the low solubility of CO in acetonitrile, high-pressure of CO gas was used. A solution of reduced **5** was stirred under 240 psig of CO(g) for 24 hours, and then the IR spectrum of the solution was measured (Figure 7.12). In the IR spectrum, a small peak at  $1883\text{ cm}^{-1}$  is observed. This peak is in the expected region for a CO stretch of a metal-carbonyl species, and the stretching frequency was computed to be  $2071\text{ cm}^{-1}$ . However, the peak is small and a peak for a bound acetonitrile is also observed (at  $2152\text{ cm}^{-1}$ ), so there seems to be a mix of CO and acetonitrile bound species. Indeed, in the mass spectrum of the solution (Figure 7.S14), both the acetonitrile-bound and CO-bound species are observed. The observation of the acetonitrile-bound species is likely due to acetonitrile being the solvent and, therefore, binding to the metal center more readily.



**Figure 7.12.** (Left) Full IR spectrum of reduced **5** in acetonitrile after stirring under 240 psig of CO(g) for 24 h. (Right) Area of interest of the IR spectrum of reduced **5** with CO. Peaks of interest are labeled in wavenumbers ( $\text{cm}^{-1}$ ). The large areas of noise in the baseline (e.g. 2750-3250  $\text{cm}^{-1}$ ) are due to the absorptions of the solvent (acetonitrile). The doublet peak at 2010  $\text{cm}^{-1}$  is dissolved CO(g).

Formic acid was added to reduced and unreduced **5** to determine if formate can bind to the metal through the oxygen as a metalloformate species. From the IR spectra, there is a small peak at 1652  $\text{cm}^{-1}$  when formic acid is added to reduced **5** (Figure 7.S19). This is assigned to a C=O stretch of a bound formate; however, the peak is fairly small, especially when compared to when CO<sub>2</sub> is used, so this might not be the preferred binding mode of formate to the metal center or might not be the observed product when CO<sub>2</sub> is added to reduced **5**. The use of a formate salt instead of formic acid might lead to more binding of formate to the ruthenium center. With unreduced **5**, a C=O stretch attributable to formate was not observed (Figure 7.S20). This implies that, in the course of CO<sub>2</sub> reduction, the bound CO<sub>2</sub> most likely results in a hydroxycarbonyl species (M-COOH) instead of a metalloformate species (M-OCOH). These results are again consistent with the computed reaction energies of binding a formate to **5**.

Electrospray ionization mass spectrometry was used to further characterize the products of the reduced complexes with  $\text{CO}_2$ ,  $\mathbf{1}_{\text{red}} + \text{CO}_2 - \mathbf{5}_{\text{red}} + \text{CO}_2$  (Figures 7.S9-S13). While the starting material is still observed in the MS spectra, each spectrum contains a peak consistent with a  $\text{HCO}_2^-$  bound to the metal,  $[\text{M} + \text{HCO}_2]^+$ . The  $\text{HCO}_2^-$  could be the result of a formate bound to metal or from a  $\text{CO}_2$  bound to the metal which is then protonated in the MS. However, it is believed that this is a formate species (Ru-COOH) formed during the experiment as protonation of  $\text{CO}_2$  is facile once  $\text{CO}_2$  binds to the metal center and should occur in the course of the reaction (see computations in SI). In the MS spectrum of  $\mathbf{5} + \text{CO}_2$  (Figure 7.S13), there is a small peak that can be assigned to a CO bound to ruthenium (observed  $m/z = 778.1514$ , predicted  $m/z = 778.1537$ ). The Ru-COOH species observed would be complex 3-4 in Figure 7.S22, and the Ru-CO complex observed would be complex 3-5.

EPR spectroscopy of reduced  $\mathbf{1}$  and reduced  $\mathbf{5}$  in a 50:50 acetonitrile:toluene mixture was attempted; however, a detectable signal above the cavity background was not observed for either complex.

Crystals of reduced  $\mathbf{5}$  and reduced  $\mathbf{5}$  with  $\text{CO}_2$  were unfortunately not able to be obtained for single crystal X-ray diffraction analysis, despite several attempts.

### *7.2.2 Proposed Catalytic Cycle*

Complex  $\mathbf{5}$  is an active photoreduction catalyst for carbon dioxide reduction. The studies performed above can be used to propose a catalytic cycle (Figure 7.13). The proposed catalytic cycle shown here is for carbon dioxide reduction to carbon monoxide with a proton source present. The pathways shown in green correspond to photosensitized photocatalysis (i.e. with an added photosensitizer), and the pathways

shown in blue correspond to self-sensitized photocatalysis. Note, this cycle would also apply to electrochemical reduction or, potentially, stoichiometric reduction using a chemical reductant (e.g.  $\text{KC}_8$ ).

To begin the catalytic cycle for self-sensitized catalysis,  $i$  is first reduced (see Figure 7.13 for numbering of complexes). Light is absorbed to drive  $i$  to an excited state ( $ii$ ), and then a sacrificial donor (SD, e.g. BIH or TEA) donates an electron, reducing  $ii$  to  $iii$ . Once reduced, the loss of the MeCN ligand allows for  $\text{CO}_2$  to bind to the complex, forming  $v$ . This reduction-first pathway is supported by the IR experiments (vide supra). Complex  $v$  is then protonated to form a hydroxycarbonyl complex,  $vi$ . The hydroxycarbonyl species was observed by IR and MS experiments. This complex absorbs light to form an excited state ( $vii$ ), which is then reduced by a sacrificial donor to form a reduced hydroxycarbonyl complex,  $viii$ . Complex  $viii$  then undergoes protonation and C-O bond cleavage to release water and form  $ix$ . Complex  $ix$  was observed in the MS and IR experiments above. CO can then be lost from the ruthenium center to produce  $x$ , which can then bind solvent (MeCN) to reform  $i$ , which can then restart the catalytic cycle.

The only difference for the photosensitized pathway is the method by which the photoabsorption and subsequent reduction occur. For these reductions, the photosensitizer (PS) absorbs light, is reduced by a sacrificial donor, and then reduces  $i$  or  $vi$ . All of the other chemical steps remain the same.

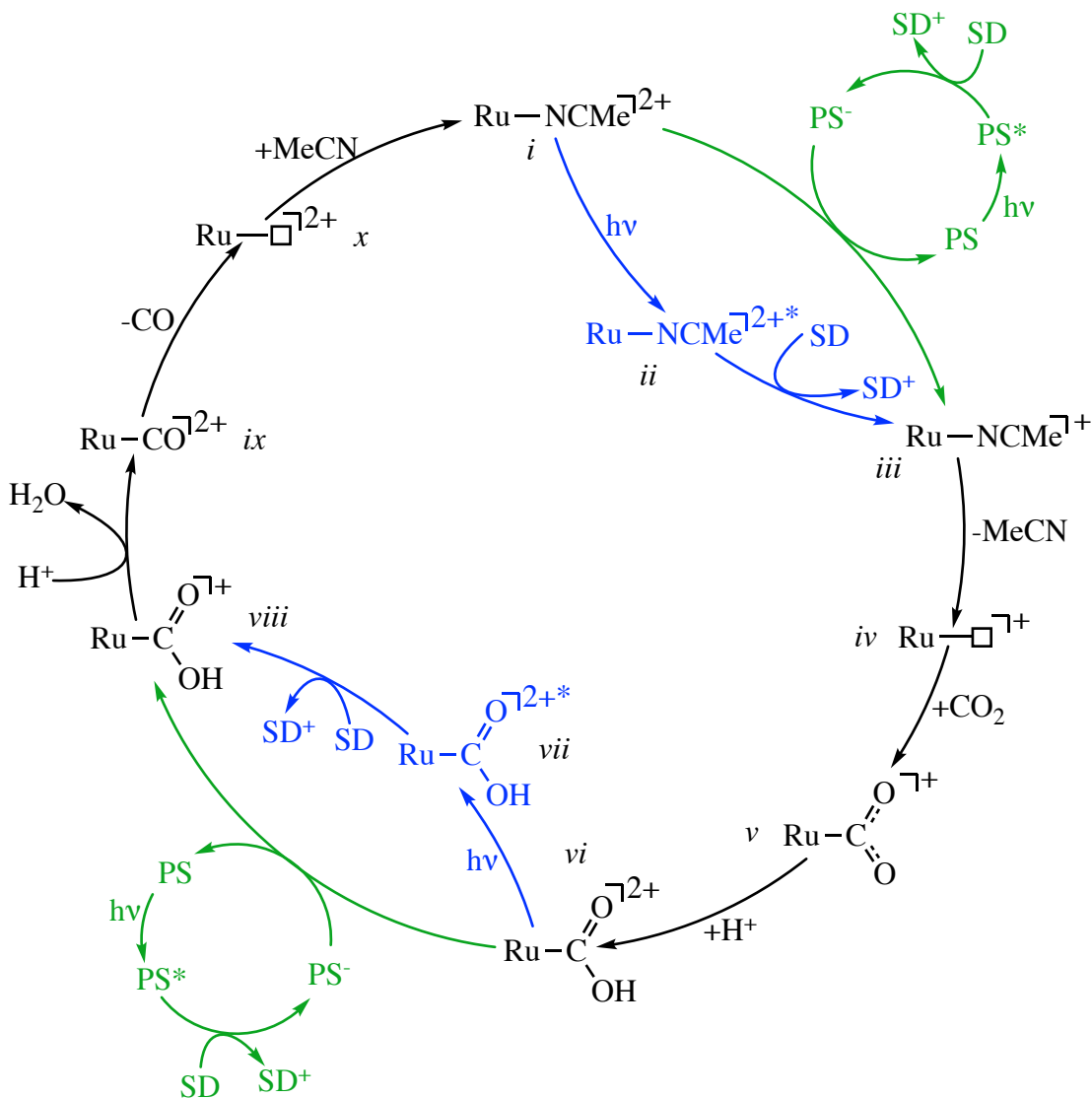


*Figure 7.13.* Proposed catalytic cycle for carbon dioxide reduction to carbon monoxide with a proton source present. Self-sensitized pathway is shown in blue, and photosensitized pathway is shown in green. Complex **5** is abbreviated as Ru-NCMe<sup>2+</sup>. The tridentate pincer and the bidentate bipyridine ligands around the metal center are not shown for clarity. SD = sacrificial donor (e.g. triethylamine (TEA) or 1,3-dimethyl-2-phenyl-2,3-dihydro-1H-benzo[d]imidazole (BIH)). PS = Photosensitizer. □ = free site on metal center.

Similar catalytic mechanisms have been proposed for CO<sub>2</sub> reduction catalysts in the literature.<sup>8, 13-14, 16</sup> The main difference between the proposed catalytic cycle herein and literature catalytic cycles is the self-sensitized pathway. Complex **5** (and also **4**) is able to absorb light to drive the catalytic reaction. The mononuclear nature of the self-

sensitized catalyst is proposed based upon TON values for experiments at low concentration of **5**. When the concentration of **5** is reduced from 100  $\mu\text{M}$  to 1 nM, the TON increases from 55 to 33,000, respectively (Table 7.1).<sup>9</sup> At lower concentration, catalyst-catalyst interactions are reduced, so if a bimolecular mechanism in which one molecule of **5** acts as a photosensitizer and another molecule of **5** acts as a catalyst is occurring, the TON would be expected to decrease at lower catalyst concentration.<sup>27-28</sup> However, the TON increases, so the same molecule of **5** is likely acting as photosensitizer and catalyst, as used in the proposed catalytic cycle.

The proposed catalytic cycle in Figure 7.13 is applicable when a proton source is present. In the absence of a proton source, a disproportionation is necessary to produce CO and  $\text{CO}_3^{2-}$ ; that scenario would proceed through a different catalytic cycle.

### 7.3 Conclusion

In summary, UV/vis and IR spectroscopies were used to study the reductions of **1-5** and the subsequent reaction with  $\text{CO}_2$ . In the IR spectra, a peak assigned to the C=O stretch of a bound hydroxycarbonyl species was observed. In situ IR spectroscopy was used to confirm the observed stretch was indeed a C=O stretch of a bound species by the use of natural abundance  $\text{CO}_2$  and carbon-13  $\text{CO}_2$ . A ruthenium-carbonyl complex was also formed in situ and observed by IR and MS. Mass spectroscopy was also used to study the reduced complexes with  $\text{CO}_2$ , and metal-hydroxycarbonyl complexes were observed for **1-5**. These results suggest that reduced **5** is able to bind  $\text{CO}_2$  to form a hydroxycarbonyl species, and reduced **5** is able to bind CO to form a ruthenium-carbonyl species, which would be an intermediate in the catalytic cycle of  $\text{CO}_2$  reduction

to CO. The results from the studies performed were used to develop a potential catalytic cycle for **5** acting as a catalyst for CO<sub>2</sub> reduction to CO.

## 7.4 Experimental

### 7.4.1 General Methods

All syntheses and manipulations were performed under a nitrogen atmosphere through Schlenk and glovebox techniques. Acetonitrile for all studies was obtained from a solvent purification system and was kept air- and water-free. <sup>13</sup>CO<sub>2</sub> (>98 % <sup>13</sup>C, <2 % <sup>18</sup>O) and <sup>13</sup>CO (99 % <sup>13</sup>C, <5 % <sup>18</sup>O) were obtained from Sigma-Aldrich. CO<sub>2</sub> (UHP grade) and CO (UHP grade) were purchased from Airgas and were used as received. All ruthenium complexes were synthesized according to literature procedures.<sup>5, 9</sup> KC<sub>8</sub> was synthesized according to literature procedure.<sup>29</sup> IR spectra were obtained under a nitrogen atmosphere with a Bruker Alpha ATR-IR spectrometer in the solid state. ReactIR spectra were measured with a Mettler-Toledo ReactIR 15 under a nitrogen atmosphere. UV-vis measurements were performed under a nitrogen atmosphere with an Ocean Optics Flame-Chem UV-vis spectrometer. MS spectra were obtained using a Waters Xevo G2-XS Qtof-ESI mass spectrometer.

### 7.4.3 General Procedure for the Isolation of Reduced Complexes, **1<sub>red</sub>**- **5<sub>red</sub>**

4 mg of the ruthenium complex was dissolved in a minimum of dry, degassed acetonitrile (0.4-1 mL). 2-4 equivalents of reducing agent (depending upon the complex, see SI) were added by micropipetting a slurry of KC<sub>8</sub> in MeCN to the ruthenium solution. The solution was stirred for 15 min and was then filtered through a 0.22 μm

nylon syringe filter. The solvent of the filtrate was removed under vacuum to yield the reduced species as a dark orange solid.

#### *7.4.4 General Procedure for the Isolation of Reduced+CO<sub>2</sub> Complexes, **1<sub>red</sub>**+CO<sub>2</sub> – **5<sub>red</sub>**+CO<sub>2</sub>*

4 mg of the ruthenium complex was dissolved in a minimum of dry, degassed acetonitrile (0.4-1 mL). 2-4 equivalents of reducing agent (depending upon the complex, see SI) were added by micropipetting a slurry of KC<sub>8</sub> in MeCN to the ruthenium solution. The solution was stirred for 15 minutes and was then filtered through a 0.22 μm nylon syringe filter. CO<sub>2</sub>(g) was bubbled through the solution until all of the solvent evaporated, yielding the reduced+CO<sub>2</sub> complex as a light orange solid.

#### *7.4.5 General Procedure for ReactIR Experiments with Gaseous Substrates*

ReactIR spectra were measured with a Mettler-Toledo ReactIR 15 under a nitrogen atmosphere on a Schlenk line. A solution of the ruthenium complex (reduced or unreduced; ~8 mM) in acetonitrile was loaded into a 3-neck round-bottom flask in a glovebox. The flask was put under a flow of nitrogen gas on a Schlenk line, and the ReactIR probe was inserted into the flask and was sealed with a glass adapter. The ReactIR instrument was started measuring. The flask was then briefly put under vacuum and was then opened to the appropriate gas (CO<sub>2</sub>, <sup>13</sup>CO<sub>2</sub>, CO, or <sup>13</sup>CO), and the vacuum was sufficient to draw the gas into the flask. The flask was then sealed to leave the flask under the appropriate atmosphere for the remainder of the experiment.

#### *7.4.6 Procedure for Forming and Measuring IR Spectrum of **5** with CO*

4.1 mg of **5** (3.8  $\mu\text{mol}$ ) were dissolved in 0.5 mL of acetonitrile under an inert atmosphere. 2 equivalents of  $\text{KC}_8$  were added, and the mixture was stirred for 15 minutes before filtering through a 0.22  $\mu\text{m}$  nylon syringe filter to yield a dark orange solution. The solution was placed in a high-pressure vessel, and the vessel was pressurized to 240 psig of  $\text{CO}(\text{g})$ . The solution was stirred under pressure for 24 hours at room temperature. After 24 hours, the solution is dark red-orange. The IR spectrum of the solution was then measured using a liquid IR cell.

## 7.5 Author Contribution

I was the intellectual lead and performed all of the experimental work included in this chapter. I was also the lead author on the paper that will be submitted from this project.

## 7.6 References

1. Robert, M. *ACS Energy Lett.*, **2016**, *1*, 281-282.
2. Mikkelsen, M.; Jørgensen, M.; Krebs, F. C. *Energy Environ. Sci.*, **2010**, *3*, 43-81.
3. Benson, E. E.; Kubiak, C. P.; Sathrum, A. J.; Smieja, J. M. *Chem. Soc. Rev.*, **2009**, *38*, 89-99.
4. Ishida, H.; Terada, T.; Tanaka, K.; Tanaka, T. *Inorg. Chem.*, **1990**, *29*, 905-911.
5. Boudreaux, C. M.; Liyanage, N. P.; Shirley, H.; Siek, S.; Gerlach, D. L.; Qu, F.; Delcamp, J. H.; Papish, E. T. *Chem. Commun.*, **2017**, *53*, 11217-11220.
6. Rodrigues, R. R.; Boudreaux, C. M.; Papish, E. T.; Delcamp, J. H. *ACS Applied Energy Materials*, **2018**, *2*, 37-46.
7. Burks, D. B.; Davis, S.; Lamb, R. W.; Liu, X.; Rodrigues, R. R.; Liyanage, N. P.; Sun, Y.; Webster, C. E.; Delcamp, J. H.; Papish, E. T. *Chem. Commun.*, **2018**, Submitted.
8. Morris, A. J.; Meyer, G. J.; Fujita, E. *Acc. Chem. Res.*, **2009**, *42*, 1983-94.

9. Das, S.; Rodrigues, R. R.; Lamb, R. W.; Qu, F.; Reinheimer, E.; Boudreaux, C. M.; Webster, C. E.; Delcamp, J. H.; Papish, E. T. *Inorg. Chem.*, **2019**, *58*, 8012-8020.
10. Smieja, J. M.; Benson, E. E.; Kumar, B.; Grice, K. A.; Seu, C. S.; Miller, A. J.; Mayer, J. M.; Kubiak, C. P. *Proc. Natl. Acad. Sci. U S A*, **2012**, *109*, 15646-50.
11. Cook, B. J.; Di Francesco, G. N.; Abboud, K. A.; Murray, L. J. *J. Am. Chem. Soc.*, **2018**, *140*, 5696-5700.
12. Sampson, M. D.; Froehlich, J. D.; Smieja, J. M.; Benson, E. E.; Sharp, I. D.; Kubiak, C. P. *Energy Environ. Sci.*, **2013**, *6*, 3748.
13. Schneider, T. W.; Hren, M. T.; Ertem, M. Z.; Angeles-Boza, A. M. *Chem. Commun.*, **2018**, *54*, 8518-8521.
14. Schneider, T. W.; Ertem, M. Z.; Muckerman, J. T.; Angeles-Boza, A. M. *ACS Catal.*, **2016**, *6*, 5473-5481.
15. Agarwal, J.; Fujita, E.; Schaefer, H. F., 3rd; Muckerman, J. T. *J. Am. Chem. Soc.*, **2012**, *134*, 5180-6.
16. Riplinger, C.; Sampson, M. D.; Ritzmann, A. M.; Kubiak, C. P.; Carter, E. A. *J. Am. Chem. Soc.*, **2014**, *136*, 16285-98.
17. Francke, R.; Schille, B.; Roemelt, M. *Chem. Rev.*, **2018**, *118*, 4631-4701.
18. Machan, C. W.; Sampson, M. D.; Kubiak, C. P. *J. Am. Chem. Soc.*, **2015**, *137*, 8564-71.
19. Mascetti, J., Carbon Dioxide Coordination Chemistry and Reactivity of Coordinated CO<sub>2</sub>. In *Carbon Dioxide as Chemical Feedstock*, Aresta, M., Ed. Wiley-VCH: Weinheim, 2010.
20. Aresta, M.; Dibenedetto, A.; Quaranta, E., *Reaction Mechanisms in Carbon Dioxide Conversion*. Springer: 2016.
21. Behr, A., *Carbon Dioxide Activation by Metal Complexes*. VCH: Weinheim: 1988.
22. Sampson, M. D.; Kubiak, C. P. *J. Am. Chem. Soc.*, **2016**, *138*, 1386-93.
23. Chung, L. H.; Cho, K. S.; England, J.; Chan, S. C.; Wieghardt, K.; Wong, C. Y. *Inorg. Chem.*, **2013**, *52*, 9885-96.
24. Cargill, R. W., *Carbon Monoxide*. International Union of Pure and Applied Chemistry: Oxford, UK, 1990; Vol. 43.
25. *Dimethyl Sulfoxide Solubility Data*. Gaylord Chemical Company: 2014; Vol. Bulletin 102.

26. Gagliardi, C. J.; Vannucci, A. K.; Concepcion, J. J.; Chen, Z.; Meyer, T. J. *Energy Environ. Sci.*, **2012**, *5*.
27. Kou, Y.; Nabetani, Y.; Masui, D.; Shimada, T.; Takagi, S.; Tachibana, H.; Inoue, H. *J. Am. Chem. Soc.*, **2014**, *136*, 6021-30.
28. Takeda, H.; Koike, K.; Inoue, H.; Ishitani, O. *J. Am. Chem. Soc.*, **2008**, *130*, 2023-31.
29. Schwindt, M. A.; Lejon, T.; Hegedus, L. S. *Organometallics*, **1990**, *9*, 2814-2819.
30. Frisch, M. J.; Trucks, G. W.; Schlegel, H. B.; Scuseria, G. E.; Robb, M. A.; Cheeseman, J. R.; Scalmani, G.; Barone, V.; Mennucci, B.; Petersson, G. A.; Nakatsuji, H.; Caricato, M.; Li, X.; Hratchian, H. P.; Izmaylov, A. F.; Bloino, J.; Zheng, G.; Sonnenberg, J. L.; Hada, M.; Ehara, M.; Toyota, K.; Fukuda, R.; Hasegawa, J.; Ishida, M.; Nakajima, T.; Honda, Y.; Kitao, O.; Nakai, H.; Vreven, T.; Jr., J. A. M.; Peralta, J. E.; Ogliaro, F.; Bearpark, M. J.; Heyd, J.; Brothers, E. N.; Kudin, K. N.; Staroverov, V. N.; Kobayashi, R.; Normand, J.; Raghavachari, K.; Rendell, A. P.; Burant, J. C.; Iyengar, S. S.; Tomasi, J.; Cossi, M.; Rega, N.; Millam, N. J.; Klene, M.; Knox, J. E.; Cross, J. B.; Bakken, V.; Adamo, C.; Jaramillo, J.; Gomperts, R.; Stratmann, R. E.; Yazyev, O.; Austin, A. J.; Cammi, R.; Pomelli, C.; Ochterski, J. W.; Martin, R. L.; Morokuma, K.; Zakrzewski, V. G.; Voth, G. A.; Salvador, P.; Dannenberg, J. J.; Dapprich, S.; Daniels, A. D.; Farkas, Ö.; Foresman, J. B.; Ortiz, J. V.; Cioslowski, J.; Fox, D. J. *Gaussian 09, Revision D.01*, Gaussian, Inc.: Wallingford, CT, USA, 2013.
31. Adamo, C.; Barone, V. *J. Chem. Phys.*, **1999**, *110*, 6158-6170.
32. Grimme, S.; Ehrlich, S.; Goerigk, L. *J. Comput. Chem.*, **2011**, *32*, 1456-1465.
33. Couty, M.; Hall, M. B. *J. Comput. Chem.*, **1996**, *17*, 1359-1370.
34. Check, C. E.; Faust, T. O.; Bailey, J. M.; Wright, B. J.; Gilbert, T. M.; Sunderlin, L. S. *J. Phys. Chem. A*, **2001**, *105*, 8111-8116.
35. Wadt, W. R.; Hay, P. J. *J. Chem. Phys.*, **1985**, *82*, 284-298.
36. Hehre, W. J.; Ditchfield, R.; Pople, J. A. *J. Chem. Phys.*, **1972**, *56*, 2257-2261.
37. Hariharan, P. C.; Pople, J. A. *Theor. Chim. Acta*, **1973**, *28*, 213-222.
38. Petersson, G. A.; Al-Laham, M. A. *J. Chem. Phys.*, **1991**, *94*, 6081-6090.
39. McLean, A. D.; Chandler, G. S. *J. Chem. Phys.*, **1980**, *72*, 5639-5648.
40. Petersson, G. A.; Al-Laham, M. A. *J. Chem. Phys.*, **1991**, *94*, 6081-6090.
41. Marenich, A. V.; Cramer, C. J.; Truhlar, D. G. *J. Phys. Chem. B*, **2009**, *113*, 6378-6396.

42. Press, W. H., *Numerical recipes in FORTRAN : the art of scientific computing*. 2nd ed.; Cambridge University Press: Cambridge England ; New York, NY, USA, 1992; p 963.
43. Marques, M. A. L.; Gross, E. K. U. *Annu. Rev. Phys. Chem.*, **2004**, *55*, 427-455.
44. Chemcraft - graphical software for visualization of quantum chemistry computations. <http://www.chemcraftprog.com>.
45. Fujita, E.; Szalda, D. J.; Creutz, C.; Sutin, N. *J. Am. Chem. Soc.*, **1988**, *110*, 4870-4871.

## 7.7 Supporting Information

### 7.7.1 UV/vis Spectra

#### 7.7.1.1 General Procedure for Obtaining UV/vis Spectra

1.00 mL of a 0.3 mM solution of the ruthenium complex (unreduced or reduced) in acetonitrile and 1.00 mL of acetonitrile or CO<sub>2</sub>-saturated acetonitrile ([CO<sub>2</sub>] = 0.28 M)<sup>45</sup> were mixed in a nitrogen atmosphere. The UV/vis spectrum was then measured under a nitrogen atmosphere.

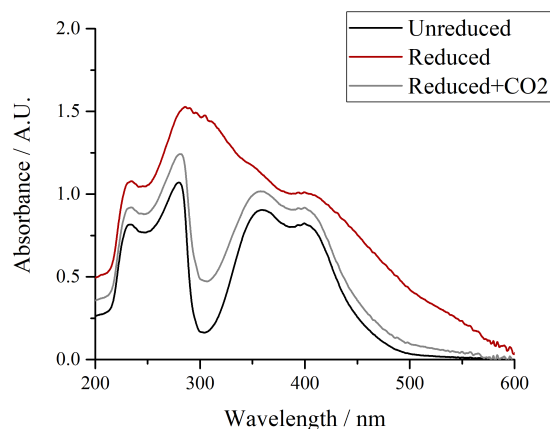


*Figure 7.S1.* UV/vis spectra of a 0.15 mM solution of **1** in acetonitrile: unreduced (black), reduced with 4 equivalents of KC<sub>8</sub> (crimson), and reduced with 4 equivalents of KC<sub>8</sub> followed by exposure to CO<sub>2</sub> (grey).

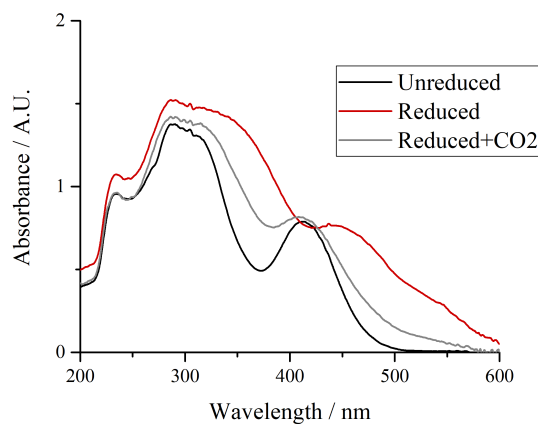


*Figure 7.S2.* UV/vis spectra of a 0.15 mM solution of **2** in acetonitrile: unreduced (black), reduced with 3 equivalents of KC<sub>8</sub> (crimson), and reduced with 3 equivalents of KC<sub>8</sub> followed by exposure to CO<sub>2</sub> (grey).

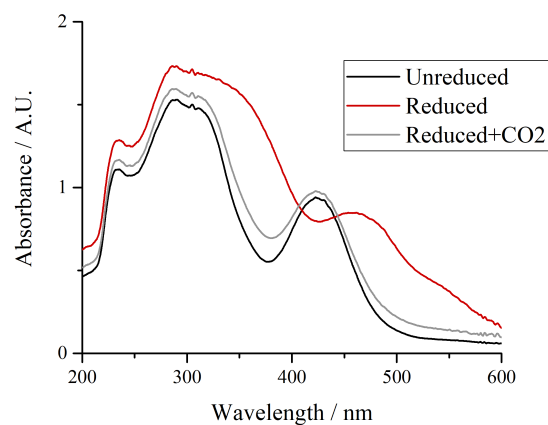


*Figure 7.S3.* UV/vis spectra of a 0.15 mM solution of **3** in acetonitrile: unreduced (black), reduced with 3 equivalents of  $\text{KC}_8$  (crimson), and reduced with 3 equivalents of  $\text{KC}_8$  followed by exposure to  $\text{CO}_2$  (grey).

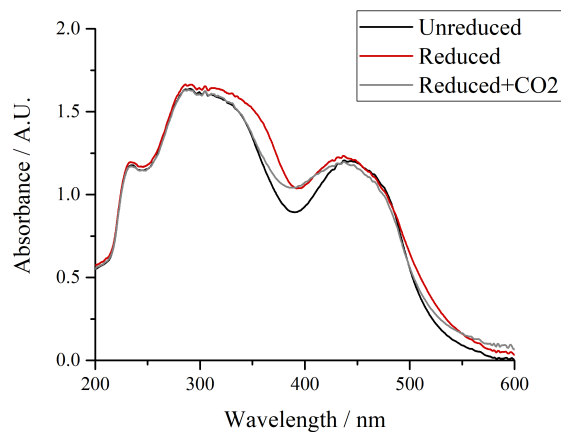


*Figure 7.S4.* UV/vis spectra of a 0.15 mM solution of **4** in acetonitrile: unreduced (black), reduced with 2 equivalents of  $\text{KC}_8$  (crimson), and reduced with 2 equivalents of  $\text{KC}_8$  followed by exposure to  $\text{CO}_2$  (grey).

## 7.7.2 IR Spectra

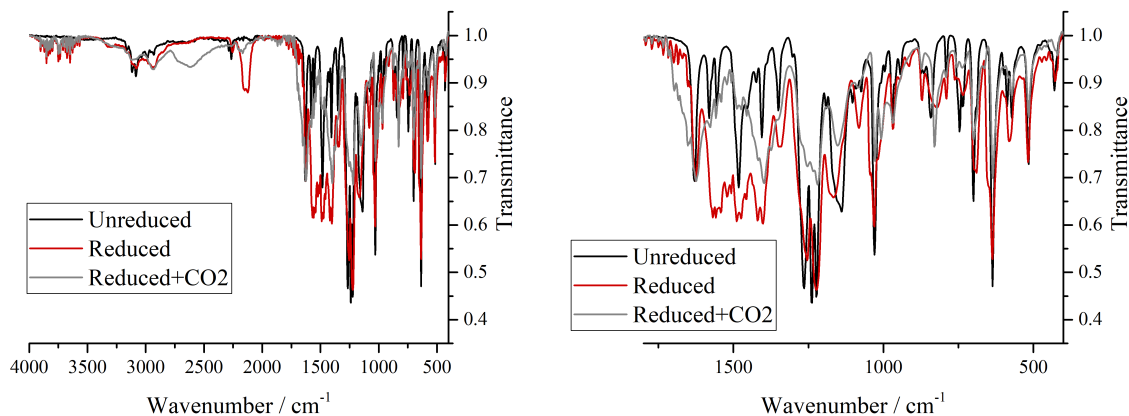


Figure 7.S5. ATR-IR spectra in the solid state of unreduced **1** (black), reduced **1** (**1<sub>red</sub>**, reduced with 4 equivalents  $\text{KC}_8$ , crimson), and reduced **1** with  $\text{CO}_2$  (**1<sub>red</sub>+CO<sub>2</sub>**, grey).

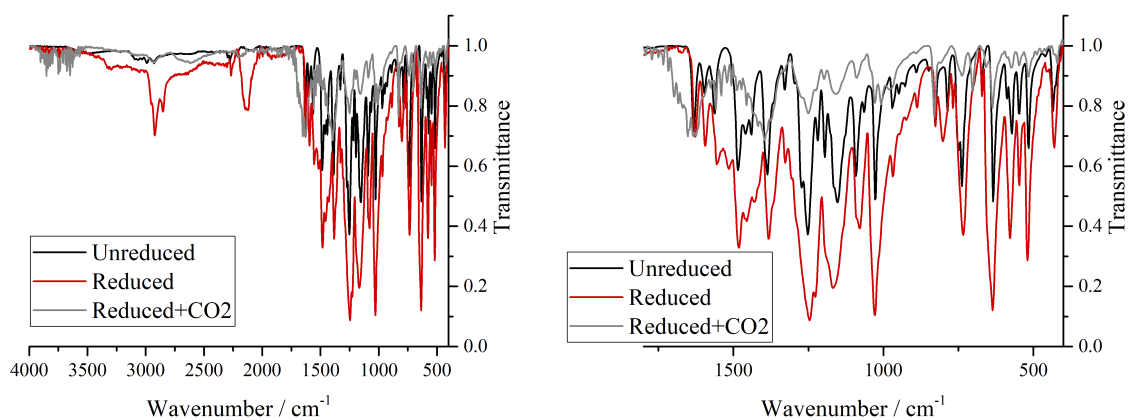


Figure 7.S6. ATR-IR spectra in the solid state of unreduced **2** (black), reduced **2** (**2<sub>red</sub>**, reduced with 3 equivalents  $\text{KC}_8$ , crimson), and reduced **2** with  $\text{CO}_2$  (**2<sub>red</sub>+CO<sub>2</sub>**, grey).

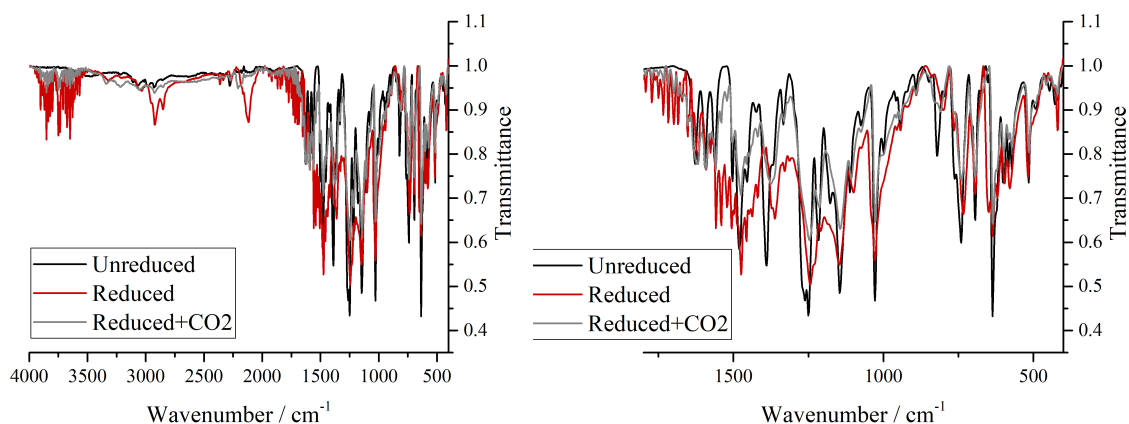
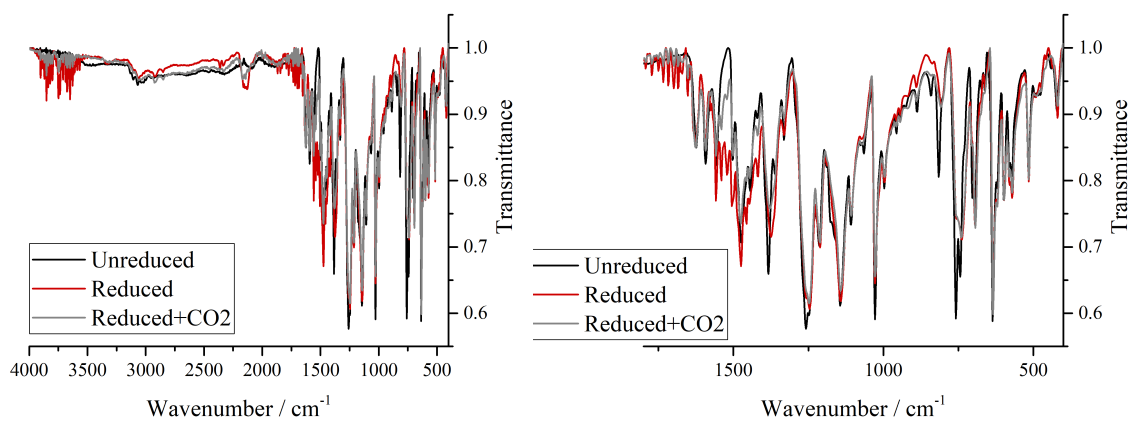


Figure 7.S7. ATR-IR spectra in the solid state of unreduced **3** (black), reduced **3** (**3<sub>red</sub>**, reduced with 3 equivalents  $\text{KC}_8$ , crimson), and reduced **3** with  $\text{CO}_2$  (**3<sub>red</sub>+CO<sub>2</sub>**, grey).



*Figure 7.S8.* ATR-IR spectra in the solid state of unreduced **4** (black), reduced **4** (**4<sub>red</sub>**, reduced with 2 equivalents KC<sub>8</sub>, crimson), and reduced **4** with CO<sub>2</sub> (**4<sub>red</sub>+CO<sub>2</sub>**, grey).

### 7.7.3 MS Spectra

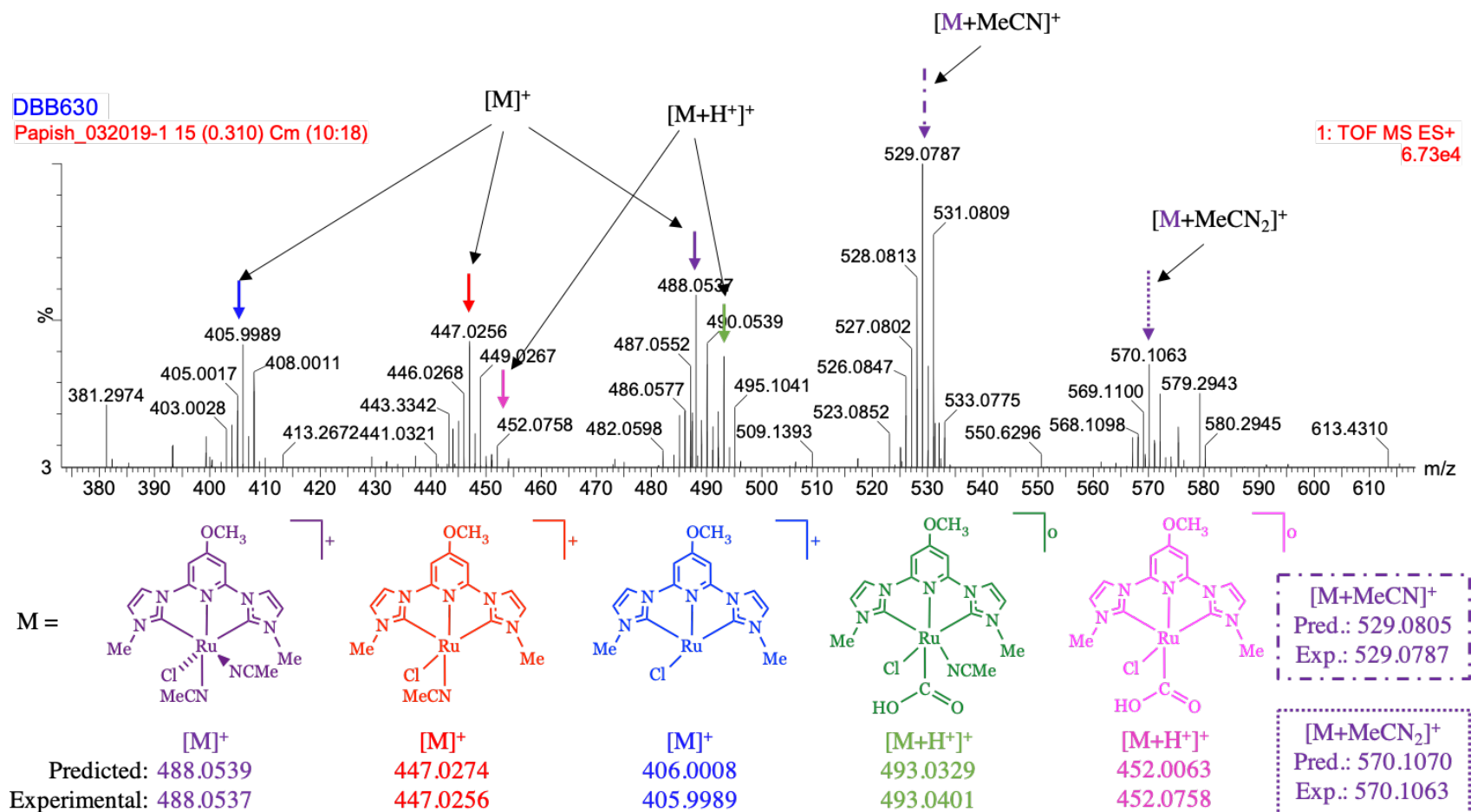


Figure 7.S9. QToF-ESI-MS of **1<sub>red</sub>**+CO<sub>2</sub>. Peaks in the spectrum are labeled with color-coded arrows which correspond to the same colored structures shown. [M] corresponds to the structure shown in the same color.

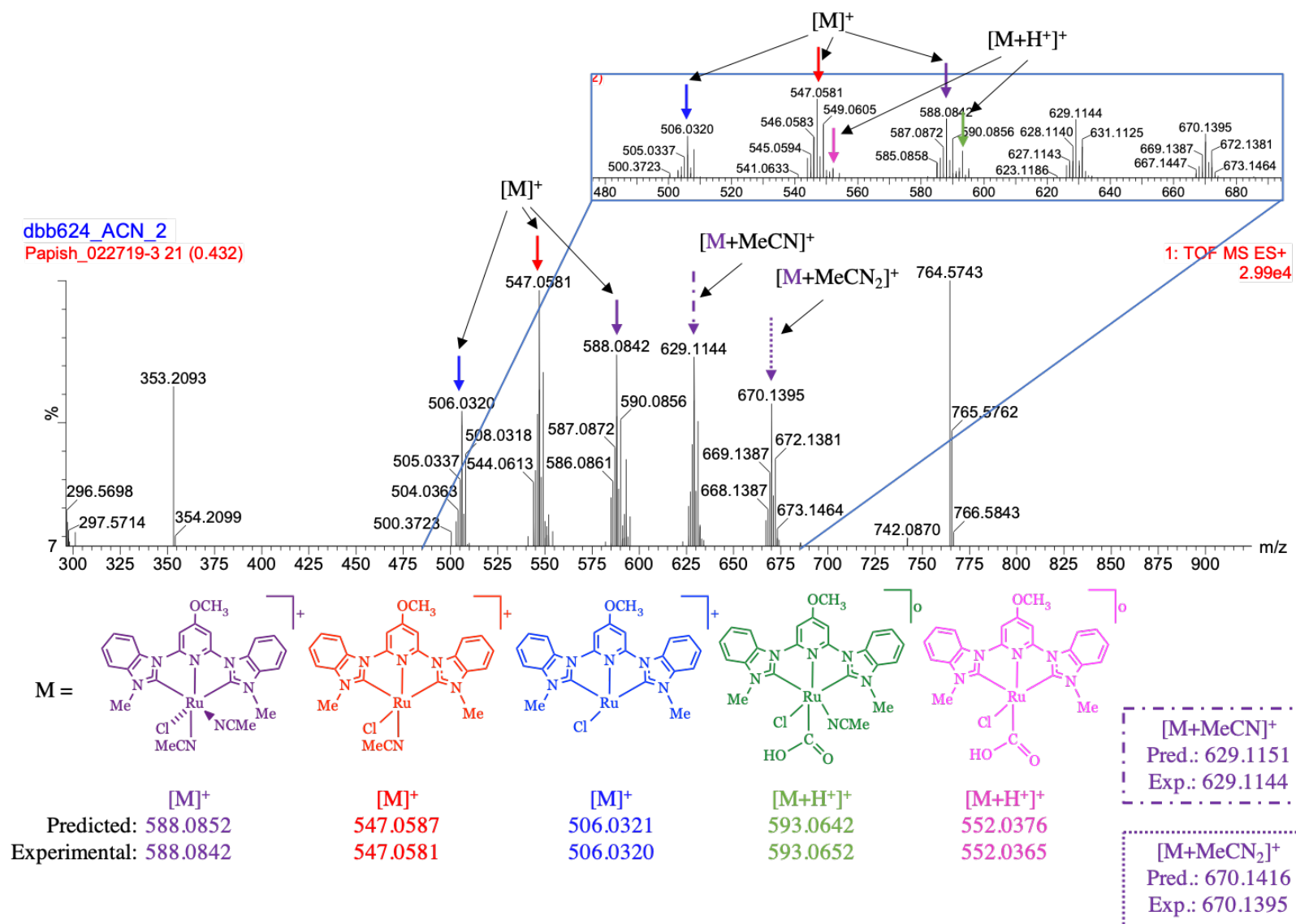


Figure 7.S10. QToF-ESI-MS of **2<sub>red</sub>**+CO<sub>2</sub>. Peaks in the spectrum are labeled with color-coded arrows which correspond to the same colored structures shown.  $[M]$  corresponds to the structure shown in the same color.

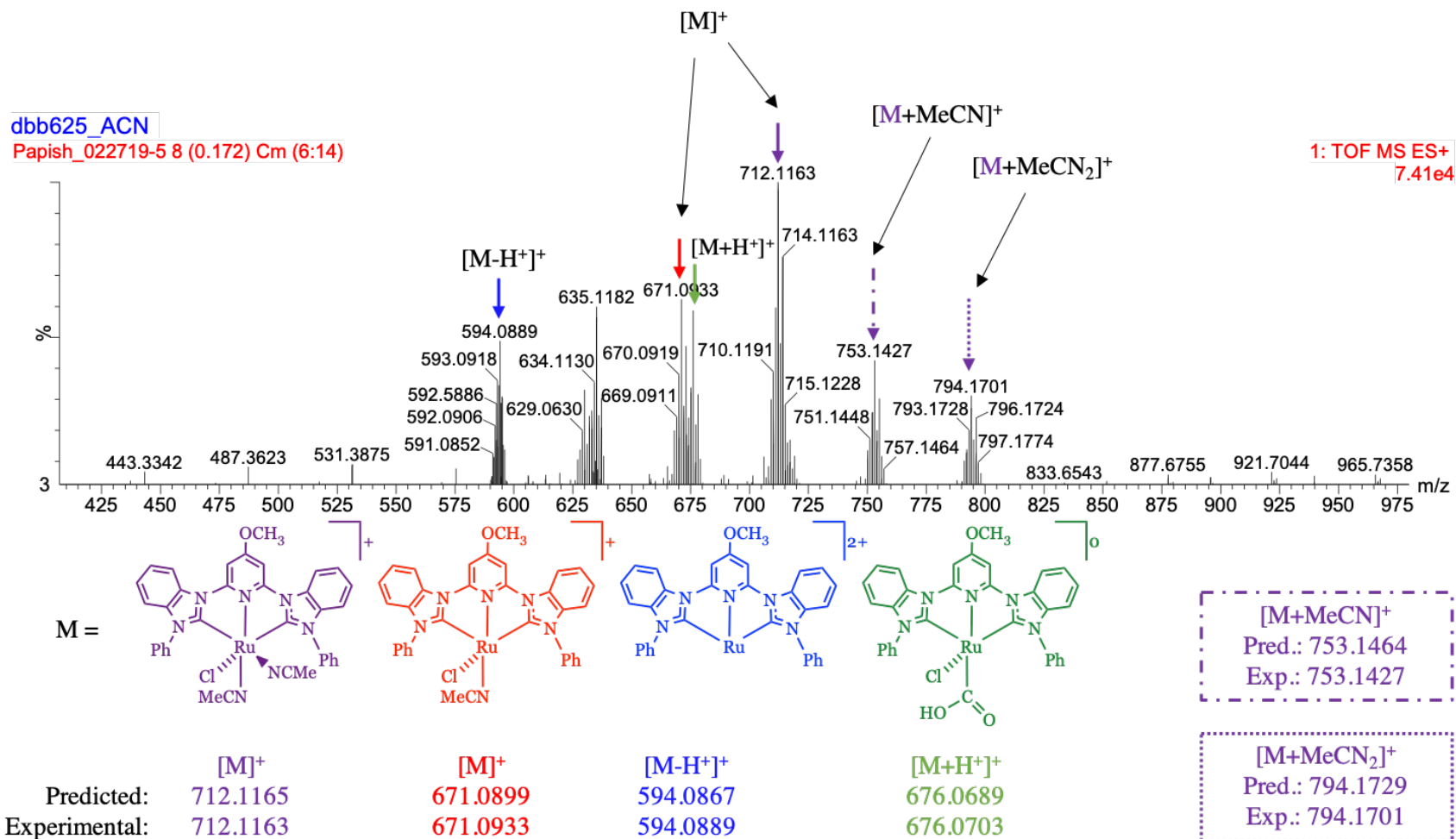


Figure 7.S11. QToF-ESI-MS of **3<sub>red</sub>**+CO<sub>2</sub>. Peaks in the spectrum are labeled with color-coded arrows which correspond to the same colored structures shown. [M] corresponds to the structure shown in the same color.

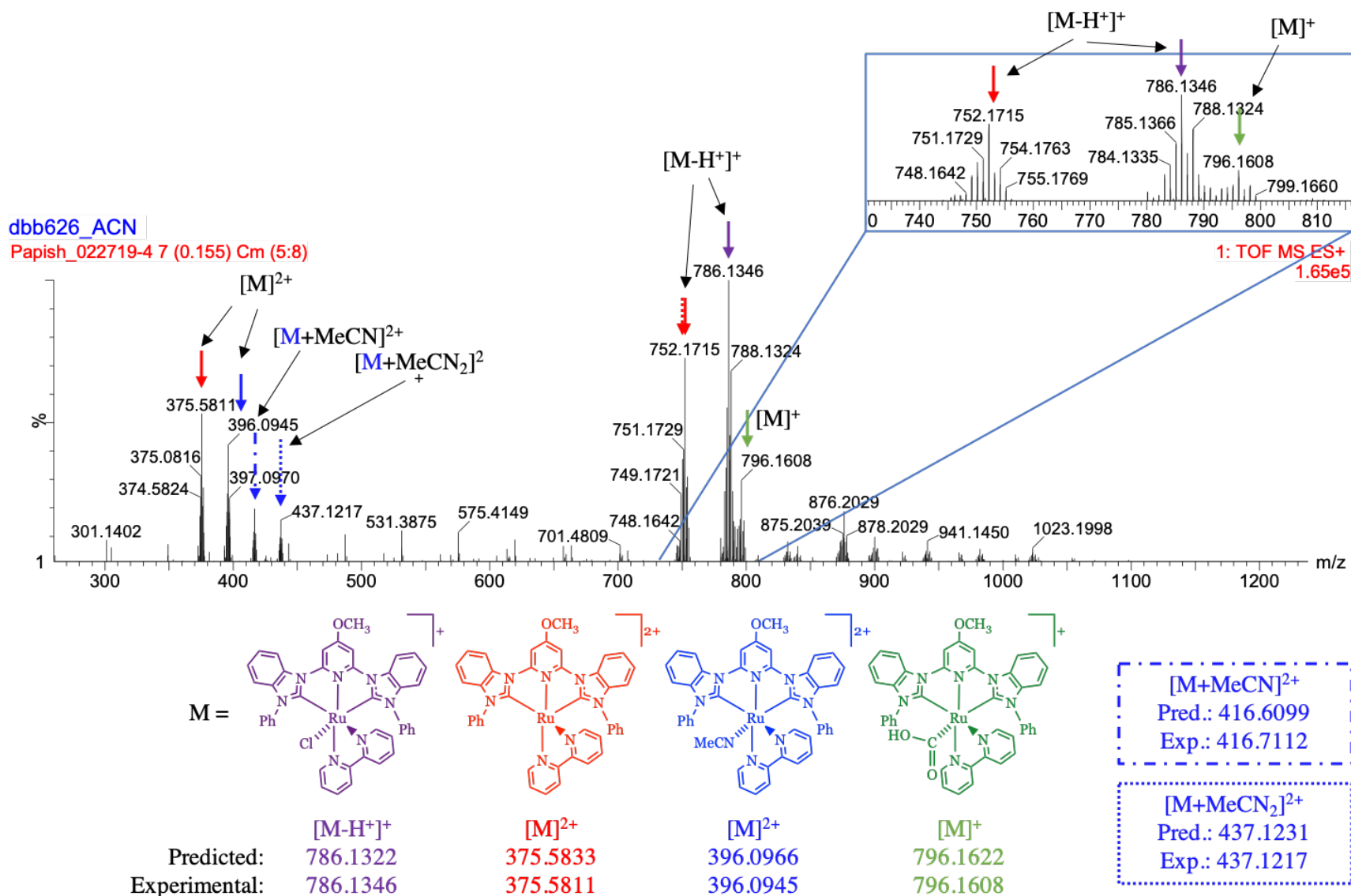


Figure 7.S12. QToF-ESI-MS of  $4_{red} + CO_2$ . Peaks in the spectrum are labeled with color-coded arrows which correspond to the same colored structures shown.  $[M]$  corresponds to the structure shown in the same color.

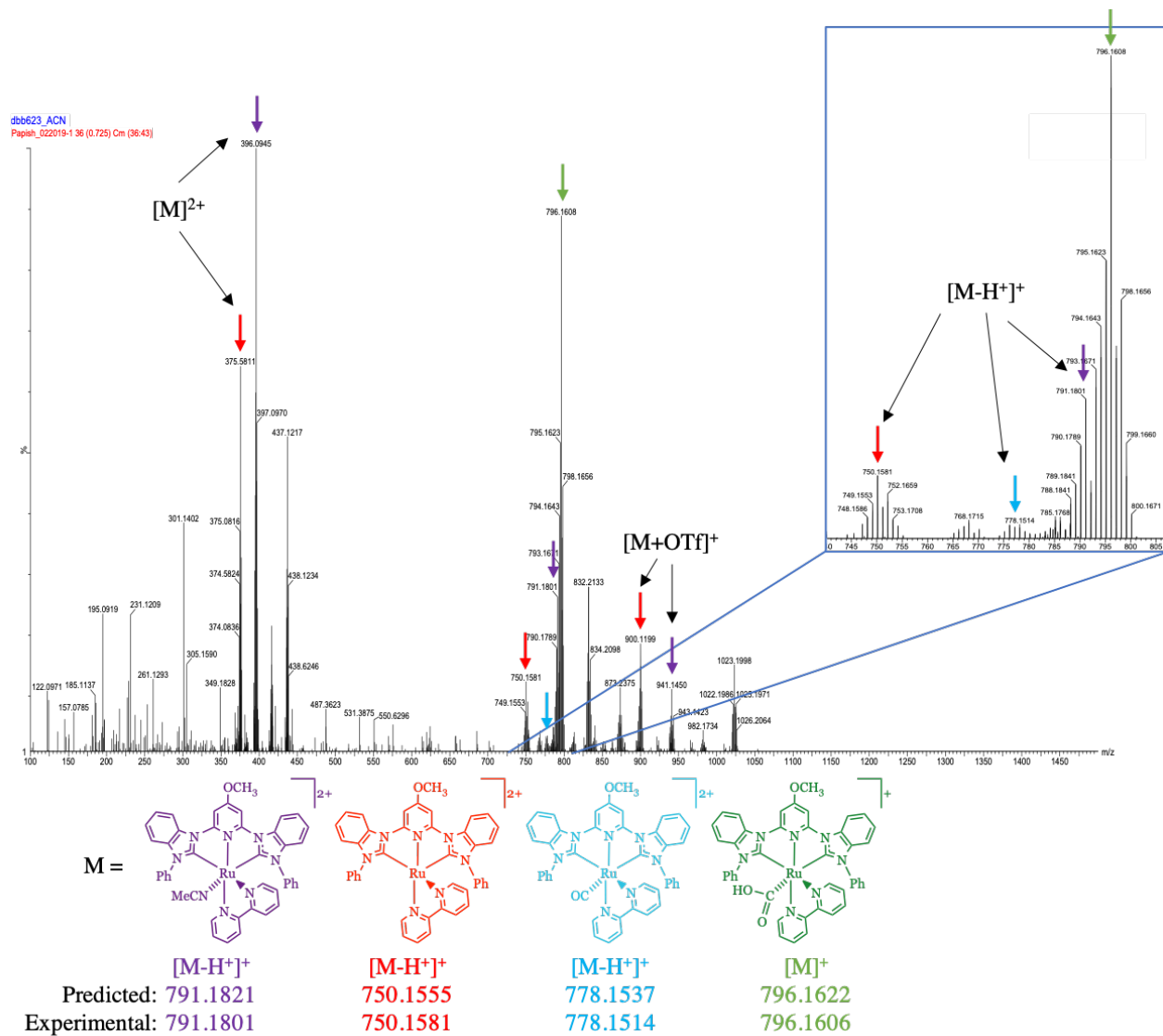


Figure 7.S13. QToF-ESI-MS of **5<sub>red</sub>**+CO<sub>2</sub>. Peaks in the spectrum are labeled with color-coded arrows which correspond to the same colored structures shown. [M] corresponds to the structure shown in the same color.

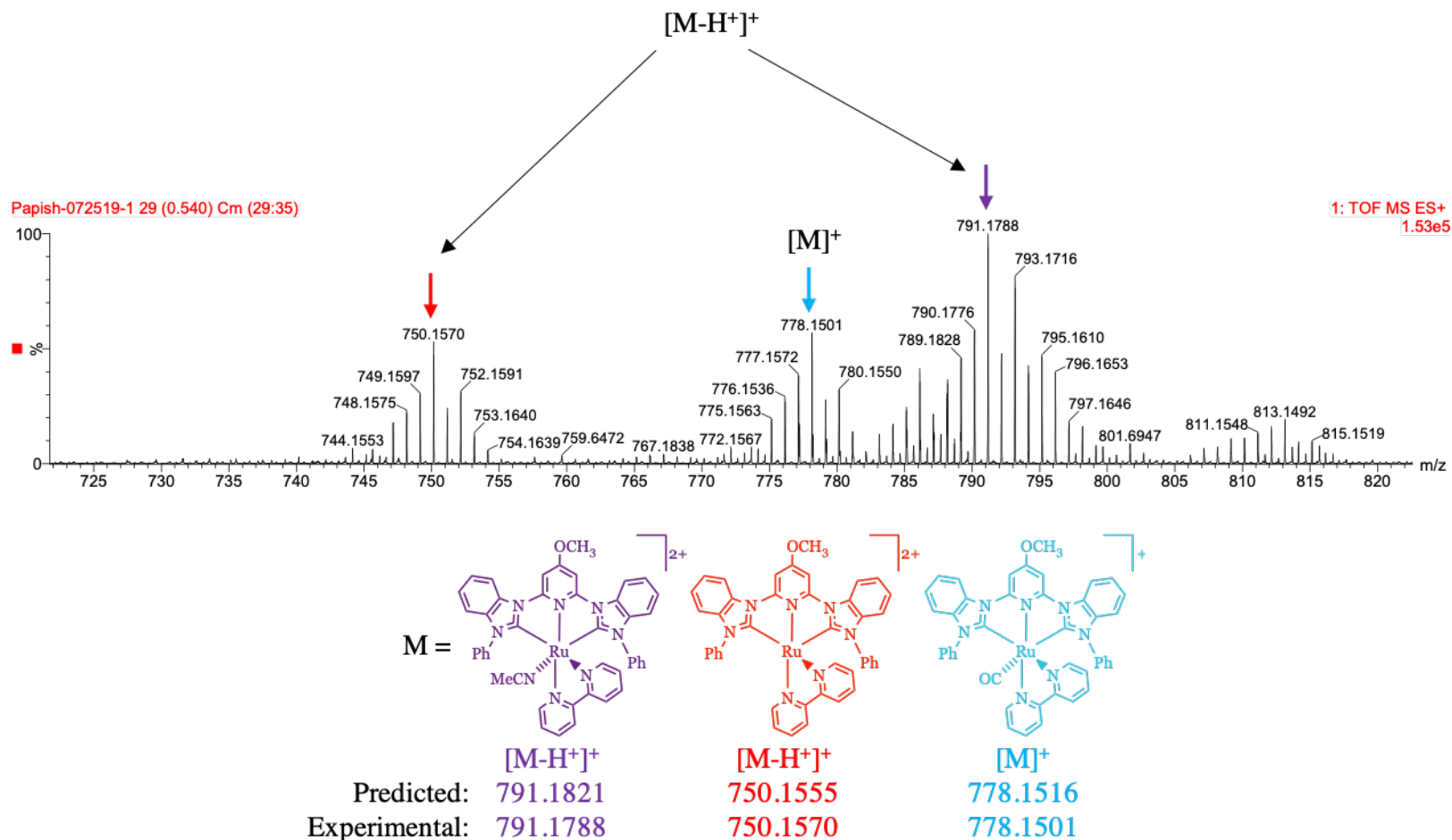
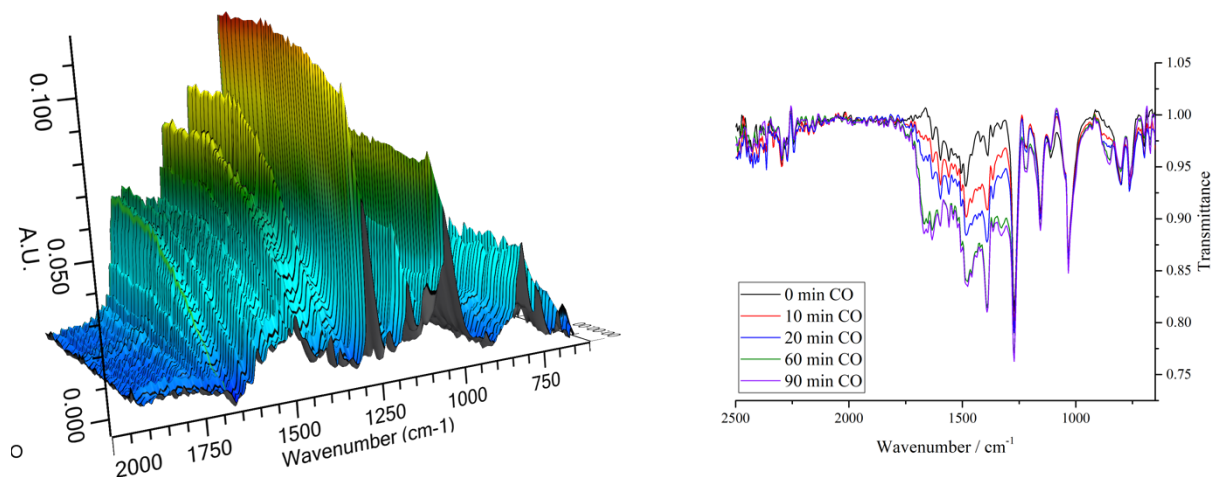
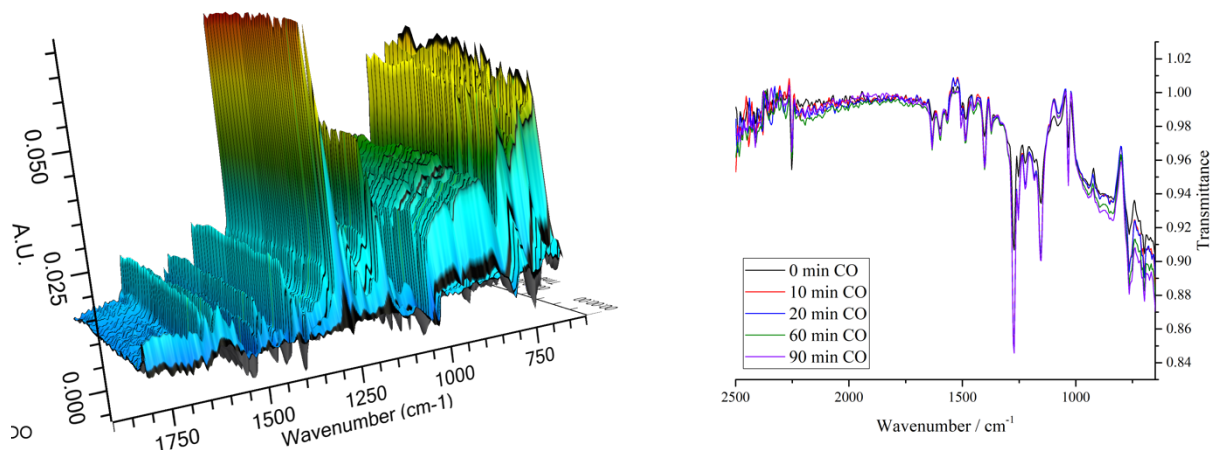


Figure 7.S14. QToF-ESI-MS of reduced 5 after stirring for 24 h under 240 psig of CO(g). Peaks in the spectrum are labeled with color-coded arrows which correspond to the same colored structures shown. [M] corresponds to the structure shown in the same color.

### 7.7.4 ReactIR Spectra



*Figure 7.S15.* (Left) ReactIR spectra of **5** (reduced with 2 eq. KC<sub>8</sub>) and CO monitored over a 90 minute period. (Right) Overlaid IR spectra obtained from the ReactIR after 0 minutes (black), 10 minutes (red), 20 minutes (blue), 60 minutes (green), and 90 minutes (purple) exposure to CO.



*Figure 7.S16.* (Left) ReactIR spectra of unreduced **5** with CO over a 90 minute period. No major changes were observed. (Right) Overlaid IR spectra obtained from the ReactIR after 0 minutes (black), 10 minutes (red), 20 minutes (blue), 60 minutes (green), and 90 minutes (purple) exposure to CO.

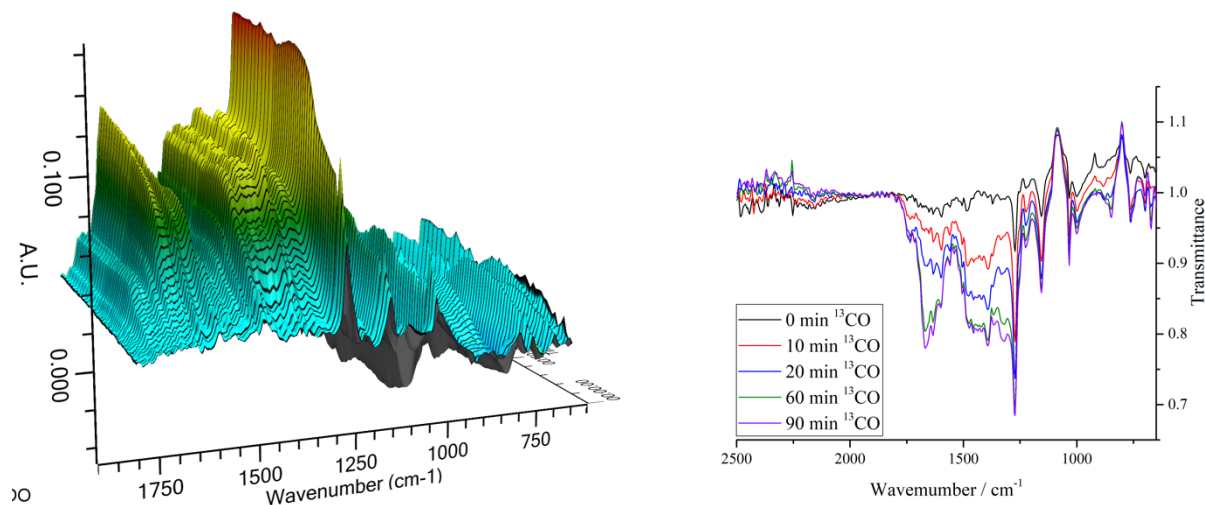


*Figure 7.S17.* (Left) ReactIR spectra of **5** (reduced with 2 eq.  $\text{KC}_8$ ) and  $^{13}\text{CO}$  monitored over a 90 minute period. (Right) Overlaid IR spectra obtained from the ReactIR after 0 minutes (black), 10 minutes (red), 20 minutes (blue), 60 minutes (green), and 90 minutes (purple) exposure to  $^{13}\text{CO}$ .

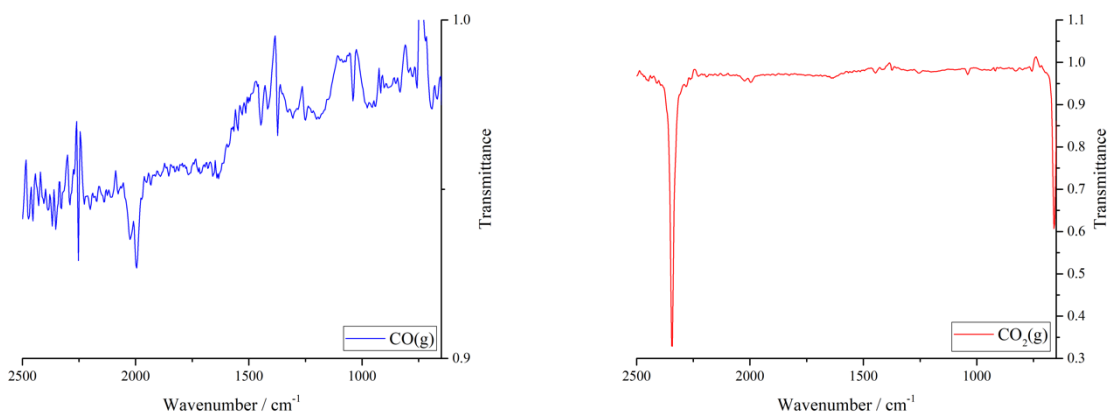


*Figure 7.S18.* (Left) IR spectrum of acetonitrile purged with  $\text{CO}(\text{g})$  for 30 minutes, measured with the ReactIR instrument. The doublet of peaks at 1995 and 2024  $\text{cm}^{-1}$  are assigned to  $\text{CO}$ . (Right) IR spectrum of acetonitrile purged with  $\text{CO}_2(\text{g})$  for 5 minutes, measured with the ReactIR instrument. For comparison,  $\text{CO}_2(\text{g})$  was bubbled through the same solution after  $\text{CO}(\text{g})$  was purged through MeCN. The absorbance of the  $\text{CO}_2$  peak is  $\sim 16$  times more intense than the absorbance of the  $\text{CO}$  peak.

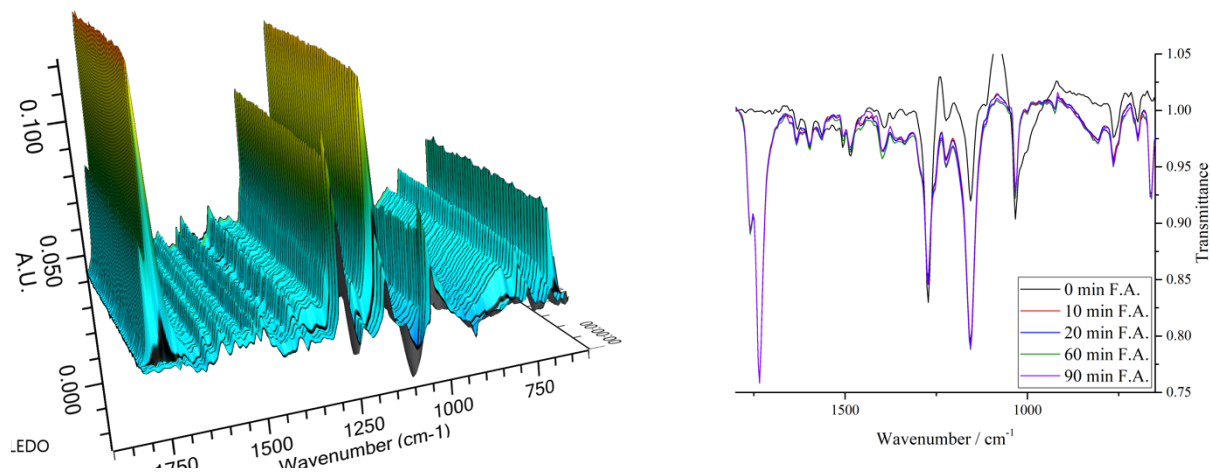


**Figure 7.S19.** (Left) ReactIR spectra of **5** (reduced with 2 eq.  $\text{KC}_8$ ) and formic acid (FA) monitored over a 90 minute period. (Right) Overlaid IR spectra obtained from the ReactIR after 0 minutes (black), 10 minutes (red), 20 minutes (blue), 60 minutes (green), and 90 minutes (purple) exposure to FA. Peaks at 1734, 1339 (broad), 1156, 830 (broad), and 664  $\text{cm}^{-1}$  are due to unbound formic acid (see Figure S24).

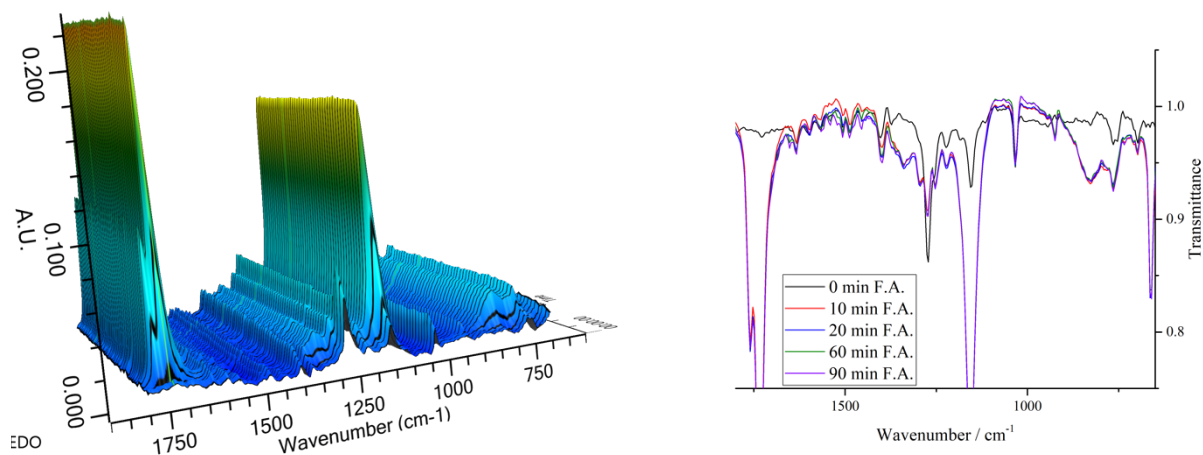


**Figure 7.S20.** (Left) ReactIR spectra of unreduced **5** and formic acid (FA) monitored over a 90 minute period. (Right) Overlaid IR spectra obtained from the ReactIR after 0 minutes (black), 10 minutes (red), 20 minutes (blue), 60 minutes (green), and 90 minutes (purple) exposure to FA. Peaks at 1734, 1339 (broad), 1156, 830 (broad), and 664  $\text{cm}^{-1}$  are due to unbound formic acid (see Figure S24).

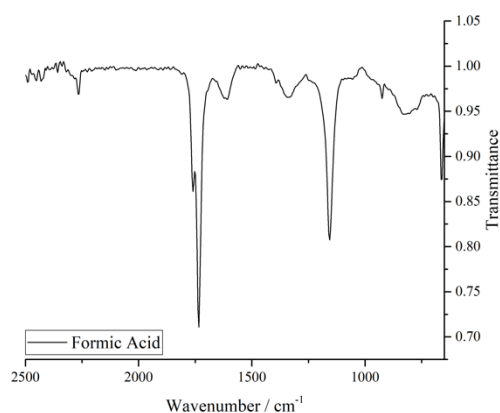


Figure 7.S21. IR spectrum of formic acid in acetonitrile.

### 7.7.5 Computational Studies

All computations were performed by Robert Lamb of the Webster group at Mississippi State University.

The energies of possible reaction pathways were also calculated (Figure 7.S25). Each complex is shown with the assigned complex name (e.g. 1-1) and computed energy in kcal/mol below the corresponding structure. Electrochemical steps are shown as vertical, down arrows, and chemical steps are shown as horizontal arrows. Therefore, each row in Figure 7.S26 is at the same oxidation state and moving down from one row to the next row corresponds to a one electron reduction. Due to the difficulties in calculating the reduction potential of BIH, the energies in each row can be compared to each other but caution should be used in quantitatively comparing energies from different rows (i.e. different oxidation states).

The most thermodynamically probable reaction pathways (that are supported by experiments) are shown in blue. From the IR experiments with unreduced **5** and CO<sub>2</sub> (Figures 7.S14-S15), it was determined that the unreduced complex likely does not bind CO<sub>2</sub>; therefore, the top row of the scheme (complex 1-1 to 1-2 to 1-3) does not seem likely

to occur and **5** must be reduced before CO<sub>2</sub> complexation occurs. This is likely due to the endergonic process of removing the MeCN ligand from the unreduced complex ( $\Delta G_{1-1 \rightarrow 1-2} = +17.1 \text{ kcal mol}^{-1}$ ); removing MeCN from the reduced complex 2-1 is less endergonic ( $\Delta G_{2-1 \rightarrow 2-2} = +5.8 \text{ kcal mol}^{-1}$ ). Complex 1-1 is thus reduced first to 2-1, which then loses MeCN and binds CO<sub>2</sub> to form complex 2-3. Complex 2-3 is then protonated ( $\Delta G_{2-3 \rightarrow 2-4} = -6.5 \text{ kcal mol}^{-1}$ ) and reduced to form the hydroxycarbonyl complex 3-4. (Complex 3-4 was experimentally observed in the MS spectrum and is assumed to be the complex observed in the IR spectrum.) It is then exergonic to protonate and undergo C-O bond cleavage to form complex 3-5 and water ( $\Delta G_{3-4 \rightarrow 3-5} = -20.1 \text{ kcal mol}^{-1}$ ). (Complex 3-5 was experimentally observed in the MS spectrum.) Releasing the CO from complex 3-5 is quite endergonic ( $\Delta G_{3-5 \rightarrow 3-6} = +37.2 \text{ kcal mol}^{-1}$ ). If 3-5 is reduced further to 5-5 (potentially accessed through proton-coupled electron transfer (PCET)), loss of CO becomes slightly less endergonic ( $\Delta G_{5-5 \rightarrow 5-6} = +13.5 \text{ kcal mol}^{-1}$ ). Loss of CO is, therefore, determined to be the rate limiting step in the reduction process of CO<sub>2</sub> to CO. Complex 5-5 may or may not be accessible under reaction conditions, even with PCET occurring; however, under photocatalytic reaction conditions, the solution is irradiated with light energy, which will help to overcome the high barrier and drive the removal of CO from the ruthenium center, as light irradiation is a common method for eliminating CO from metal-carbonyl complexes.

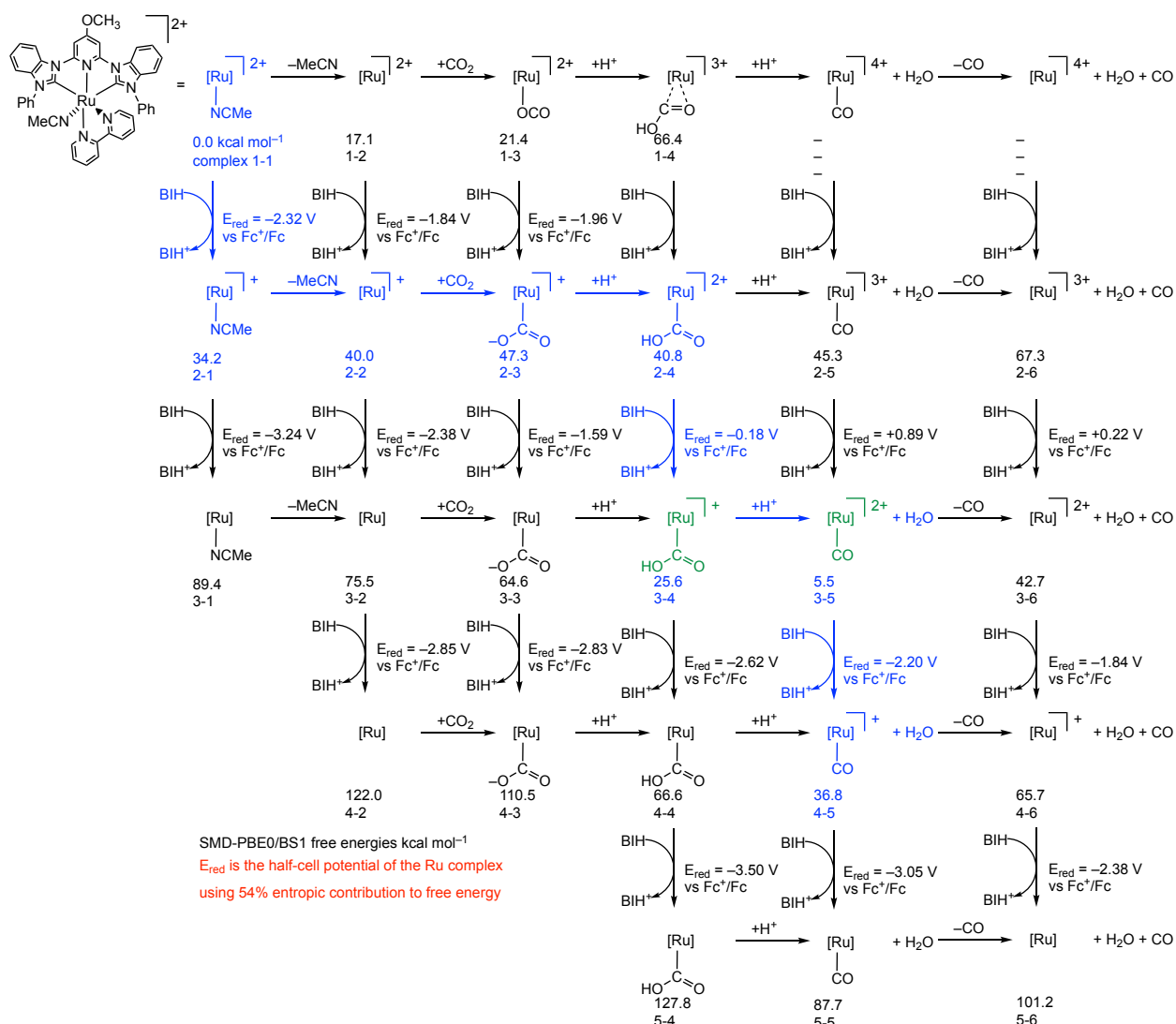


**Figure 7.S22.** Possible reaction pathways with computed energies. The most thermodynamically possible routes are shown in blue. Complexes that have been observed spectroscopically are shown in green. Energies in kcal/mol and complex names are shown below the corresponding structure.

There also exists the potential to undergo proton-coupled electron transfer (PCET). In PCET, the reduction and protonation are concerted and occur in one step instead of two—the equivalent of moving diagonally in Figure 7.S25 (e.g. complex 3-4 to complex 4-5). This can avoid high-energy reductions, especially when the subsequent protonation is highly exergonic. While PCET pathways were not calculated, it is possible

that under reaction conditions PCET will occur which will make some of the high-energy reductions more possible to occur.<sup>3, 26</sup>

### 7.7.6 Computational Methods

All computations were carried out using Revision D.01 of the Gaussian 09<sup>30</sup> suite of programs with non-default ( $10^{-6}$ ) convergence SCF convergence criteria [SCF(CONVER=6)]. The PBE0 functional<sup>31</sup> with Grimme's D3 dispersion with Becke-Johnson damping (D3BJ)<sup>32</sup> was used for all computations. The basis set combination (BS1) is defined as follows: for Ru and Fe, the Couty and Hall modification<sup>33</sup> (mod-LANL2DZ) to the valence basis set of LANL2DZ+ECP combination;<sup>9</sup> for Cl, when present, the LANL2DZ(d,p)+ECP combination;<sup>34-35</sup> and for C, H, N, and O the 6-31G(d')<sup>36-38</sup> basis sets (the 6-31G(d') basis sets have the d polarization functions taken from the 6-311G(d)<sup>39</sup> basis sets rather than the default value of 0.8<sup>40</sup> for C, N, and O). Spherical harmonic d functions were used throughout; *i.e.* there are 5 angular basis functions per d function. All geometries were fully optimized employing the SMD<sup>41</sup> implicit solvation model with parameters consistent with acetonitrile as the solvent. All stationary points were confirmed to be minima by an analytical frequency calculation at the same level of theory. Simulated IR absorption spectra were generated using an in-house Fortran program by convoluting<sup>42</sup> the computed normal modes and intensities from the analytical frequency calculation with a broadening of 5  $\text{cm}^{-1}$ . UV-VIS absorption spectra were simulated using TD-DFT<sup>43</sup> single points on the optimized geometries (TD-DFT//PBE0-D3BJ/BS1). To simulate the absorption spectra, the first 30 vertical excitations were solved iteratively [TD(ROOT=1,NSTATES=30)]. Simulated absorption spectra were generated using an in-house Fortran program by convoluting<sup>42</sup>

the computed excitation energies and oscillator strengths with a Gaussian line-shape and a broadening of 20 nm. Orbital images were generated in Chemcraft<sup>44</sup> using a contour value of 0.02.

## CHAPTER 8: CONCLUSION AND FUTURE WORK

In this dissertation, several transition metal-containing complexes with protic ligands were studied as they applied to the catalysis of water oxidation and carbon dioxide reduction.

In Chapter 2, the protic ligand 6,6'-dhbp was studied by UV/vis, IR, NMR, and computational methods to investigate the protonation states and tautomeric conformations of the free ligand. The neutral 6,6'-dhbp species was found to be in the lactam tautomer instead of the pyridinol tautomer and to be oriented in a trans-configuration. When fully deprotonated to form 6,6'-dhbp<sup>2-</sup>, the pyridinol and cis conformation was found to be the preferred conformer. These results should be applicable to the synthesis of catalysts containing 6,6'-dhbp, as syntheses performed under basic conditions result in 6,6'-dhbp being oriented in the appropriate pyridinol tautomer and cis conformation for binding to a metal center.

A copper-dhbp complex, [Cu(6,6'-dhbp)<sub>2</sub>]<sup>2+</sup>, was studied as a catalyst for electrochemical water oxidation in Chapter 3. It was found to have three p*K*<sub>a</sub> values at 5.2, 6.2, and 8.3 (2 protons) and to undergo demetallation at low and high pH. The proximal O-/OH groups of the 6,6'-dhbp ligand were found to likely play a role in proton transfer events, leading to improved catalysis; however, non-productive reaction pathways were also observed. Under basic conditions of water oxidation, the non-

innocent nature of the 6,6'-dhbp ligand helped to accelerate PCET events, which resulted in a lower overpotential.

Chapter 4 reported the catalytic ability of complexes containing bidentate ligands composed of NHC and pyridinol, as well as 6,6'-dhbp and 6,6'-dmbp, for CO<sub>2</sub> hydrogenation and formic acid dehydrogenation. The iridium complexes of the new NHC-py<sup>OR</sup> ligand are less active than the Ir(dhbp) complex and undergo decomposition and transformations during catalysis. Under basic conditions during CO<sub>2</sub> hydrogenation, Ru(dhbp) was nearly as active as Ir(dhbp) due to the second coordination sphere effects of deprotonated 6,6'-dhbp. The Lewis acidic alkali metal (i.e. Na<sup>+</sup> from the sodium bicarbonate base) was found to have a role in the mechanistic pathway, as the absence of an alkali metal results in lower TON. For CO<sub>2</sub> hydrogenation, complexes with the protic ligand 6,6'-dhbp—Ir(dhbp) and Ru(dhbp)—resulted in greater TON values under basic conditions (i.e. when 6,6'-dhbp is deprotonated) than the analogous complexes with 6,6'-dmbp, showing the impact that the deprotonated group has on catalysis.

In Chapter 5, the ruthenium analogs of the iridium NHC-py<sup>OR</sup> complexes from Chapter 4 were reported. The crystal structures of five of these complexes were reported. The PF<sub>6</sub><sup>-</sup> anion of one complex was found to undergo hydrolysis to form a PO<sub>2</sub>F<sub>2</sub><sup>-</sup> anion. Two of the complexes were preliminary tested as catalysts for CO<sub>2</sub> hydrogenation and formic acid dehydrogenation; however, they were found to undergo undesirable transformations under catalytic conditions.

Chapter 6 focused on a nickel-pincer complex containing a CNC-pincer composed of NHCs and a protic pyridinol. The nickel-pincer complex was synthesized and characterized by UV/vis, IR, MS, and EA, and the p*K*<sub>a</sub> of the complex was determined to

be 5.4(4) in DMSO. This complex was tested as a catalyst for photocatalytic CO<sub>2</sub> reduction to CO, and the oxygen anion of the ligand was found to have a large impact on catalysis—the complex with an oxygen anion was more active than the analogous complexes with a hydroxy group or a hydrogen in the same position. By changing the pH, the catalyst is able to be turned on or turned off.

Ruthenium-pincer complexes were studied spectroscopically and mechanistically in regard to their ability as CO<sub>2</sub> reduction catalysts in Chapter 7. UV/vis and IR spectroscopies and mass spectrometry were used to study the reduction of the complexes and the subsequent reaction with CO<sub>2</sub>. In situ IR spectra were measured of a reduced complex with CO<sub>2</sub>. Computations were also used to help determine a possible catalytic cycle for the reduction of CO<sub>2</sub> to CO.

Future work to continue studying the CO<sub>2</sub> reduction catalysts mechanistically should include the formation and observation of a ruthenium-carbonyl species. This would help further understanding of the catalytic intermediates and should be possible due to the exergonic nature of binding CO. ReactIR experiments with the reduced catalyst and a formate salt (e.g. sodium formate) should be performed to determine if the more nucleophilic formate binds to the ruthenium center more than formic acid. Experiments to probe the catalytic cycle that goes through a disproportionation would lead to a further understanding of how these catalysts work under varying conditions.

Several general conclusions can be drawn from these studies. Deprotonation of an OH group to form an O<sup>-</sup> led to increased TON for both water oxidation catalysis and CO<sub>2</sub> reduction catalysis, even when the O<sup>-</sup> group was remote from the metal center (e.g. the nickel-pincer complex in Chapter 6). However, under acidic conditions, when the O<sup>-</sup>

group is protonated to form OH, the catalyst behaves similarly to an OMe group (e.g. Chapter 4).

## REFERENCES

1. *Global Energy and CO<sub>2</sub> Status Report: The Latest Trends in Energy and Emissions in 2018*. International Energy Agency: Paris, France, 2019.
2. Hsiang, S.; Kopp, R.; Jina, A.; Rising, J.; Delgado, M.; Mohan, S.; Rasmussen, D. J.; Muir-Wood, R.; Wilson, P.; Oppenheimer, M.; Larsen, K.; Houser, T. *Science*, **2017**, *356*, 1362-1369.
3. Allen, M. R.; Dube, O. P.; Solecki, W.; et al., *Global Warming of 1.5 C: An IPCC Special Report. Chapter 1*. Intergovernmental Panel on Climate Change, 2018.
4. Blakemore, J. D.; Crabtree, R. H.; Brudvig, G. W. *Chem. Rev.*, **2015**, *115*, 12974-3005.
5. Mikkelsen, M.; Jørgensen, M.; Krebs, F. C. *Energy Environ. Sci.*, **2010**, *3*, 43-81.
6. Alonso, D. M.; Bond, J. Q.; Dumesic, J. A. *Green Chemistry*, **2010**, *12*, 1493-1513.
7. Krylova, A. Y.; Gorlov, E. G.; Shumovskii, A. V.; Yas'yan, Y. P.; Niskovskaya, M. Y. *Chemistry and Technology of Fuels and Oils*, **2018**, *54*, 243-248.
8. Demirbas, A. *Energy Conversion & Management*, **2001**, *42*, 1357-1378.
9. Wang, W.-H.; Ertem, M. Z.; Xu, S.; Onishi, N.; Manaka, Y.; Suna, Y.; Kambayashi, H.; Muckerman, J. T.; Fujita, E.; Himeda, Y. *ACS Catalysis*, **2015**, *5*, 5496-5504.
10. Onishi, N.; Xu, S.; Manaka, Y.; Suna, Y.; Wang, W. H.; Muckerman, J. T.; Fujita, E.; Himeda, Y. *Inorg. Chem.*, **2015**, *54*, 5114-23.
11. Suna, Y.; Himeda, Y.; Fujita, E.; Muckerman, J. T.; Ertem, M. Z. *ChemSusChem*, **2017**, *10*, 4535-4543.
12. Badiei, Y. M.; Wang, W. H.; Hull, J. F.; Szalda, D. J.; Muckerman, J. T.; Himeda, Y.; Fujita, E. *Inorg. Chem.*, **2013**, *52*, 12576-86.
13. Nieto, I. L., M. S.; Sacci, J. B.; Reuther, L. E.; Zeller, M.; Papish, E. T. *Organometallics*, **2011**, *30*, 6339-6342.
14. DePasquale, J.; Nieto, I.; Reuther, L. E.; Herbst-Gervasoni, C. J.; Paul, J. J.; Mochalin, V.; Zeller, M.; Thomas, C. M.; Addison, A. W.; Papish, E. T. *Inorg. Chem.*, **2013**, *52*, 9175-83.
15. Lewandowska-Andralojc, A.; Polyansky, D. E.; Wang, C.-H.; Wang, W.-H.; Himeda, Y.; Fujita, E. *Phys. Chem. Chem. Phys.*, **2014**, *16*, 11976-11987.

16. Umena, Y.; Kawakami, K.; Shen, J. R.; Kamiya, N. *Nature*, **2011**, *473*, 55-60.
17. Kawakami, K.; Umena, Y.; Kamiya, N.; Shen, J. R. *J. Photochem. Photobiol. B*, **2011**, *104*, 9-18.
18. Gersten, S. W.; Samuels, G. J.; Meyer, T. J. *J. Am. Chem. Soc.*, **1982**, *104*, 4030-4032.
19. Concepcion, J. J.; Jurss, J. W.; Brennaman, M. K.; Hoertz, P. G.; Patrocinio, A. O. T.; Murakami, I. N. Y.; Templeton, J. L.; Meyer, T. J. *Acc. Chem. Res.*, **2009**, *42*, 1954-1965.
20. McDaniel, N. D.; Coughlin, F. J.; Tinker, L. L.; Bernhard, S. *J. Am. Chem. Soc.*, **2008**, *130*, 210-217.
21. Hull, J. F.; Balcells, D.; Blakemore, J. D.; Incarvito, C. D.; Elsenstein, O.; Brudvig, G. W.; Crabtree, R. H. *J. Am. Chem. Soc.*, **2009**, *131*, 8730-8731.
22. Blakemore, J. D.; Schley, N. D.; Balcells, D.; Hull, J. F.; Olack, G. W.; Incarvito, C. D.; Eisenstein, O.; Brudvig, G. W.; Crabtree, R. H. *J. Am. Chem. Soc.*, **2010**, *132*, 16017-16029.
23. Limburg, J.; Vrettos, J. S.; Liable-Sands, L. M.; Rheingold, A. L.; Crabtree, R. H.; Brudvig, G. W. *Science*, **1999**, *283*, 1524-1527.
24. Shimazaki, Y.; Nagano, T.; Takasue, H.; Ye, B.-H.; Tani, F.; Naruta, Y. *Angew. Chem., Int. Ed.*, **2003**, *43*, 98-100.
25. Ellis, W. C.; McDaniel, N. D.; Bernhard, S.; Collins, T. J. *J. Am. Chem. Soc.*, **2010**, *132*, 10990-10991.
26. Singh, A.; Spiccia, L. *Coord. Chem. Rev.*, **2013**, *257*, 2607-2622.
27. Rigsby, M. L.; Mandal, S.; Nam, W.; Spencer, L. C.; Llobet, A.; Stahl, S. S. *Chem. Sci.*, **2012**, *3*.
28. Nakazono, T.; Parent, A. R.; Sakai, K. *Chem. Commun.*, **2013**, *49*, 6325-7.
29. Barnett, S. M.; Goldberg, K. I.; Mayer, J. M. *Nat. Chem.*, **2012**, *4*, 498-502.
30. Zhang, M. T.; Chen, Z.; Kang, P.; Meyer, T. J. *J. Am. Chem. Soc.*, **2013**, *135*, 2048-51.
31. Garrido-Barros, P.; Grau, S.; Drouet, S.; Benet-Buchholz, J.; Gimbert-Suriñach, C.; Llobet, A. *ACS Catalysis*, **2019**, *9*, 3936-3945.
32. Wang, D.; Bruner, C. O. *Inorg. Chem.*, **2017**, *56*, 13638-13641.

33. Gagliardi, C. J.; Vannucci, A. K.; Concepcion, J. J.; Chen, Z.; Meyer, T. J. *Energy Environ. Sci.*, **2012**, *5*.
34. Pletcher, D. *Electrochem. Comm.*, **2015**, *61*, 97-101.
35. Francke, R.; Schille, B.; Roemelt, M. *Chem. Rev.*, **2018**, *118*, 4631-4701.
36. Aresta, M., *Carbon Dioxide as Chemical Feedstock*. Wiley-VCH: Weinheim, 2010.
37. Benson, E. E.; Kubiak, C. P.; Sathrum, A. J.; Smieja, J. M. *Chem. Soc. Rev.*, **2009**, *38*, 89-99.
38. Pegis, M. L.; Roberts, J. A.; Wasylenko, D. J.; Mader, E. A.; Appel, A. M.; Mayer, J. M. *Inorg. Chem.*, **2015**, *54*, 11883-8.
39. Bernskoetter, W. H.; Hazari, N. *Acc. Chem. Res.*, **2017**, *50*, 1049-1058.
40. Jadhav, S. G.; Vaidya, P. D.; Bhanage, B. M.; Joshi, J. B. *Chem. Eng. Research and Design*, **2014**, *92*, 2557-2567.
41. Kar, S.; Kothandaraman, J.; Goeppert, A.; Prakash, G. K. S. *Journal of CO2 Utilization*, **2018**, *23*, 212-218.
42. Singh, A. K.; Singh, S.; Kumar, A. *Cat. Sci. Technol.*, **2016**, *6*, 12-40.
43. Zell, T.; Butschke, B.; Ben-David, Y.; Milstein, D. *Chemistry*, **2013**, *19*, 8068-72.
44. Langer, R.; Diskin-Posner, Y.; Leitus, G.; Shimon, L. J.; Ben-David, Y.; Milstein, D. *Angew. Chem., Int. Ed.*, **2011**, *50*, 9948-52.
45. Mellone, I.; Gorgas, N.; Bertini, F.; Peruzzini, M.; Kirchner, K.; Gonsalvi, L. *Organometallics*, **2016**, *35*, 3344-3349.
46. Bertini, F.; Gorgas, N.; Stöger, B.; Peruzzini, M.; Veiros, L. F.; Kirchner, K.; Gonsalvi, L. *ACS Catalysis*, **2016**, *6*, 2889-2893.
47. Inoue, Y.; Izumida, H.; Sasaki, Y.; Hashimoto, H. *Chem. Lett.*, **1976**, 863-864.
48. Sanz, S.; Benítez, M.; Peris, E. *Organometallics*, **2010**, *29*, 275-277.
49. Azua, A.; Sanz, S.; Peris, E. *Chemistry*, **2011**, *17*, 3963-7.
50. Tanaka, R. Y., M.; Nozaki, K. *J. Am. Chem. Soc.*, **2009**, *131*, 14168-14169.
51. Huff, C. A.; Sanford, M. S. *ACS Catalysis*, **2013**, *3*, 2412-2416.
52. Ziebart, C.; Federsel, C.; Anbarasan, P.; Jackstell, R.; Baumann, W.; Spannenberg, A.; Beller, M. *J. Am. Chem. Soc.*, **2012**, *134*, 20701-4.

53. Federsel, C.; Boddien, A.; Jackstell, R.; Jennerjahn, R.; Dyson, P. J.; Scopelliti, R.; Laurenczy, G.; Beller, M. *Angew. Chem., Int. Ed.*, **2010**, *49*, 9777-80.
54. Fong, H.; Peters, J. C. *Inorg. Chem.*, **2015**, *54*, 5124-35.
55. Federsel, C.; Ziebart, C.; Jackstell, R.; Baumann, W.; Beller, M. *Chem. - Eur. J.*, **2012**, *18*, 72-5.
56. Jeletic, M. S.; Mock, M. T.; Appel, A. M.; Linehan, J. C. *J. Am. Chem. Soc.*, **2013**, *135*, 11533-6.
57. Spentzos, A. Z.; Barnes, C. L.; Bernskoetter, W. H. *Inorg. Chem.*, **2016**, *55*, 8225-33.
58. Zeller, K.-P.; Schuler, P.; Haiss, P. *E. J. Inorg. Chem.*, **2005**, *2005*, 168-172.
59. Wang, W.-H.; Himeda, Y.; Muckerman, J. T.; Manbeck, G. F.; Fujita, E. *Chem. Rev.*, **2015**, *115*, 12936-12973.
60. Steynberg, A., *Fischer-Tropsch Technology*. Elsevier Science: 2004; Vol. Vol. 152.
61. Barnard, C. F. J. *Organometallics*, **2008**, *27*, 5402-5422.
62. Liu, Q.; Zhang, H.; Lei, A. *Angew. Chem., Int. Ed.*, **2011**, *50*, 10788-99.
63. Brennfuhrer, A.; Neumann, H.; Beller, M. *Angew. Chem., Int. Ed.*, **2009**, *48*, 4114-33.
64. Morris, A. J.; Meyer, G. J.; Fujita, E. *Acc. Chem. Res.*, **2009**, *42*, 1983-94.
65. Huckaba, A. J.; Sharpe, E. A.; Delcamp, J. H. *Inorg. Chem.*, **2016**, *55*, 682-690.
66. Sato, S.; Morikawa, T.; Kajino, T.; Ishitani, O. *Angew. Chem., Int. Ed.*, **2013**, *52*, 988-92.
67. Zhang, B.; Sun, L. *Chem. Soc. Rev.*, **2019**, *48*, 2216-2264.
68. Wang, J.-W.; Zhong, D.-C.; Lu, T.-B. *Coord. Chem. Rev.*, **2018**, *377*, 225-236.